Numerical modelling and metallurgical characterization of Cr-Mo steels processed by directed energy deposition

by

Shaun Cooke
B.Eng, University of Victoria, 2019

A Thesis Submitted in Partial Fulfillment of the
Requirements for the Degree of

MASTER OF APPLIED SCIENCE

in the Department of Mechanical Engineering

© Shaun Cooke, 2021
University of Victoria

All rights reserved. This thesis may not be reproduced in whole or in part, by photocopying or other means, without the permission of the author.

Numerical modelling and metallurgical characterization of Cr-Mo steels processed by directed energy deposition

by

Shaun Cooke
B.Eng, University of Victoria, 2019

Supervisory Committee

Dr. Keivan Ahmadi, Co-Supervisor
(Department of Mechanical Engineering)

Dr. Rodney Herring, Co-Supervisor
(Department of Mechanical Engineering)

ABSTRACT

Additive manufacturing (AM) provides unique opportunities to push the boundaries of material properties and free form fabrication. However with this novel manufacturing technique a number of defects not commonly found in conventional processes such as machining or casting can arise. Both experimental and numerical studies can help better understand the printed material on a more fundamental level in order to optimize the process and mitigate these defects. Electron microscopy can provide essential information about the as-built microstructure and characteristic defects while numerical modelling can help determine a correlation between process parameters and the resulting properties.

First, an initial investigation of directed energy deposition (DED) processed 4140 steel was conducted using various microscopy methods to better understand the defects and microstructure of the printed alloy. A martensite dominate microstructure within a bainitic matrix with increasing degrees of tempering further down the build was revealed. Additional sample preparation was conducted with a focused ion beam and analyzed with the transmission electron microscope to investigate features such as grain boundaries, mechanical twins and interplanar spacing. This interplanar spacing was measured for a number of different diffraction images and compared with the theoretical values. The deviation between the measured and theoretical values can be attributed to defects such as residual stress which causes lattice strain and consequently a smaller or larger spacing between atomic planes. Lastly, diffraction images were characterized and compared with the literature to determine the Miller indices and the specific zone axis orientations.

A thermo-mechanical-metallurgical finite element model for 42CrMo4 steel was then developed in ABAQUS to identify the correlation between processing parameters and resulting properties by predicting the temperature history, and resulting residual stresses and metallurgical phase fractions for the DED process. A preprocessing framework was implemented in order to allow the modelling of complex geometries and laser trajectories while experiments were conducted to validate the fidelity of the model. Four separate cases were fabricated with varying processing parameters and geometries. In addition to in-situ temperature measurements, post-build residual stress and substrate distortion data was also collected. Furthermore, metallurgical analysis was performed for each case and compared with the simulated

phase fractions. The accuracy of the distortion profile increased with increasing dwell time while the accuracy in predicting the metallurgical phase fractions and residual stresses demonstrated the opposite trend.

Contents

Supervisory Committee ii

Abstract iii

Table of Contents v

List of Tables viii

List of Figures ix

Acknowledgements xvi

1 Thesis Overview 1

1.1 Objectives . . . 1
1.2 State of the art contributions . . . 2
1.3 Outline . . . 3

2 Literature Review 4

2.1 Introduction . . . 4
2.2 Printer Technology and Methods . . . 5
2.2.1 Powder Atomization Techniques . . . 6
2.2.2 Powder Bed Fusion Systems . . . 8
2.2.3 Direct Energy Deposition . . . 9
2.2.4 Laser Melting vs. Electron Beam Melting . . . 10
2.2.5 Binder Jetting Systems . . . 11
2.3 Melt Pool Characterization . . . 14
2.4 Common Defects in Metal AM . . . 17
2.4.1 Porosity . . . 18
2.4.2 Lack of Fusion During the Printing Process . . . 19
2.4.3 Ball Formation . . . 19

2.4.4 Residual Stresses and Cracking 20
2.5 Current Alloys in Metal Additive Manufacturing 22
2.5.1 Pure Metals 22
2.5.2 Pre-Alloyed Metals 24
2.6 Process Control and Optimization Techniques 32
2.6.1 Grain Morphology 32
2.6.2 Process Monitoring Techniques 39
2.7 Computational Modelling 42
2.7.1 Computational Fluid Dynamics 42
2.7.2 Finite Element Modelling 44
2.7.3 Microstructure Growth and Nucleation Modelling for AM processes 48
2.8 Post Processing Methods 51
2.8.1 Hot Isostatic Pressing 51
2.8.2 Heat Treatment 52
2.8.3 Polishing Techniques 53
2.9 Conclusion 57

3 Investigation of direct energy deposition processed 4140 steel using electron microscopy methods 59
3.1 Introduction 59
3.2 Background 60
3.3 Experimental Procedure 62
3.3.1 DED Process and Conditions 62
3.3.2 Materials 63
3.3.3 TEM Specimen Preparation 65
3.4 Material Characterization 66
3.4.1 Microstructure and macroscopic defects 66
3.4.2 TEM imaging 73
3.5 Conclusion 78
3.6 Future Work 79

4 Thermo-mechanical-metallurgical modelling, validation and characterization of 42CrMo4 steel processed by directed energy deposition 80

4.1 Introduction 80
4.2 Numerical model 82
4.2.1 Pre-processing 83
4.2.2 Thermal analysis 85
4.2.3 Mechanical analysis 91
4.3 Materials 94
4.4 Case studies and experimental setup 95
4.4.1 Case Studies 95
4.4.2 Experimental setup 96
4.5 Modelling implementation 99
4.5.1 FEM mesh 99
4.5.2 Laser Trajectory 100
4.5.3 Material property input data 100
4.5.4 Initial and boundary conditions 102
4.6 Results and discussion 104
4.6.1 Thermal analysis 104
4.6.2 Metallurgical analysis 110
4.6.3 Mechanical analysis 117
4.7 Conclusions 121
4.8 Future work 122

5 Conclusion **125**

A Metallurgical data for AISI 4140 steel **127**

B Johnson–Mehl–Avrami–Kolmogorov diffusional transformation model data **130**

C Bead size determination **132**

Bibliography **134**

List of Tables

Table 2.1 Comparison of mechanical properties of SLM processed maraging steel using water and gas atomized powders. Modified from [35] 8

Table 3.1 Machine Specifications for the printer used in this experiment. Information provided by the Royal Canadian Navy. 63
Table 3.2 Process parameters used during printing for the fabrication of the column. Information provided by the Royal Canadian Navy. . . 63
Table 3.3 Gas-atomized 4140 steel powder composition 64
Table 3.4 Lattice parameters and interplanar spacing for cubic systems . . 76
Table 3.5 Interplanar spacing values 77

Table 4.1 Constraints imposed in the metallurgical framework to control the nucleation of each phase. 90
Table 4.2 Volume fraction percentages comparing the values obtained from the 4140 steel continuous cooling transformation diagram [302, 323] and the metallurgical framework developed for this study. . 91
Table 4.3 Chemical composition of 42CrMo4 steel compared to AISI 4140 steel [327] in percentages 94
Table 4.4 Processing parameters used in each case for this experiment . . 95
Table 4.5 Machine specifications for the Optomec LENS HY-20-CA system with a YLR-1000-MM-WC laser used in this study. 97
Table 4.6 Temperature dependent thermal and mechanical properties for 4140 steel from [329] 101
Table 4.7 Thermal expansion and volume changes of steel phases from [304] 102
Table 4.8 Error between experimental and simulated data cases for each thermocouple during printing 107

List of Figures

Figure 2.1 Powder metallurgy processes used to produce powder feedstock for AM systems a) gas atomization process. Reproduced with permission from [31]. b) water atomization process courtesy of [32] 7

Figure 2.2 Water atomized (a) and gas atomized (b) stainless steel 316L powders. Reproduced with permission from [37]. 8

Figure 2.3 Various additive manufacturing printing technologies including: a) laser powder bed fusion from [55] b) electron powder bed fusion; courtesy of GE additive [13, 56] c) direct energy deposition powder feed with laser [5] d) direct energy deposition wire feed with electron beam courtesy of Sciaky, Inc. EBAM® is a registered trademark of Sciaky, Inc. [57] e) binder jetting printing and f) spreading and drying process modified from [48]. Images reproduced with permission. 13

Figure 2.4 Computational fluid dynamics simulation of Marangoni turbulence in the melt pool during metal additive manufacturing reproduced with permission from [66]. Red corresponds to temperature scale at 4000K and blue is 293K. 15

Figure 2.5 Relative density of as-built SLM-processed AlSi10Mg samples with respect to (a) laser power, (b) energy density, (c) hatch spacing, and, (d) scan speed reproduced with permission from [75]. 17

Figure 2.6 Common defects in metal additive manufacturing: a) large pores on the range of 20 µm and b) micro-pores on the scale of 200 nm in SLM processed 316L c) lack of fusion between layers from [83] d) ball formation during printing process from [84] and e) residual stress distribution in SLM processed 316L where i-iii) are top surface displacements and iv) is a scaled up deformation schematic from [85]. Images reproduced with permission. 21

Figure 2.7 Microstructures of conventional and AM processed alloys; a) cast microstructure and b) SLM processed 316L stainless steel from [109] c) wrought and d) SLM microstructure of 17-4 PH stainless steel from [113] e) conventional and f) LAM processed microtrucutre of H13 tool steel from [125] g) conventional and h) laser metal deposition (LMD) EBSD images showing microstrucuture and amount of austenite within martensite of M300 from [117] i) IN 718 cast and j) SLM microstrucutres [132] k) EBM processed CoCrMo and l) wrought CoCrMo microstructures from [154] m) cast $AlSi_{10}Mg$ alloy from [182] n) and SLM counterpart from [157] o) conventional Al 6061 microstrucutre [183] and p) SLM microstructure from [164] q) Wrought and r) SLM microstrucutre for Ti64 from [173]. All images reproduced with permission. 31

Figure 2.8 Types of grain growth with respect to temperature gradient as a function of interface velocity. Image reproduced with permission from [192]. 33

Figure 2.9 Melt pool solidification of an alloy on a base metal substrate with a crystallographic orientation along the <100> directions during welding and similar AM processes. Reproduced with permission from [185] 35

Figure 2.10a) Solidification map for Ti-6Al-4V and b) process map for controlling the microstructure for Ti-6Al-4V. Reproduced with permission from [199]. 36

Figure 2.11Closed-loop feedback experimental setup to monitor the thermal gradients using infrared cameras to adjust the printing parameters and control the microstructure. Reproduced with permission from [216]. 41

Figure 2.12CFD analyses for the AM process a) laser scan on powder bed during SLM process [230] b) CFD simulation of keyhole formation [234]. Both images reproduced with permission. 43

Figure 2.13Finite element modelling of the DED process: a) thermal analysis illustrating inactive or quiet elements from [222] b) metallurgical analysis reproduced from [196], with the permission of the Laser Institute of America. c) mechanical analysis from [221]. All images reproduced with permission. 45
Figure 2.14Metallurgical nucleation and grain growth simulations of the AM process a) cellular autonoma simulation compared with experimental results [193] b) Monte Carlo simulation compared with experimental results [204]. Images reproduced with permission. 50
Figure 2.15Surface roughness of as-built LPBF processed 316L 52
Figure 2.16a) HIP treatment of SLM-processed 316L composites reinforced with 15 vol.% of TiB2 where i) is before HIP treatment and using ball-milled powder and ii) after two HIP treatment cycles from [251] b) EBSD images of solution heat treatment for SLM processed and wrought 17-4PH SS from [113] c) electrolytic polishing of pure AM built Ti where i) as built surface ii) treated for 60s at 30V and iii) treated for 600s at 30V from [270] d) SEM micrograph showing the junction between laser polished and as-built SLM surface of 316L stainless steel [271] e) Shot peened surface of SLM processed $AlSi_{10}Mg$ [274]. All images reproduced with permission. 56

Figure 3.1 Build session schedule showing the number of layers for each build and the date it was printed. Information provided by the Royal Canadian Navy. 62
Figure 3.2 The printer head and chamber for the DED system used in this experiment. 64
Figure 3.3 As-recieved gas atomized 4140 powder (left) and recycled powder sieved and reused after 25 cycles (right). 65
Figure 3.4 Initial cuts on fib for tem specimen 66
Figure 3.5 Optical micrographs of DED processed 4140 steel along the plane parallel to building direction showing a) top layer defects b) top layer microstructure c) weld track lines and d) mid section microstructure 67

Figure 3.6 SEM images of DED processed 4140 steel along the plane parallel to build direction showing large martensite lath and bainite in the top section in a) and b), tempered martensite in the middle section in c) and d), and smaller rounded tempered martensite within a bainitic matrix on the bottom in e) and f). 69
Figure 3.7 Optical micrographs of DED processed 4140 steel along the plane orthogonal to building direction showing a) microstructure at 20x mag b) microstructure at 50x mag c) weld track lines and d) microporosity 70
Figure 3.8 SEM images of DED processed 4140 steel along the plane orthogonal to the building direction showing tempered martensite lath within bainite matrix in the bulk of the material in a) and b), and finer microstructure along the weld lines in c) and d). . 71
Figure 3.9 Optical micrographs of wrought 4140 steel a) equiaxed grains at 10x mag parallel to rolling direction b) microstructure at 50x mag parallel to rolling direction c) equiaxed and elongated grains at 10x mag orthogonal to rolling direction and d) microstructure at 50x mag orthogonal to rolling direction 72
Figure 3.10 SEM images of wrought 4140 steel at a) 2200x magnification and b) 7000x magnification 72
Figure 3.11 Schematic of the zone axis direction in relation to atomic planes 73
Figure 3.12 First lattice image with corresponding diffraction pattern obtained through a fast Fourier transformation. Diffraction pattern indexed according to ref. [285] and the associated zone axis direction was determined to be along the $[\bar{1}11]$ direction. 74
Figure 3.13 Second lattice image with corresponding diffraction pattern obtained through a fast Fourier transformation. Diffraction pattern indexed according to ref. [285] and the associated zone axis direction was determined to be along the [011] direction. 75
Figure 3.14 Systematic rows captured in reciprocal space in the TEM with a beam blocker blocking the intensity of the main beam. 76
Figure 3.15 Lattice images showing grain boundaries with a) the distinction in contrast between the top half and the bottom half and b) three separate grains with lines added highlighting the different atomic plane orientation. 77

Figure 3.16Different images taken on the TEM showing a) bright field image showing the contrast variation within the sample and b) a mechanical twin with the atomic plane orientations and twin boundaries highlighted. 78

Figure 4.1 Flow chart for the thermo-mechanical-metallurgical model illustrating the subroutines and material models used. The finite element model was developed in ABAQUS 2020 and the subroutines were written in FORTRAN. 83
Figure 4.2 Input files and the relevant softwares used to produce the element activation array and laser coordinate array for the FEM software modified from [310] 84
Figure 4.3 Schematic of element activation with respect to laser position and element centroid modified from [310] 85
Figure 4.4 Goldak double ellipsoid volumetric heat source showing a) the schematic modified with permission from [299, 315] and b) the distribution with the parameters used in this study 88
Figure 4.5 Water atomized 42CrMo4 steel powder 95
Figure 4.6 Post build dimensions for a) case 1 with 0s dwell b) case 2 with 20s dwell c) case 3 with 40s dwell d) case 4 cube with 0s dwell 96
Figure 4.7 Build setup on cantilever substrate secured at one end 97
Figure 4.8 Thermocouple location on 4140 steel substrate for case 1 - 3 . . 98
Figure 4.9 Finite element mesh for the 38.1mm x 3.6mm x 6mm thinwall cases on the cantilevered substrate and fixture constructed by a total of 75,013 elements and 84,720 nodes. 100
Figure 4.10Laser scanning strategy for a) case 1-3 starting from n=0 to 10 for a total of 20 layers and b) case 4. The cube outline remains constant across all layers but the internal scanning strategy is rotated 90° counter clockwise each layer. 101
Figure 4.114140 steel plasticity data at a strain rate of approximately 0.002/s adopted from data collected by Ref. [330]. 102
Figure 4.123D surface plot of convection coefficient with respect to z-step and radial distance form laser center for a) wall and b) top of the substrate 103

Figure 4.13Plots showing the simulated and experimental data for the bottom and side thermocuples during printing for all four cases. . . 106
Figure 4.14Simulated and experimental meltpool areas as a function of build time. The upper and lower limits on the experimental data represent the smallest and largest measurements made within a 5 second window. The actual value plotted was taken on the lower end of this range with multiple measurements with similar values. The large range in measurements arise from incandescent vapour and spatter greatly increasing the measured area while the lowest range could represent a meltpool which as not been fully developed. 108
Figure 4.15Measured meltpool area obtained form the meltpool sensor during printing of case 4 and the simulated meltpools at the corresponding build time and their associated calculated areas. The grey area in the simulation represents points within the model which have exceeded the liquidus temperature (1420°C) of 4140 steel. 109
Figure 4.16Experimental metallography analysis for case 1 on the top, middle and bottom sections. Simulated phase fractions along the middle cross-section is also compared with the observed microstructural constituents. 111
Figure 4.17Experimental metallography analysis for case 2 on the top, middle and bottom sections. Simulated phase fractions along the middle cross-section is also compared with the observed microstructural constituents. 113
Figure 4.18Experimental metallography analysis for case 3 on the top, middle and bottom sections. Simulated phase fractions along the middle cross-section is also compared with the observed microstructural constituents. 114
Figure 4.19Experimental metallography analysis for case 4 on the top, middle and bottom sections. Simulated phase fractions along the middle cross-section is also compared with the observed microstructural constituents. 116

Figure 4.20Post-build distortion profile from the clamped end to the free end of the AISI 4140 steel substrate used for a) case 1 b) case 2 and, c) case 3. 117
Figure 4.21Measured and simulated normal residual stresses along the y-direction 119
Figure 4.22Simulated residual stress contours for thinwall cross-sections. . . 120

Figure A.1 Fe-C equilibrium phase diagram highlighting microstructural changes and the A1 and A3 points for a 0.4%C hypoeutectoid steel taken from [304, 339] with permission. 127
Figure A.2 Time-temperature-transformation diagram for 4140 steel taken from [304, 319] with permission. 128
Figure A.3 Continuous-cooling-transformation diagram for 4140 steel indicating the percentages of each phase formed at a variety of cooling rates taken from [302, 323] with permission. 129
Figure A.4 Continuous heating transformation diagram for 4140 steel for various heating rates modified with permission from [340]. . . . 129

Figure B.1 Avrami curves calculated for each temperature based on determined k and n coefficients for 4140 steel 130
Figure B.2 Additivity rule used to transform the isothermal JMAK equations to an iso-kinetic formulation. Taken from [302] with permission. 131

Figure C.1 Contour plot of bead width with respect to laser power and scanning speed. This relationship was determined empirically for the model so the element activation distance could be set within the model. 133

ACKNOWLEDGEMENTS

I would like to thank:

My family, for being supportive of my goals and helping me achieve everything I have.

Drs. Keivan Ahmadi and Rodney Herring, for their mentoring, support, encouragement, and patience throughout both my undergraduate and master's degree.

Dr. Sardar Malekmohammadi for his time and effort in the examination of this thesis and providing valuable comments to improve the quality of this work.

NSERC and the Government of British Columbia for providing me with scholarships to support my research.

Drs. Gregory Sweet and Paul Bishop, at Dalhousie University for their collaboration and expertise in helping me run experiments.

Tom Percy, Christopher Chang, Barry Ross and Matthew Raine at the Department of National Defence and Royal Canadian Navy for their collaboration and generosity.

Drs. Elaine Humphrey, Arthur Blackburn and Cristina Cordoba in the Advanced Microscopy Facility for their patience and help using the electron microscope for the results of this thesis.

Chapter 1

Thesis Overview

Metal additive manufacturing (AM) uses data from a three-dimensional (3D) computer-aided design (CAD) file to fuse together materials through layer-by-layer deposition to fabricate the desired component. This allows for the development of complex geometries and properties unattainable by conventional processes [1]. Contrast to conventional subtractive processes where a block of metal is machined into shape, this process uses metal powder (most often) to additively build up the component from a substrate. Metal AM has seen a large surge in literature contributions and industry interest over the past decade [1]. However, due to the unique manufacturing technique and different material properties compared to conventionally manufactured components, there are many obstacles to overcome in order to drive metal AM for mainstream adoption. For example, the mechanical properties and metallurgical characteristics of the printed alloy vary greatly depending on the type of printer and the associated processing parameters. Thus, understanding the underlying physics of the process and characterizing the associated defects is crucial in order to validate AM processed components for engineering applications. Experimental data and numerical modelling of the process can construct a correlation between the processing parameters and the resulting properties. Eventually, such models can be used to optimize the AM process to then control the microstructure and mitigate any defects.

1.1 Objectives

The goal of this thesis to better understand the unique characteristics that Cr-Mo steels (specifically, 42CrMo4 and AISI 4140 steel) exhibit during the directed energy deposition process (DED). In addition to investigating the as-built microstructures and defects, a thermo-mechanical-metallurgical (TMM) numerical model of the DED process was developed to provide insight about the correlation between printing pa-

rameters and the evolution of material properties during deposition. The main objectives of this study are as follows:

- To provide a comprehensive review of metal additive manufacturing and identify current gaps in the literature.
- Investigate and characterize the defects and microstructure of 4140 steel fabricated by DED using electron microscopy methods. This provides a deeper understanding of the printed alloy on a more fundamental level.
- Develop an accurate numerical model of the DED process for 42CrMo4 steel for a variety of process parameters validated by experimental measurements. This model is developed so that eventually it could provide the capability to accurately model various geometries and be used to optimize the printing parameters to control the microstructure and reduce residual stresses.

1.2 State of the art contributions

Currently, little research has been conducted on Cr-Mo steels processed by AM while there are no FE models of 42CrMo4 or 4140 steel processed by DED in the literature. Wang et al. [2] presented their results on 4140 steel processed by laser powder bed fusion (LPBF). They characterized the microstructure using optical and scanning electron microscopes and the as-built yield strength through tensile testing. It can be noted however, that LPBF components do not always exhibit the same characteristics as parts fabricated by the DED process [1]. Additionally, they did not look deeper into the material using transmission electron microscopy to image sub-microstructural defects and characteristics. This thesis provides the following contributions to the current state of the art:

- Characterization of DED processed 4140 steel using electron microscopy methods to investigate nano-twins, crystallographic orientation and interplanar spacing.
- Unified TMM model for 42CrMo4 steel capable of accurately predicting the thermal history, residual stress, substrate distortion and microstructure.

1.3 Outline

This thesis is divided into five separate chapters to help convey the material being presented. The layout is as follows:

- Chapter 1 provides a brief overview of metal AM, the objectives of this thesis and the contributions to the state of the art.
- Chapter 2 presents a comprehensive literature review of the metal AM field. The different types of printer technologies are discussed which is followed by a review of the laser-material interaction and meltpool formation. Defects characteristic of the AM process are then discussed, followed by the current library of printable alloys compared to their wrought counterparts. The rest of the paper presents a number of process optimization methods, numerical models and post-processing treatments.
- Chapter 3 provides an experimental study of DED processed 4140 steel on a µm and nm scale. Samples were prepared by the Royal Canadian Navy and specimens were fabricated using a focus ion beam for the transmission electron microscope. Here, the microstructure, grain boundaries, twinning and interplanar spacing is investigated. It is important to better understand the printed material on a more fundamental level to discern the complexities introduced by this manufacturing method.
- Chapter 4, presents the methodology and validation of a finite element thermo-mechanical numerical model for the DED process. A pre-processing framework is implemented to allow for complex geometries and laser trajectories directly from the specified G-code. This model then predicts the temperature, microstructure, residual stresses and substrate distortion during printing. A number of experimental data was collected to validate the thermal and microstructural history during deposition and the post-build residual stresses and substrate distortion.
- Chapter 5 provides the conclusions of this thesis and highlights the outcomes of this study.

Chapter 2

Literature Review

Reprinted from Journal of Manufacturing Processes, Volume 57, S. Cooke, K. Ahmadi, S. Willerth, R. Herring, Metal additive manufacturing: Technology, metallurgy and modelling, Pages 978-1003, Copyright (2020), with permission from Elsevier.

2.1 Introduction

Additive manufacturing (AM) uses data contained in a 3D model to join together materials by repeated layer deposition to generate the target structure [3]. This method allows for the development of geometrically complex objects unable to be manufactured by conventional means and the ability to perform rapid prototyping [4, 5]. Complex internal lattice structures can only be achieved using AM and can maintain the overall strength of the part while greatly reducing its weight by lowering density and using coarser mesh in low stress bearing areas [6]. This one-step method of manufacturing minimizes manufacturing time and waste of energy and materials due to its ability to produce objects on demand [7]. Additionally, AM provides a new frontier in terms of controlling and tuning the microstructure of the target product and consequently, the mechanical properties of the printed structure [4, 8, 9]. The metal AM industry has seen a surge in 3D printer technology with highly advanced devices and methods, however, the number of metal alloys than can be reliably printed is minimal. The vast majority of metal alloys used in conventional processes are unable to produce adequate parts in AM [8].

During the printing process, cyclic phase transformations (liquid-solid and solid-solid) occur due to the repeated layer deposition and rapid solidification [9] which varies between AM equipment, geometry and printing parameters [10]. These variables greatly influence the microstructure, which can yield long columnar grains,

porosity and irregular cracks, which consequently degrade the mechanical properties of the material [5,8,11]. Since AM fabricated alloys experience repeated melting and rapid solid-state phase transformations, complexities not typically found in conventional processes are introduced. However, metal components manufactured by AM usually exhibit finer microstructures than their conventionally manufactured counter parts and thus can have higher yield and ultimate strengths [8].

Wohlers Report 2019, a 3D printing industry analyst, stated that for additive manufacturing: "revenue from metals grew an estimated 41.9%, continuing a five-year streak of more than 40% growth each year" [12]. The automotive and aerospace industries are quite keen on exploiting the advantages of metal AM. Due to the large surge in AM, it is incumbent to better understand the connection between the material properties, microstructure and processing method in order to produce consistent, qualified and reliable parts suitable for engineering applications.

There are many excellent and detailed review papers on metal AM but in a fast-growing industry, new technology and discoveries are being published often. Most review papers on metal AM are either several years old [5,13] or focus are tailored to specific areas including defects [10,14,15], processing and optimization methods [16–18], materials [4,7,19–22] and, mechanical properties [23–25], but few have provided a complete picture of metal AM and its capabilities in the industry. This review paper takes a different approach by outlining the most prevalent processing methods in AM and introducing the complex physics of the process and the relationship between process parameters and defects. Furthermore, the common defects associated with metal AM are discussed, as well as the various current AM processable alloys. Lastly, process optimization, computational modelling, and post processing treatments are investigated.

2.2 Printer Technology and Methods

Metal AM systems require a metal feedstock to be melted and deposited on a substrate to then construct layers which eventually form a desired geometry. Although some systems used a solid wire feed, most commercial methods use metal powder. All AM systems work on the same principal of building a structure additively from a substrate,

however the two most common commercialized methods for metal AM include Powder Bed Fusion (PBF) and Direct Energy Deposition (DED) [8, 13]. While each method has advantages and disadvantages, the most available systems on the market are laser powder bed fusion (LPBF) printers due to their superior resolution with a typical layer thickness between 10–50 µm while powder-fed DED printers have around a 250 µm layer thickness [13]. However, an important factor in both the precision and quality of the build begins with the development of the alloy powder.

2.2.1 Powder Atomization Techniques

The metal powder morphology serves as a key component in the final quality of the printed part. Thus, a consistent powder geometry, composition and flowability is required to ensure the repeatability of the metal printed structures [4, 13, 26]. The atomized metal used in AM must have a specific size to ensure a good packing behavior and limit porosity [26]. The average particle size distribution used in LPBF is 10-45 µm and 20-200 µm in DED [13]. Additionally, powder flowability improves with increased sphericity and therefore dictates the quality of the finished product [4]. However, if the powder is too flowable, then spreading defects can be produced so some roughness or irregularity helps keep the powder in place during deposition. The required powder properties also vary depending on the AM system that is used [13], therefore extensive research is still required to allow the same metal powder to be reliably printed on different machines. If the metal powder properties such as size, sphericity, surface texture and chemical composition vary within a single batch, the printed part may contain more prominent defects, such as high porosity and poor surface finish [27].

Several techniques exist for atomizing the metal including: gas atomization, high-pressure water atomization, plasma rotating electrode, plasma atomization, electrolytic processing, and mechanical crushing [28]. However, the most common and preferred method in industry is predominantly gas atomization and in some circumstances, high-pressure water atomization [29, 30] which are illustrated in figure 2.1. Both processes pour molten metal through a nozzle which then comes in contact with a high-pressure fluid stream. This stream separates and quenches the metal into small particulates which can then be used for metal AM.

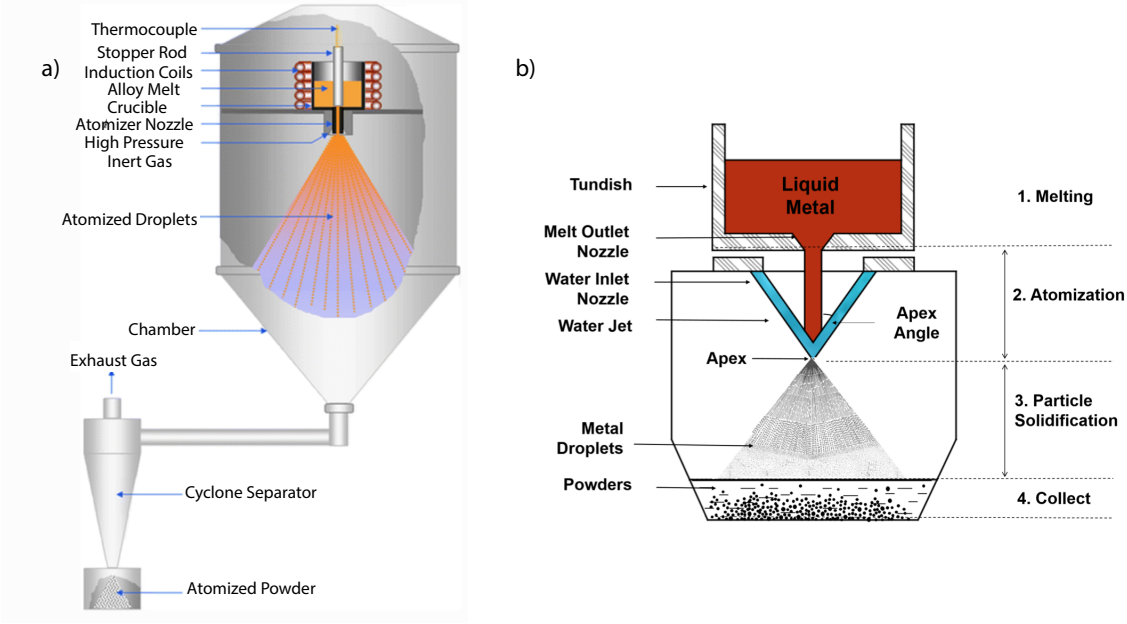

Figure 2.1: Powder metallurgy processes used to produce powder feedstock for AM systems a) gas atomization process. Reproduced with permission from [31]. b) water atomization process courtesy of [32]

Water atomized powders are usually less expensive than the gas-atomized counterparts, however these powders usually are irregular in shape which affect the flowability and quality of the printed part [33]. This is due to the rapid quenching and the high energy water jet impacting the molten stream which is less desirable as it reduces flowability and packing density [30]. Gas atomization usually uses steam, natural air or an inert gas to produce extremely small, spheroidal metal particles within a diameter between 10 and 300 µm [28]. However, gas atomization is frequently used for high quality powders with high sphericity, purity and low oxygen content [29]. Since the powder quality and size distribution can affect the density, surface quality and, mechanical properties, a high number of fine particles is required to optimize the part while limiting the number of large particles [34]. Smaller particles produce a thinner layers since they pack more efficiently than large particles [4].

Small particles with a homogeneous size distribution and spherical shape ensure equivalent melting and cooling rates along the layers, yielding a higher quality product. If the metal powder has a low packing density ($< 50\%$), then the gas present in the particles have a high probability to dissolve in the melt pool and yield

defects such as pores [10]. A study by Hoeges et al [35] compared the mechanical properties of laser PBF processed age-hardened maraging steel with gas and water atomized powder feedstocks. Table 2.1 illustrates the contrast in density, ultimate tensile strength, elongation and hardness for both samples. It is evident that gas-atomized powders yield superior mechanical properties to water-atomized powders, making them mostly preferred [36]. SEM images of water and gas atomized powders can be seen in figure 2.2.

Table 2.1: Comparison of mechanical properties of SLM processed maraging steel using water and gas atomized powders. Modified from [35]

Material	**Density (g/cm3)**	**UTS (MPa)**	**Elongation at break (%)**	**Hardness (HRC)**	**Impact Energy (J)**
GA-maraging 300	8	2006	3.1	52	7
WA-maraging 300	8.04	1793	1.4	43	5

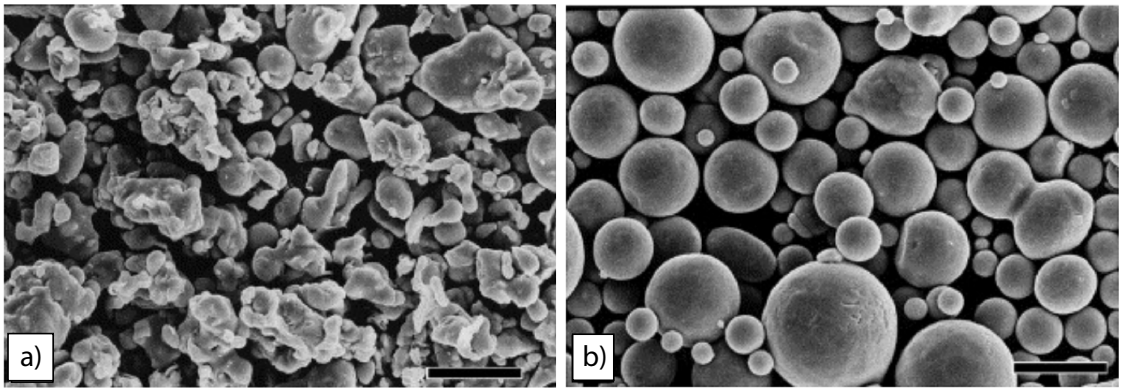

Figure 2.2: Water atomized (a) and gas atomized (b) stainless steel 316L powders. Reproduced with permission from [37].

2.2.2 Powder Bed Fusion Systems

A PBF system can produce high resolution features and components with dimensional controls and the ability to fabricate parts with internal channels – providing two key advantages over traditional manufacturing techniques [5]. The basic components of a PBF system contain an enclosed chamber with a heat source (laser or electron beam), scanner, powder bed, metal supply bed, re-coater arm or rake, and usually an inert gas supply [5, 8, 13, 38, 39]. As discussed earlier, powder packing and size distribution

determines the level of porosity in the printed part, and are the most crucial factors to the effectiveness of this AM method [8].

PBF systems with an electron beam are classified as electron powder bed fusion (EPBF) or electron beam melting (EBM) and those with a laser are called LPBF or selective laser melting (SLM). Another name commonly used for LPBF is direct metal laser sintering (DMLS). DMLS is used when uncoated and pre-alloyed powders are used, while SLM uses polymers or coated metal powders as the sintering material [38]. Depending on the heat source, either deflection coils or mirrors are used in EBM and SLM, respectively, to raster the beam along the powder bed and fabricate the desired structure [5]. An example of an EPBF and LPBF system is illustrated in figure 2.3a and figure 2.3b.

These PBF systems form the powder bed by continuously raking/rolling metal powder from the metal supply bed onto the build platform into a compacted several powder particle thick layer between 20 and 60 µm [38,39]. The build platform provides the necessary mechanical and thermal stability for the build which can influence the quality of the printed part [13]. The laser then scans the powder bed at particular locations predefined by an uploaded CAD file and the process is repeated until the entirety of the structure is complete [39]. The surrounding un-melted powder in the bed provides mechanical support to the printed structure during printing [40]. After the printing process has concluded, excess powder in the bed must be removed from the build chamber to extract the printed structure. For EBM constructed parts, the powder is directly removed and recycled for another build while SLM processes sift the powder before it can be reused due to the formation of satellites and irregularities through agglomeration that can occur during printing [13, 27]. The main disadvantage for PBF systems includes slow processing times and high associated costs [8].

2.2.3 Direct Energy Deposition

Direct energy deposition (DED) or laser engineered net shaping (LENS) uses the focused thermal energy from the heat source to melt and fuse the feed stock as they are deposited onto the substrate. Due to the lower accuracy and required post-processing of printed parts, DED is much less common [38]. The main advantage for

DED printers is the ability to produce large part volumes and repair damaged parts by using them as the substrate or build plate in contrast to PBF systems [5]. DED systems offer more flexibility in terms of heat source and feedstock. A laser, arc or e-beam heat source can be used with a DED system as well as metal wire or powder for the feed stock [13].

DED technology can add additional kinematic degrees of freedom to improve the quality and complexity of the printed part. Additionally, DED processing time is much quicker than other methods such as powder bed fusion (PBF) and the mechanical properties can be finely tuned by controlling the microstructure through thermal gradients and chemical composition control. Another benefit of DED systems is that they can be coupled with subtractive machining manufacturing techniques such as a milling machine for surface finishing and dimensional tolerances, which is commonly exploited in the aerospace industry [8]. A consequence of these systems is that more maintenance is required to verify powder flow rates to ensure repeatability of printed components [13].

Similar to PBF, the build volume is enclosed in a chamber while inert gas can either be injected into the chamber with cyclic purging [13] or the gas can be released by the nozzle to shield the solidifying metal similar to gas metal arc welding [41]. The working process of a powder feed and wire feed DED system is shown in Figure 2.3c and figure 2.3d, respectively.

2.2.4 Laser Melting vs. Electron Beam Melting

SLM systems use a motor driven mirror system to deflect the focused laser beam at different points on the powder bed to develop the structure. Whereas EBM systems require a vacuum in the build chamber since the mean free path of electrons at sea level in atmospheric pressure is only a few µm. The working principle of the electron beam is similar to that of a scanning electron microscope (SEM) where electrons are extracted from a metallic filament through a high electrostatic potential or accelerating voltage which are then deflected with magnetic coils through a column to raster the beam in the designated areas [13, 39]. Laser and electron beam DED systems are generally quite similar where the main difference stems from the build atmosphere (argon/nitrogen purged versus vacuum).

For LPBF systems, the substrate can be heated and maintained at approximately 90°C [39], reducing the effective temperature gradient between the melt pool and substrate. This temperature gradient and subsequent cooling rate has been directly linked to the local microstructure development of the melt pool [42]. The complex process of the repeated particle melting, and solidification requires an inert environment to avoid oxidation of the melt pool [41, 43]. Absorption of oxygen in the case of Titanium has shown to cause embrittlement, reducing the fatigue life due to an oxygen enriched region beneath the surface of the printed structure [44]. The chamber is thus purged with purified argon or nitrogen gas to reduce the impurities of the printed part [13].

For EPBF systems, the powder bed platform is heated to 80% of the powder melting temperature to greatly reduce the thermal gradients experienced during printing [39]. A subsequent final melt scan provides the liquefaction and construction of the part. Thus, since the preheat temperature is much higher in EBM and there is no convective cooling, it experiences shallower solidification rates which can help reduce residual stresses [39]. For example, SLM-processed Ti-6Al-4V parts tend to be dominated by thin α' martensite platelets compared to acicular α phase, while EBM parts to contain an α phase grain structure with β phase boundary areas [4]. However, Vrancken et al. has shown that subsequent heat treatment of Ti-6Al-4V alloys can transform the brittle α' martensite phase to a lamellar mixture of α + β [45].

2.2.5 Binder Jetting Systems

Binder jetting systems were developed in the 1990's but have only recently become popular metal AM systems [46]. This technology has provided a lower cost printing system capable of producing complex geometries out of various metals and ceramics [46]. The working principle of binder jetting systems is similar to PBF in that the printer head selectively deposits a liquid binder onto the powder bed for each layer. A powder re-coater lays down a fresh sheet of powder for the next layer to be binded. [13,46]. After deposition, depending on the machine and binder chemistry, the binder can be either partially cured between layers giving sufficient strength to be removed shortly after printing or is required to completely dry where it can then be removed from the powder-bed system and cured up to 12 hours [13].

Once all layers have been deposited, the "green" part needs to be processed further [47]. This printing technique can involve several post processing methods depending on the machine which are not usually found in DED or PBF systems which can include: curing, de-powdering, sintering, infiltration, annealing, and finishing [46–48]. The furnace is held at a specific temperature between 650–700$°C$ to allow the binder to burnout before ramping up to the sintering temperature for the specific alloy [49]. Since the binder jetting process does not involve melting, the amalgamation occurs by sintering, where porosity volume, size and shape can differ between various parts in the same collection [46,50]. However, due to the decoupling between printing and consolidation in the BJP process, the homogeneous sintering environment can provide a uniform final microstructure for the component [51].

One of the main drawbacks for BJP is the relatively low density the process is able to obtain (only 50-60% in some cases) [13, 51]. Similar to other AM methods, the particle size is critical for optimal build quality. Large particles are essential for powder spreading, while fine powders are critical for sinterability, resolution and surface quality [52]. However, there are a number of ways to drastically increase the density of BJP parts through infiltration, supersolidus liquid phase sintering (SLPS), optimized sintering control and, small dose additives to achieve greater than 90% relative densities [13, 51, 53, 54]. Infiltration is a common post-processing technique to densify the sintered parts in which a liquid metal is drawn into the metal through capillary action [13]. For stainless steels, bronze is a common infiltrator which can increase the density from 60% to 95% [13]. However, since the binder jetting process requires significantly more post processing treatments than DED or PBF systems, these builds can take much longer to complete while their mechanical properties with weaker infiltration materials are usually inferior [46]. Figure 2.3e and figure 2.3f illustrate the binder jetting printing process.

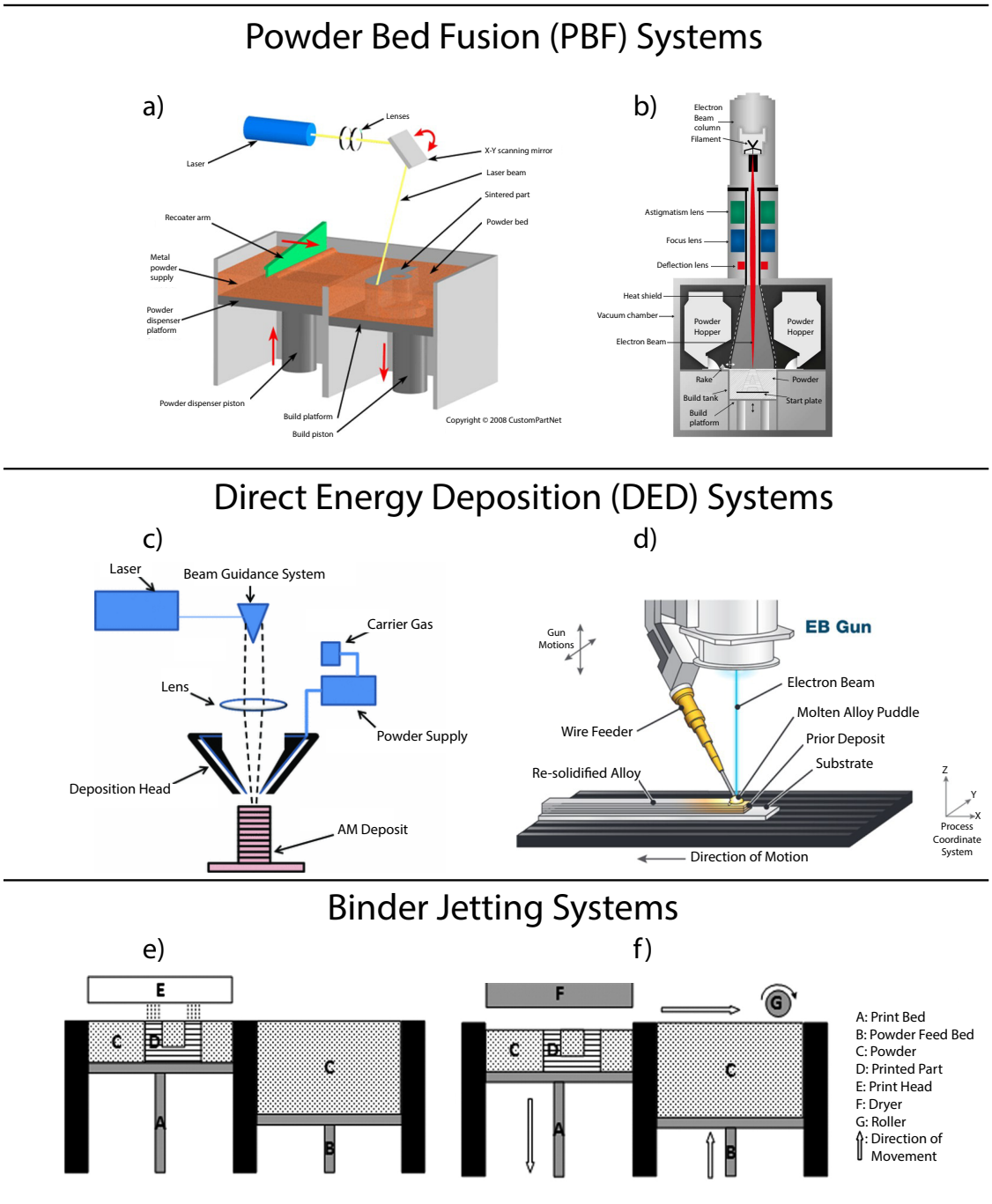

Figure 2.3: Various additive manufacturing printing technologies including: a) laser powder bed fusion from [55] b) electron powder bed fusion; courtesy of GE additive [13, 56] c) direct energy deposition powder feed with laser [5] d) direct energy deposition wire feed with electron beam courtesy of Sciaky, Inc. EBAM® is a registered trademark of Sciaky, Inc. [57] e) binder jetting printing and f) spreading and drying process modified from [48]. Images reproduced with permission.

.

2.3 Melt Pool Characterization

The melt pool used during the AM process is similar to that of laser welding and is an extremely important and complex process that determines the overall quality of the printed part [58]. The melt pool characteristics are defined by numerous physical phenomenon such as ablation pressure, vapor plume effects, surface tension, gravity, Marangoni turbulence, recoil pressure, etc. [59, 60]. There are two modes of melt-pool formation during laser and electron beam AM: conduction and keyhole mode [61]. Conduction mode locally melts the material to form a molten pool and is characteristic by a shallow and wide ellipse mitigating defects [61]. However, if the energy density is high enough, keyhole mode can occur and form a deep narrow pool where the metal evaporates generating recoil pressure and a capillary called a keyhole [62–64].

The processing parameters during the printing process such as laser power and scanning speed affect the size and depth of the keyhole generated and the collapse of this keyhole has shown to affect porosity and other processing related defects [58, 65]. The rapid solidification impedes vapor bubbles from leaving the melt pool which leaves a keyhole pore within the part [15]. Qiu et al [65] showed that the Marangoni turbulence and recoil pressure were the main driving forces which cause instability of the melt pool flow. During the melting process, un-melted particles are in contact with the melt pool which causes surface tension to pull the fluid at the surface toward the colder region, generating Marangoni turbulence, causing gaps and pores [66]. This convection drives an outward circulation flow of the melt pool [67] as shown in figure 2.4. Furthermore, recoil pressure is generated by the evaporation in the keyhole which generates a vapor jet and subsequent fluid flow in the keyhole and melt pool [68].

Due to the extremely high temperatures generated by the heat source, the melt pool surface easily exceeds the material boiling point, increasing the pressure within the molten material. This recoil pressure is applied on the melt-pool due to the vaporization of the metal and results in a high velocity vapor plume [69]. An increase in the vapor recoil can give enough energy for the vapor plume to exit the keyhole and eject particles by momentum transfer through neighboring particles called “spatter” [67, 70]. Spatter is the ejection of fluid particles from the melt pool

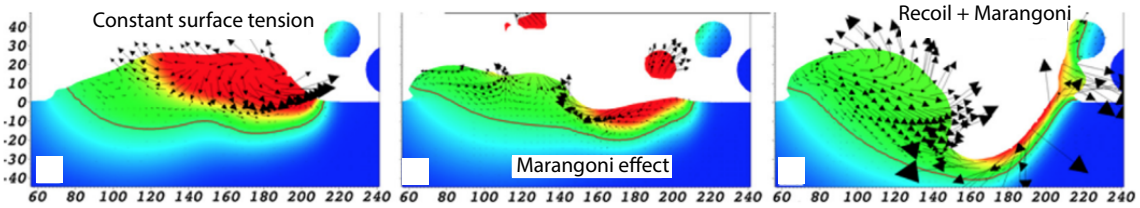

Figure 2.4: Computational fluid dynamics simulation of Marangoni turbulence in the melt pool during metal additive manufacturing reproduced with permission from [66]. Red corresponds to temperature scale at 4000K and blue is 293K.

and is a common defect in AM and laser welding [71]. Li et al [70] studied the weld pool convection during laser welding and determined weld pool behaviour was a key factor in the generation of spatter. Additionally, Liu et al [72] found that the energy input greatly influenced the spatter size, scattering direction and height.

In laser welding, spatter causes mass loss of the metal, generating defects such as underfilling and undercutting at the top and bottom of the melt pool [70]. During the deposition process, liquid builds up ahead of the scanning laser and can be pinched off to produce spatter particles on the build [66]. Spatter and ejected particles generated during AM can greatly affect the surface roughness of the printed part, therefore in laser-based systems, the inert gas flow is also used to relocate these particles [73]. It is evident that the metal-laser interaction is one of the most influential steps during the building process in AM. Thus, optimizing all processing variables which affect the melt pool formation are required in order to produce high quality metallic parts in AM.

Two common techniques of laser melting in PBF systems consist of continuous wave and modulated melting. Continuous wave (CW) melting irradiates the metal powder under a constant flux as it rasters each layer of the build. During this process, the scan lines comprised of the molten and solidified melt pools will overlap on each successive pass which partially re-melts the previous raster line. In contrast to CW, modulated lasers alternate between on and off positions to create a series of short irradiation exposures between 1 and 20 μs where each exposure overlaps with the former one [74].

The laser power and spot size is highly dependent on the machine. The power

is the source of the heat flux transferred to the metal powder while the spot size is the diameter of the focused beam which can be altered depending on the focusing system. The scanning speed is the velocity of the laser spot traversing across the build. For CW laser melting, this is defined by the distance travelled within a certain time step while in modulated melting it is defined as the exposure time. The hatch distance is the spacing between adjacent melt scan paths which usually requires overlap to partially melt and fuse neighboring welds. Lastly, the layer thickness is the depth of powder thickness to be melted for each layer for PBF systems and the powder feed deposition rate for DED systems. [74]

Based on the processing graphs shown in figure 2.5, there is a direct correlation between the as-built density and the laser power and scanning speed. Mainly, the resulting quality depends on the energy density achieved through these two parameters. As the laser power increases and the scanning speed is decreased, the energy density around the laser spot will increase and vice versa for an increase in scanning speed or decrease in laser power [74]. In addition to this, it can also be noted that as the hatch spacing or scanning speed increases, the porosity increases as a result [75] which can be seen in figure 2.5c and figure 2.5d. It is evident that optimizing printing parameters will achieve the desired as-built density.

It is important to note that optimal processing parameters can vary significantly between LPBF, EPBF and DED. For example, the heat in the melt-pool during DED will dissipate downward through the substrate and previously deposited layers through conduction as well as convectively cooled from the argon gas flow [76, 77]. While in PBF processes, the surrounding powder conductively dissipates most of the heat away from the melt-pool [77]. Thus, the solidification mechanism and resulting properties vary between methods. Additionally, the scanning speeds and laser power between these printing methods also vary greatly, contributing to different optimal parameters. For example, the Optomec 750 (DED) has a scanning speed of 0.001-0.04 m/s and a max laser power of 500W while the Realizer SLM50 ranges from 0.3-1 m/s with a maximum laser power of 120 W. However, for the Arcam EBM S12, the scanning speeds and laser powers are much higher with ranges between 200 and 1000m/s and a maximum power of 3500W [77]. Due to the large variation in processing parameters between method, machine and alloy, it is not surprising that the current literature on process modelling is readily expanding for new alloys and machines.

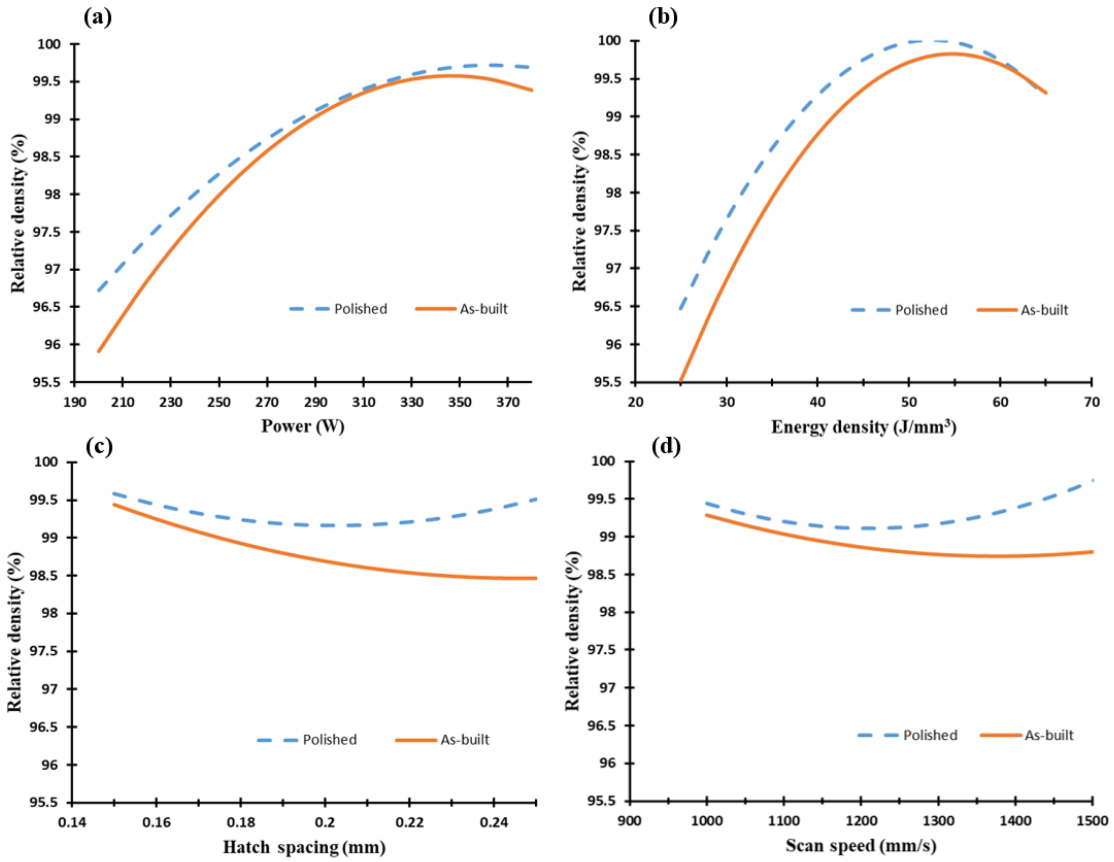

Figure 2.5: Relative density of as-built SLM-processed AlSi10Mg samples with respect to (a) laser power, (b) energy density, (c) hatch spacing, and, (d) scan speed reproduced with permission from [75].

2.4 Common Defects in Metal AM

Due to the complex physics governing metal AM, many defects are likely to occur if the process parameters such as laser power and scan speed are not optimal [10, 13, 24, 78] or the feedstock material and build chamber are inadequate [13, 24]. Some common defects in the production of metal AM components include: porosity, cracking, delamination, poor surface quality, balling, distortion and residual stresses [10, 13, 19]. The defect density in a 3D printed material severely hinders the fracture toughness and mechanical properties [24].

2.4.1 Porosity

Porosity is an extremely common defect in the AM process since the binding mechanisms during layer deposition are driven by temperature gradients, capillary forces and gravity [19]. Porosity has shown to greatly hinder the mechanical properties of 3D printed parts [19] by acting as crack initiation sites reducing toughness and fatigue strength [8, 79]. Pores are usually very small, with less than 100 µm in diameter [10]. Due to the high temperature gradients and rapid solidification during deposition, porosity can develop through un-optimized process parameters [8, 10, 13, 78–80]. It has been shown that porosity density generally decreased with an increase in laser power and scanning speed [79]. Gong et al [78] and Puebla et al [80] showed that increasing scanning speed at lower laser power yielded an increase in porosity, likely due to entrapped gas and un-melted powder particles. Similarly, relatively low scan speeds and high laser power increases the energy input and subsequently the temperature in which porosity defects are developed [10].

Another important source for porosity includes gas entrapment [7, 10] which may form in the powder feedstock during atomization [13]. Additionally, the rapid solidification rate of the melt pool inhibits the gas bubbles to rise and escape, causing entrapment in lower regions [10, 24, 78]. As a new layer is being scanned, the gas is superheated to where it expands and removes the molten metal above it as it solidifies into a pore [81]. This rapid solidification promotes microstructure refinement and increased porosity at the same time [80]. The high melt pool temperatures decrease the activation energy for diffusion, and therefore increasing the solubility of gas in the metal [10]. Furthermore, Qie et al [79] determined that horizontally built samples generally had a higher level of porosity than samples built vertically. Figure 2.6a and figure 2.6b illustrate an example of porosity present in a 3D printed part.

Aside from controlling the process parameters to reduce or eliminate pore generation, hot isostatic pressing (HIP) may be used as a post-processing method to alleviate printing defects including pores [8, 24, 79]. HIP involves the application of a high isostatic pressure, coupled with a high temperature applied to the printed part to enhance ductility and fatigue properties [8]. As-built Ti-6Al-4V printed parts usually consist of long martensitic columnar grains which can be fully transformed into $\alpha + \beta$ phases through HIP in addition to closing the majority of pores [79].

2.4.2 Lack of Fusion During the Printing Process

Lack of fusion defects occur due to a deficiency in energy input during the melting process, causing the melt pool and un-melted powder particles on the deposited layer to not fully penetrate and fuse with the previous layer [7, 10, 13, 79]. This lack of fusion greatly contributes to the anisotropy and heterogeneity in the AM processed parts, which can degrade the surface and mechanical properties [24]. Furthermore, irregular-shaped pores are formed due to the lack of fusion between the interface of adjacent layers, further increasing the defect density [79]. In alloys that are oxidized easily such as aluminum and zirconium alloys, a thin oxide film can be produced at the surface of the deposited material which inhibits the successive later to bond as it blocks the molten metal flow [10]. Examples of fusion defects are shown below in figure 2.6c.

2.4.3 Ball Formation

Melt ball formation or "balling" is the tendency for the melt pool to separate into small spheres or beads which "wets" the subsequent layer or substrate [13, 82] of the printed material. Surface tension is the main driving force contributing to balling which occurs when the length-diameter ratio of the melt pool is greater than 2:1 in which the pool transforms into a bead [13]. When the total surface of the molten pool exceeds that of a sphere with the same volume, there is a reduction in surface free energy, initiating melt ball formation [82]. High laser power and scanning speeds are likely to elongate the melt pool and introduce melt ball formation, while at low scanning speeds and laser powers it has been shown that no balling occurs [13, 82]. Not only does balling affect the surface quality of the printed part, but inter-layer connection between adjacent layers is also impeded [82]. Therefore, printing parameters should be optimized to reduce the length-diameter ratio as much as possible [13, 82]. Figure 2.6d illustrates melt ball formation from AM processing.

2.4.4 Residual Stresses and Cracking

Cracking in the AM process is largely attributed to thermal residual stresses generated due to the large temperature gradients and rapid solidification resulting in melt pool shrinkage [10, 13, 19]. Relatively low scan speeds with a high energy input have the possibility to yield high thermal residual stresses. These stresses tend to be compressive in the centre for DED and PBF manufactured parts and tensile along the egdes with a high concentration near the substrate interface [13]. As the input energy is increased, the molten metal contracts to a higher degree which could result in cracking [10]. Although deformation and cracking due to residual stresses is common, the degree and type of cracking are dependent on the material that is used [19]. If the residual stress within the material exceeds the local yield stress of the material, warping or plastic deformation occurs and if this stress exceeds the local ultimate tensile stress, cracking can occur [13]. Cracks are also likely to nucleate from the deposited metal adhered to un-melted metal particles [10,19] and pores [13], signifying the importance of optimized process parameters. An example of thermal residual stress distributions in an AM processed part is shown in figure 2.6e.

Laser heated systems operate at much lower temperatures yielding higher thermal gradients and larger residual stresses, while electron beam systems are often preheated, truncating the local thermal gradient [13]. Additionally, alloys with low thermal conductivity and high thermal expansion such as stainless steels and Inconel are more susceptible to crack generation during the printing process [10]. Two common types of cracking are solidification cracking and grain boundary cracking [13]. Solidification cracking occurs when too much energy is present in the melt pool and stresses are induced between solidified and un-melted areas of the melt pool. This process depends greatly on the material's dendritic, cellular or planar nature of solidification and melt pool viscosity [13]. Grain boundary cracking nucleates alongside the material grain boundaries due to the formation of dissolution of precipitate phases [13, 19].

Thermal stresses during the printing process can be mitigated through various techniques including process optimization, preheating the substrate, inclusion of monitoring devices such as thermal imaging systems and, material composition [13,19]. This topic will be discussed further in the "Process Optimization" section in

addition to controlling the grain morphology during the deposition process.

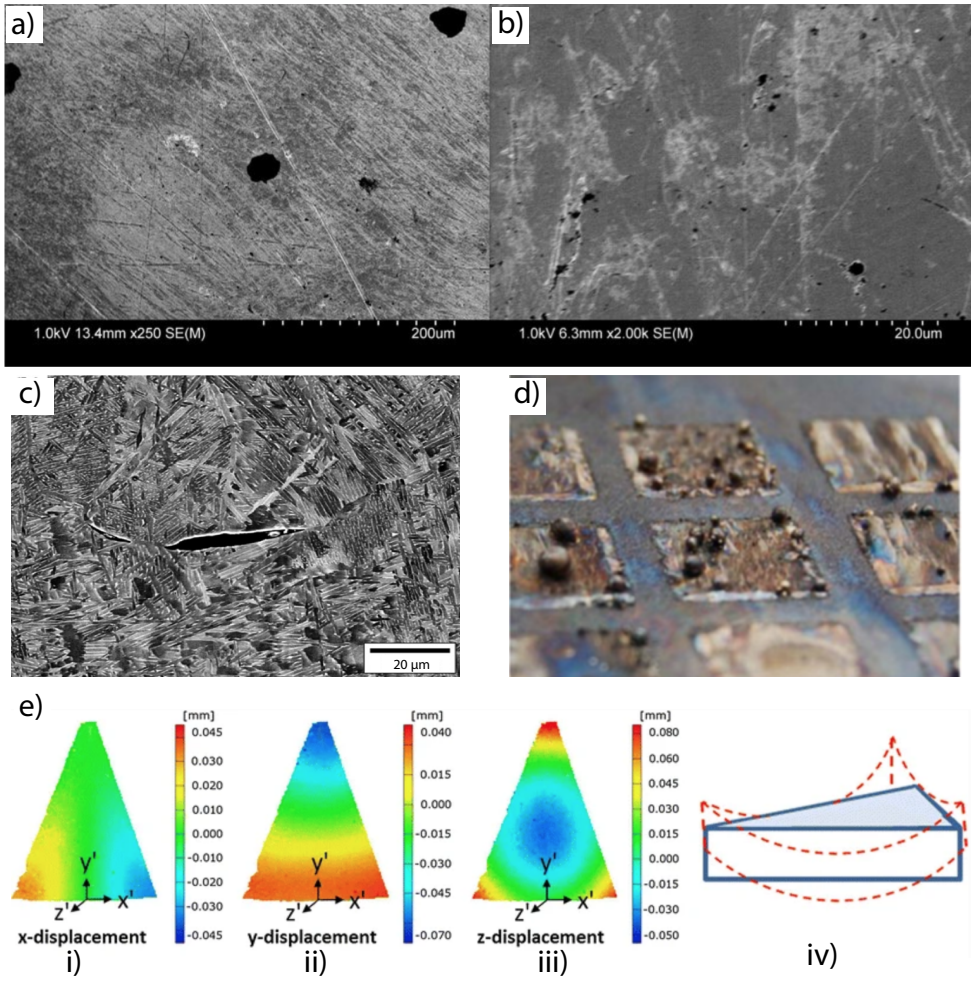

Figure 2.6: Common defects in metal additive manufacturing: a) large pores on the range of 20 µm and b) micro-pores on the scale of 200 nm in SLM processed 316L c) lack of fusion between layers from [83] d) ball formation during printing process from [84] and e) residual stress distribution in SLM processed 316L where i-iii) are top surface displacements and iv) is a scaled up deformation schematic from [85]. Images reproduced with permission.

2.5 Current Alloys in Metal Additive Manufacturing

The library of commercially available AM alloys is currently very limited compared to the vast number of conventional alloys being used today. Due to the large potential in metal AM and the increase in industry and academic participation, this library is increasing quite rapidly. However, some conventional alloys which may not be suitable for AM processes can be chemically tailored in order to fully exploit the advantages of AM. This section discusses and compares the metallurgical properties of most commercially available AM alloys with their conventionally manufactured counterparts.

2.5.1 Pure Metals

Additive manufacturing of pure metals is difficult since they exhibit relatively poor mechanical properties [86]. High strength to weight metals such as pure Ti have been explored in additive manufacturing. Due to the complexities in Ti crystal structure, a body centered cubic (BCC) structure is present at temperature above $833°C$ while below this, a hexagonal-close-packed (HCP) exists [86]. However, Ti β phase with BCC structure can be stabilized at room temperature with alloying additions such as Mo, V, Ta, and Nb [87] while alloying additions which promote the α phase include: O, Al, Sn and N [88, 89]. SLM produced Ti in an Ar purged chamber has shown an increase in Vickers hardness compared to wrought titanium due to an increase in oxygen absorption [90]. The density after SLM production yielded only 92% density, which could be increased to 98% after process optimization or HIP [90]. However, the porosity observed in AM processed pure Ti has found value in the biomedical industry to create a mechanical interlock from growth of bone into the porous Ti and help reduce stress shielding on load bearing implants [91].

SLM processed pure Au possesses a high level of porosity in between layers due to a lack of fusion [92]. The gold powder has a high reflectivity around 85%, increasing as the gold melts which can greatly lower the transfer of energy to the previously deposited layers [92]. Furthermore, pure Cu has been investigated for well

over a decade and has generally produced low density parts during SLM due to its high thermal and electrical conductivity [93]. An early 2003 study by Pogson et al [94] showed that certain process parameters melt the pure copper powder on a stainless steel substrate while no combination of laser power and scanning speed could melt the powder on a copper substrate. EBM fabricated copper with a purity of 99.8% has also been investigated to which the balancing component was a copper oxide (Cu2O) called cuprite [95]. The cuprite formed precipitates in the Cu matrix with cell-like, equiaxed arrays perpendicular to the build direction with sizes between 1 and 3 um, greatly increasing the hardness of the copper [95]. Since copper has a high conductivity, instabilities could arise in melt pool formation which can produce lack of fusion between adjacent layers of the build [96].

EBM fabricated BCC metals such as pure Fe and Nb both exhibit irregularities not found in conventional processes [20]. EBM processed Nb yielded columnar grains with relatively high dislocation densities revealed by Transmission Electron Microscopy (TEM) originating form thermal stresses during the deposition process [20]. Unlike conventionally manufactured Fe which produces αferrite [97], EBM processed pure Fe produced equiaxed αgrains containing delta-iron platelets due to rapid cooling [20]. Additionally, AM processed pure metals such as Ta exhibited large amounts of porosity [98], where pure W showed a clear network of crack formation [99]. These studies demonstrate some of the issues with printing pure metals and demonstrate why it is more common to see metal alloys used when 3D printing.

The BJP process has shown remarkable capability to produce pure metal components such as copper [52, 54, 100], titanium [47, 100] and iron [100, 101]. Bai et al [54] used a bimodal powder mixture of 5µm and 15µm of pure copper giving both powder flowability and sintering capability. With this bimodal powder mixture, they were able to achieve a maximum sintered density close to 94% with a heating rate of 5°C/min. Rishmawi et al [101] achieved a density of 91.3% for pure iron with a sintering temperature of 1490°C for 6 hours. They found a distinct relationship between sintering time and temperature to achieve densities between 64% and 91%, with possibilities for even higher densities with increasing sintering time. Lastly, a study by Wheat et al [47] on pure titanium saw the highest sintered density at 92.9%. They concluded that the finer powder particles improved the sintered density of the part but increased the level of shrinkage and anisotropic density distribution parallel

to the build direction.

2.5.2 Pre-Alloyed Metals

To date, the most common pre-alloyed materials that are commercially available in AM and those with a considerable amount of research are: Fe-based, Al-based, Ti-based Co-based and Ni-based [86] while elements such as Cr, Mo have shown to be a useful alloying addition for printability. The most common method to produce these alloys is using SLM-PBF systems based on data taken from leading metal AM companies such as EOS (Germany), Renishaw (United Kingdom) and Stratasys (Israel).

Fe-Based Alloys

Fe-alloys, such as steel, are the most common engineering materials used today [102], however only a tiny fraction of Fe alloys are available for AM. Currently, the most researched steels in the literature consist of stainless steels [102] such as 316L [22, 103–109], 17-4PH [105,110–113], maraging steel 1.2709 (MS1/M300) [114–119] , H13 tool steel [120–125] and invar 36 [126–128]. Although these materials are currently available for engineering applications, research is still being conducted to improve reliability and performance of these alloys.

316L stainless steels generally exhibit an austenitic grain morphology after AM processing with a general chemical composition of $Fe_{17}Cr_{12}Ni_3MoMn$ [102]. The high percentage of Ni lowers the eutectic point, allowing austenite to be stabilized at lower temperatures [129] yielding an FCC crystal structure with paramagnetic properties [105]. 316L SS is used across many industries due to its high strength, ductility and exceptional corrosion resistance [104,105,108]. Overlaps between molten pool boundaries (MPBs) are typically observed in SLM processed 316L and IN625, while Ti-6Al-4V and ferrous matrix alloys do not exhibit MPBs [22]. Around MPBs boundaries, large concentrations of C, O and Si are often present forming non-metallic inclusions which greatly hinder the mechanical properties of the printed part [22].

Additionally, processing by the high energy laser can induce hardening ef-

fects through the small martensitic transformation in localized areas as a result of the high thermal gradients and rapid solidification [105]. Saeidi et al [108] observed the microstructure using XRD analysis after printing and as expected, a single austenitic phase was revealed with preferential growth along the <110> plane. Comparable with other studies, dendritic fine columnar grains with size of approximately 0.5 µm were found in individual larger grains with sizes between 10-100 µm [104, 108]. Figure 2.7a and figure 2.7b illustrate the microstructure of cast and SLM processed 316L stainless steel, respectively.

Unlike 316L, 17-4PH stainless steel is a ferromagnetic precipitation hardened martensitic maraged steel which ultimately exhibits higher strength at the cost of ductility [105]. The precipitation hardening mechanism is activated by a copper alloying addition during aging or cooling [105, 130]. The general composition of 17-4PH consists of (15–17.5 Cr, 3–5 Ni, 3–5 Cu, <1 Mn, Si, 0.15–0.45 Nb, balance Fe in wt%) with Cu-rich spherical particles embedded in the martensitic matrix [112]. Although a martensitic microstructure is dominant, metastable retained austenite can be observed in SLM fabrication [110, 112]. Similar to 316L, columnar austenitic grains can grow along the thermal gradient [110]. The martensitic microstructure is generally composed of columnar bundles of lath martensite between 5 and 50 µm with dense tangles of dislocations oriented in the <200> and <110> planes perpendicular and parallel to the build direction, respectively [112]. Figure 2.7c and figure 2.7d illustrate the wrought and SLM processed microstructures of 17-4 PH.

Unlike stainless steels, H13 is a hot work tool steel with a relatively high carbon concentration and has excellent hardenability and toughness [121]. Hot-wire AM processed H13 tool steel yields fine acicular tempered martensite since the material experiences an initial air quench after deposition and subsequent tempering during deposition of successive layers [121]. XRD analysis of SLM DED processed H13 revealed that BCC ferrite and BCT martensite dominated the grain morphology, however some retained austenite was observed [120]. Similar to previous results, low parts of the build were subjected to tempering, corresponding to a drop in hardness [120]. Lastly, SLM H13 tool steel was examined and the corresponding microstructure was consistent with previously discussed results in that very fine martensite was observed on the top layer, while retained austenite was found in between the martensitic laths with coarsened grains at lower layers in the build [122]. Chen et al. [125] investigated

the differences in heat treatment between conventionally produced H13 and LAM manufactured treated at 550°C and is illustrated in figure 2.7e and figure 2.7f.

Maraging steels contain very low amounts of carbon with high amounts of nickel and other alloying additions such as Mo, Co, Ti and Al [118]. These alloys exhibit extremely high strength, hardness and toughness and are widely used in aerospace and tooling industries [117, 118]. Maraging steel alloy with 18 wt% Ni is usually identified as 1.2709/MS1(EOS)/M300 with a chemical composition of X3NiCoMoTi18-9-5 [114]. The high concentration of Ni achieves a martensitic microstructure, contrary to C in carbon steels [114, 117]. Conventionally manufactured maraging steels are usually solution annealed and quenched, yielding fully martensitic structure without the presence of precipitates unless subsequent ageing treatment between $480°C$-$510°C$ is imposed [117]. This produces finely dispersed intermetallic phases such as Ni_3Ti, Ni_3Mo and Fe_7Mo_6 to increase strength and toughness [115]. Electron backscattered scanning diffraction (EBSD) images of M300 produced through conventional processes and LMD are shown in figure 2.7g and figure 2.7h. The SLM and DED processed microstructure of M300 by Jägle et al. showed microsegregation, yielding retained austenite where in the conventionally manufactured M300, the austenite is non-existent [117]. However, observations recorded by Casalino et al [118] showed that a fine cellular/dendritic columnar martensitic grain structure was produced by SLM processing with intercellular spacing less than 1 um.

The last Fe-base alloy is an Fe-Ni alloy, Invar 36 which has a composition of 64 wt% Fe- 36 wt% Ni [128]. Invar has an extremely low thermal expansion behavior and is therefore used in applications that require dimensional precision and stability [128]. SLM processing of Invar 36 yields a fan-like microstructure comprised of vertical columnar austenitic grains combined with α phase nano-precipitates [126]. There are many conventional Fe-based alloys which are not yet tested or optimized for AM processing but is changing due to the ongoing research for AM processed steels.

Ni-Based Alloys

Ni-based alloys such as Inconel is an austenitic precipitation hardenable superalloy which is mainly comprised of Ni and Cr and provide extremely high yield strength,

corrosion resistance and high temperature operating temperatures [86, 131]. Inconel is used extensively in the marine nuclear and aerospace industries and has been at the forefront of AM research in the past decade [86]. Inconel alloys are known for their good weldability thus making it a suitable alloy for AM [132]. Specific Inconel alloys such as IN 625 [133–137], IN 718 [73, 132, 138–144] are standard cast and wrought alloys which have been qualified and certified for engineering applications by AM processing.

The microstructure of SLM processed IN 718 has been observed to be smaller by a factor of 10 compared with superior mechanical properties compared to the as-cast counterpart [132]. The delta phase present in Inconel 718 was originally thought to be harmful to the mechanical properties of the material but has been shown to help block grain boundary sliding and control the grain size and is precipitated through aging along the grain boundaries [145]. The microstructure of conventionally processed IN 718 showed an average grain size of 25um with equally distributed carbides along and within the grain boundaries and grains [145]. SLM processing of IN718 yielded distinct regions of course columnar grains with a cellular structure with fine dendrites stretched along the <001> plane parallel to the building direction surrounded by a fine-grained matrix [139, 140, 143]. However, high dislocation densities were found within the as-built samples due to the large plastic strain imposed during the deposition process [140]. The cast and SLM processed microstructures of IN 718 are shown in figure 2.7i and figure 2.7j.

The IN 625 alloy has a composition of 64.61 Ni, 21.25 Cr, 8.45 Mo, 4.65 Nb and 1.06 Fe (in wt.%) with notably higher Mo and Ni concentration than IN 718 [137]. The microstructure of wrought IN 625 contains a thick film of carbides along the grain boundaries with additional undissolved particles dispersed throughout inter and intragranular regions [146]. The microstructure of LPBF components are most similar to that seen in wrought Inconel 625 in its non-annealed state [136]. The microstructure of as-built SLM parts are mostly columnar dendrites throughout the structure [137], similar to IN 718. The various Inconel alloys discussed in this section have been thoroughly researched for AM processes and have exceptional mechanical properties compared to their conventional counterparts.

Co-Based Alloys

Cobalt-base alloys are extremely useful for high-temperature and high wear resistance applications in industries such as aerospace, nuclear and biomedical [86, 147]. These alloys also exhibit excellent biocompatibility and are therefore often used for dental and orthopedic prostheses [148–150]. Cobalt has an HCP structure at room temperature which transforms to BCC above $400°C$. Alloying additions such as Cr, Mo and W which are inherent BCC stabilizers can be added to increase the transformation Co temperature [151, 152]. The main Co-base alloys currently being processed in AM is Co-Cr-Mo [20, 86, 149, 153, 154], which commercially available for most AM systems.

Like most metallic alloys, the addition of alloys can greatly alter the microstructure and mechanical properties of the material. For as-cast Co-Cr-Mo, the addition of Mo improves ductility and increases the range of solidification and produces additional amounts of eutectic carbides at grain boundaries [151]. The general microstructure produced for as-cast Co-Cr-Mo alloys typically have dendritic solidification with two phases consisting of a dendritic matrix and interdendritic precipitates of different Co-Cr-Mo solid solutions [155]. As-built SLM-processed Co-29Cr-6Mo has shown cellular dendrites arranged in fine lamellae extended along the build direction contrast to the coarser dendrites observed in casting [150]. Similar results were seen in EBM-processed Co-Cr-Mo where columnar structures of carbides are embedded in an FCC CoCr matrix orientated preferentially along the build direction [20]. Figure 2.7k and figure 2.7l show the EBM processed and wrought microstructures of CoCrMo alloy, respectively.

Al-Based Alloys

Currently, the most available AM processed Al alloys in the literature and on the market contain combinations of Mg, Si or Cu alloying additions. $AlSi_{10}Mg$ [11, 156–163] is the most researched and available Al-alloy in the literature and on the market, however, $AlSi_9Cu_3$ [163] is also certified and printable by companies such as Frauenhofer and SLM solutions. The aluminum alloy $AlSi_{10}Mg$ is widely used in casting and has good weldability since it is hypoeutectic but near the eutectic composition of 12.5% Si [159, 161]. The addition of Mg (0.5 wt%) to the Al-Si system allows Si and

Mg to form a β phase precipitate (Mg_2Si) in the Al matrix during heat treatment or ageing to strengthen the alloy [157, 159]. High strength conventional alloys such as 7075 and 6061 exhibit large columnar grains with cracks in the intercolumnar regions during AM as these alloys are susceptible to hot cracking [11]. Improvements have been researched by refining the grain structure with TiB_2 or WC nanoparticles to produce a uniform equiaxed grain structure with no cracking [11].

SLM processing of $AlSi_{10}Mg$ in the as-built conditions has shown to produce a cellular dendritic α Al matrix with inter-dendritic Si particles [157, 161]. However, the printed structure was subject to heat affected zones (HAZ) where coarser dendrites emerged and produced a heterogeneous microstructure [161]. In DED processed $AlSi_{10}Mg$, columnar dendrites dominate the growth regime however, three distinct solidification structures are observed throughout the build [158]. Cellular growth was observed closest to the substrate and transitioned to a columnar dendritic along the build direction until a small equiaxed dendritic region was observed at the uppermost layers [158]. The cast and SLM microstructures of $AlSi_{10}Mg$ are illustrated in figure 2.7m and figure 2.7n.

More recently, prevalent Al alloys such as 6061, 1000 and 2000 series have found success in AM with companies like Elementum 3D making them commercially available. 6000 and 7000 series Al alloys are notoriously unweldable due to their large solidification range which allows volumetric shrinkage and a high degree of thermal contraction which induces voids and initiates cracks [164, 165]. Uddin et al. [164] imposed high temperature powder bed heating along with modified processing conditions to deter crack formation in Al 6061 without composition modification. The high pre-heat temperature removed melt-pool banding (crescent shaped melt-pool solidification tracks seen in micrographs) and the nucleation of large non-coherent precipitates to yield crack-free Al6061 with mechanical properties comparable to its wrought counterpart as shown in figure 2.7o and figure 2.7p.

In contrast to this method, Carluccio et al [166] improved the printability of Al6061 through alloying additions of Tibor and scandium. Both additions were successful in refining the grain structure and improving the mechanical properties of SLM processed Al6061. The addition of 0.42% scandium resulted in mixture of fine crystals and columnar grains while Tibor (0.34% Ti and 0.06% B) was able to achieve a fine homogeneous equiaxed grain structure. Although unweldable aluminum alloys

initially have had significant problems in AM, it is evident that there are solutions in order to make these prevalent alloys printable.

Ti-Based Alloys

Titanium alloys are extremely important in the aerospace industry which requires light-weight materials with critical load bearing capabilities [167]. However, since Ti alloys have poor material-processing, AM provides the perfect means to produce complex and exceptionally strong titanium parts [167, 168]. AM processed Ti alloys such as the αand βphase Ti-6Al-4V [5, 25, 78, 102, 167–173] have been used for over a decade in aerospace and medical applications and is the most researched alloy in the literature [5, 18]. An example of Ti components that have utilized this technology in the aerospace industry are the cabin brackets for the Airbus A350 XWB which were milled and machined out of aluminium alloy prior to AM implementation [174]. Other α- β alloys such as SLM processed Ti-6Al-7Nb have been investigated and produced as-built microstructures of α' martensite with second phase precipitates dispersed throughout [175]. Furthermore, β phase dominant Ti alloys such as SLM processed Ti-10V-2Fe-3Al [176] have shown αphase rods dispersed in a β matrix consisting of large columnar grains while SLM processed Ti-1Al-8V-5Fe [177] yielded a very fine β structure contrast to larger grains seen in casting.

As discussed earlier, Ti-6Al-4V is a prominent alloy in the aerospace and medical industry due to its high strength to weight ratio, excellent corrosion resistance and hypoallergenic properties for biomedical implants [5, 78, 169, 171]. Ti-6Al-4V has been heavily researched for over 15 years and early studies characterized LENS processed Ti-6Al-4V to be susceptible to the formation of long columnar grains for a large range of laser powers [178]. Within the columnar grains, a basket weave structure of αand β laths sizes increases as the laser power increased [178]. SLM processed Ti-6Al-4V was observed to contain very fine α' acicular martensite [169] which can be arranged in a "herringbone" pattern caused by the alternation in scanning direction [179]. Similarly, EBM and DED processed parts also yielded martensite composed of columnar β grains which were delineated by α grain boundaries [180, 181]. Wrougth and SLM microstructures of Ti64 are shown in figure 2.7q and figure 2.7r. Titanium alloys play a very important role in a variety of industries and will continue to be explored for AM implementation.

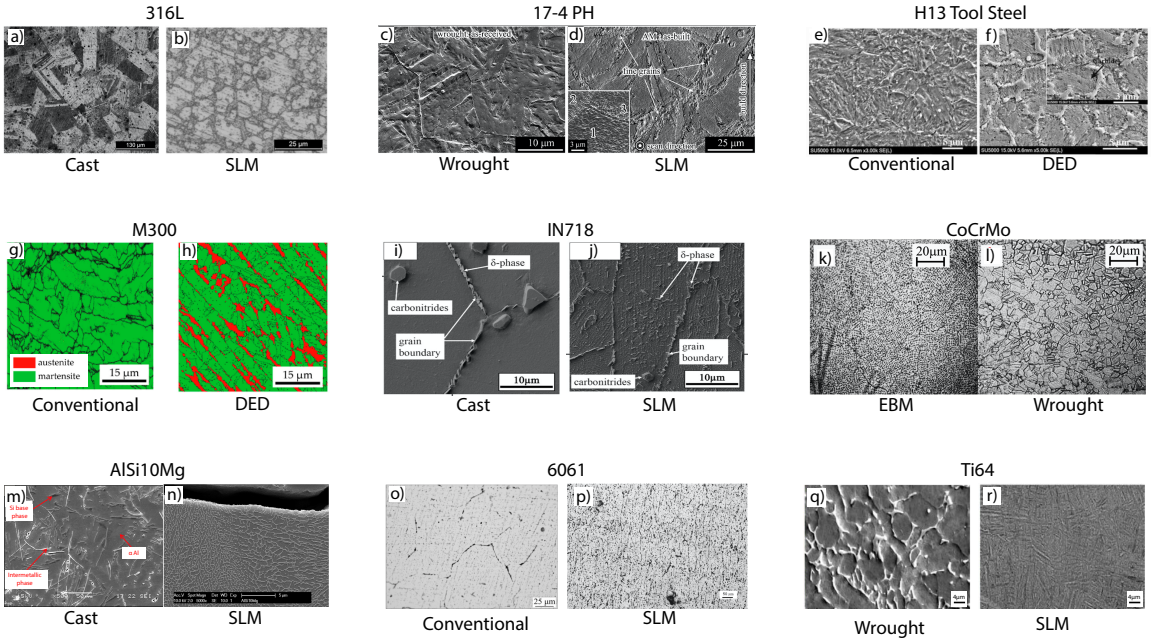

Figure 2.7: Microstructures of conventional and AM processed alloys; a) cast microstructure and b) SLM processed 316L stainless steel from [109] c) wrought and d) SLM microstructure of 17-4 PH stainless steel from [113] e) conventional and f) LAM processed microtrucutre of H13 tool steel from [125] g) conventional and h) laser metal deposition (LMD) EBSD images showing microstrucuture and amount of austenite within martensite of M300 from [117] i) IN 718 cast and j) SLM microstrucutres [132] k) EBM processed CoCrMo and l) wrought CoCrMo microstructures from [154] m) cast $AlSi_{10}Mg$ alloy from [182] n) and SLM counterpart from [157] o) conventional Al 6061 microstrucutre [183] and p) SLM microstructure from [164] q) Wrought and r) SLM microstrucutre for Ti64 from [173]. All images reproduced with permission.

2.6 Process Control and Optimization Techniques

The AM process can be enhanced through a variety of techniques to control or optimize the microstructure of the printed material. This section begins with an introduction to grain growth during the AM process and exploring the ability to predict and control the grain morphology during printing. Additionally, process monitoring techniques are discussed and how imaging systems can be implemented to optimize the printed material.

2.6.1 Grain Morphology

Obtaining the proper grain structure during the printing process yields superior mechanical properties. The grain morphology can be controlled spatially to optimize the material for a specific application by tuning the printing parameters [5, 8, 11]. In doing so, fine equiaxed grains can be produced to enhance strength and ductility, contrast to the highly textured epitaxial columnar grains that spread over several layers along the build direction [9, 167]. Generally, grain growth can be cellular, planar or dendritic columnar and/or equiaxed grain morphologies [9, 184, 185] and in special circumstances, amorphous or single crystal morphologies may be produced [186–189] depending on solidification rates and material composition [9].

Grain Growth Mechanisms

Dendritic grains grow radially throughout the casting at various nucleation sites to form equiaxed grain growth during casting processes [190]. Equiaxed crystals grow at a certain velocity determined by the local temperature and is inhibited when the grains impinge one another, or they reach a columnar front [190]. Similarly, the growth of columnar grains is usually concluded with the presence of an equiaxed zone or band. Equiaxed grains usually form outside a casting or in this case, directly above the substrate preceding the growth of columnar grains [191] which grow parallel to the build direction [9]. For equiaxed grain growth, the heat flows from the crystal into the undercooled metal and in columnar growth, heat flows from the superheated metal into the cooler crystal [184].

Solidification of a pure metal at the solid/liquid interface is most frequently planar if undercooling has not been imposed. The criterion for stable planar growth states that the ratio between the thermal gradient and the growth rate must be less than the ratio of the freezing range and the lower the diffusion coefficient to avoid undercooling [185]. Higher growth rates will result in cellular or dendritic growth and as the degree of undercooling increases grain growth will transform from planar to cellar, cellular to columnar dendritic, and then to equiaxed dendritic [185]. The topology of the melt pool, the thermal gradient and the velocity of the solidification front greatly influence the corresponding grain growth mechanism [185] as shown in figure 2.8.

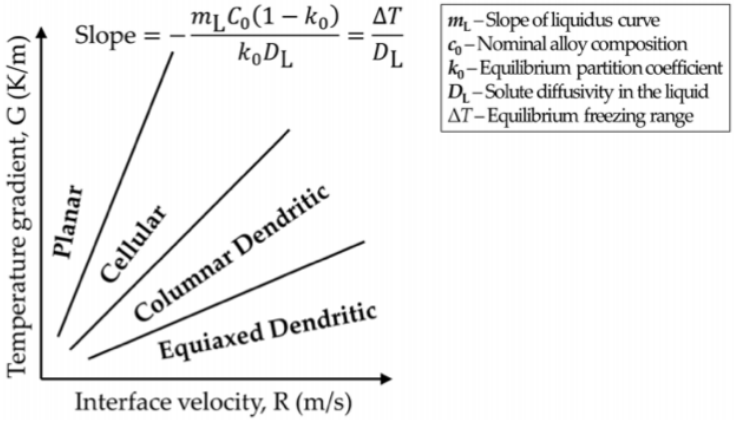

Figure 2.8: Types of grain growth with respect to temperature gradient as a function of interface velocity. Image reproduced with permission from [192].

Since equiaxed grain growth nucleates multi directionally, inoculants can be inserted to promote heterogenous nucleation, which refines the grain structure and enhances the toughness of the material [11, 191]. This effect can be seen during the AM process when un-melted particles act as nucleation sites for equiaxed grain growth [9,167,168]. Residual metallic powders are common in DED systems when the powder feed is too fast and heterogenous nucleation occurs at the top of the melt pool as well as the bottom which restrains epitaxial growth for long columnar grains [9]. Long columnar grains that spread several layers across the build have a specific orientation and are developed through epitaxial growth from the substrate or previous layer as seen in epitaxial laser repair of single crystal turbine blades [184, 190, 191].

Grain Structure Optimization

Since the quality of the AM produced part is directly related to the microstructure developed [9] which, in many cases (especially SLM processes) leads to brittle α' martensite formation [4]. Being able to control and tailor the grain morphology spatially throughout the build will reduce production time and cost [9, 186, 193]. In certain cases, it may even be beneficial to develop a finer, tougher grain morphology in higher stress areas and less so in relatively load free areas. Generating fine structures in the as-built condition ensures adequate mechanical properties and is important to inhibit grain growth in post processing heat treatment [9].

Due to the high temperature of the melt pool, the previous deposited layer is re-melted in which equiaxed grains nucleate heterogeneously from partially melted powders and a negative temperature gradient with an epitaxial, cellular or dendritic solidification front [9, 167, 168]. Additionally, the large columnar grains are a direct result of epitaxial growth from the substrate at the bottom of the melt pool which can be restrained by the equiaxed grain growth at the top of the melt pool [9, 167]. It can then be assumed that if epitaxial grain growth is dominant, the grain size of the substrate determines the final transverse grain size in the as-built materials [9]. Additionally, due to the dominant epitaxial growth, grains with their growth direction parallel to the direction of the highest thermal gradient grow preferentially. This effect can be seen in figure 2.9 for the growth direction and variations in solidification modes during deposition [185].

During the deposition process, each spatial location within the build is subjected to initial rapid solidification and successive reheating and cooling with the addition of layers [194]. An important mechanism in the deposition process and the subsequent grain morphology, is the presence of Heat Affected Zones (HAZ) similar to welding, affecting the adjacent areas around the melt pool. The solid area adjacent to the melt pool reaches high enough temperatures to cause solid-state transformations of the microstructure causing grain growth and recrystallization [68]. However, modifying process parameters such as increasing scanning speed yields smaller HAZ zones [62]. Brandl et al [161] observed that the as-built printed $AlSi_{10}Mg$ alloy contained cellular dendrites of αphase Al and inter-dendritic Si particles while the HAZ had coarser dendrites which resulted in a heterogenous microstructure.

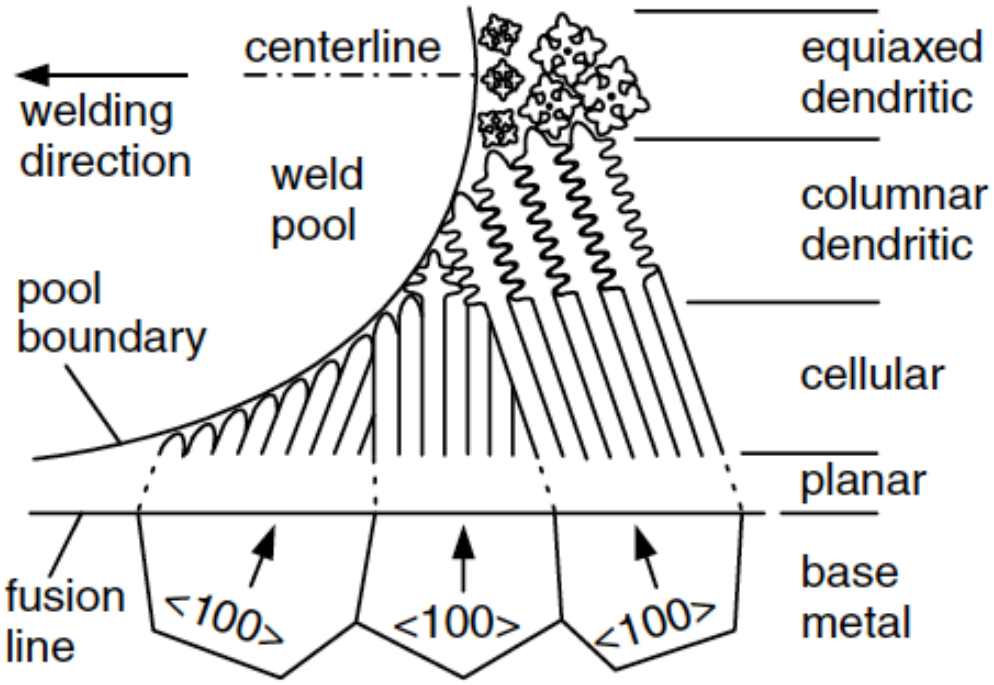

Figure 2.9: Melt pool solidification of an alloy on a base metal substrate with a crystallographic orientation along the <100> directions during welding and similar AM processes. Reproduced with permission from [185]

A study by Zhu et al [168], studied the alloying addition percentage Mo had on various Ti-Al alloys. They determined that the volume fraction of equiaxed grains present in the as-solidified structure increased gradually with an increase in alloying content due to the functioning of constitutional supercooling and remaining powders in the melt pool. Furthermore, Li et al. [195] altered the original Ti-6Al-4V AM alloy by adding Mo, Zr and Si to produce Ti-6Al-2V-1.5Mo-0.5Zr-0.3Si. It was found that the additions of the Mo, Zr and Si alloying elements increased the microhardness and yielded a better combination of strength and plasticity compared to the Ti-6Al-4V alloy through solid solution strengthening. The as-built microstructure of the Ti-6Al-2V-1.5Mo-0.5Zr-0.3Si alloy yielded a basket-weave lamellar α phase which was finer than the Ti-6Al-4V alloy which contributes to the improved microhardness.

Finite element modelling (FEM) can spatially model the microstructure during the build [196–198]. Commercial software such as ABAQUS allow the implementation of user subroutine scripts to provide realistic simulations in predicting

the microstructure, residual stresses, etc. in terms of the printing process parameters [199]. The resulting data from the simulations can be used to develop a process map specific to each alloy [21,199–201]. The solidification data of the alloys is mapped by the thermal gradient as a function of solidification rate (figure 2.10a) where the FEM simulation then converts this map to a laser power versus scanning velocity map (figure 2.10b) to identify the grain structure [199, 201].

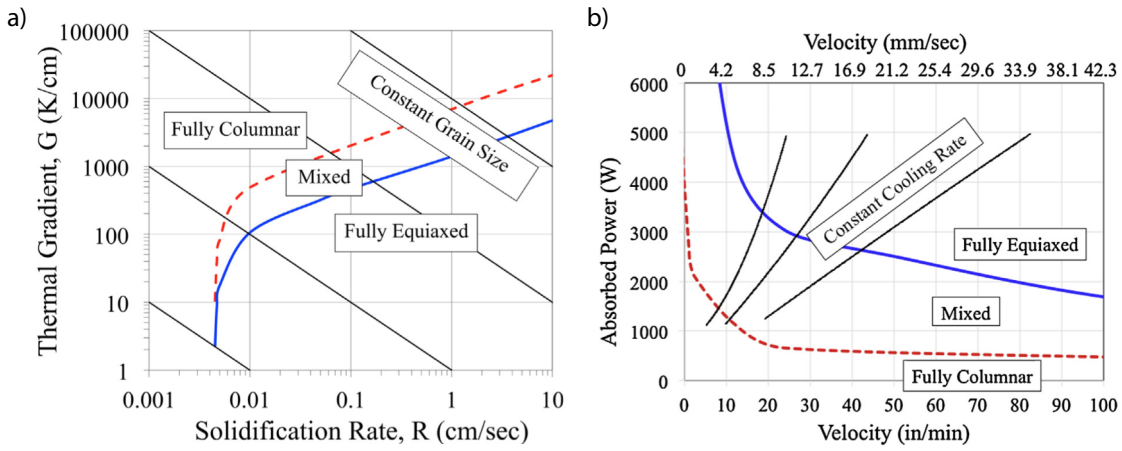

Figure 2.10: a) Solidification map for Ti-6Al-4V and b) process map for controlling the microstructure for Ti-6Al-4V. Reproduced with permission from [199].

A set of studies from Gockel and colleagues [199, 201] developed these process maps for Ti-6Al-4V to control the melt pool length to depth ratio and found that it can be used control the grain structure. Additionally, they found that by achieving a constant melt pool cross- sectional area, a constant grain size could be achieved throughout the process. Another study by Narraa et al [200] used a similar process mapping approach for Arcam EBM processing and successfully controlled the β grain width in Ti-6Al-4V alloys in multi-layer blocks. These results were further used to vary the microstructure spatially within the build by integrating a melt pool dimension control strategy by easily tuning the control variables.

Keller et al [202] developed an FEM and phase field simulation for IN625 by modelling the moving melt pool shape and compared the thermodynamic driving forces for nucleation against experimental observations of precipitates identified by electron and X-ray diffraction analyses. They determined that the maximum solidification rates occurred at 0.2 times the laser scan speed with a cooling rate of 10^5 K/s.

They also used several models for solidification modelling to compute the maximum degree of micro-segregation of Nb in the IN625 alloy. Furthermore, a phase field simulation of the PBF process to study the melt pool geometry, porosity and grain structure was developed by Lu et al [203]. They found that the depth and length of the melt pool increased as the energy density increased, similar to other studies. Additionally, they also found that the depth of the melt pool, the grain structure density and the porosity followed a scaling relation with laser power density. Low power density gave rise to partially melted powder particles, acting as nucleation sites for equiaxed grain growth while intermediate energy density, a columnar grain structure dominated the growth regime. Lastly, high energy density suppressed columnar grain growth due to the high thermal gradient, while rapidly decreasing the width of the grains.

Lastly, a study conducted by Rodgers et al [204] used a kinetic Monte Carlo Potts model to simulate the microstructure of DED printed IN718 and 304L and, EPBF Ti64 from separate case studies in the literature. They compared these simulated results with experimental results to verify the accuracy of the model. This model was used the shape of the melt pool, the neighboring temperature gradient, and the scan strategy to model microstructural evolution during printing. The comparison between the model and the experimental observations from the cases were reasonably accurate in predicting the as-built microstructure. It is evident that the ability to control and predict the as-built microstructure is essential to produce high-quality AM parts that are reliable and repeatable [205]. Metallurgical simulations of the AM process will be discussed further in the "Modelling" section of this paper.

Single Crystal and Amorphous Grain Morphology Possibilities with AM

Single crystal and amorphous metals are both on opposite sides of the microstructural spectrum but exhibit superior mechanical properties to their polycrystalline counterparts. Single crystal metals are absent of any grain boundaries which greatly contribute to failure mechanisms within the material. The long columnar grains that can spread over several layers across the build have a specific orientation. This orientation is developed through epitaxial growth from the substrate and previous layer [184, 190, 191]. This phenomenon can be exploited if the columnar to equiaxed transition (CET) is eliminated to develop fully directional columnar grains or single

crystals [184] yielding extremely hard materials as seen in nickel and 4-base super alloys for turbine blades [206]. As of now, little work as been successfully completed in producing a fully single crystal component using additive manufacturing. However, through advanced process optimization techniques and utilizing epitaxial growth it could be possible to manufacture components as a single crystal.

The other side of the spectrum for superior mechanical properties are amorphous metals which do not exhibit a crystalline structure and therefore do not contain dislocations. Due to the unique discorded structure and absence of grain boundaries and crystal defects, amorphous metals exhibit high mechanical strength, ductility and corrosion resistance [207, 208]. Amorphous metals, also called bulk metallic glasses (BMG), contain an amorphous grain morphology similar to glass and have unique mechanical properties that can be extremely advantageous [187–189]. The main issue for producing BMG is its limited glass-forming ability (GFA), therefore amorphous part volumes are usually kept below 90mm [188]. BMG's ambient temperature brittleness greatly affects its processability and thus heterogeneous microstrcutures are introduced to improve their plasticity [188,209,210]. Additionally, high entropy alloys (HEA) which contain 5 or more elements of similar atomic % are exploited to obtain amorphous phases in metals to generate extremely high yield strengths without conventional failure sources such as dislocations and grain boundaries [211]. Thus, BMG alloys have extremely high fracture toughness and prevent crack propagation since plastic deformation dissipates the fracture energy [189].

In order for the amorphous phase to be maintained upon solidification, cooling rates between 103-108 K/s are easily achieved during AM to ensure no crystallization occurs in the melt pool [188]. Thus, an entirely amorphous structure can only be achieved if the incubation time for the crystal is longer than the processing time, therefore a high laser power and fast scanning speed is required [188]. However, the concentrated heat flux induces high thermal gradients and subsequently, residual stresses and other defects such as pores and cracking due to the limited malleability [188, 189, 212].

A study by Li et al. [188] on SLM processed $Fe_{43.7}Co_{7.3}Cr_{14.7}Mo_{12.6}C_{15.5}B_{4.3}Y_{1.9}$ (at.%) powder revealed that micro cracks were unable to be mitigated through process optimization. Thus, soft crystalline powders with a high Poisson's ratio, good thermal conductivity and comparable thermal expansion were mixed with the amorphous powder to form a composite. It was revealed that cracks were completely eliminated by mixing 50 wt% of one of Cu, CuNi20, and CuNi35 powders. TEM micrographs revealed nanocrystals embedded within the Fe-based BMG matrix which may be located in HAZ formed by the crystallization of the BMG during printing. It was concluded that 3D printed Fe-based amorphous metals are extremely susceptible to micro cracks due to the high thermal stress concentrated around pores. Rather than process optimization, the content/category of the second phase formation can be tuned to yield superior mechanical properties and the Cu addition increased the fracture toughness by 20 times compared with the original Fe-based BMG.

2.6.2 Process Monitoring Techniques

Although FEM models can provide a high degree of accuracy in predicting the overall grain structure, being able to monitor and control the printed part's properties during the deposition process is important in order to produce high quality and repeatable parts. In situ process monitoring with feedback control is one area that can provide the AM industry with high-quality parts [21, 213, 214]. However, in situ process monitoring is difficult in PBF processes compared to DED due to inadequate access to the melt pool [21]. Various equipment can be used to monitor the deposition process such as pyrometers, cameras, thermocouples and displacement sensors [16].

Pyrometers relate the intensity of the radiation given off by the melt pool (grey body) to that of a black body using Planck's and Stefen-Boltzmann law. Photodiodes detect this radiation and convert it to an electrical signal to be then processed by the computer. Similarly, digital cameras (visible and infrared) are used to monitor the deposition process and melt pool temperature in real time [16]. Clijsters et al [215] developed a system to monitor the quality of the SLM in real time and provide estimates of the printed part quality. Their setup consists of an optical sensor setup that ensures a high-quality measurement of the melt pool while a data analysis sys-

tem translates and visualizes the measured sensor values into quality images. This is done through a mapping algorithm which transfers the measurements into a position domain from a time-domain. The accuracy and reliability of the in-situ monitoring setup was then investigated with several printed alloys and revealed great similarities between the actual defects and those revealed by the setup.

Farshidianfar et al [216] constructed a novel infrared (IR) imaging system to monitor the surface temperatures during the deposition process. Infrared cameras record the cooling rates and melt-pool temperatures and use this data to calculate thermal gradients and control the microstructure during deposition. Since grain growth is directly related to the cooling rate, this real-time controller provides the capability of producing different local grain structures spatially throughout the build. This gives the ability to tune the mechanical properties at high stress areas of the structure and fully exploit the capabilities of AM. The experimental set up for this real-time control setup is shown in figure 2.11. The IR camera is placed above the work envelope to produce thermographic images of the build where they are then processed in real-time to generate melt-pool temperatures, cooling rates and thermal maps. The control system receives this data to adjust the input process parameters (laser power and scanning speed) to reduce or increase the thermal gradients. Experimental results have shown that this system is capable of producing a consistent controlled microstructure during the deposition process [216]. Another approach that is more unique was developed by Shevchik et al [217] who are developing an acoustic emission device for real-time in situ quality monitoring of AM. This setup combines acoustic emissions and sensors that is coupled with a machine learning software for in situ, real-time quality monitoring. This device is currently only effective for PBF SLM systems, but future development could make this technology applicable to all AM processes.

X-ray computed tomography (XCT), a more established process in the AM industry, provides detailed information on internal defects such as porosity and residual stresses. [218]. XCT develops 3D depictions of an object by imaging the structure around an axis of rotation with an x-ray emitter and receiver. This technology also provides the ability to validate printed structure against the desired CAD models for dimensionality and defect detection purposes [218]. For binder jetting processed parts, XCT measures observe porosity, sinter neck size, pore size and particle size in

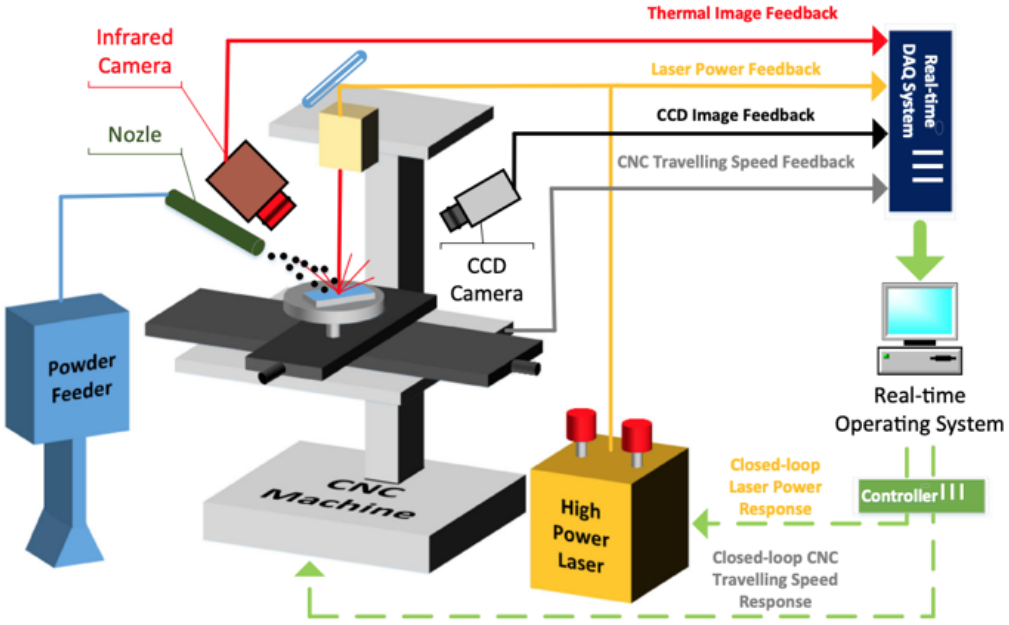

Figure 2.11: Closed-loop feedback experimental setup to monitor the thermal gradients using infrared cameras to adjust the printing parameters and control the microstructure. Reproduced with permission from [216].

both the green and sintered parts [47]. Although XCT is a process used after the part has already been printed, similar technology is being developed using x-rays for in-situ real time process monitoring of the AM process [219, 220].

Leung et al [219] used x-ray imaging system for monitoring defects and melt pool dynamics during the AM process. Their setup exposes key mechanisms during the deposition process including porosity, spatter, denudation zone and the evolution of melt tracks using synchrotron X-ray imaging. With this, they have developed a mechanism map to provide information on the melt track behaviour with respect to different process parameters. In addition to real-time monitoring, this technology is a useful tool for further understanding the melt pool and laser-matter dynamics.

Similarly, Zhao et al [220] use the same synchrotron x-ray imaging technology for real-time monitoring of PBF process. In addition to studying the melt pool dynamics, their study incorporated high-speed diffraction imaging to estimate the cooling and phase transformation rate. By observing the intensities from the HCP and BCC states of Ti-6Al-4V with their cooling rates, it was determined that a β to

α diffusionless phase transformation occurs. In addition, this imaging technique was used to measure keyhole formation and closure in great details. The high-speed imaging software was able to identify a formation-closure time of 50 µs, which generated voids deep inside the material. Process monitoring techniques are an extremely important tool in AM and will further help this industry expand its library of printable alloys and fully exploit the advantages of AM.

2.7 Computational Modelling

Computational simulations of the AM process are complex and include a number of different models such as thermal, mechanical, metallurgical, fluid dynamics. Finite Element Models (FEM) of the AM process [196, 221–225] are commonly used to simulate the thermo-mechanical stresses induced by the laser-material interaction and repeated melting and solidification effects [66, 226]. Computational fluid dynamics (CFD) simulations [65,66,227] are used to develop macro-scale simulations of solidification processes [226] and can model Marangoni turbulence, recoil pressure, drag and buoyancy forces which greatly attribute to the instability of the melt pool [65, 66]. Some simplifications in the FEM models include: treating the metal powder as a continuum solid body with equivalent thermomechanical properties and ignoring the vigorous dynamics of the melt pool fluid dynamics by assuming a steady state [66]. Some challenges in CFD modelling is quantifying the effects which variations in temperature and chemistry have on surface tension, affecting Marangoni turbulence and the resulting melt pool shape [226]. One way to address these missing pieces is a coupled CFD-FEM [228–231] approach to further increase the accuracy of these models and encompass most of the complex physics.

2.7.1 Computational Fluid Dynamics

CFD simulations discretize the control volume into a mesh using either a finite element approach or the finite volume method [232, 233]. CFD simulations are focused more towards the physical interaction between the heat source and the metal rather than the physical effects through layer addition. As discussed earlier, important CFD

models include melt pool geometry, melting mode (keyhole or conduction), Marangoni turbulence, vapor plume effects and recoil pressure. These studies using CFD analysis give greater insight into how processing parameters will affect the quality of the printed part. Some examples of CFD simulations are shown in figure 2.12.

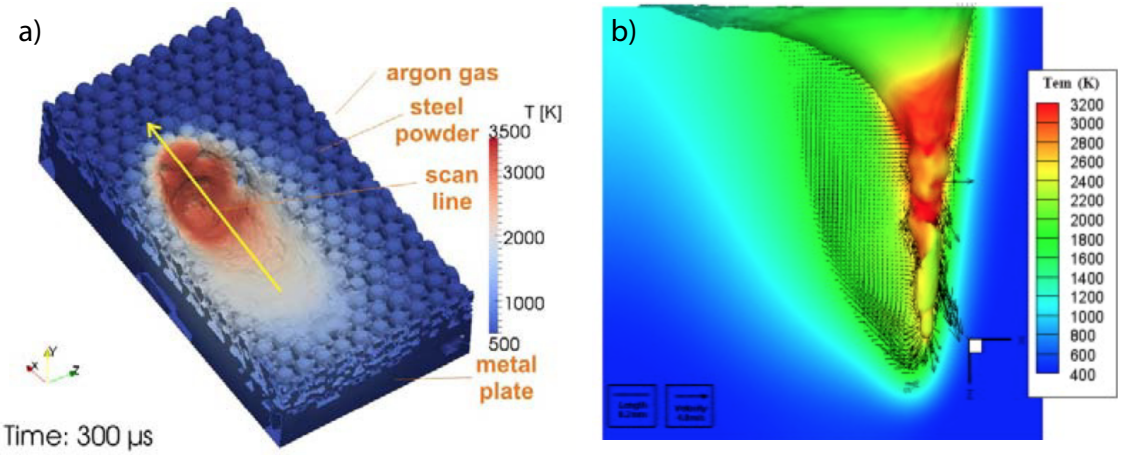

Figure 2.12: CFD analyses for the AM process a) laser scan on powder bed during SLM process [230] b) CFD simulation of keyhole formation [234]. Both images reproduced with permission.

Coupled CFD simulaions with an FE analysis are used to account for thermo-fluid effects inside the melt pool but are limited to localized mesoscale simulations due to the computational costs [235]. A coupled CFD-FEM simulation was developed by Jamshidinia et al [228] to study the thermal and stress distribution of EBM fabricated Ti-6Al-4V. This model is able to integrate fluid convection effects into a thermal stress FEM analysis. The modelling process begins with a CFD thermal analysis where the temperature histories are then imported to an FEM software for residual stress calculation. This analysis made important conclusions about the deposition process such as: a negative temperature coefficient of surface tension was responsible for the outward flow of the molten pool and the cooling rate was the most important parameter that influenced the thermal stresses. Complex models which can fully encompass the physical phenomena of the AM process will provide an efficient and effective way to qualify materials and processes for industry.

2.7.2 Finite Element Modelling

Complete FEM models for the AM processes typically contain 3 analyses: thermal, mechanical and metallurgical which can then be sequentially coupled. Software such as ABAQUS/CAE offer coupled temperature-displacement analyses to model the residual stresses in one simulation but are often much more computationally expensive with little increase in precision. A study by Marion et al [196] used this sequentially coupled approach to observe the residual stresses generated through AM deposition. A thermal analysis was conducted and the resulting temperature histories were used in a mechanical and metallurgical analysis. Phase volume fraction changes due to the temperature change from the metallurgical analysis were also input into the mechanical analysis for a more accurate representation of calculated stresses. Figure 2.13 illustrates the thermal, mechanical and metallurgical models for the AM process and their coupling relationship. The solid arrows represent the included physical phenemona such as: the effect of temperature on phase changes (1) and mechanical deformation (5), and the phase volume fraction influence on the mechanical behavior (3). The dashed arrows represent low contributions to the model compared to the laser source which can be ignored such as: latent heat of fusion (2) and plasticity induced thermal dissipation (6). As well as the stress induced phase transformations (4) which are insignificant compared to the thermal-induced phase transformations [196].

Modelling the deposition processes is similar to welding, although many more passes are made during AM [236]. To simulate layer addition, active/inactive or quiet elements can be used [196, 221, 222, 236, 237]. In both cases, elements are activated when a certain percentage of heat flux is experienced by inactive elements or when the laser or melt pool comes within a specific distance of the inactive element centroids [237].

The active/inactive approach assigns volume fractions to each element where all inactive elements are assigned 0 and as they are activated they are assigned 1. The inactive elements in this method are completely absent in the overall stiffness matrix which can make computation times quicker. However some artificial internal heat generation during activation has sometimes been observed which contributes to some inaccuracies [236]. The quiet method employs a different approach in that the thermal

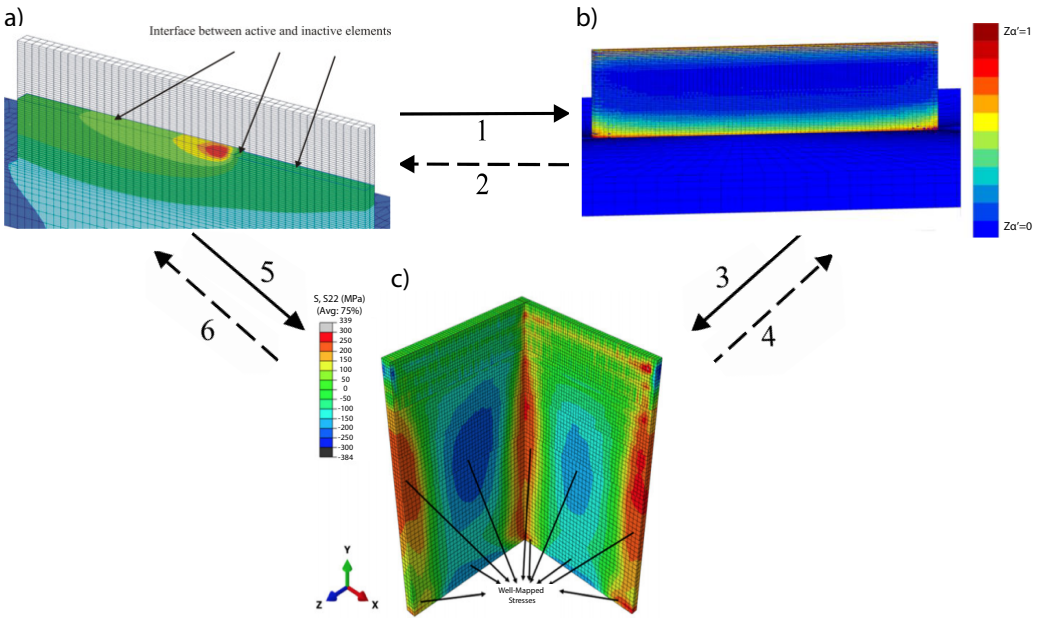

Figure 2.13: Finite element modelling of the DED process: a) thermal analysis illustrating inactive or quiet elements from [222] b) metallurgical analysis reproduced from [196], with the permission of the Laser Institute of America. c) mechanical analysis from [221]. All images reproduced with permission.

conductivity and Young's modulus of inactive elements are scaled down to near-zero values so the have very little effect on the printed material. As elements are activated, these values are restored to their rightful values however, all elements (inactive and active) are included in the global stiffness matrix which increases computation times. Additionally, the scaling down of material properties can yield instabilities within the Jacobian matrix which can cause convergence issues during computation [236]. Figure 2.13 illustrates thermal, metallurgical and mechanical analyses of the DED process which employ this type of element activation.

Thermal Analysis

Thermal modelling of the AM processes requires a transient analysis due to the non-homogeneous rapid heating and cooling that occurs after the laser comes in contact with the metal [225]. This process requires simulation of a moving heat source (laser or electron beam) through the use of user defined subroutines and scripts [226]. In

many cases, heat transfer through mass transport is neglected [222] and some studies ignore heat loss due to radiation [221] since convective heat loss is much larger. A model developed by Michaleris et al [222] accounts for the heat transfer through mass transfer by introducing its effects through a distributed heat input model using a Lagrangian reference frame.

The volumetric heat source from the laser can be modelled in several different ways such as a Goldak double ellipsoid [238, 239] or a Gaussian distribution [239]. In arc welding simulations, the Gaussian distribution model proved to show inaccuracies as it neglected the arc stiffness [239]. To account for this, a semi-ellipsoidal was proposed which was further refined to a double ellipsoid to address the steeper temperature gradients seen experimentally [239]. In FEM software such as ABAQUS, user-defined subroutines are required to model the desired position, shape and penetration of the laser source for each time increment. The accuracy of the thermal analysis is the most important component for the whole simulation since it determines the corresponding microstructure, mechanical properties and dimensional accuracy [225].

Moreover, the melt pool geometry has a significant effect on the resulting microstructure, and thus an accurate representation of the laser-material interaction is crucial in predicting realistic residual stresses throughout the build [226]. As expected, the highest temperature experienced in the melt pool is directly below the laser penetration depth and decreases and the distance increases away from the heat source [240]. The temperature profile of the melt pool can be seen in figure 2.13b.

Mechanical Analysis

A sequentially coupled model is most common in the literature, where a thermal analysis is initially conducted and the nodal temperature history is used as a thermal load in a mechanical analysis to calculate the residual stresses throughout the build [221, 241]. The mechanical analysis in FEM software assumes small strain and deformation and use elasto-plastic constitutive model [235]. The elastic behaviour is modeled with the isotropic formulation of Hooke's law using temperature dependent values for both the Young's modulus and Poisson's ration [241]. Von Mises yield criterion is often used and a time-independent kinematic plasticity model is often used for plastic behavior to capture the cyclic non-linear work hardening called the Baushinger

effect [235, 241]. In addition to the Young's modulus and Poisson's ratio, the temperature strain-hardening rates (plastic tangent modulus) and yield strengths are required [235, 241] for plasticity modelling. An example of mapped thermal stresses for an as-built AM processed component produced by Hajializadeh et al. is shown in figure 2.13.

Metallurgical Analysis

The metallurgical model is highly dependent on both the thermal history and the state of the material [196–198]. Due to the cyclic heating that occurs during the AM processes, there is a complex set of phase transformations that occur spatially throughout the build such as HAZ (similar to welding) which greatly affect the mechanical properties. Due to the rapid solidification of the melt pool during the AM process, kinetics have a strong influence on the resulting microstructure and thus equations for diffusion and diffusionless transformations similar to alloy specific time-temperature-transformation (TTT) curves can be used to map the grain morphology based on temperature and cooling rate. Additionally, the composition of the alloy has a strong influence on equilibrium of phases. For example in Ti-6Al-4V, Al is an α stabilizer while V is a β stabilizing element [242] which yields the characteristic $\alpha + \beta$ microstructure. Additional phases for this alloy include the α' phase which is the HCP microstructure produced from the β phase at high temperatures and then rapidly quenched.

The volume fractions of each phase can be described by the tendency to move towards equilibrium and the resulting equations can be implemented into a FEM software. Diffusional transformations can be modelled by the isothermal Avrami equations applied to non-isothermal applications by imposing the additivity rule to discretize the cooling curve into small time steps. However, martensitic diffusionless transformations are most commonly modelled by the Koistinen-Marburger (K-M) equations. Equations 2.1 - 2.2 represent the volume fraction diffusional transformation equations required for metallurgical modelling of Ti-6Al-4V [196].

$$z_\alpha + z_{\alpha'} + z_\beta = 1 \tag{2.1}$$

$$z_i = (1 - \exp(-kt^n))\, z_{i_{eq}} \tag{2.2}$$

Where z_a, $z_{a'}$, z_β are the volume fractions for the α , α' and, β phases of Ti-6Al-4V. Similarly, $z_{i_{eq}}$is the equilibrium proportion of phase i (α, β, α') which can be found at temperature T and k and n are temperature dependent parameters determined using the the alloys' TTT diagram. Since the amount of α' martensite is highly dependant on the degree of undercooling below the martensite start temperature (Ms), the K-M equation can be used to calculate the volume fraction of martensite [196, 242] as shown in Equation 2.3. This expression is required to be updated to consider the eventual amount of α' at the beginning of the transformation and the retained β phase [196].

$$z_{\alpha'} = 1 - \exp(-\gamma\,(M_s - T)) \tag{2.3}$$

For this equaution, γ is a constant and M_s is the martensite start temperature. It can be noted that the K- M equation yields a parabolic shape instead of a sigmoidal shape [243] as observed on TTT diagrams. This dissimilarity causes values to deviate from experimental data significantly for the first 10-20% of martensite formation [243]. Figure 2.13 illustrates the computed fractions of martensite of a DED built wall. Various models have been proposed which apply temperature as a variable but are still an approximation and yield some degree of error. Thus a more accurate approach could be to conduct a thermo-mechanical FEM model and incorporate the metallurgical model using software which can model the grain growth and nucleation of the metal during solidification. Recent work conducted by Zhang et al. [244] used the temperature history from an FEM analysis for a metallurgical analysis of the AM process.

2.7.3 Microstructure Growth and Nucleation Modelling for AM processes

More accurate metallurgical modelling tools can be used and coupled with the thermo-mechanical FEM models. Two common modelling approaches for microstructure and

particle dynamics include phase-field (PF) and molecular dynamics (MD) [226]. PF modelling [202, 203, 205, 245] has been the more popular approach for predicting detailed grain morphologies and solidification dynamics [226] as MD is much more computationally expensive than PF. MD describes the evolution of a system based on the motion of individual particles while PF modelling is based on the evolution of continuous local order parameter field to describe solidification phenomena on a mesoscopic length scale [246]. MD simulations can be used to define the complex material properties since they provide a link between interaction potential and properties such as kinetic coefficients, interfacial free energies and dependence on crystallographic orientation [246]. Bulk interfacial property data from MD simulations can be incorporated into PF models as an input for a more accurate model of the processs [246].

Some specific refined models for simulating the metallurgical phenomena of the AM processes are stochastic cellular autonoma (CA) and the MD Monte Carlo (MC) simulations for modelling solidification structure [246, 247] and can be coupled with finite element [248] or difference methods [247]. CA methods have been developed to resolve issues in PF models which lack the prediction of grain competition [193]. This method provides coupled predictions of thermal behaviour and grain morphology by incorporating crystallographic texture [204]. CA methods are able to have a much coarser mesh size than that of PF models which can greatly reduce the computation expense [249].

CA methods have been further refined for simulation of crystal growth in order to incorporate more detailed local conditions for dendrite morphology [249]. A modified CA method proposed by Peng et al [249] for crystal growth during casting, coupled the macroscopic heat and microscopic mass transport equations and designated the nucleus site in a mesh to apply grain growth models to each mesh. The model for nucleation and growth consists of four pieces: 1) cell geometry, 2) state of each cell, 3) neighborhood configuration and 4) transition rule that determines the state of the cell during each time step. Koepf et al [193] proposed a similar model for the AM processing of IN 718. Their CA model simulated the microstructure prediction of several millimeters of build height with remarkable detail and can be seen in figure 2.14a.

MC methods are a form of MD models which can predict three dimensional microstructures during solidification and solid-state evolution with many passes by the

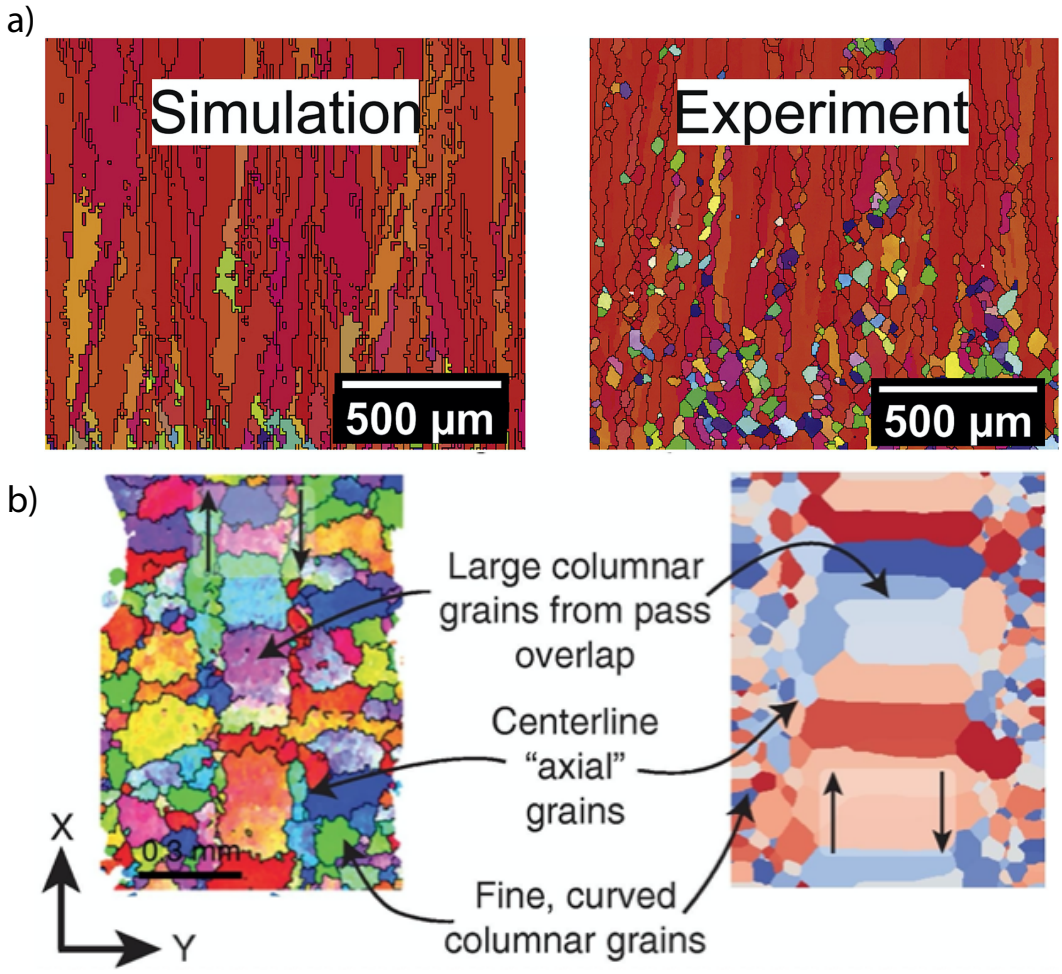

Figure 2.14: Metallurgical nucleation and grain growth simulations of the AM process a) cellular autonoma simulation compared with experimental results [193] b) Monte Carlo simulation compared with experimental results [204]. Images reproduced with permission.

laser source with idealized molten zones [204] as shown in figure 2.14b. The concept behind MC methods is the thermodynamic free energies of volume site interactions [245]. The Gibbs free energy is calculated for an element with its crystallographic orientation where a random selection of a new crystallographic orientation is assigned and the free energy difference is compared [245]. The orientation that minimizes the free energy is chosen and this process is repeated millions of times which results in a systematic free energy decay [245]. Open-source software such as SPPARKS based on the Potts Monte Carlo technique has been used to model the microstructure evolution during metal deposition in AM processes [226]. Cubic lattice sites are characterized

with "spins" to represent the individual grains and as the heat source travels and generates the melt pool through these sites, the spins are randomized and their grain assignment is lost [226].

2.8 Post Processing Methods

As discussed earlier, there are a number of defects present in AM parts that are not commonly seen in conventionally manufactured metals. Defects such as high surface roughness, porosity, residual stresses, anisotropy and undesired microstructures are unacceptable for most applications. Post processing methods for AM parts such as hot isostatic pressing (HIP) [250–253], heat treatment [45,133,140,149,254,255], polishing [256,257] and machining [258,259] can greatly improve the mechanical properties and aesthetics of AM processed parts. Illustrated in figure 2.15 are SEM images of the as built surface of PBF processed 316L stainless steel.

In addition, AM processed parts for assemblies that need fasteners, alignment components and high dimensional accuracy require drilling and tapping for their desired functionality [259]. However, the AM industry is constantly pushing towards further advancing printing technology to eliminate the requirements of post processing to increase efficiency and productivity. New technologies such as hybrid manufacturing combines additive and subtractive (machining) technologies into one process and is a rapidly developing field with a lot of promise. This method of manufacturing allows the component to be polished or shaped with high precision in tandem with DED processing [260,261], providing a one-step process and filling some of the current gaps in AM technology.

2.8.1 Hot Isostatic Pressing

HIP is a severe post processing technique to eliminate porosity throughout a metal structure and is used in many processes including forming, casting, diffusion welding and conventional sintering [250, 262]. This process involves heating the part to high temperatures while applying high pressures close or equal to the yield point in an inert atmosphere, causing plastic deformation to densify and homogenate the microstruc-

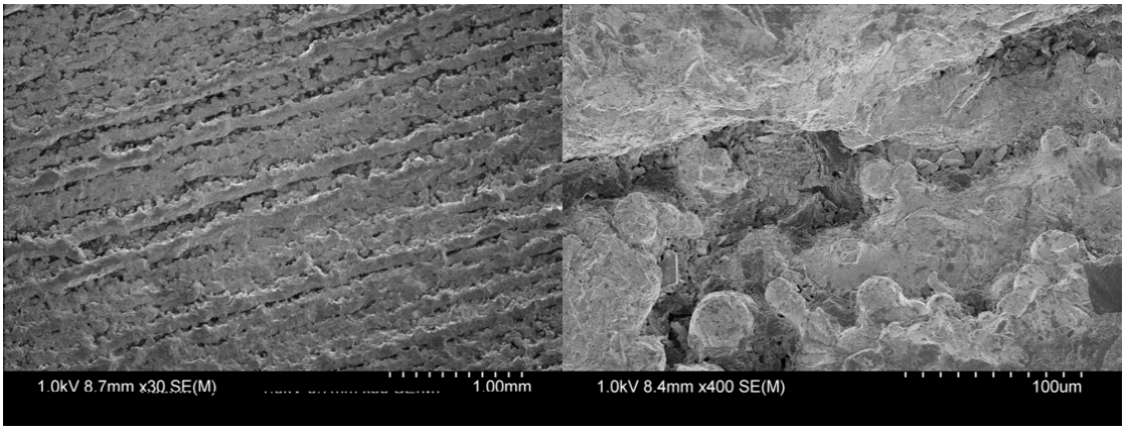

Figure 2.15: Surface roughness of as-built LPBF processed 316L

ture of the material [262]. The high pressures and temperatures cause entrapped gases in the pores to dissolve in the metal where the pore then collapses [252, 262]. Since pores act as crack nucleation sites and greatly decrease fatigue life, HIP has confirmed significant improvement in fatigue strength through eliminating or reducing pore size [252, 253]. AlMangour et al [251] studied the effects of post processing HIP on SLM processed TiB_2/316L composite. It was concluded that HIP eliminated major pores and cracks which were developed through unoptimized process parameters during deposition. Two HIP cycles were conducted, and longer times increased the diffusion rate and subsequently the binding strength to further increase density to 99.5%. Additionally, as the HIP holding time was increased, the grain morphology evolved from an equiaxed structure to agglomerated nanoparticles (showing a decrease in hardness). Examples of HIP treatment can be seen in figure 2.16a.

2.8.2 Heat Treatment

Heat treatment has played a major role in metallurgy for hundreds of years, as various desired mechanical properties and grain morphologies are unattainable otherwise. Although similar heat treatment methods for wrought and cast alloys are conducted for AM processed parts, the purpose behind the heat treatment can be different since the defects and as-built microstructures vary between processes. For example, AM processed $AlSi_{10}Mg$ is often solutioned, quenched and aged to dissolve the anisotropy developed from the layer-by-layer deposition [254] which is not an issue in conven-

tional processes. Additionally, heat treatments designed for cast alloys may not be suitable for AM processed alloys. A study by Aboulkhair et al [263] investigated a conventional T6-like heat treatment on SLM processed and cast $AlSi_{10}Mg$. It was observed that the hardness increased after heat treatment for the cast alloy as expected but decreased for the SLM processed alloy. This demonstrates the dissimilarities between the processed alloys and the need to develop specific heat treatments tailored to AM processed parts.

A similar study was conducted by Philpott et al [264] to investigate the effects of conventional heat treatment between cast and SLM processed IN 939. The as-built cast IN 939 consists of large equiaxed grains with large precipitates while the as-built SLM sample contained very fine columnar grains with extremely small precipitates. However, throughout the various stages of heat treatment, the SLM processed alloy showed large recrystallization and the fine columnar grains were replaced with larger, lower aspect ones. The cast alloy experienced very little change during the treatment processes. In addition, a network of very fine carbides formed during the heat treatment of the SLM processed alloy which may have different effect on the properties compared to the cast alloy. It was concluded that a shorter heat treatment may be beneficial for the SLM processed alloy since the carbide precipitation continued into the final stages of the treatment, further showing the requirement of specific heat treatments for AM produced alloys. A comparison of heat treatment for wrought and SLM processed 17-4PH can be seen in figure 2.16b.

2.8.3 Polishing Techniques

Other common post processing techniques that are usually required is polishing and machining, which reduce the "staircase effect" commonly observed in AM processed parts giving them a high surface roughness finish. Aesthetics, dimensional accuracy, fastening features and surface roughness are addressed by these methods. High surface roughness greatly attributes to inaccuracies in dimensions, poor fatigue properties and unappealing aesthetics. The fatigue properties of as-built AM parts have been shown to have much lower limits than those that were polished or machined after processing [265,266]. After post process machining or polishing was conducted, it was found that while surface finish has been found to contribute to reduced fatigue life, presence of

residual stress and near surface porosity had a more significant impact [266]. Spierings et al [267] measured the fatigue performance for SLM 316L. The surface roughness (Ra) was measured as 10.0, 0.4 and 0.1 µm for the as-fabricated, machined and polished specimens, respectively. The polished material showed the highest fatigue limit with little difference to the machined specimen.

Electrolytic Polishing

Another post processing technique to improve the surface roughness of AM processed parts is electrolytic polishing. Electrolytic polishing is driven by an electric potential where particles on the surface of the metal move toward the cathode through a pathway enabled by electrolyte [268]. A study by Urlea et al [269] on electro polishing of SLM-processed Ti-6Al-4V showed that the surface roughness could be improved by as much as 92% in a few cases. Additionally, effective internal polishing would be feasible with this method, contrast to other polishing methods. Other investigative works on electropolishing include Jung et al [270], who studied the surface shape control of pure Ti samples fabricated by EBM. Various samples were exposed to different electrolytic conditions at different voltages and times. Promising results were achieved, especially at high times and voltages which can be seen in figure 2.16c.

Laser Polishing

There are a number of polishing methods for AM processed parts which include laser polishing [256,271,272], electrolytic polishing [268] and, shot peening [273,274]. Laser polishing smooths the topography of the AM-processed part with the heat source and provides a fast, localized and waste free polishing method compared to abrasive mechanical post processing methods [256, 271, 272]. Laser polishing is a non-invasive technique which can be integrated into a five-axis system to compliment industrial 3D metal printers and treat the surfaces of complex geometries [256]. Bhaduri et al [271] studied laser polishing of 3D printed 316L and saw a 94% maximum reduction of surface roughness from 3.8 to 0.2 um. Additionally, they observed a thin oxide surface layer of Fe and Cr up to 0.5um deep when polishing in atmospheric conditions while it was negligible when polishing in an Ar purged environment. It was concluded that the optimized laser polishing technique eliminated all scratch marks, pits, holes and

other irregularities for the AM parts. Figure 2.16d illustrates the junction between the laser polished material and base as-built part.

Shot Peening

Shot peening is a traditional post processing technique that has been used on wrought and cast alloys for many years. This technique cold works the surface of the metal and induces a residual compressive state which has shown to improve fatigue properties [275, 276]. Compared to as-built AM samples, the shot peened samples have a refined microstructure on the surface yielding better surface roughness, hardness, wear resistance and compressive yield strength [224]. The surface morphology of shot peened SLM-processed $AlSi_{10}Mg$ was investigated by Uzan et al [274] and revealed a reduction of surface roughness by 25-30 µm with distinct craters formed by the collisions with the balls [274]. Additionally, the fatigue limit showed an increase from 75 MPa to 110 MPa when subjected to shot peening. Figure 2.16e illustrates the shot peened surface of SLM processed $AlSi_{10}Mg$.

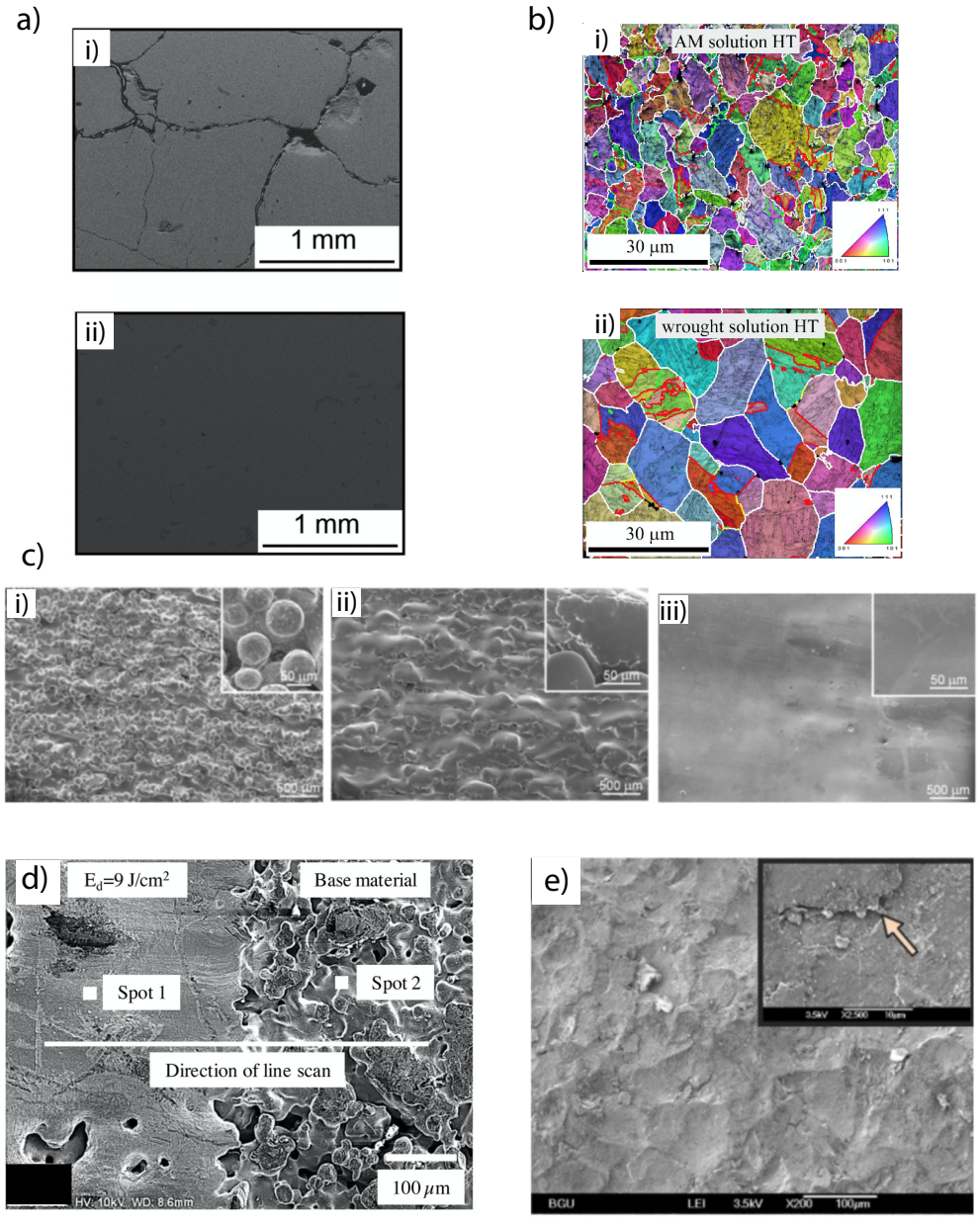

Figure 2.16: a) HIP treatment of SLM-processed 316L composites reinforced with 15 vol.% of TiB2 where i) is before HIP treatment and using ball-milled powder and ii) after two HIP treatment cycles from [251] b) EBSD images of solution heat treatment for SLM processed and wrought 17-4PH SS from [113] c) electrolytic polishing of pure AM built Ti where i) as built surface ii) treated for 60s at 30V and iii) treated for 600s at 30V from [270] d) SEM micrograph showing the junction between laser polished and as-built SLM surface of 316L stainless steel [271] e) Shot peened surface of SLM processed $AlSi_{10}Mg$ [274]. All images reproduced with permission.

2.9 Conclusion

This review paper focuses mainly on the physics of metal AM, however it is important to note other critical subjects such as process standardization (ISO, ASTM) and file formats (STL, OBF, AMF, 3MF) are important topics in AM and are left for more dedicated studies. Some of the most important aspects of metal AM are addressed which include: current technologies, melt-pool characterization, processing defects, printable alloys, process optimization, numerical modelling and, post processing treatments. The three most common metal printing methods which include PBF, DED and binder jetting were discussed as well as the differences between laser and electron beam heat sources. A relatively new style of printing for metal AM are fused deposition modelling (FDM) style desktop metal printers which are starting to get attention. These systems use a solid feed stock and deposit the material on a substrate but similar to the binder jetting process, require washing and sintering.

The complex physics of the melt pool and its importance to the as-built quality of the printed part was discussed. The relationship between printing parameters and defects such as balling, porosity and lack of fusion was illustrated and it was determined that the laser power and scanning speed could be tuned to stay within the conduction mode zone. The associated defects characteristic of the AM process were discussed in further detail and the significance of residual stresses induced during the printing process was addressed. Furthermore, the most prevalent printable alloys currently being used in metal AM were discussed and their microstructures compared with their conventional counterparts. Alloys such as Ti_6Al_4V, $AlSi_{10}Mg$ and SS 316L have been the focus in the literature over the last few years and are widely available from most manufacturers. However, some upcoming alloys which have shown promise in the literature or have recently been released by industry is 4140 steel and high entropy alloys used to produce amorphous metallic components.

The validation process for AM built alloys is generally focused on processing parameters, microstructure and defects such as porosity and residual stresses. Due to the dissimilarities in AM processed parts compared to their conventional counterparts, there is still plenty of research needed on characterizing the material on a fundamental level by looking at dislocation densities and movement under load and, alloy segregation. Process optimization techniques were then discussed for grain

structure optimization and the possibilities of producing single crystal and amorphous alloys in AM. Some studies included: FEM modelling, alloying additions and closed-feedback in-situ temperature measurements to tune the processing parameters during printing. These studies showed promise for in-situ microstructure control however, further empirical data and testing is needed from a wider range of materials and systems for industry adaptation [215]. In addition to this, FEM modelling was discussed in detail with respect to how thermo-mechanical-metallurgical analyses are conducted as well as nucleation and grain growth modelling of the microstructure using MC and CA methods.

Each type of numerical model for AM yields different information about the complex physics of the process. Generally, localized CFD and grain nucleation studies are used to model the complex meltpool characteristics and microstructures. Whereas FEM models generally model the macroscopic grain volume fractions and residual stresses. There are significant challenges, such as computation time with incorporating all three model types into one unified simulation and is still an outstanding problem in the field. Lastly, various post-processing techniques such as HIPing, heat treatment, laser and electrolytic polishing and shot peening were explored. It was determined that the same heat treating process imposed on wrought and AM built components yielded different properties; thus demonstrating the vast amount of research that is still required in this field. Currently, AM technology is not yet at a point where no post-processing is required, therefore AM specific treatments will need to be established.

Chapter 3

Investigation of direct energy deposition processed 4140 steel using electron microscopy methods

3.1 Introduction

The microstructure, defects, and sub-microstructural characteristics of materials have a significant effect on the resulting mechanical properties. Therefore, investigating the material on a µm to nm scale is crucial in order to understand the significant changes inflicted by the specific processing method. The Royal Canadian Navy (RCN) is currently conducting research with their DED metal printer to eventually print components for their naval fleet. Since even the smallest of defects can be catastrophic on some of these vessels, specifically the submarines, the manufactured parts go through extensive non-destructive testing to ensure premature failure does not occur. Although metal AM has seen significant progress towards part qualification, the printed components at the RCN are not validated or qualified to be used on board their fleet. Thus, further investigation needs to be conducted to better understand the printed materials in order to be implemented.

Although a popular alloy for the automotive industry, 4140 steel has not seen enough research in additive manufacturing. This is partly due to the fact that AISI 4140 steel has a tendency for cold cracking [2]. The alloying additions of Cr and Mo increase this alloy's hardenability and thus, the formation of martensite when subject to steep thermal gradients commonly seen in welding. A pre-heat temperature of 232°C is usually required to weld 4140 steel [2] and because of this, additive manufacturing of this alloy can be difficult. Few studies [2, 277, 278] have

investigated 4140 steel processed by various AM methods and have received promising results. Wang et al [2] discovered a variety of microstructural constituents in as-built DMLS (laser PBF) 4140 steel with fresh martensite, tempered martensite, bainite and carbides. Contrast to their wrought 4140 steel, which was dominated by martensite, it also contained higher amounts of sulfides and oxides.

The purpose of this study is to investigate the microstructural characteristics of DED processed 4140 steel manufactured by the RCN. Several microscopy methods are used which include transmission electron microscopy (TEM), scanning electron microscopy (SEM) and optical microscopy. Using these tools, we can identify some of the complex characteristics in printed 4140 steel.

3.2 Background

There are a number of defects that can occur in a crystal lattice which can greatly affect the mechanical properties of the material. Defects such as dislocations, stacking faults (which are usually unstable in BCC materials) and twin boundaries are commonly found within crystalline materials [279]. The main strengthening mechanism in metals is through blocking the movement of dislocations by manipulating the microstructure to include higher grain boundary density, secondary phases and other internal interfaces. However, this strengthening mechanism usually comes at the expense of ductility. Several methods such as coherent twin boundaries, bimodal (coarse and fine) grain sizes and secondary phase morphology control have been shown to be able to retain the ductility while improving the strength [280].

Dislocations are defects or irregularities in the crystal structure which allow the material to deform through atomic movement also known as slip which plays a major role in the strength of a poly-crystalline material [279]. They cannot be terminated within a crystalline structure and thus form a continuous network [281]. Dislocations interact with several features within the microstructure such as grain boundaries, solute atoms, precipitates and other dislocations [279, 281]. The interaction of these dislocations impedes motion and creates dislocation segments between pinning points. Here, the dislocation density and the segment length are the main components which determine the strength and deformation of the alloy. As stress is

applied, these segments move but remain attached to their respective pinning points. The motion of dislocations then occur by exiting these segments [281]. Depending on the manufacturing method, dislocations densities can greatly vary through grain refinement, cold working, etc. and significantly alter the mechanical properties of the processed alloy [279].

Another deformation mechanism in crystalline materials is twinning, which occurs when a shear force acts parallel along the twin boundary and shifts the atoms to move out of their original location. A twin boundary occurs when there is a unique mirror image distortion of the crystal lattice. Thus, the shifted atoms between the twin boundaries can interfere with the slip mechanics of the alloy. Mechanical twinning can greatly effect plastic deformation in two ways [282]:

1. grain subdivision which increases the work hardening rate and the number of barriers for slip
2. decreases the work hardening rate through twinning shear

Twinning can occur during deformation or heat treatment. Consequently, during the metal AM process, there is a high number of intrinsic heating cycles occurring on previously deposited layers which could induce twinning. However, a study by Pham et al [283] discovered that the dominant twinning activity was a consequence of the nitrogen gas used in the chamber. They state that nitrogen can lower the steel's stacking fault energy which then leads to dislocation dissociation and encourages the formation of twins. Furthermore, they conclude that the twinning does not instigate a large amount of hardening due to the porosity formed during printing which causes a negative effect on hardening.

Furthermore, a study by Liu et al [280] studied the dislocation networks in SLM processed 316L stainless steel. Through TEM work, they showed that the dislocation network and alloying element segregation acted as a barrier for dislocation motion. Furthermore, it was found that the motion of partial dislocations was hindered but not entirely halted through cell walls and the presence of dislocation networks which enhanced strength without compromising ductility. Since metal AM is still in its infancy, the exact influence on dislocation density and other sub-microstructural defects has not been thoroughly investigated, particularly in 4140 steel.

3.3 Experimental Procedure

3.3.1 DED Process and Conditions

A 37.084mm x 37.084mm x 110mm rectangular column was printed over several days with each session printing 10 - 34 layers as illustrated in figure 3.1. The substrate is made from 1020 plain carbon steel, however the samples analyzed in this study were extracted from the last build session comprised of 26 layers. The top most layers were chosen as they best represent the as-built properties of 4140 steel deposited through DED. Layers deposited during earlier build sessions would be subject to different dwell times and heating cycles, greatly altering the microstructure, dislocation characteristics and other defects. Thus the analyzed layers were built on top of previously deposited 4140 steel as the substrate.

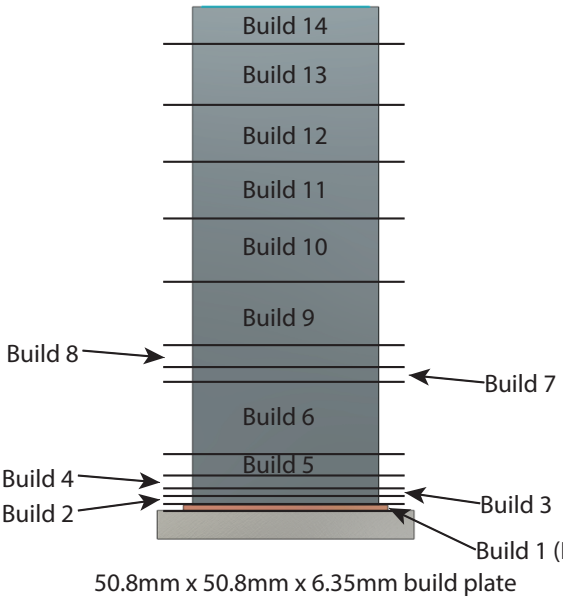

Build Session	Layers Built	Date
1	10 (Raft)	18-Sep-17
2	10	18-Sep-17
3	10	21-Sep-17
4	15	25-Sep-17
5	19	26-Sep-17
6	34	28-Sep-17
7	15	29-Sep-17
8	19	02-Oct-17
9	33	03-Oct-17
10	32	04-Oct-17
11	31	05-Oct-17
12	28	06-Oct-17
13	30	10-Oct-17
14	26	11-Oct-17

Figure 3.1: Build session schedule showing the number of layers for each build and the date it was printed. Information provided by the Royal Canadian Navy.

The machine specifications for the printer used in this study are listed in table 3.1. A similar fibre laser and spot size as chapter 3 was used however the oxygen concentration in this study is much greater between 80-150 ppm. Furthermore, the process parameters used for printing are shown in table 4.4. A traverse speed of

7.62 mm/s and an average laser power of 295W was used. However, unlike the laser power in chapter 3 which was held constant, the peak laser power was 1230W during printing with a layer height and width of 0.289mm and 0.343mm, respectively.

Table 3.1: Machine Specifications for the printer used in this experiment. Information provided by the Royal Canadian Navy.

Laser Type	**Spot Size**	**Substrate Dimensions**	**Oxygen Concentration**
Yb Fibre	600 µm	100x100x200mm	80-150 ppm

Table 3.2: Process parameters used during printing for the fabrication of the column. Information provided by the Royal Canadian Navy.

Parameter	**Value**	**Units**
Peak Laser Power	1230	W
Avg Laser Power	295	W
Traverse Speed	7.62	mm/s
Step over	0.343	mm
Z step up	0.289	mm
Powder feed rate	22	g/min

The build chamber setup is shown figure 3.2. There are two deposition nozzles, one for the powder feed and the other for the laser and argon gas flow. Unlike the setup in chapter 3, these nozzles are not co-axial and are offset from one another at an angle.

3.3.2 Materials

As received gas atomized 4140 steel powder with a maximum particle size of 75 µm manufactured by Sandvik Osprey Ltd. was used in this study. The chemical composition of the powder is illustrated in table 3.3. In this study, the powder was sieved and re-used with a maximum powder size of 106 µm after two separate 15-20 layers builds (approximately 12-15 mm). The recycled powder was mixed with virgin powder for each subsequent build session. The maximum virgin powder sized is recorded to be 75 µm. For the analyzed build session, approximately 260g of 7kg (4%) of initial powder was re-used from the previous build.

An SEM image of the powder used in this experiment can be seen in fig-

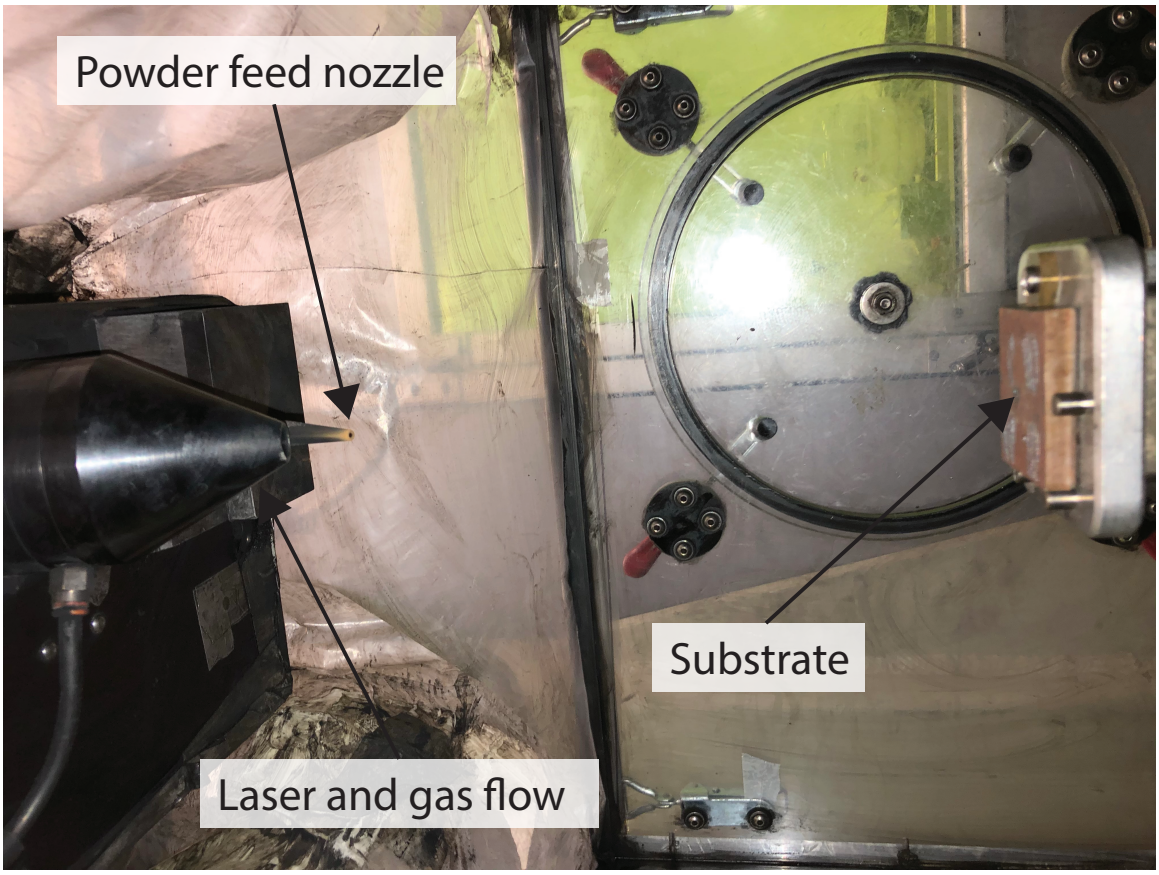

Figure 3.2: The printer head and chamber for the DED system used in this experiment.

Table 3.3: Gas-atomized 4140 steel powder composition

Powder Analysis (Weight %)			
Element	**Minimum**	**Actual**	**Maximum**
Cr	0.80	1.02	1.10
Mn	0.75	0.85	1.00
C	0.38	0.39	0.43
Si	0.15	0.31	0.35
Mo	0.15	0.23	0.25
Fe	**Balance**		

ure 3.3. Due to the nature of gas atomized powders, the powder has high sphericity, uniform particle size which results in an extremely flowable powder which likely yield a consistent meltpool [1]. Furthermore, the wrought 4140 steel sample used in this study is prepared from a cold drawn 4140 steel bar stock which was softened to a pearlitic structure prior to cold drawing [284].

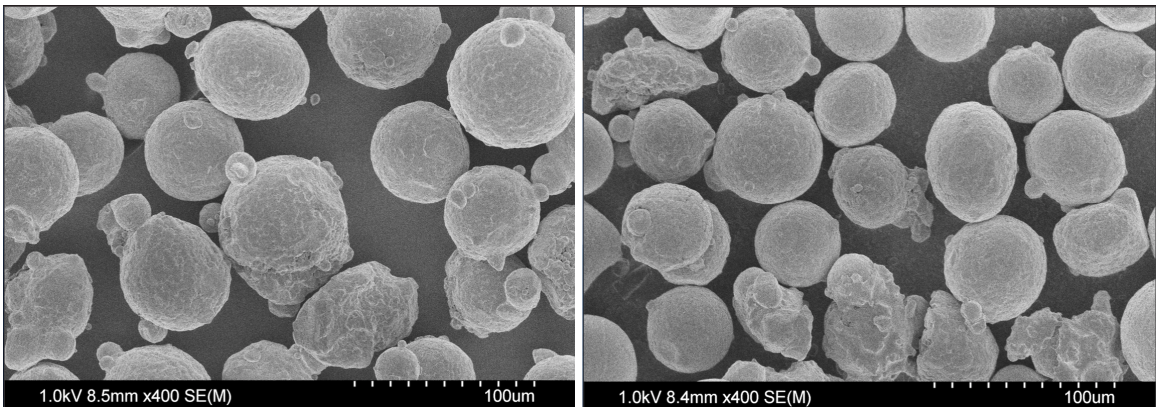

Figure 3.3: As-recieved gas atomized 4140 powder (left) and recycled powder sieved and reused after 25 cycles (right).

3.3.3 TEM Specimen Preparation

Due to the high magnetic flux density steel contains, the resolution on the TEM is severely reduced when using a larger specimen. Thus, the sample is required to be attached to a copper grid using a focused ion beam (FIB). Samples analyzed with the TEM were prepared using a FIB with a Ga source emitter. A standard procedure was conducted for specimen preparation in that 4 cuts are made to create a specimen which is approximately 20 µm x 5 µm. There is a small bridge between the bulk material and the specimen so it can be welded to a probe for a lift out. Figure 3.4 illustrates the 4 cuts made to cut the specimen to size. The stage is then tilted 60 degrees where the the beam cuts underneath the specimen to create a thin piece which can be further refined once removed from the bulk material. The stage in then returned to its original position where the probe is positioned to the right of the specimen and welded with the metallic gas. Once secured to the probe, the bridge can then be cut and the specimen lifted out.

The copper grid is then be inserted into the chamber where the probe with the specimen attached can be brought close to one of the prongs for attachment. Similar to the probe welding, the sample is welded on to the copper grid and then the probe is cut of the specimen. The specimen is then thinned in several increments creating a staircase so there is a small piece near the end with that is approximately 100 nm in thickness. This is then put into the ion miller for 5-10 minutes at a 10 degree milling angle to clean up the specimen and provide the final thinning for

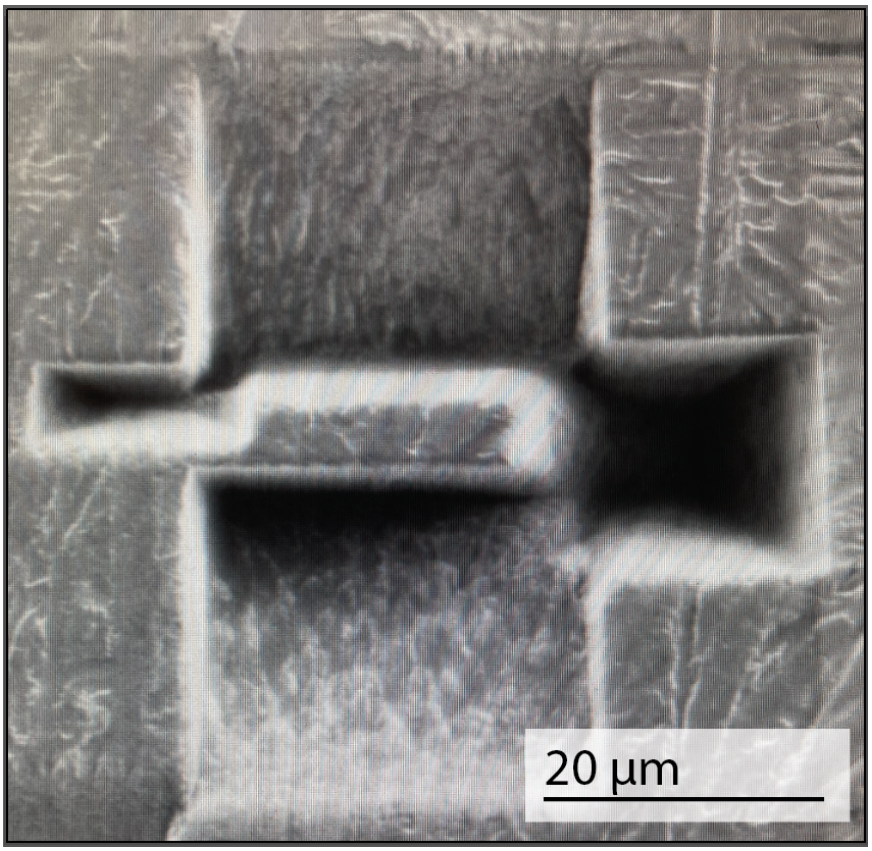

Figure 3.4: Initial cuts on fib for tem specimen

imaging.

3.4 Material Characterization

3.4.1 Microstructure and macroscopic defects

Samples from the most recent build session at the top of the 4140 DED build were taken for metallurgical analysis. Two separate samples were cut so the viewing plane parallel and perpendicular to the building direction could be examined. Furthermore, the wrought 4140 steel sample was cut at two viewing planes parallel and orthogonal to the rolling direction. The specimens were then mounted in conductive bakelite, ground and polished using a Struers Tegramin-20 autopolisher using a conventional series of SiC foils and diamond suspensions. They were then etched with sodium

metabisulphite diluted to 10% and examined under an optical microscope until an adequate distinction of phases could be observed.

Figure 3.5 shows several optical micrographs on the plane parallel to the build direction so the variance between the top and bottom layers can be observed. In figure 3.5 a, it can be observed that some large pores are present near the top few layers. This is due to the lack of fusion between adjacent layers and not enough energy density in this particular location. Throughout the build, there are several melt pool boundaries with a higher concentration of ferrite and a more refined grain structure as shown in figure 3.5 b. The contrast in these phases can be seen in figure 3.5 c which outlines the melt pool boundaries from each laser pass. Figure 3.5 d shows a closer look at the mid section of the specimen. It is not clear from the optical micrographs what the microstructural constituents are so further investigation is required.

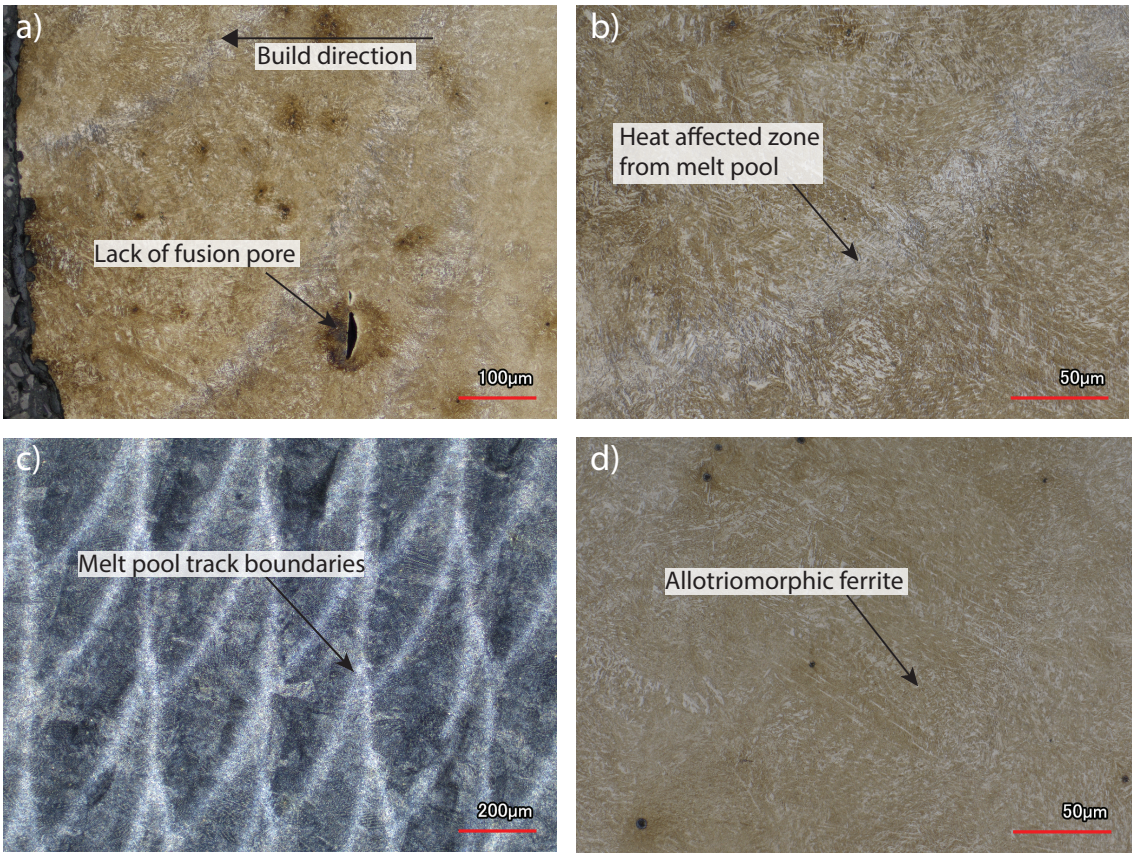

Figure 3.5: Optical micrographs of DED processed 4140 steel along the plane parallel to building direction showing a) top layer defects b) top layer microstructure c) weld track lines and d) mid section microstructure

These phases were examined closer using the SEM. Figure 3.6 a and b are Representative of the upper most layers, figure 3.6 c and d show the middle section while e and f are the bottom most layers. The evidence of extremely fast cooling is apparent in the top layers as long, sharp martensite laths within a bainite matrix are observed. Martensite is present along the entirety of the sample analyzed, however the level of tempering increases further down the specimen. Long martensite laths with rounded edges and a low aspect ratio are observed in the middle section in figure 3.6 c and d while smaller tempered martensite nodules broken down from previously longer laths are evident at the bottom within a bainitic matrix in figure 3.6 e and f.

Parallel to the building direction, figure 3.7 illustrates the microstructure at the top surface of the build. Similar to figure 3.5, distinct meltpool boundaries can be observed in figure 3.7 c. At the viewing plane in figure 3.7 b, allotriomorphic ferrite along prior austenite grain boundaries can be distinguished which is similar to the micrographs of the 4140-like 42CrMo4 steel presented in Chapter 3. Furthermore, the pores observed in figure 3.7 d are small and more spherical than the lack of fusion pores in figure 3.5, indicating gas entrapment or unmelted powder particles.

Similarly, SEM images were taken along the x-y view in figure 3.8 along the plane parallel to the building direction. Fine bainite with martensite is evident throughout the entirety of the top layer. The martensite looks similar to that of the bottom layer in the x-z view plane which indicates the preferred orientation for the martensite laths along the build direction. Furthermore, along the weld boundaries, a finer grain structure can be observed.

The micrographs taken from the wrought 4140 sample are quite different than the DED-processed one in figure 3.5 and 3.7. Small, uniform, equiaxed grains are present along the plane perpendicular to the rolling direction in 3.9 a. However, along the plane parallel to the rolling direction, elongated deformed grains in the same orientation as the rolling direction can be observed in 3.9 c. Looking closely at 3.9 b and d, small dark nodules can be observed inside the grains. These dark grains seem to be located along the grain boundaries and were etched much quicker than the bulk material. Further investigation would be required but it is likely that these are carbides which have been relocated to the grain boundaries after cold drawing.

Lastly, SEM imaging of the wrought 4140 steel is presented in figure 3.10.

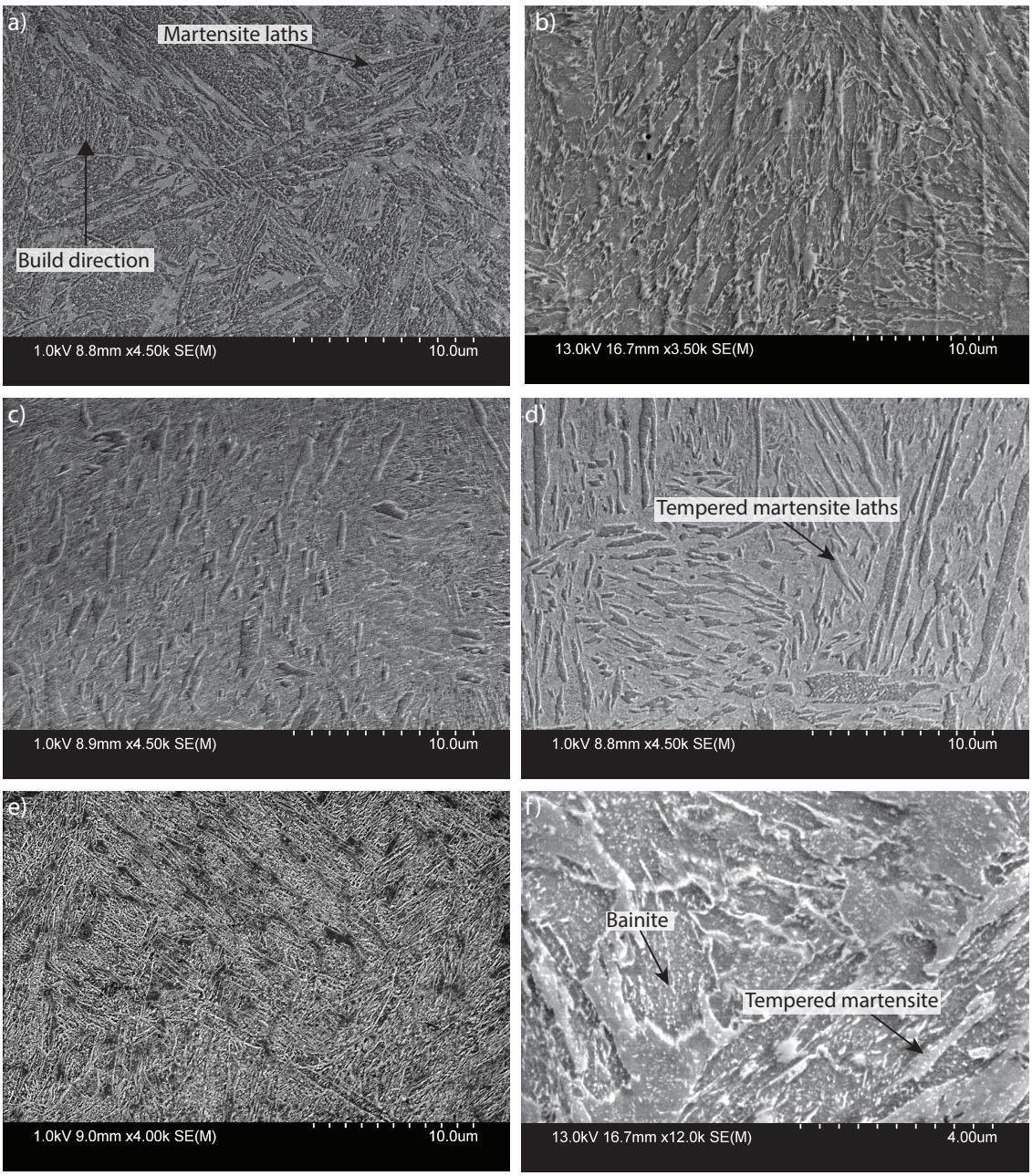

Figure 3.6: SEM images of DED processed 4140 steel along the plane parallel to build direction showing large martensite lath and bainite in the top section in a) and b), tempered martensite in the middle section in c) and d), and smaller rounded tempered martensite within a bainitic matrix on the bottom in e) and f).

At this scale, the microstructure is identical parallel and perpendicular to the rolling direction. A grain size between 10 and 30 um is observed with a high aspect ratio.

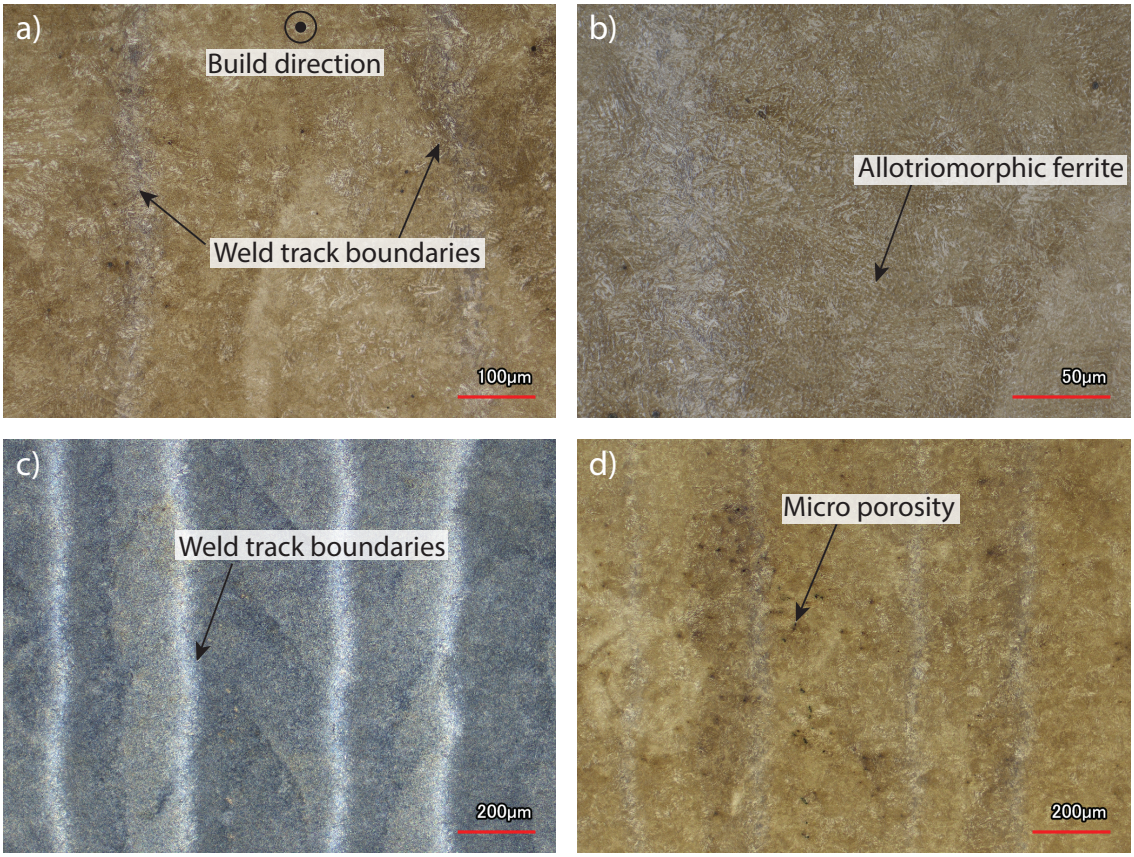

Figure 3.7: Optical micrographs of DED processed 4140 steel along the plane orthogonal to building direction showing a) microstructure at 20x mag b) microstructure at 50x mag c) weld track lines and d) microporosity

The pearlite lamellar structure is shown closer in figure 3.10 b. As noted before, the wrought steel used in this study is softened to a pearlitic structure prior to cold drawing. Other wrought samples used in different studies report a martensitic structure and was likely processed in a different way or a heat treatment cycle was imposed.

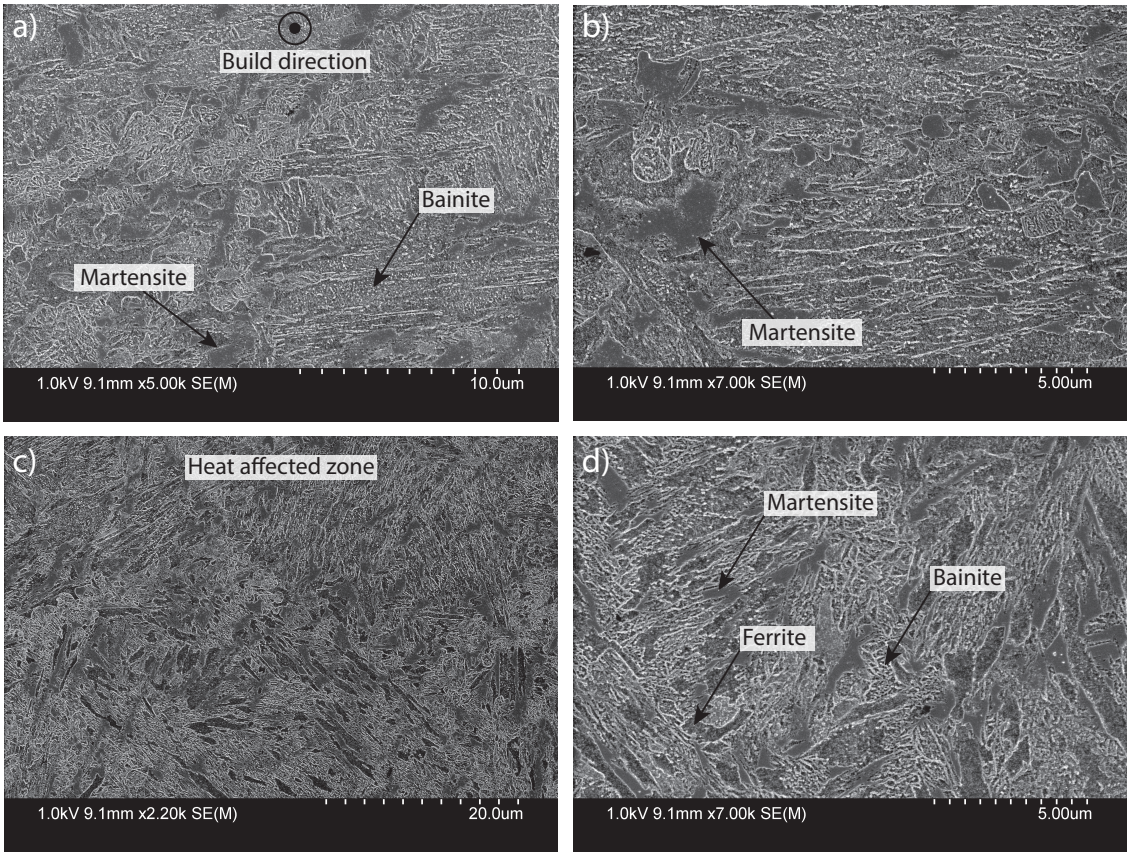

Figure 3.8: SEM images of DED processed 4140 steel along the plane orthogonal to the building direction showing tempered martensite lath within bainite matrix in the bulk of the material in a) and b), and finer microstructure along the weld lines in c) and d).

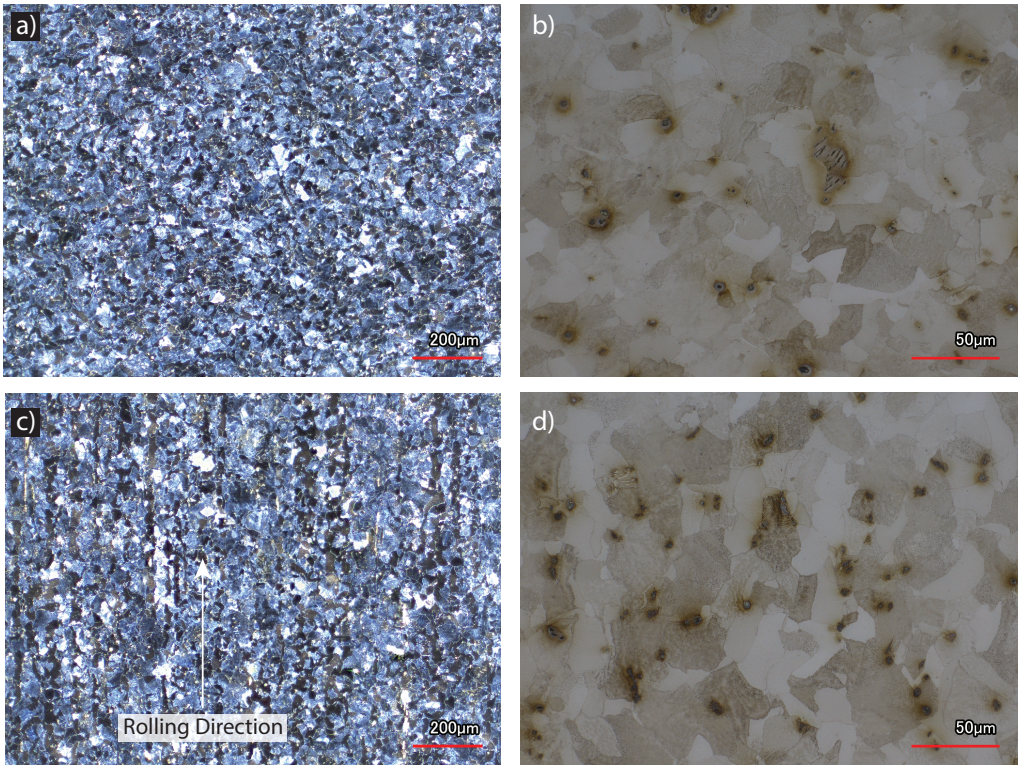

Figure 3.9: Optical micrographs of wrought 4140 steel a) equiaxed grains at 10x mag parallel to rolling direction b) microstructure at 50x mag parallel to rolling direction c) equiaxed and elongated grains at 10x mag orthogonal to rolling direction and d) microstructure at 50x mag orthogonal to rolling direction

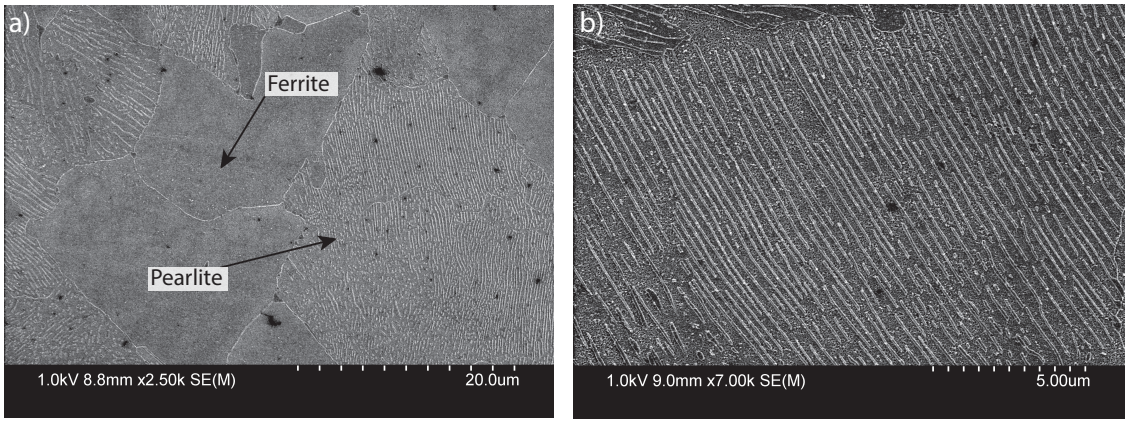

Figure 3.10: SEM images of wrought 4140 steel at a) 2200x magnification and b) 7000x magnification

3.4.2 TEM imaging

Prior to imaging, the specimen and holder were cleaned in a zone cleaner for 30 minutes and then inserted into the microscope. Imaging was conducted with a Hitachi scanning transmission holography electron microscope (STHEM) at 200kV. A number of diffraction and lattice images were taken to characterize some the defects and material characteristics revealed by the microscope. The diffraction image in TEM characterization reveals important information about the crystalline material such as the specific zone axis. The zone axis is a lattice row which is parallel to the normal vector along the intersection of 2 or more families of lattice planes as illustrated in figure 3.11.

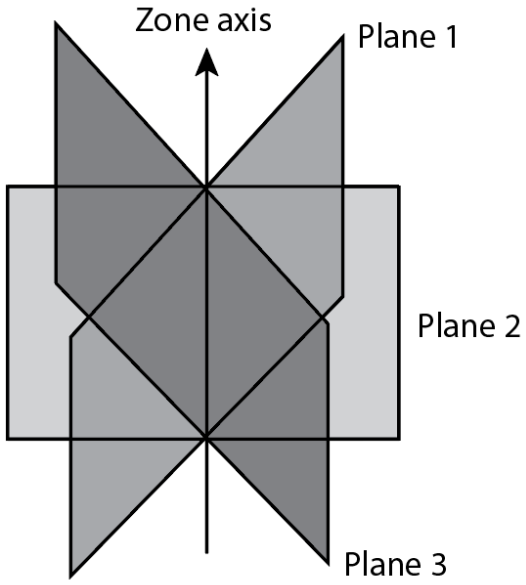

Figure 3.11: Schematic of the zone axis direction in relation to atomic planes

Figure 3.12 illustrates a lattice image taken at 540k magnification. Sections of this image were extracted and transformed using the fast fourier transformation (FFT) method in the Gatan image processing software. The distance between each mirrored fringe and angle between adjacent fringes can be measured and compared to a library of patterns to determine this zone axis direction. The angle was determined to be 59.5° using the cosine law. Due to a number of factors such as the manual measurements, poor resolution diffraction image, and lattice strain, it can be assumed to be 60°. According to ref. [285], the same diffraction pattern with an angle of 60

degrees between each diffracted beam represents a $[\bar{1}11]$ zone axis. This zone axis was found to be common across various images analyzed and between different specimens from the same printed block.

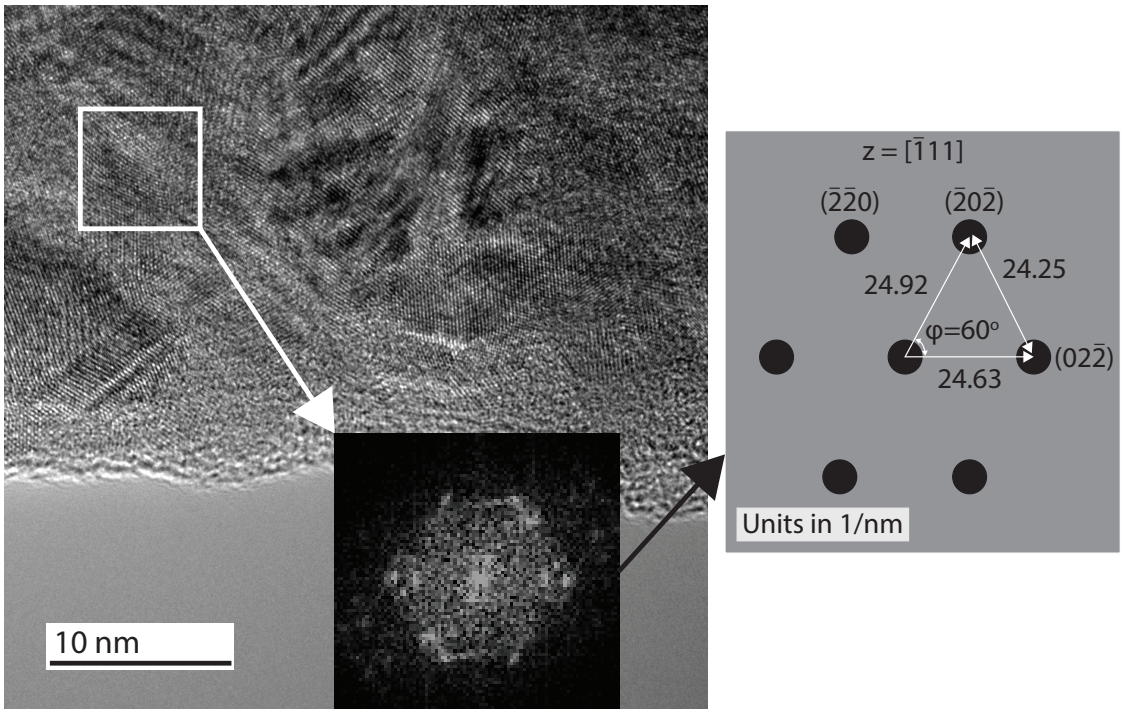

Figure 3.12: First lattice image with corresponding diffraction pattern obtained through a fast Fourier transformation. Diffraction pattern indexed according to ref. [285] and the associated zone axis direction was determined to be along the $[\bar{1}11]$ direction.

Although the $[\bar{1}11]$ zone axis was observed the most, another diffraction pattern was also found and is shown in figure 3.13. The same analysis procedure was conducted as the previous pattern and compared with the diffraction pattern library determined by Edington [285]. The angle determined between the vertical fringe at 90° from the main beam and the adjacent fringe to the right is approximately 57°. The angle between this fringe and the next fringe farthest to the right yielded an angle of 33°. According to the indexed diffraction patterns in ref. [285], angles of 54.74° and 35.26° for the same fringes represent a [011] zone axis. Considering again, the error in the manual measurements, the poor resolution for the FFT diffraction pattern, and lattice strain, it can be assumed that this pattern represents the same [011] zone axis. It can also be noted that the distance in reciprocal space between fringes is much

smaller in figure 3.13 than figure 3.12. This means that the interplanar spacing is larger for the second diffraction pattern than it is for the first in figure 3.12.

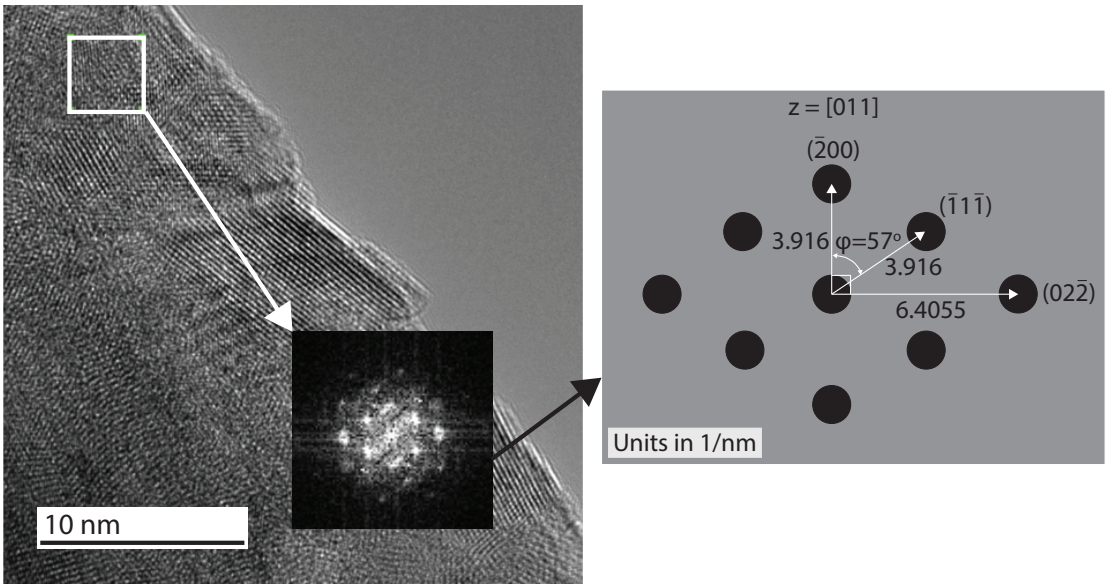

Figure 3.13: Second lattice image with corresponding diffraction pattern obtained through a fast Fourier transformation. Diffraction pattern indexed according to ref. [285] and the associated zone axis direction was determined to be along the [011] direction.

Two different systematic rows were observed in reciprocal space as shown in figure 3.14. Systematic rows are a series of reflections which are spaced periodically along a specific path due to Bragg reflection [286]. The different angles of diffracted rows between figure 3.14 a and b is likely due to the rotation of the crystal lattice when traversing across the specimen during imaging. Furthermore, the diffused scattering around each diffracted beam in figure 3.14 b is due to contamination on the top and bottom of the specimen. After several hours of imaging, the amorphous contamination layer tends to migrate toward the beam, which causes the electron beam to diffract and creates a diffused intensity around the main fringes.

The interplanar spacing can be measured as the distance between spots along the same line and comparing this value with calculated ones corresponding to a specific set of miller indices. The formula for the interplanar spacing and the associated lattice parameters for body centered cubic (BCC) ferrite and body centered

tetragonal (BCT) martensite systems are shown in table 3.4. In this table, d_{hlk} is the interplanar spacing between atomic planes, hkl are the miller indices of the atomic plane along the diffracted beam, and a and c are the lattice parameters.

Table 3.4: Lattice parameters and interplanar spacing for cubic systems

Cubic System	Lattice Parameter	Interplanar spacing d_{hlk}
BCC	a = 2.866 [279]	$d_{hlk} = \frac{a}{\sqrt{h^2+k^2+l^2}}$ [285]
BCT	a = 2.855 c=2.9 [287]	$\frac{1}{d_{hlk}^2} = \frac{h^2+k^2}{a^2} + \frac{l^2}{c^2}$ [285]

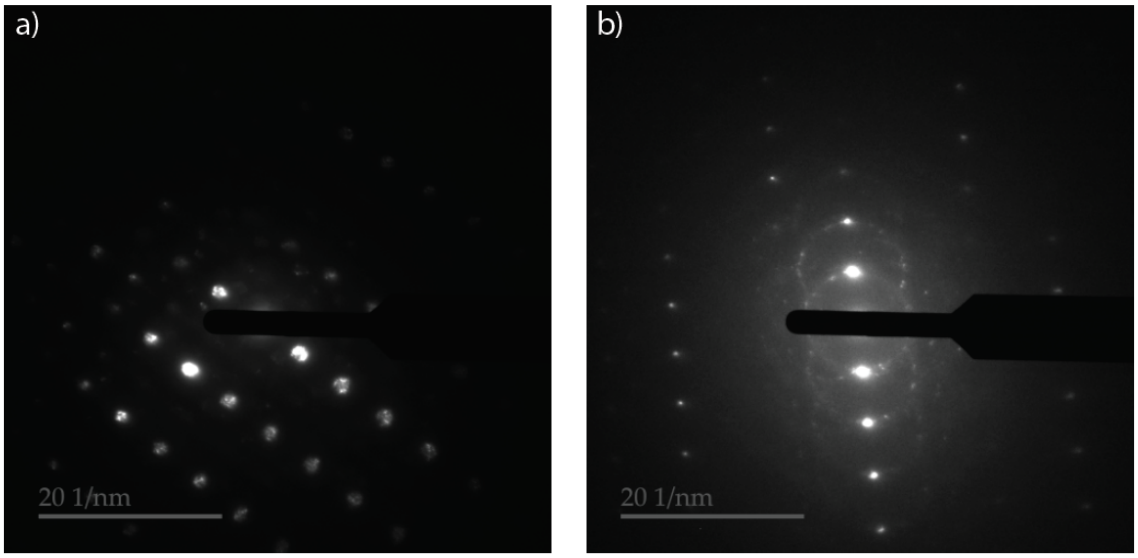

Figure 3.14: Systematic rows captured in reciprocal space in the TEM with a beam blocker blocking the intensity of the main beam.

A number of measurements were made on each figure 3.14 a and figure 3.14 b to compare with the calculated values. The lattice parameters for ferrite and martensite were used with a varying set of miller indices to find the closest set of values that matched the experimental measurements. For BCC and BCT systems, the sum of h,k and l is required to be an even number [285]. A number of calculations were made with different miller indices under these conditions and the measured and calculated values are shown in table 3.5. The results matched the theoretical values best for the BCT system which aligns well with the mostly martensitic structure observed through SEM imaging.

Although the experimental values don't fall within the theoretical data for their respective standard deviations, it can be noted that there are several factors

Table 3.5: Interplanar spacing values

Systematic Row	Measured d_{hlk}	(h,l,k)	Calculated d_{hlk}
Fig 3.14 a	1.85 +/- 0.012 Å	(1,1,0)	2.019 Å
Fig 3.14 b	1.84 +/- 0.07 Å	(1,1,0)	2.019 Å

which can further skew the experimental lattice spacing. One large reason for the difference in interplanar spacing is caused by strain. As discussed in chapter 3, residual stress is a common defect present in metal AM and causes the atomic planes to expand or contract. This shift is what was measured during the XRD measurements and related to the amount of tensile or compressive residual stress. Thus, considering the processing conditions for this experiment produced a primarily martensitic structure, the volume change due to this phase change will cause significant strain within the material. Since the measured strain is less than the theoretical value, it is likely that the imaged area is subject to a compressive strain. Further lattice imaging revealed grain boundaries and is shown in figure 3.15 which shows a distinct grain boundary between two adjacent grains. In figure 3.15 b, lines were added to highlight the grain boundaries and lattice orientation in each grain. Three separate grains were revealed, each with a different lattice orientation.

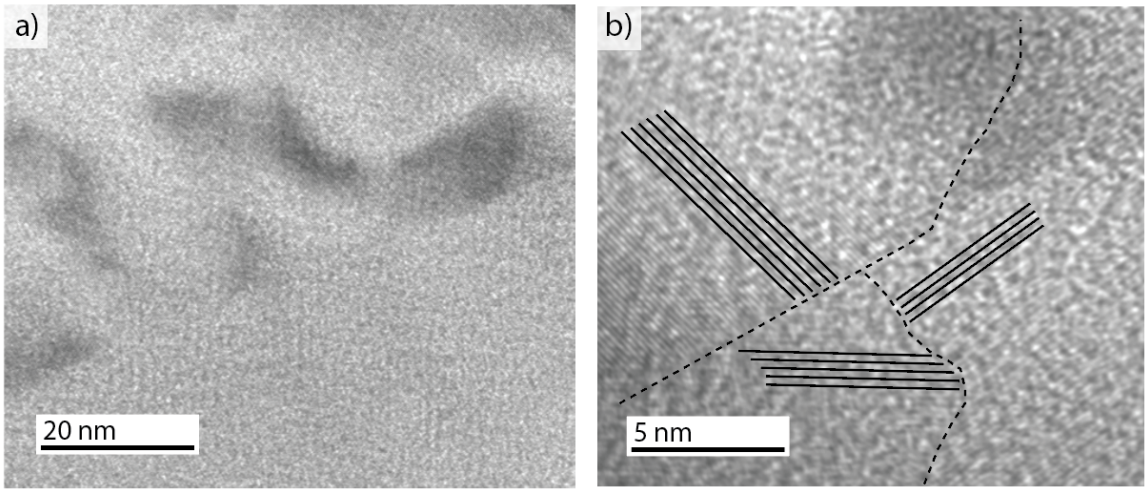

Figure 3.15: Lattice images showing grain boundaries with a) the distinction in contrast between the top half and the bottom half and b) three separate grains with lines added highlighting the different atomic plane orientation.

Lastly, figure 3.16 a shows diffraction contrast at a low magnification while Figure 3.16 b illustrates a twinning boundary within the lattice image. The diffrac-

tion contrast along the specimen is evident in the bright field image which could be attributed to several defects such as dislocation networks, alloy segregation or other phenomena. Further research would need to be conducted to identify the exact cause of this contrast. For figure 3.16 b, lines were added to the twin to highlight the change in lattice direction at each twin boundary. Nano-twins are likely to have a large effect on dislocation motion to stabilize strain hardening as described by the Hall-Petch relationship [280] which relates a materials strength as a function of grain size [288]. Liu et al [280] found that the nano-twins in AM processed 316L stainless steel were promoted by the dislocation network and thus provided stress relief to delay the necking point of the alloy.

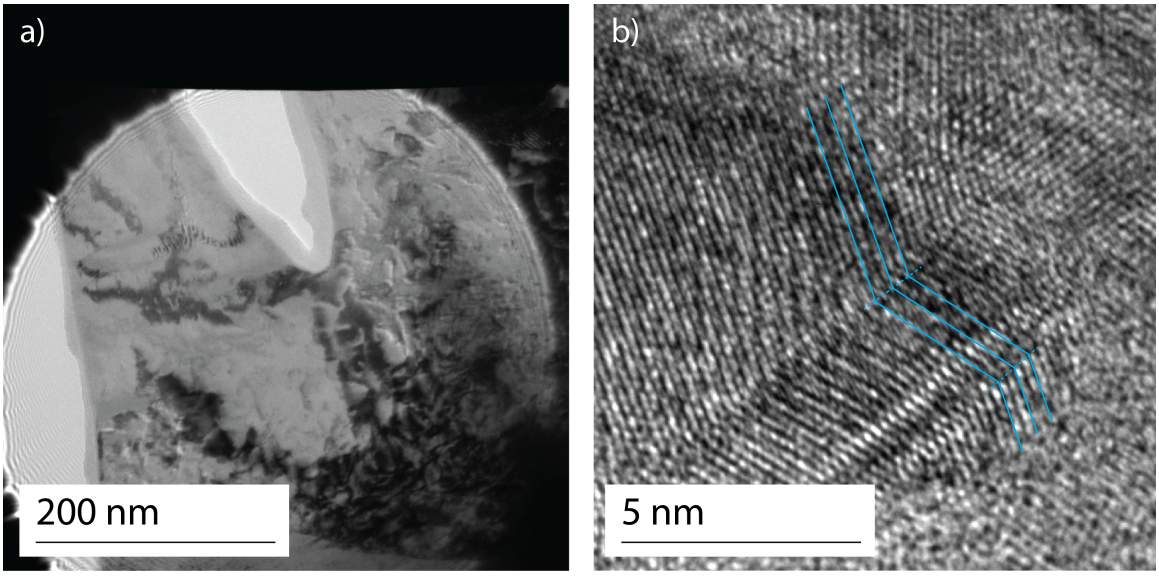

Figure 3.16: Different images taken on the TEM showing a) bright field image showing the contrast variation within the sample and b) a mechanical twin with the atomic plane orientations and twin boundaries highlighted.

3.5 Conclusion

In this chapter, 4140 steel processed by directed energy deposition by the Royal Canadian Navy was examined using various microscopy methods. First, optical and SEM imaging was conducted on both the printed steel and its wrought counterpart to observe the differences in microstructural constituents. A mainly martensitic and bainitic structure was observed for the printed part with high degrees of tem-

pered martensite laths further down the build. The wrought microstructure was comprised of small equiaxed ferritic and pearlitic grains which were elongated along the rolling/drawing direction.

Furthermore, TEM imaging was conducted on the printed steel. A focused ion beam was used to prepare and weld the specimen onto a copper grid for imaging. Various lattice images were obtained and their diffraction patterns characterized. It was determined that the [111] and [011] zone axes were most common based on the specific angles and distance between the diffraction spots. The interplanar spacing was also determined from the systematic rows and compared with the theoretical values. A spacing of 1.85 +/- 0.012 Å and 1.84 +/- 0.07 Å was measured which was close to the theoretical value of 2.019 Å for the body centered tetragonal system of martensite. Due to residual stress and other defects causing lattice strain, the measured value will slightly differ from the theoretical values. Since a mainly martensitic microstructure was observed, a larger degree of lattice strain is to be expected. Lastly, images of grain boundaries and twinning within the material were also captured and presented.

3.6 Future Work

Further investigation on this material could involve a more detailed investigation on dislocation imaging and characterization. Since dislocations play a significant role on the material properties, identifying the unique dislocation mechanics compared to its wrought counterparts would be extremely valuable. Moreover, electron energy loss spectroscopy (EELS) could be conducted in the TEM to identify alloy segregation and compositional gradients.

Chapter 4

Thermo-mechanical-metallurgical modelling, validation and characterization of 42CrMo4 steel processed by directed energy deposition

Manuscript submitted to the Journal of Manufacturing Processes published by Elsevier.

4.1 Introduction

DED processing of chrome-molybdenum steel alloys is being adopted in a wide range of applications in aerospace, automotive, and marine industries. Despite the clear advantages of DED over conventional manufacturing processes, defects not typically found in conventional methods such as high residual stresses, porosity, keyhole formation and lack of fusion can contribute to the inferior properties that metal additively manufactured components exhibit under unoptimized conditions [1, 289–292]. Additionally, the microstructure of printed metallic parts and consequently their mechanical properties vary significantly by DED process parameters such as heat source intensity, scanning speed, and dwell time in between layers [1,293]. It is therefore critical to characterize the correlation between processing parameters and the resulting microstructure and defects. As an alternative to enervating trial and error experiments, which are often expensive and time consuming, numerical modelling of the metal additive manufacturing (AM) process is used to study the underlying physics of the process and ultimately optimizing the process parameters. However, accurately

simulating the process physics requires simultaneously modeling the complex thermal, mechanical, and metallurgical evolution of the material as it undergoes a cyclic high-gradient thermal evolution.

Finite element (FE) modelling is a common numerical method to simulate the DED process and predict the temperature evolution and residual stresses for various printing parameters. Heigel et al. [294] and Denlinger et al. [293] present excellent results for their thermo-mechanical model of Ti-6Al-4V (Ti64) and Inconel®625 validated through in-situ thermocouples, displacement sensors and post-build residual stress measurements. However, due to the limited knowledge on solid-state transformation strains for Ti64, their model was limited by the absence of a metallurgical framework to compute these strains. Instead, they implemented a modified term to the strain tensor which accounted for the stress relaxation from phase transformations. Baykasoglu et al. [295] developed an FE model to predict the evolving microstructure of Ti64 during the DED process but did not conduct a mechanical analysis to compute the residual stresses associated with these transformations. Moreover, Zhang et al. [198] applied their Ti64 metallurgical framework to 5140 steel for a number of constant cooling rates. Although their model was validated for Ti64, they did validate the computed 5140 steel phase fractions or test this model against the complex cyclic heating and cooling nature of the AM process.

The focus for FE models of the DED process have generally been centered around titanium and Inconel® alloys [198,240,293–301]. There are FE models of 4140 steel developed for heat treatment (heating, quenching and tempering) [302,303], laser hardening [304–307] and welding [308], which exhibit many of the same characteristics as the DED process. Nonetheless, there is a gap in the literature on the modelling and characterization of 42CrMo4 or AISI 4140 steel for the DED process. Similar studies by Bailey et al [304] and Yaakoubi et al [305] developed a thermo-mechanical model of the laser hardening process for 4140 steel. They accurately predicted both the hardness of the heat affected zones and the residual stresses induced through both thermal strain and phase transformations using ABAQUS/CAE. Most recently, Chen et al. [309] developed a thermo-mechanical-metallurgical (TMM) model for a low temperature transformation (LLT) clad layer of EH40 steel weldment processed by laser DED. Their model predicted the temperature history, microstructural evolution and residual stresses induced by the clad of the LLT alloy. They conclude that

the interlayer idle time (dwell time) is fundamental in determining the martensitic transformation and consequently, the generation of tensile stresses. However, their study is validated with small laser clads and not larger components which would be necessary in order for a more practical prediction of the DED process.

This chapter presents the methodology, results and experimental validation for a unified TMM FE model of DED processed 42CrMo4 steel. First, a pre-processing framework is implemented to provide the possibility to model complex geometries and laser trajectories based on the specified G-code. Additionally, a metallurgical framework was developed to model the microstructural evolution during deposition and capture the contributions to residual stress and latent heat. Three separate thinwall cases with varying dwell times were conducted to verify the fidelity of the model while a 10mm cube with a more complex laser trajectory was printed to test the limits of the thermal and metallurgical analysis. In addition to conducting experiments to validate the temperature history, distortion and residual stresses, the microstructure of the as-built components are characterized and compared to the simulated phase fractions.

4.2 Numerical model

A sequentially coupled TMM model was developed using
ABAQUS/CAE 2019. The nodal temperature histories from the thermal analysis is used as an input for a thermal load in the mechanical analysis to model the residual stresses. Additionally, the solid-state phase transformations due to heating and cooling cycles were calculated within the thermal analysis and their respective latent heat generations were added to the energy balance. The same framework was also included in the mechanical analysis to update the strain tensor with the dilational components from the phase transformations. The modelling sequence employed is illustrated in Figure 4.1 outlining the various subroutines used and their respective purpose.

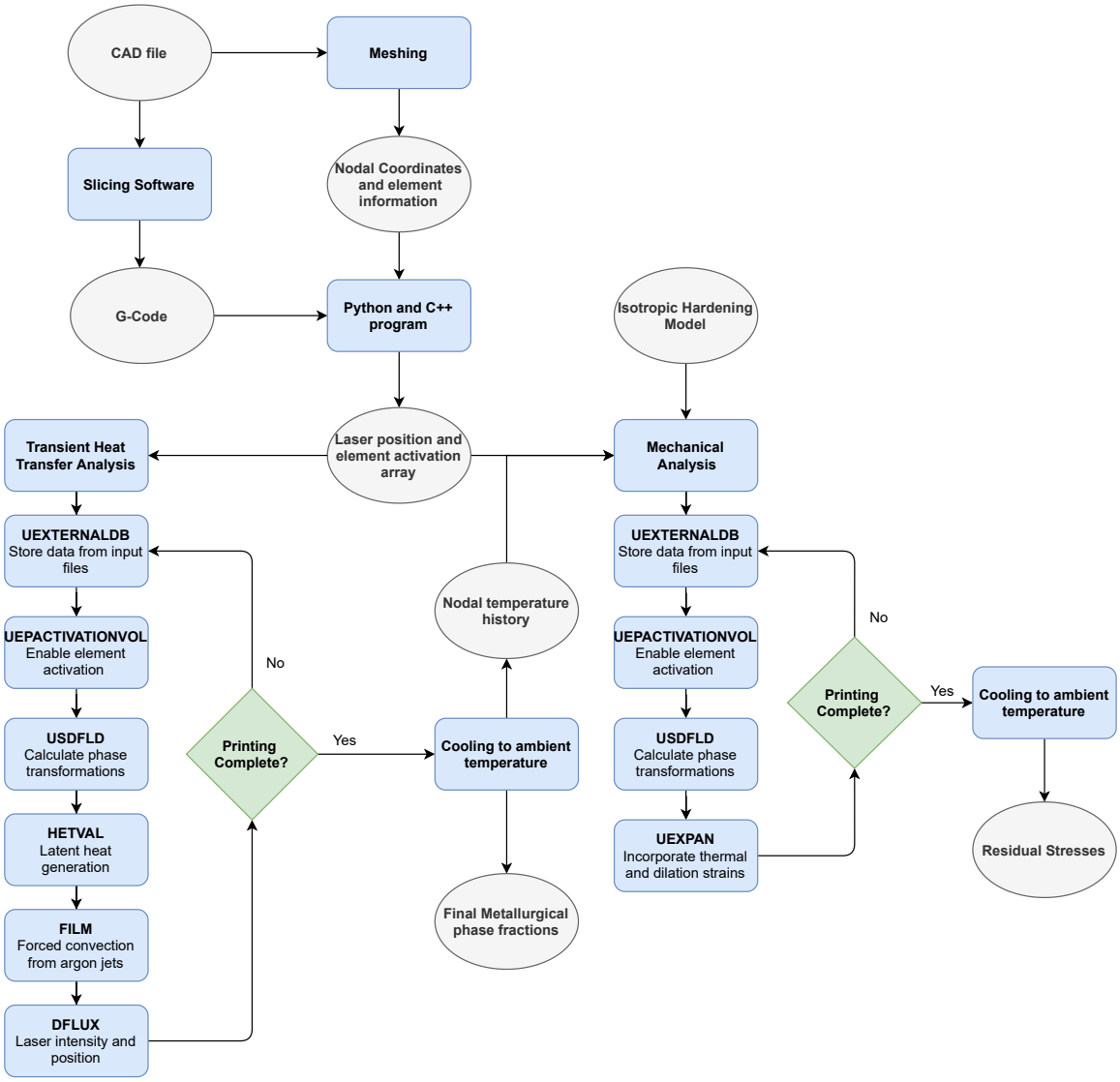

Figure 4.1: Flow chart for the thermo-mechanical-metallurgical model illustrating the subroutines and material models used. The finite element model was developed in ABAQUS 2020 and the subroutines were written in FORTRAN.

4.2.1 Pre-processing

In order to model the laser trajectory during a build, pre-processing is required so that ABAQUS can generate the same laser path that is being printed. The general pre-processing methodology from Dantin et al [310] was used and is illustrated in Figure 4.2. The programs were written in Python and C++ to yield the resulting arrays for ABAQUS:

1. The x-y-z coordinates of the laser at each user defined time step and laser power for the moving heat source from the G-code file

2. The element number and activation time to simulate the material deposition based on the bead width and height

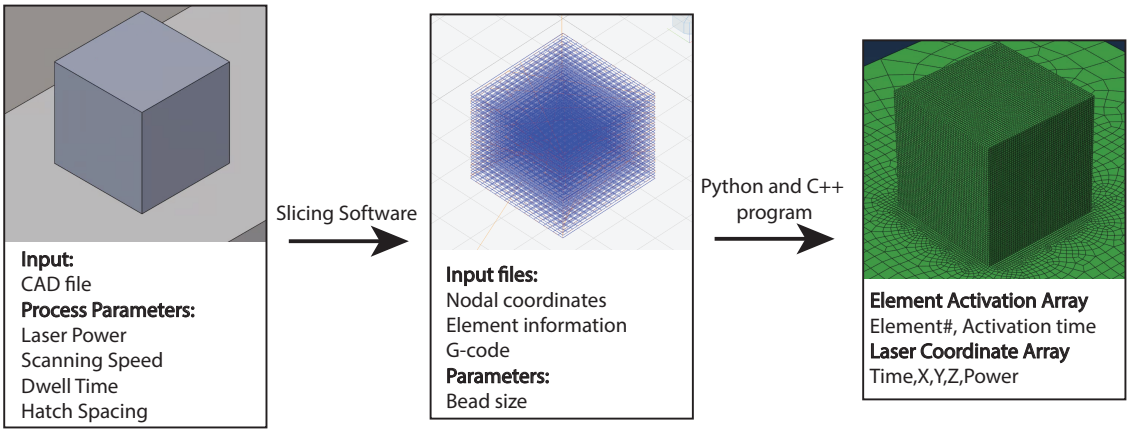

Figure 4.2: Input files and the relevant softwares used to produce the element activation array and laser coordinate array for the FEM software modified from [310]

The desired CAD file is sliced by the printing software to create the corresponding G-code which contains information about the laser path, scanning speed, laser power, dwell times and deposition rate. A program developed in Python reads and discretizes each G-code command to output the temporal and spatial position of the laser at every time step. The laser coordinates are then used as an input into the element activation program which checks a series of conditions as the laser moves throughout the build. The element centroids of the part being fabricated is repeatedly checked with the radial distance from the laser center and the corresponding z-height. The activation radius is set to the machine deposited bead width and elements are activated once these conditions are met. Once an element is activated, it cannot be removed or reactivated. This schematic for element activation is illustrated in Figure 4.3. The symbols R_{active} is the radial distance between the laser center and element centroid which is set to 0.6 mm to model a 1.2mm bead size and dR is the incremental distance as the laser travels.

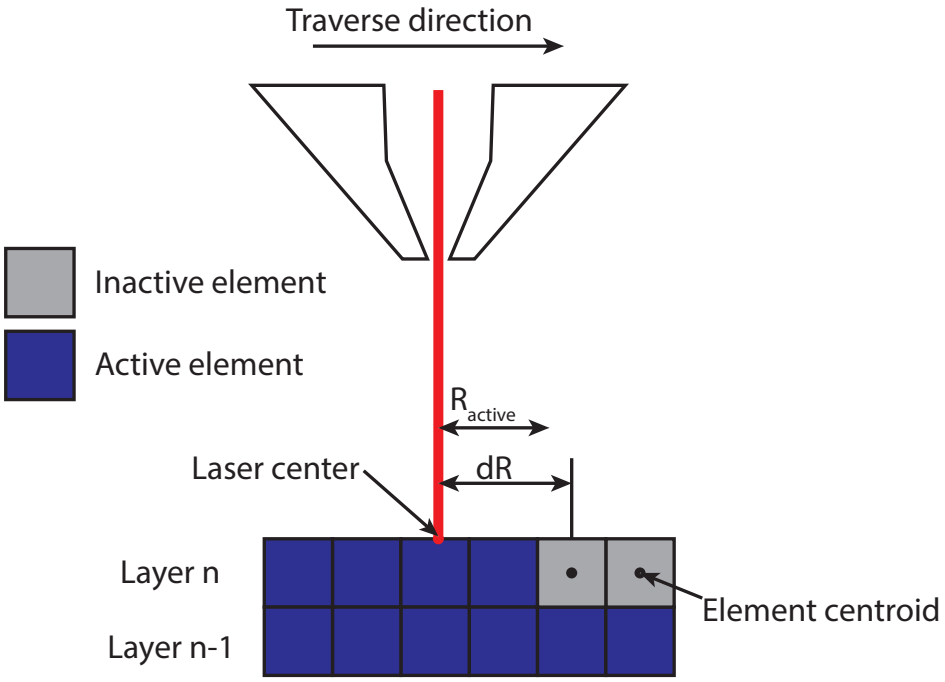

Figure 4.3: Schematic of element activation with respect to laser position and element centroid modified from [310]

4.2.2 Thermal analysis

A transient heat transfer analysis is first developed to model the non-homogeneous rapid heating and cooling that occurs during laser melting [225]. The accuracy of the thermal analysis is the most important component for the simulation since it mainly determines the corresponding microstructure, mechanical properties and dimensional accuracy [225]. A number of user subroutines were used in order to accurately encompass the conditions of the printer. UEXTERNALDB, which is called once at the start of every increment was used to read and store the laser coordinate and element activation arrays to be used in subsequent subroutines. UEPActivationVol is used to activate elements and simulate the deposition process based on the element activation times determined during pre-processing. The ABAQUS tool-path intersection module is invoked through the use of this subroutine and is used to apply convection and radiation to evolving free surfaces. Furthermore, heat transfer through mass transport is accounted for with temperature and phase dependent thermal conductivity. The energy balance in a Lagrangian reference frame used in the analysis is shown in

Equation 4.1:

$$Q(\mathbf{x},t) - \frac{dH}{dt}(\mathbf{x},t) - \nabla \cdot \mathbf{q}(\mathbf{x},t) = 0 \tag{4.1}$$

where Q is the volumetric heat source, H is the enthalpy which is a function of the density and specific heat, $\mathbf{x}$ is the reference spatial coordinate, ∇ is the vector differential operator, t is the temporal coordinate and $\mathbf{q}$ is the heat flux vector defined in Equation 4.2:

$$\mathbf{q} = -k(T)\nabla T \tag{4.2}$$

where T is the temperature at the integration point and $k(T)$ is the temperature dependent thermal conductivity. The heat loss through the surface due to convection and radiation is applied through boundary conditions and are represented in Equation 4.3 and 4.4, respectively.

$$\mathbf{q}_{conv} = h\,(T - T_\infty) \tag{4.3}$$

$$\mathbf{q}_{rad} = \epsilon\sigma_b\,(T^4 - T_\infty^4) \tag{4.4}$$

where h is the heat transfer coefficient, ε is the surface emissivity of the material, σ_b is the Stefan–Boltzman constant and T_∞ is the ambient temperature. The heat release due to phase transformations was considered as an internal heat source in the material using user subroutine HETVAL and is shown in Equation 4.5.

$$\dot{q}_{phase} = \sum_{i=F,P,B,M} \Delta H_i(T)\frac{\Delta X_i}{\Delta t} \tag{4.5}$$

where ΔH_i is the amount of latent heat as a function of temperature, T while ΔX_i is the change in the ith phase fraction during time step Δt. The ith phase fraction subscript can be represented by F, P, B, or M for ferrite, pearlite, bainite

and martensite, respectively. The latent heat contributions for the transformations of ferrite, pearlite and bainite can be seen in Equations 4.6 and 4.7 defined by [311] and for martensite in Equation 4.8 defined by [312].

$$\Delta H_{\mathrm{F}}\left(\mathrm{Jcm}^{-3}\right) = 1769.0 - 5.725T + 0.0063T^2 - \left[2.303 \times 10^{-6}T^3\right] \tag{4.6}$$

$$\Delta H_{\mathrm{P}}\left(\mathrm{Jcm}^{-3}\right) = \Delta H_{\mathrm{B}} = 953.0 + 0.409T - 0.00012T^2 \tag{4.7}$$

$$\Delta H_{\mathrm{M}}\left(\mathrm{Jcm}^{-3}\right) = 640 \tag{4.8}$$

The volumetric heat source from the laser is modelled as a Goldak double ellipsoid [238, 239]. Subroutine DFLUX was used to model the heat source and its location throughout the build using the information from the laser coordinate array. There are several volumetric heat source models which can be used such as a Goldak double ellipsoid [238,239] or a Gaussian distribution [239]. In arc welding simulations, the Gaussian distribution model proved to show inaccuracies as it neglected the arc stiffness [239]. To account for this, a semi-ellipsoidal model was proposed which was then further refined to a double ellipsoid model by Goldak to address the need for the steeper temperature gradients seen experimentally compared to the Gaussian model [239]. The Goldak model is shown in Equation 4.9.

$$Q = \frac{6\sqrt{3}P\eta f}{\mathrm{abc}\pi\sqrt{\pi}} e^{-\left[\frac{3x^2}{a^2}+\frac{3y^2}{b^2}+\frac{3(z+v_w t)^2}{c^2}\right]} \tag{4.9}$$

where P is the nominal laser power and η is the laser melting efficiency. The nominal laser power is used although the actual laser power might slightly differ from the nominal value according to wrok conducted by Ref. [294]. The laser melting efficiency was determined to be 38% by adjusting η so that the predicted and measured peak temperatures were in good agreement. This value is within the range of measured values for a ground steel surface according to Refs. [313, 314] with a similar 1.06 µm Nd:YAG fiber optic laser system. Variables x, y, and z are the local Cartesian

coordinates while f is the weighting fraction and is assumed to be 1 such that the front and rear distributions of the heat source are equal. Coefficients a, b, and c are shape parameters of the volumetric heat source and v_w is the traverse speed as illustrated in Figure 4.4. This volume is defined with a circular radius equal to half the deposition track width of 0.6mm and applied to a depth of 0.9mm [294].

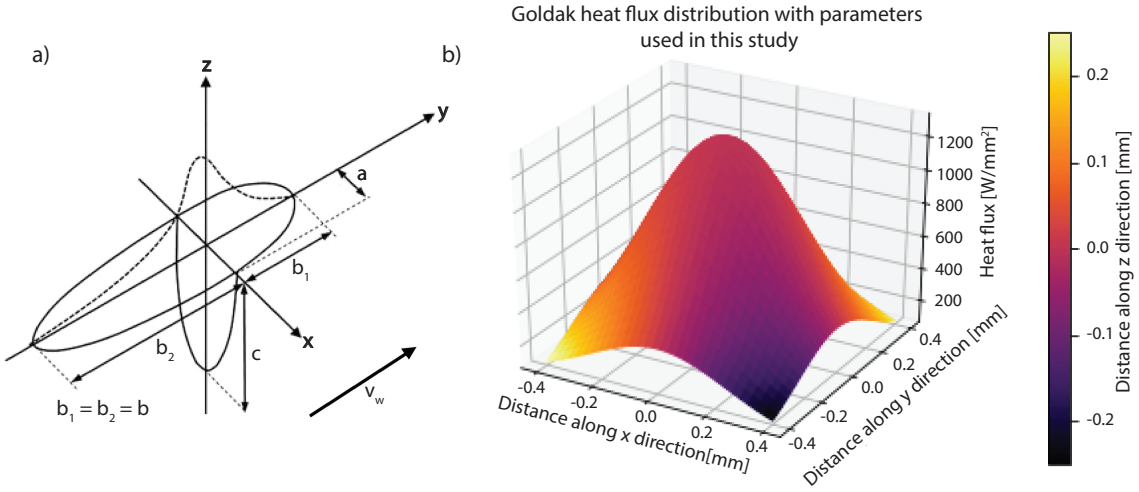

Figure 4.4: Goldak double ellipsoid volumetric heat source showing a) the schematic modified with permission from [299, 315] and b) the distribution with the parameters used in this study

Metallurgical framework

The metallurgical framework only considers thermal transformations and not stress-induced phase changes. The solid-state phase transformations were calculated based on a modified diffusional Johnson–Mehl–Avrami–Kolmogorov (JMAK) relationship in Equation 4.10 for pearlite, ferrite, bainite and austenite, while the displasive Koistinen-Marburger (KM) relationship in Equation 4.11 was used for martensite [302, 304, 316–318]. Although the transformation mechanism of bainite can be both displasive and diffusional, this model assumes that the nucleation of bainite is valid under the JMAK diffusional model [304]:

$$X_i = X_i^{\text{eq}} \left(1 - \exp\left(-k_i t^{n_i}\right)\right) \tag{4.10}$$

$$X_{\text{mart}} = X_{\text{ra}} \left(1 - \exp\left(-\alpha \left(M_S - T\right)\right)\right) \tag{4.11}$$

where, X_i^{eq} is the fraction of the ith phase at equilibrium from the Fe-C phase diagram, k_i and n_i are rate constants for the ith phase and t is the overall time since the transformation began. In Equation 4.11, X_{ra} is the amount of remaining austenite, M_s is the martensite start temperature and α is a constant, which for 4140 steel is 0.011 [302]. The rate constants k and n, were determined from the time temperature transformation (TTT) diagram illustrated in Appendix A in Figure A.2 at a number of temperatures for 4140 steel [319] by taking the double natural logarithm of the JMAK relationship. The resulting relationship is shown in Equation 4.12 and Equation 4.13.

$$n = \frac{\ln\left\{\frac{\ln(1-X_{\text{s}})}{\ln(1-X_{\text{f}})}\right\}}{\ln\left(\frac{t_{\text{s}}}{t_{\text{f}}}\right)} \tag{4.12}$$

$$k = -\frac{\ln\left(1 - X_{\text{s}}\right)}{t_{\text{s}}^n} \tag{4.13}$$

where, X_s is the fraction of phase transformed (usually 0.01) at the start time t_s and X_f is the final fraction of the phase (usually 0.99) at the end time t_f [302]. The additivity rule suggests that a transformation begins when the sum of time steps of the current transformation is greater than the incubation time of the phase at the current temperature. Further explanation of the additivity rule is provided in Appendix B. For simplicity, data from the continuous cooling transformation diagram for 4140 steel was used to constrain the transformation of phases [320]. The relative cooling rates for which each phase was present is used to limit or initiate the transformation. For example, according to experimental data in the continuous cooling transformation (CCT) for 4140 steel, which is illustrated in Appendix A in Figure A.3, bainite is not evident at cooling rates below 3.83 °/s and above 10.167 °/s. Therefore at lower cooling rates, only pearlite and ferrite are initiated while bainite is constrained to cooling rates lower than 10.167 °/s and higher than 3.833 °/s.

In addition to cooling rates, the start and finish temperatures of each phase were also specified according to the TTT diagram. This limits the nucleation of

martensite between M_S and M_F temperatures of 345°C and 115°C, respectively [321]. Similarly, bainite only forms below the B_S temperature of 545°C and above the M_S temperature. Furthermore, the nucleation of proeutectoid ferrite between the austenization temperature (A3) of 777°C and the eutectoid temperature (A1) of 727°C and at cooling rates lower than 6.67°/s is also represented. The A3 temperature was determined from the relationship defined by Hougardy et al. [322] based on the measured chemical composition of the 42CrMo4 powder. It is well known that proeutectoid ferrite nucleates along austenite grain boundaries for hypoeutectoid steels. To control the amount of ferrite and pearlite nucleation, the computed phase fractions based on the JMAK equations were scaled down by their maximum fraction formed at the current cooling rates specified by the CCT diagram. Since proeutectoid ferrite forms between the A3 and A1 temperature, the amount of ferrite formed below the A1 temperature is scaled down so that the model does not over estimate the amount of ferrite. Moreover, the pearlite fraction is only scaled down if the cooling rate is greater than 3.833°/s so that it does not occupy the space in which bainite should form at higher cooling rates.

Furthermore, the continuous heating of ferrite to austenite was considered from the continuous heating transformation (CHT) diagram illustrated in Appendix A in Figure A.4. It is assumed that as the temperature exceeds the eutectoid point (A1) of the steel, pearlite, bainite and martensite transform into a combination of ferrite and austenite until the A3 point in which a single-phase austenitic state is achieved. The diffusional JMAK relationship for continuous heating between the A1 and A3 temperature is employed. Table 4.1 summarizes the constraints implemented in the metallurgical model.

Table 4.1: Constraints imposed in the metallurgical framework to control the nucleation of each phase.

Transformation	**Type**	**Temperature Gradient**	**Temperature Range**	**Cooling Rate [°/s]**
Aus to Ferr	Diffusional	Negative	B_S <T <A3	$\Delta T/\Delta t$ <6.67
Aus to Pearl	Diffusional	Negative	B_S <T <A1	$\Delta T/\Delta t$ <6.67
Aus to Bain	Diffusional	Negative	M_S <T <B_S	3.83 <$\Delta T/\Delta t$ <10.167
Aus to Mart	Displasive	Negative	M_F <T <M_S	$\Delta T/\Delta t$ >5.67
Ferr to Aus	Diffusional	Positive	A1 <T <A3	N/A
Pearl to Aus	Diffusional	Positive	T >A1	N/A
Bain to Aus	Diffusional	Positive	T >A1	N/A
Mart to Aus	Diffusional	Positive	T >A1	N/A

Subroutine USDFLD was used to calculate these phases during the thermal

analysis. Passed in parameters such as the incremental time step and temperature were used to determine the cooling rate and the previous phases were saved in solution dependent variables to be used in the next increment. The metallurgical phase fractions were compared with those observed on the experimental CCT diagram for 4140 steel at various cooling rates shown in Table 4.2. Additionally, the microstructures of the as-built components were imaged and compared with the model for validation and is presented in Section 4.6.

Table 4.2: Volume fraction percentages comparing the values obtained from the 4140 steel continuous cooling transformation diagram [302, 323] and the metallurgical framework developed for this study.

CCT / Model				
Cooling Rate [°/s]	**% Ferrite**	**% Pearlite**	**% Bainite**	**% Martensite**
2.67	70 / 76	30 / 24	0 / 0	0 / 0
3	67 / 73	33 / 27	0 / 0	0 / 0
3.83	53 / 60	47 / 40	0 / 0	0 / 0
4.83	38 / 27	17 / 12	45 / 50	0 / 0
5.33	9 / 16	5 / 3	72 / 70	0 / 0
5.67	0 / 0	6 / 4	85/ 80	0 / 0
6.67	0 / 0	0 / 0	75 / 55	25 / 45
8.33	0 / 0	0 / 0	45 / 45	55/55
10.17	0 / 0	0 / 0	0 / 0	100/100

4.2.3 Mechanical analysis

The mechanical analysis was conducted separately and is sequentially (one-way) coupled with the thermal analysis, meaning that the thermal field affects the mechanical analysis but the mechanical analysis does not influence the temperature or phase fractions. The temperature dependent mechanical analysis is conducted quasi-statically in which inertial effects are neglected to greatly reduce computational costs [299]. A study by Yang et al. [299] conducted thermo-mechanical models with both quasi-static and dynamical simulations and determined that both produce similar results. The stress equilibrium for a quasi-static mechanical analysis neglecting the effects of the body force (gravity) [293, 294] is shown in Equation 4.14:

$$\nabla \cdot \sigma = \mathbf{0} \tag{4.14}$$

Where σ is the Cauchy stress and ∇ is the vector differential operator.

Equation 4.15 below represents Hooke's law which relates strain to stress.

$$\{\sigma\} = [D]\{\varepsilon\} \tag{4.15}$$

where D is the element stiffness matrix and εis the overall strain tensor.For the sequential analyses, the nodal temperature history is used as input for the thermal load. Subroutine UEXPAN is used to incorporate the thermal and volumetric strain components to the overall strain tensor, in Equation 4.16. In this study, the transformation plasticity strain was ignored as it is relatively insignificant compared to the volumetric strains based on the results from [304]. The total strain tensor is comprised of elastic (ε_E), plastic (ε_P), thermal (ε_{th}) and volumetric ($\varepsilon_{\Delta V}$) strain components [235]:

$$\varepsilon = \varepsilon^E + \varepsilon^P + \varepsilon^{th} + \varepsilon^{\Delta V} \tag{4.16}$$

The thermal and volumetric strains are shown in equations 4.17 and 4.18, respectively.

$$\varepsilon^{th}(T) = \int_{T_{Ref}}^{T} \alpha_{th} dT \tag{4.17}$$

$$\varepsilon_{ij}^{\Delta V} = \frac{1}{3}\frac{\Delta V}{V}\Delta X \delta_{ij} \tag{4.18}$$

where α_{th} is the temperature dependent thermal expansion, ΔV/V is the incremental volumetric change ratio of each phase, ΔX is the incremental phase fraction change between increments, δ_{ij} is the Kronecker delta, and ε_{ij} is the volumetric strain tensor for dilation volume change. Subscripts i and j represent the component in the respective tensor indicating the strain direction or the multiplier from the Kronecker delta (if i=j, δ_{ij}=1, else δ_{ij}= 0). The thermal expansion is calculated based on the

current phase fractions present and is illustrated in Equation 4.19.

$$\alpha_{th} = \sum_{i=F,P,B,M} \alpha_{\mathrm{i}} X_{\mathrm{i}} \tag{4.19}$$

where α_i is the thermal expansion for the i_{th} phase and X_i is the phase fraction of the i_{th} phase at the current time step. The product of the phase fraction and the thermal expansion coefficient for that particular phase is summed across the number of present phases to obtain the overall thermal expansion coefficient for the thermal strain component. The elastic and plastic strains are governed by the isotropic elasto-plasticity constitutive model in ABAQUS [324]. It is assumed that the plastic flow is independent of strain rate and material hardening is isotropic. Elastic strain is expressed in Equation 4.20 [304, 325].

$$\varepsilon_{\mathrm{ij}}^{E} = \frac{1+\nu_r}{E}\sigma_{\mathrm{ij}} - \frac{v_r}{E}\sigma_{\mathrm{kk}}\delta_{\mathrm{ij}} \tag{4.20}$$

Here, Young's modulus, E, and Poisson's ratio, ν_r, are both functions of temperature. As temperatures increase, the effect of strain relief is implemented in ABAQUS by specifying the annealing temperature at 815 °C. At this point, ABAQUS assumes that the material loses any prior work hardening and thus the equivalent plastic strain is set to zero [324]. The temperature-dependent plastic strain rate [304, 325] is shown in Equation 4.21:

$$\Delta\varepsilon_{ij}^{P} = \widehat{G}\left(\frac{\partial F}{\partial \sigma_{\mathrm{kl}}}\dot{\sigma}_{\mathrm{kl}} + \frac{\partial F}{\partial T}\dot{T}\right)\frac{\partial F}{\partial \sigma_{\mathrm{ij}}} \tag{4.21}$$

where $\hat{\mathrm{G}}$ is the hardening function [304, 325] and is represented in Equation 4.22:

$$\frac{1}{\widehat{G}} = -\left(\frac{\partial F}{\partial \varepsilon_{\mathrm{mn}}^{P}} + \frac{\partial F}{\partial \kappa}\sigma_{\mathrm{mn}}\right)\frac{\partial F}{\partial \sigma_{\mathrm{mn}}} \tag{4.22}$$

where F is the temperature-dependent von Mises yield function in Equation 4.23 and $\overline{\sigma}(\varepsilon,\mathrm{T})$ is the temperature-dependent flow stress of the material. κ

represents the work hardening parameter while S_{ij} is the deviatoric stress tensor shown in Equation 4.24. The subscripts m and n represent the tensor location which are different than i and j previously defined. Unlike thermal strains, the plastic and elastic strains are assumed to be independent of material for simplicity [304, 325].

$$F = \frac{1}{2} S_{\mathrm{ij}} S_{\mathrm{ij}} - \frac{1}{3} \bar{\sigma}^2(\varepsilon, T) = 0 \tag{4.23}$$

$$S_{\mathrm{ij}} = \sigma_{\mathrm{ij}} - \frac{1}{3} \sigma_{\mathrm{kk}} \delta_{\mathrm{ij}} \tag{4.24}$$

4.3 Materials

Water atomized 42CrMo4 steel powder was used with particle size between 36 and 126 µm and a powder feed rate of approximately 4.2 g/min. The chemistry and a scanning electron microscope (SEM) image of the powder used in this study are shown in table 4.1 and Figure 4.5, respectively. The printed components are manufactured from the 42CrMo4 powder while the substrates are made form AISI 4140 steel. Prior machining, grounding and sandblasting of the substrates introduces residual stresses which were relieved by conducting a full anneal following the process outlined in ASM metals handbook Vol. 4C [326]. Since AISI 4140 steel and 42CrMo4 steel are almost chemically equivalent and the material library for 4140 steel is more frequently used in the literature, data for 4140 was used in place of 42CrMo4.

Table 4.3: Chemical composition of 42CrMo4 steel compared to AISI 4140 steel [327] in percentages

Name	**Cr**	**Cu**	**Mn**	**Mo**	**Ni**	**Si**	**C**	**S**
42CrMo4	1.034	0.102	0.85	0.19	0.066	0.031	0.44	0.008
AISI 4140	0.8-1.15	0	0.7-1.0	0.15-0.25	0	0.15-0.3	0.36-0.44	0.04

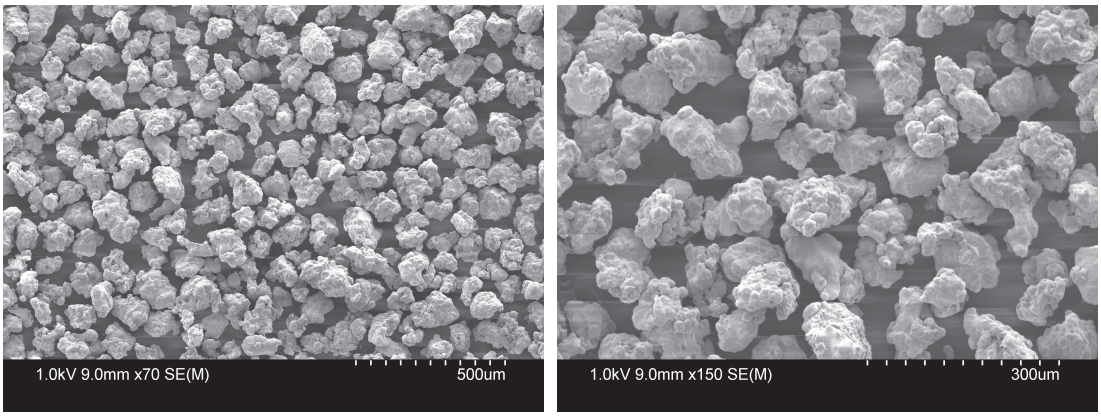

Figure 4.5: Water atomized 42CrMo4 steel powder

4.4 Case studies and experimental setup

4.4.1 Case Studies

A similar approach to Heigel et al. [294] and Denlinger et al. [293] was used to validate the model. Four separate cases were conducted with varying parameters and the process parameters used for each case are summarized in table 4.4.

Table 4.4: Processing parameters used in each case for this experiment

Case	**1**	**2**	**3**	**4**
Geometry	Thin wall	Thin wall	Thin wall	Cube
Laser power [W]	600	600	600	500
Traverse speed [mm/s]	8	8	8	8
Powder feed rate [g/min]	4.2	4.2	4.2	4.2
Hatch spacing [mm]	1.2	1.2	1.2	0.5
Z-step size [mm]	0.3	0.3	0.3	0.3
Dwell time [s]	0	20	40	0

The first three cases consist of a 20-layer thin wall with dimensions 37mm × 3.6mm × 6mm deposited onto a 76.2mm × 25.4mm × 6.5mm 4140 steel substrate. A hatch spacing of 1.2 mm was used so that there was little to no overlap between bead tracks in order to more accurately encompass the limitations of element activation in the model. The dwell times between each layer were altered between case 1, 2 and 3

specified at 0s, 20s and 40s, respectively. The purpose of the varying dwell times is to observe the expulsion of heat between layers. The geometry and scanning strategy was altered for case 4 in which a 10mm cube was generated at the same feed rate and z-step but with a lower laser power of 500W. A more practical hatch spacing of 0.5mm was used in order to model the current optimal build conditions known for this alloy through previous experiments on this machine. The post-build dimensions of each case is illustrated in Figure 4.6.

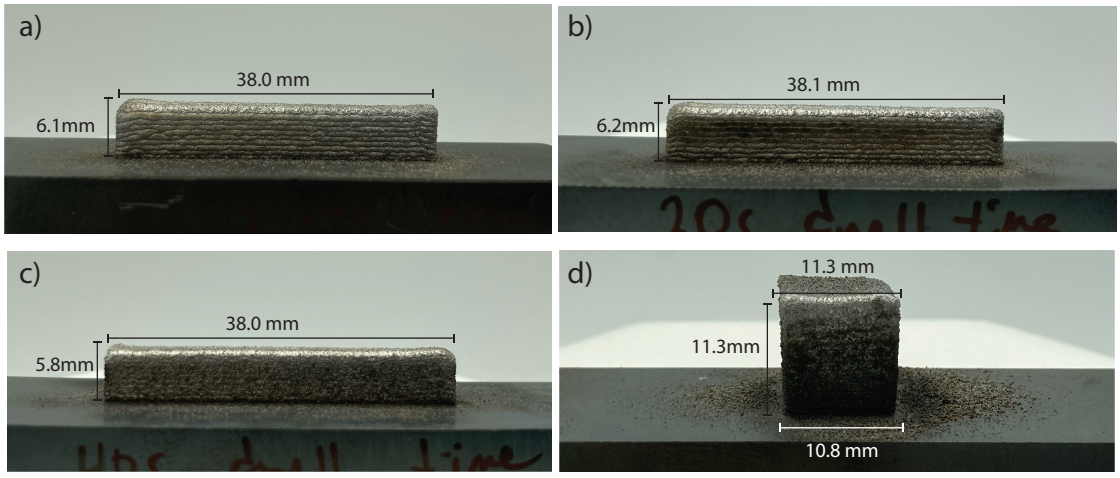

Figure 4.6: Post build dimensions for a) case 1 with 0s dwell b) case 2 with 20s dwell c) case 3 with 40s dwell d) case 4 cube with 0s dwell

4.4.2 Experimental setup

The experimental validation was conducted with an Optomec LENS MTS 500 metal printer. The build chamber is purged with argon gas and kept under relatively constant conditions through the argon recycling and filtering network. Some of the machine specifications of this printer are summarized in table 4.5. The deposition head geometry is similar to the Optomec system used in Ref. [294].

Furthermore, the bead dimensions were determined for various laser powers and scanning speeds in order to translate this to the model. For a scanning speed of 8 mm/s, a bead width of 1.17mm was measured for a 600W laser power while a bead width of 1.07mm was measured for a 500W laser power. The bead height was not affected by the laser power but rather the powder feed rate and the scanning speed

Table 4.5: Machine specifications for the Optomec LENS HY-20-CA system with a YLR-1000-MM-WC laser used in this study.

Machine Specification	**Value**	**Units**
Laser spot size	600	µm
Oxygen content	5	ppm
Argon flow through nozzles	42	L/min

and thus is held constant across all cases at 0.3mm. The results of this study are shown in Appendix C. All cases were built on a cantilevered 4140 steel substrate fixed at one end with an M8 bolt as shown in Figure 4.7.

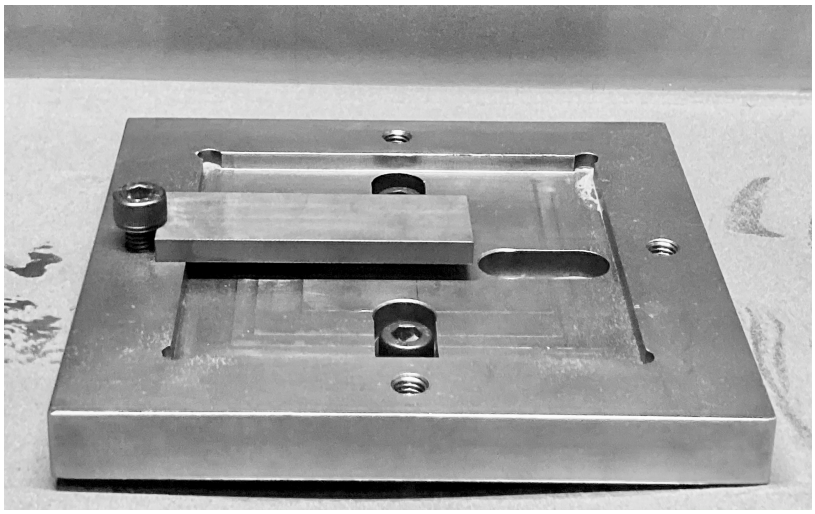

Figure 4.7: Build setup on cantilever substrate secured at one end

K-type thermocouples were welded at various locations to measure the temperature field during deposition. For case 1-3, two thermocouples are welded onto the substrate at various locations illustrated in Figure 4.8. Insulating tape was used to secure the wires to the substrate so that the weld between the point of interest and the thermocouple was more secure. Furthermore, ceramic sleeves were used along the length of the wire in contact with the substrate in order to avoid insulation failure that would comprise the measurements. For case 4, two thermocouples were welded onto the substrate in a similar fashion as the other three cases, however the side thermocouple (TCside) is located on the top of substrate and 1mm from the edge along the middle. Since case 4 has an entirely different geometry and laser trajectory, the thermocouple was moved closer to the build to try and distinguish the laser passes.

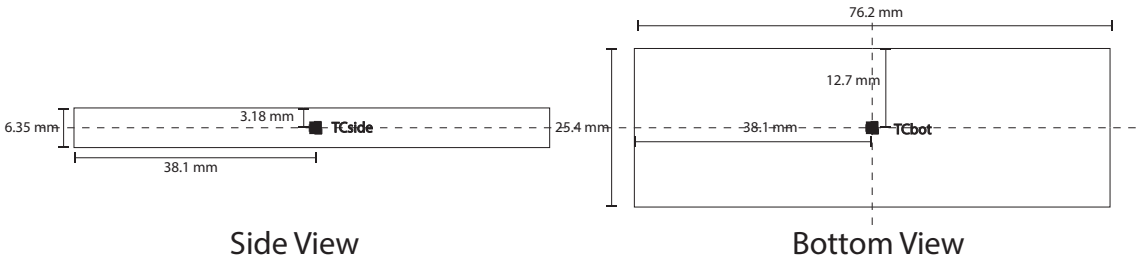

Figure 4.8: Thermocouple location on 4140 steel substrate for case 1 - 3

A meltpool sensor is also used in order to capture and calculate the area of the molten region during deposition. The sensor is situated directly above the deposition nozzle so it is able to have a clear, unobstructed view of the meltpool. The sensor is unable to record the temperature however, it collects the emission of the incandescent liquid alloy and the pixel space it occupies in order to translate that into the approximate meltpool area in square milimeters. This data is compared with the molten region in the model above the liquidus point at various times throughout the build.

Distortion of the substrate after the component was cooled to ambient temperature was determined by measuring the vertical displacement of the substrate using a Keyence VK-X1000 3D laser scanning confocal microscope. In similar studies by refs. [294] and [293], an in-situ laser displacement sensor (LDS) is used to provide distortion history throughout the build at a single point. This data is then compared with the same point within model as a function of printing time. For this study, the Keyence laser confocal microscope was used to map the displacement profile from the clamped end to the free end. The data was normalized so the deflection at the clamped end begins at zero. The data obtained from the microscope required stitching of multiple images to acquire the profile of the entire length of the substrate and thus artificial peaks and valleys were introduced in the data. Although only post-distortion data can be compared with the model, the entire profile of the distorted substrate can be plotted against the experimental data rather than at just one point.

Residual stress was measured with a Proto LXRD stress using a Cr tube source using the K_α wavelength of 2.2910 Å. The stress analyzer uses Bragg's law to determine the interplanar spacing of the atomic planes for a number of incident angles relative to the hkl plane. The change in lattice spacing compared to the theoretical

values is then converted to a stress value. XRD measurements were made along the top surface on the middle of each thinwall case. A general uncertainty of +/- 35 MPa is specified by the manufacturer along with the measured error calculated during the measurement.

Furthermore, the as-built microstructures of each case was analyzed. Each sample was cut into an appropriate size along the build direction and mounted along the z-y plane (building in z-direction) so the spatial variation in microstructural constituents could be observed. The specimens were mounted in conductive bakelite, then ground and polished using a Struers Tegramin-20 autopolisher using a conventional series of SiC foils and diamond suspensions. All samples were then etched using sodium metabisulphite diluted to 10%. The microstructure of each build was then compared with the predicted volume phase fractions calculated in the model based on temperatures and cooling rates. Both optical and scanning electron images were obtained using the Keyence microscope and a Hitachi S-4800 SEM, respectively.

4.5 Modelling implementation

4.5.1 FEM mesh

The same mesh was used for both the thermal and mechanical analyses. DC3D8 block elements were used for the thermal analysis while C3D8R block elements were used in the mechanical analysis. The mesh for case 1-3 is shown in Figure 4.9. Each 38.1mm $\times$ 3.6mm $\times$ 6mm wall is comprised of 34,200 elements and 39,360 nodes while the 76.2mm $\times$ 25.4mm $\times$6.35mm cantilevered substrate is assembled by 36,725 elements and 40,138 nodes. The substrate is secured to a 316L stainless steel fixture plate comprised of 4,487 nodes and 3,600 elements while the representative screw clamping the substrate contains 735 nodes and 488 elements. The walls have a fixed element size of 0.4mm$\times$0.4mm$\times$0.15mm such that the bead width is comprised of 3 elements wide and 2 elements in height which is similar to other studies [222, 293, 294, 299]. However, since the cube in case 4 is built using 500W laser power, the bead width was determined to be 1.1mm and thus a fixed element size of 0.37mm$\times$0.37mm$\times$0.15mm is used. The mesh for the cube has 48,114 elements and 52,528 nodes while the

substrate for case 4 now contains 25,233 elements and 27,972 nodes.

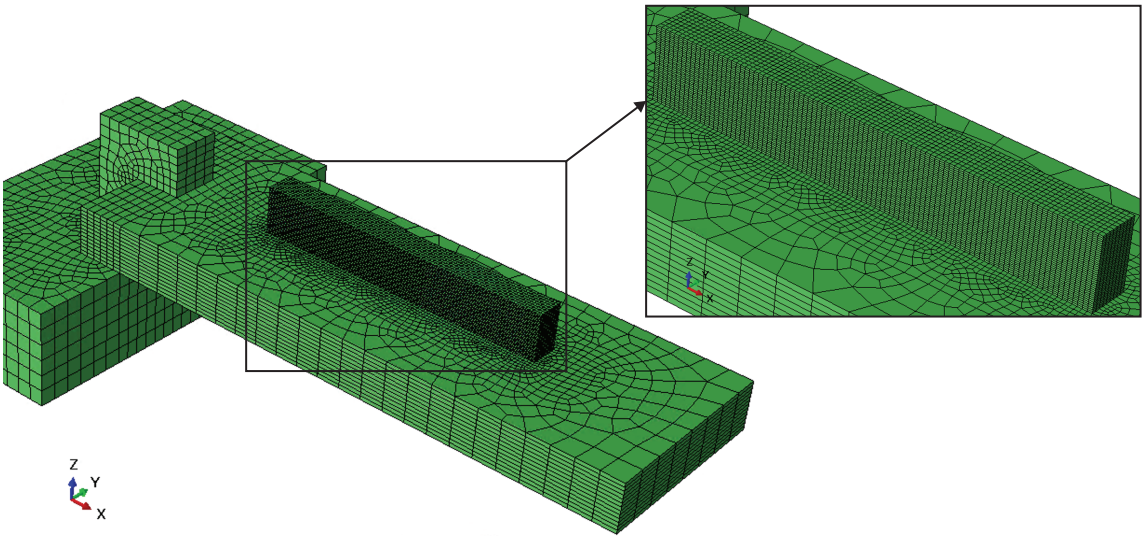

Figure 4.9: Finite element mesh for the 38.1mm x 3.6mm x 6mm thinwall cases on the cantilevered substrate and fixture constructed by a total of 75,013 elements and 84,720 nodes.

4.5.2 Laser Trajectory

The laser trajectory was kept constant for the thinwall cases in 1, 2 and 3 while case 4 was altered due to the different geometry. As noted earlier, the hatch spacing for case 1-3 was set to the bead width of 1.2mm meaning there is virtually no overlap between adjacent laser scans. This best represents the conditions in the model where element activation is limited to a constant bead width as new material is being deposited adjacent to another bead. As the hatch spacing decreases, the bead widths between weld tracks start to vary between one another in the model and in some cases all elements on a layer can be activated while the laser continues to build the layer. The scanning strategies used in this study are illustrated in Figure 4.10.

4.5.3 Material property input data

The temperature dependent material properties for 4140 steel is listed in table 4.6. ABAQUS uses linear interpolation to obtain values between each defined data point

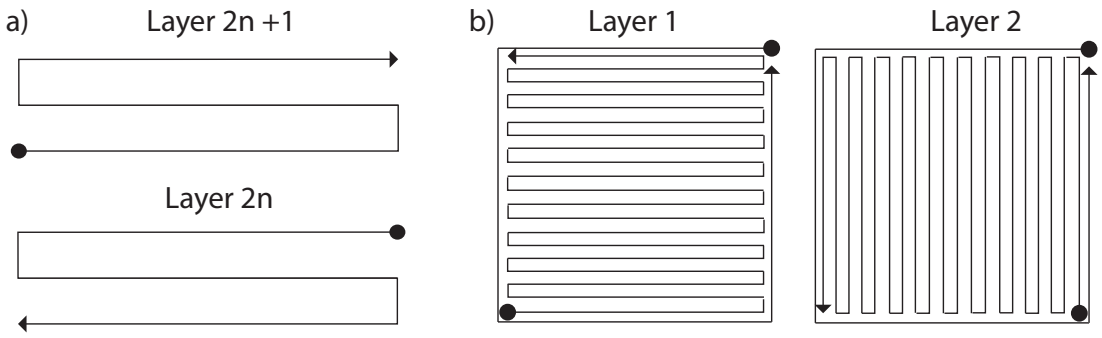

Figure 4.10: Laser scanning strategy for a) case 1-3 starting from n=0 to 10 for a total of 20 layers and b) case 4. The cube outline remains constant across all layers but the internal scanning strategy is rotated 90° counter clockwise each layer.

and the last value is taken when exceeding the last specified point. The density and emissivity is assumed to be a constant at 7850 kg/m^3 and 0.55, respectively. The emissivity value was chosen based on the acceptable range between 0.5 and 0.75 for AISI 4140 steel [328]. The latent heat of fusion values is specified as 250 kJ/kg and is spread over a temperature range from 1420°C to 1460°C. Furthermore, table 4.7 lists the relative volume changes and thermal expansion for each metallurgical phase used in the strain tensor equations.

Table 4.6: Temperature dependent thermal and mechanical properties for 4140 steel from [329]

Temperature [°C]	Specific Heat [J/Kg·°C]	Thermal Conductivity [W/m·K]	Young's Modulus[GPa]
25	475	46	220
200	525	41	200
400	560	37.5	175
600	730	33	155
800	825	30	120
1000	600	28	110
1200	600	30	90
1400	600	30	75

Plasticity data for 4140 steel was used from a high temperature mechanical property study by Abed et al. [330]. Plastic data from 25 to 650°C at a strain rate of approximately 0.002/s was used for the isotropic hardening model and is illustrated in Figure 4.11. Above this temperature the mechanical properties are assumed to be constant until the annealing temperature in which there is no more work hardening.

Table 4.7: Thermal expansion and volume changes of steel phases from [304]

Phase (from austenite)	**Volume change [%]**	**α[1/°C]**
Pearlite	0.33	1.53E-05
Ferrite	0.38	1.61E-05
Martensite	1.026	1.15E-05
Bainite	1.026	1.15E-05
Austenite	N/A	2.2E-05

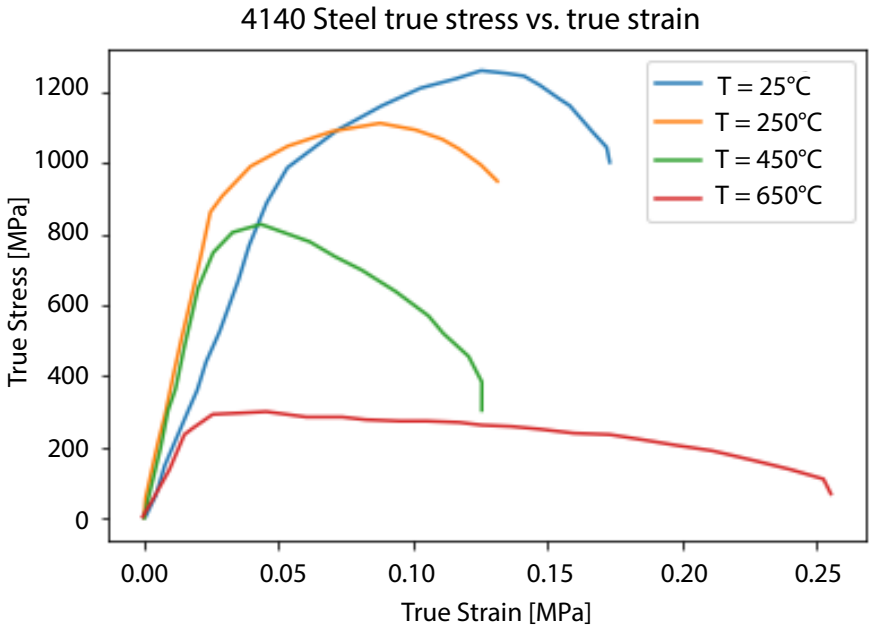

Figure 4.11: 4140 steel plasticity data at a strain rate of approximately 0.002/s adopted from data collected by Ref. [330].

4.5.4 Initial and boundary conditions

In order to encompass the proper conditions of the Optomec DED printer, agitation by the argon jets needs to be considered. Since the printer head geometry and experimental steup is similar to that in Heigel et al [294], their measured convection data on the substrate and thin wall was used in this study. However, to account for the small differences in argon gas flow rate and z offset, the values were adjusted to best fit the data in this study. Heigel's setup has 34L/min across all jets with a 9.3mm z-offset while the setup in this study uses a 42L/min flow rate and a 6.35mm z-offset. Thus,

the distribution defined by Heigel is scaled up to better approximate the conditions in our setup due to the smaller z-offset and larger gas flow.

The modified relationship between convection coefficient, radial distance from laser center and z step is shown in Equation 4.25 and Equation 4.26 for the wall and substrate, respectively with their distribution illustrated in Figure 4.12. Modifications were made from the original formulation by Heigel et al. [294] by multiplying the curve by a factor of 2 but leaving the diminishing value at 25 and 30 W/m^2K for the wall and surface, respectively. This was to account for the larger volume flow and smaller z-offset in this study which would cause a higher convection value at the center of the nozzle but would likely decay in a similar fashion due to the same nozzle geometry. After printing and all the argon jets are turned off, the normalizing convection value is set to 5 W/m^2K for all surfaces. For more information on the experimental setup for measuring the convection values from the argon jets, the reader is recommended to visit the original work conducted by Heigel et al. [294].

$$h_{\text{wall}} = 2((-2.717d_z + 37.174)\mathrm{e}^{-(0.107r)^{2.7}}) + 25 \tag{4.25}$$

$$h_{\text{surface}} = 2(1.9(-2.717d_z + 37.174)\mathrm{e}^{-(0.031r)^{1.4}}) + 30 \tag{4.26}$$

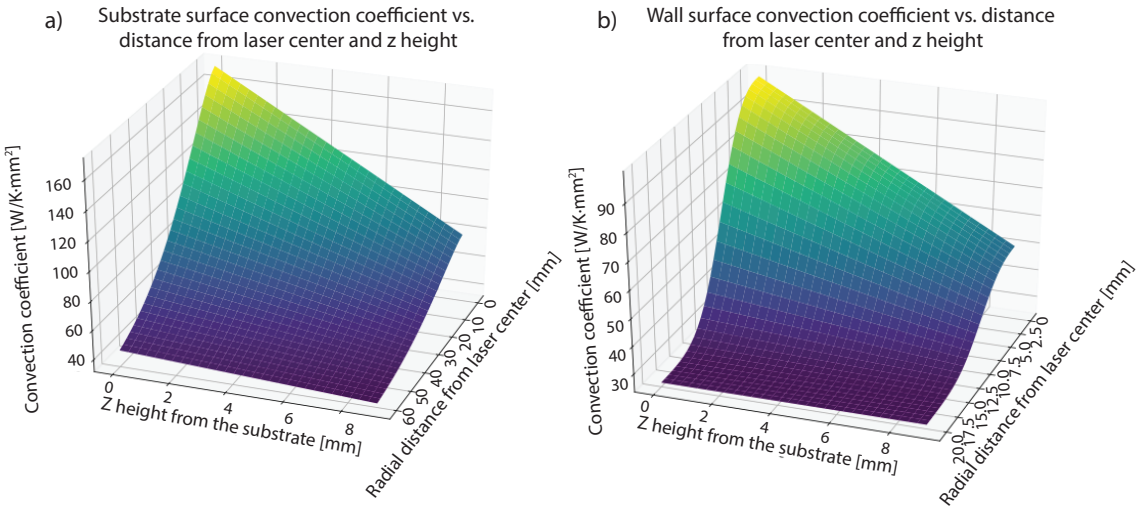

Figure 4.12: 3D surface plot of convection coefficient with respect to z-step and radial distance form laser center for a) wall and b) top of the substrate

In Equations 25 and 26, h is the convection coefficient in W/m^2K, d_z is the vertical distance from the substrate and r is the radial distance from the center of the laser. For the cases with 20s and 40s dwell times, after each layer is completed the deposition head clears the part and moves to the other side of the chamber so there is no more agitation from the forced argon flow. This movement adds approximately 7s to the dwell time making the total dwell in between layers 27s and 47s for case 2 and 3, respectively. Since there is no agitation in between dwell times, a natural convection value of 10 W/m^2K is used according to similar studies [294]. Furthermore, since only a portion of the stainless steel fixture was included in the model, a higher convection coefficient of 20 W/m^2K was implemented to account for the heat that would be lost through conduction. The convection coefficients were calibrated on case 2 to best match the measured thermocouple data which were then held constant across all four cases.

The initial temperature of the build is set to $27°C$ and newly activated elements are set to the liquidus point of $1420°C$. The initial microstructural composition of the annealed substrate in the model is assumed to be 70% ferrite and 30% pearlite based on the fractions produced at the slowest cooling rate on the CCT diagram. The boundary conditions for the mechanical analysis were set so that the clamped end was fixed in all directions and rotations around the screw and substrate contact points. This allows for the free end of the substrate to deflect and compare with measured experimental data. During deposition, the node conditions from previously active elements which are coincident with newly active elements are tied with one another and merged so no large discontinuities are encountered.

4.6 Results and discussion

4.6.1 Thermal analysis

Figure 4.13 illustrates the temperature history across all four cases. The simulated and experimental data from the thermocouples can be compared in Equation 4.27 to determine the average error across the data set for each location [293, 294]. It is clear that the simulated temperature field closely agrees with the recorded thermocouple

data across all four cases. It can be noted that the normalizing cooling conditions after printing vary between the model and the experimental results. Due to the complex heating and cooling cycles encountered during printing, the ambient is subject to large fluctuations throughout the build. A constant value of $27°C$ is imposed in the model, so the normalizing cooling rate is faster than that observed experimentally. This deviation is more significant for case 1 and 4 due to the larger temperature at the end of build. It can be noted that for the side thermocouple in case 4 (TCside), there are some irregular spikes which are likely caused from spatter hitting the sensor during printing. The error during printing between the simulated data and the experimental measurements can be calculated in Equation 4.27.

$$\% \text{ Error } = \frac{100 \sum_{i=1}^{N} \left| \frac{(T_{\text{exp}})_i - (T_{\text{sim}})_i}{(T_{\text{exp}})_i} \right|}{N} \tag{4.27}$$

where N is the number of recorded points and simulated time increments, i is the current time increment, T_{exp} is the value of the thermocouple, T_{sim} is the value obtained from the model during printing. A summary of the percent errors calculated across all cases at each thermocouple is depicted in table 4.8. It is evident that the simulated temperature results agree very closely with the experimental TC data. Most of the calculated errors during printing fall within 3% - 4% while the largest error between the thinwall cases is on the bottom thermocouple for case 1 with a 7.95% error.

Case 4 presented much larger errors than the thinwall cases at 8.59% and 10.09% for the bottom and side, respectively. The temperature curves during printing for case 4 between the simulated and measured data show a larger error halfway through the build. The thermocouples show a decrease in temperature while the simulation holds at the same temperature around $520°C$ for the remainder of the build. This is likely due to the convection model adopted from Ref. [294]. Their model was measured for a 3mm width thin wall case in which the convection coefficient drops sharply as the distance from the laser center surpasses this width. This is to account for the difference between the top of the wall and the side of the wall. For the cube case, the width is approximately 10mm and thus, this distribution would need to be modified to account for the larger area of agitation on the top of the cube. Further development of a convection model to account for a number of geometric features such

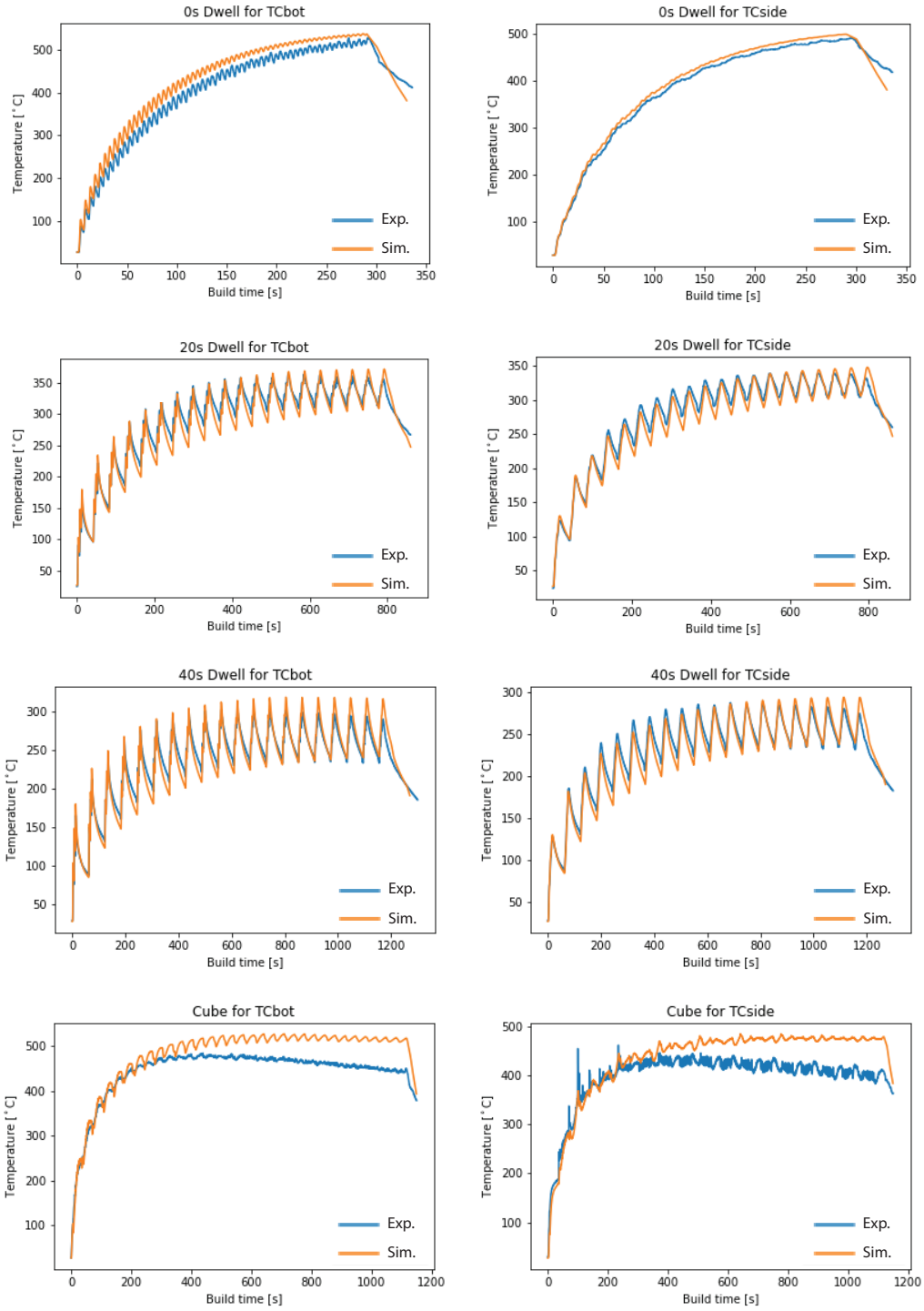

Figure 4.13: Plots showing the simulated and experimental data for the bottom and side thermocuples during printing for all four cases.

as length, width and height would be needed to simulate more practical geometries rather than just a thinwall.

Table 4.8: Error between experimental and simulated data cases for each thermocouple during printing

Case	Geometry	Dwell time [s]	% Error TCbot	% Error TCside
1	Thinwall	0	7.95	2.85
2	Thinwall	20	3.96	3.30
3	Thinwall	40	3.91	3.81
4	Cube	0	8.59	10.09

The meltpool sensor was used to record the average area of the meltpool throughout case 4. The overall trend in size is shown in Figure 4.14 while the comparison between the experimental and simulated captures are shown in Figure 4.15. Since the incandescent vapour and spatter caused a significant over estimation of the meltpool area at various points during the 600W thinwall cases, only data from the 500W cube build will be presented and compared to the model. The laser power in case 4 is set to 500W, lower than the 600W nominal power set for cases 1-3 and thus, a clearer image of the meltpool was able to be captured without a significant amount of incandescent vapour and spatter greatly skewing the measured area values.

Since incandescent vapour and spatter still caused some deviation in the recordings, the clearest image of the meltpool with a measured value on the lower end between the highest and lowest values in a 5 second window were taken to be compared with the model. For example, if there were readings ranging from $5mm^2$ to $3mm^2$, a recorded value with a clear meltpool image at $3.5mm^2$ would be taken but only if there was another measurement around this value. This approach was taken to try and capture the true area of the meltpool without the spatter and incandescent vapour. However, the lowest value was not taken in the event that the meltpool was not fully developed from the laser modulation. Since the measured meltpool values can vary greatly within a few seconds, consistent values on the lower end were deemed most likely to represent the true size of the meltpool. These values were compared to similar points in the model at eight different locations during deposition. The meltpool areas were calculated by setting a contour limit maximum at the liquidus temperature of 1420°C and measuring the axes along the length and width of the meltpool.

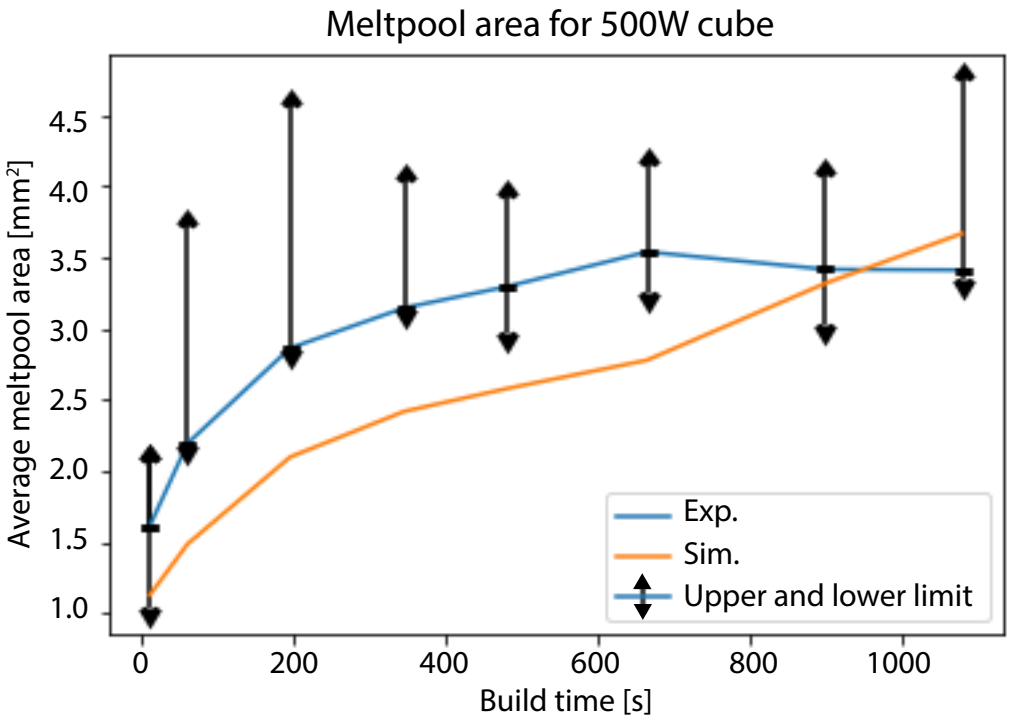

Figure 4.14: Simulated and experimental meltpool areas as a function of build time. The upper and lower limits on the experimental data represent the smallest and largest measurements made within a 5 second window. The actual value plotted was taken on the lower end of this range with multiple measurements with similar values. The large range in measurements arise from incandescent vapour and spatter greatly increasing the measured area while the lowest range could represent a meltpool which as not been fully developed.

The measured values mostly show a slightly larger area than the simulated counterparts. Part of this discrepancy is likely due to some spatter and incandescent vapour still being measured but since both these values are approximations, the values are in very close agreement. Furthermore, the meltpool area as a function of time is also presented showing the trend in both experimental data and simulated points for case 4. This trend is consistent with the overall temperature profile seen for the thermocouple data in case 4. The meltpool area increases until it peaks at approximately 11 minutes where it then begins the decrease. However, this trend is not seen in the simulated data since the temperature holds at a relatively constant temperature just above $520°C$ for the remainder of the build while the experimental data show a slight cooling after its peak at around 400s. The trend between the

simulated and measured meltpools follow the same curve up to around 700s where the measured data plateaus and the simulated meltpools continue to increase. It is likely that a more refined convection model to fit more geometries based on their overall dimensions could fit this curve better with the experimental data. Overall, the meltpool size and trend generally agrees with the experimental data.

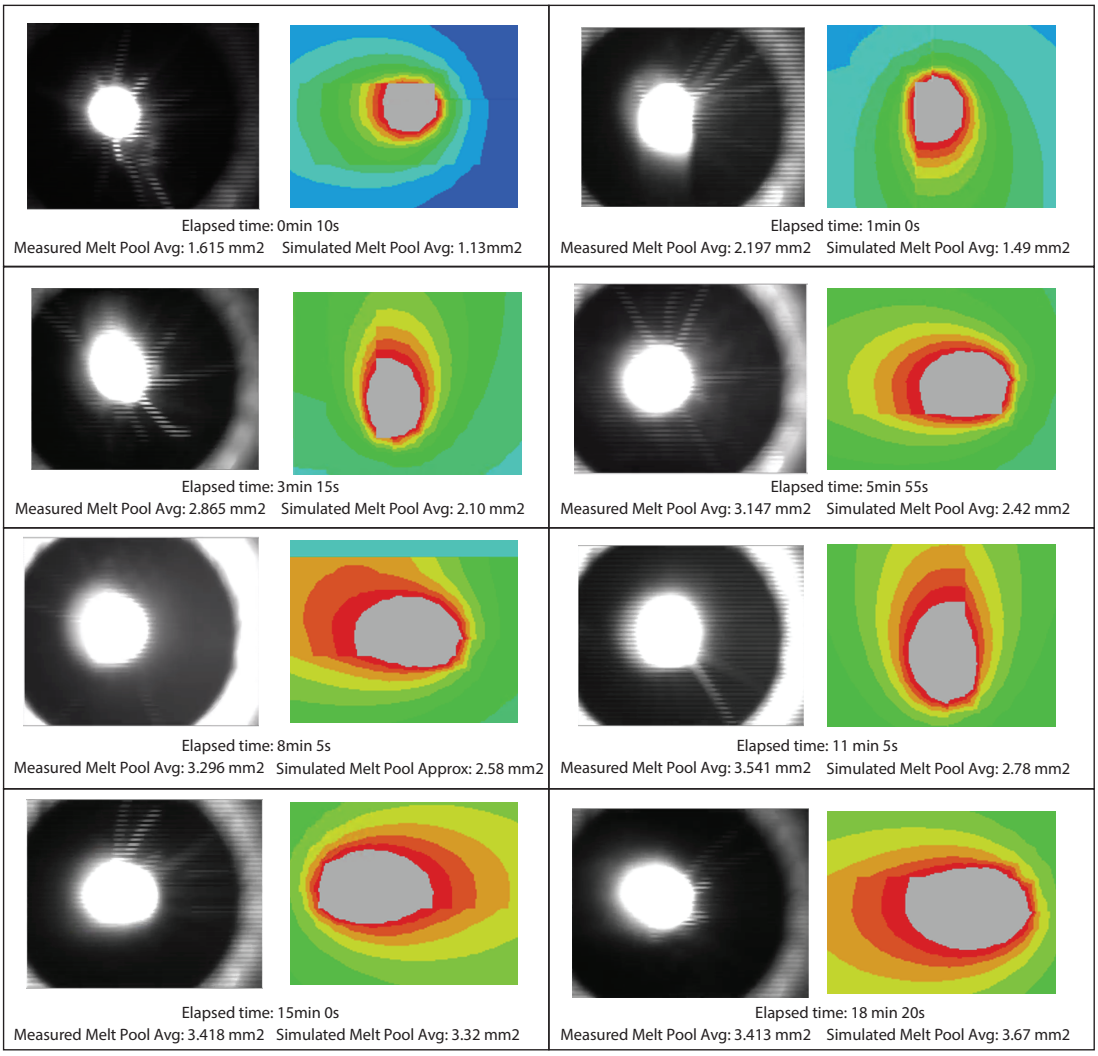

Figure 4.15: Measured meltpool area obtained form the meltpool sensor during printing of case 4 and the simulated meltpools at the corresponding build time and their associated calculated areas. The grey area in the simulation represents points within the model which have exceeded the liquidus temperature (1420°C) of 4140 steel.

4.6.2 Metallurgical analysis

Cross-sections of each case were prepared, mounted and polished so the microstructural constituents could be characterized and compared with the model. Each case is presented with optical and SEM images from the top, middle and bottom sections which are then compared to the calculated phase fractions from the simulation.

Case 1

For case 1, a mostly bainitic and ferritic structure was observed and simulated as shown in Figure 4.16. Small pearlite clusters were observed through SEM imaging near the middle of the wall which was also captured in the simulation. However, a small amount of martensite was shown in the heat affected zone on the substrate where this was not observed experimentally. Since the metallurgical framework does not consider any martensite decomposition, the A1 temperature is required to be reached in order to dissolve any present martensite into ferrite and austenite. Thus, if this temperature is not reached, the martensite remains where in reality the martensite is likely to decompose when held at high temperatures below the A1 point.

Furthermore, tempered bainite [331] was found throughout the middle and bottom sections while small amounts of bainite and martenstie laths within untempered bainite in the top layers was found within the top layers. According to a similar microstructures observed in bainitic duplex steels by Xu et al. [332], the matrix is composed of a granular bainitic ferrite laths with ductile allotriomorphic ferrite. In this study, there is evidence of allotriomorphic ferrite present along prior austenite grain boundaries which is commonly seen across all four cases. These observations agree with similar characterization studies for AISI 4140 steel [2, 332–335].

Case 2

The top layers on case 2 are noticeably different than the rest of the material as revealed by the etchant. This is due to the dwell time allowing heat to leave the material between layers and therefore generate sharper thermal gradients in range of the martensite start temperature. Thus, during the last few layers, the argon gas

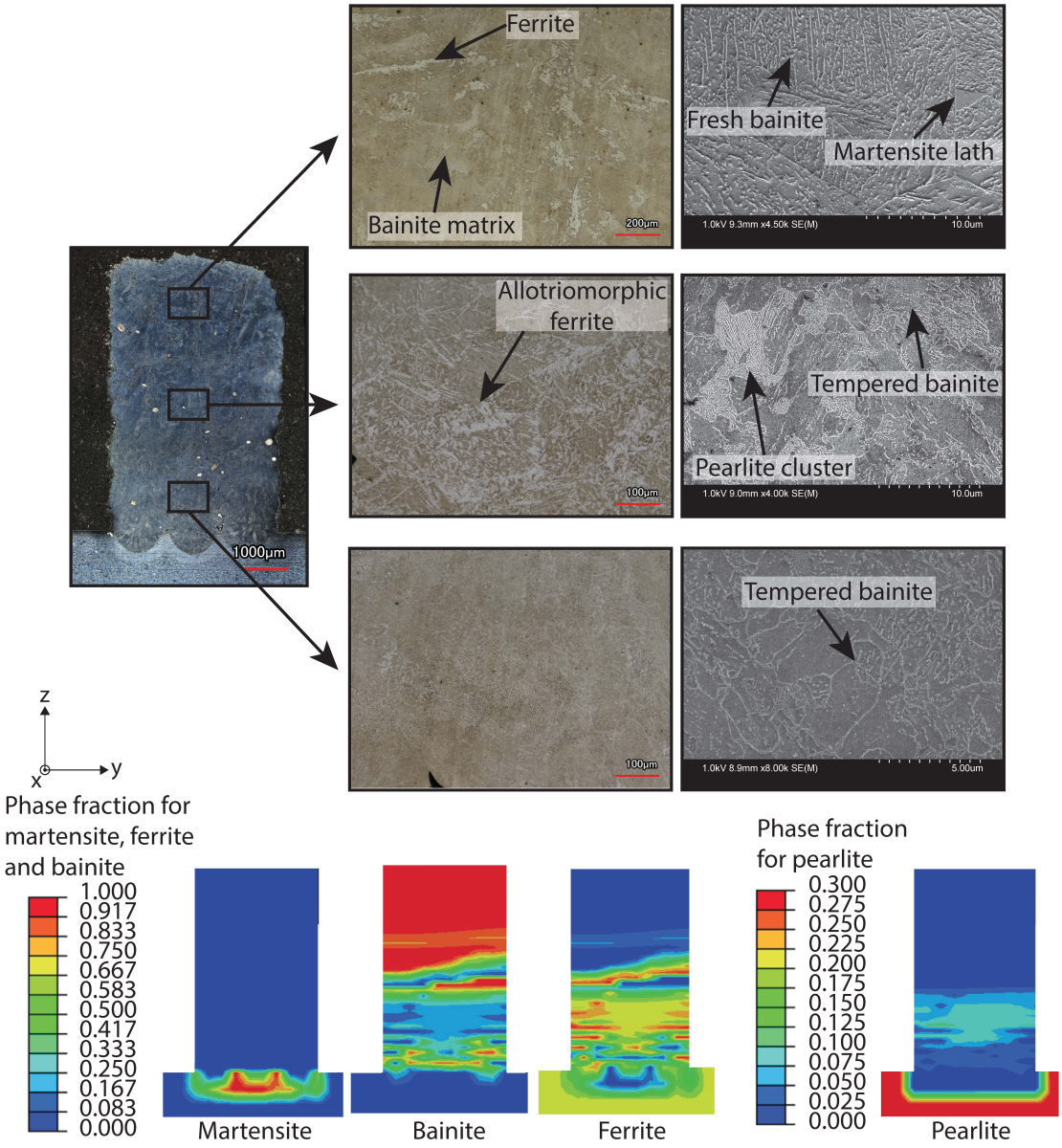

Figure 4.16: Experimental metallography analysis for case 1 on the top, middle and bottom sections. Simulated phase fractions along the middle cross-section is also compared with the observed microstructural constituents.

from the jets are able to quench the top layers while not being affected by the large temperature of the rest of the wall which greatly slows the cooling rate as seen in case 1.

The microstructure produces similar microstructural constituents with bai-

nite and ferrite, however a considerable amount of martensite is also present. The top layer shows larger mertensite laths consitent with Ref. [336] within the bainite matrix [336] while further down small tempered martensite nodules are scattered throughout the bainite and ferritic matrix. The tempered martensite is evident in the optical micrograph in the middle section showing dark nodules with a high aspect ratio which closely resembles work done by Wang and Kelly [2] who investigated 4140 steel processed by selective laser melting (SLM). The simulations predict the presence of these three phases but the location of the martensite in some areas does not agree. The simulated microstructure shows a fully bainitic top section with a larger amount of martensite in the middle and bottom section. This again is largely due to the fact that this model does not include carbon diffusion and thus martensite in the bottom sections remain if the A1 temperature is not achieved. The small amount of martensite observed in the top layers is likely not captured since the cooling rate is just below the critical cooling temp for martensite formation as defined by the CCT diagram which in reality is much more fluid.

Case 3

Case 3 presented similar findings to case 2 with more martensite in the top layers and tempered martensite throughout the rest of the thinwall. The upper most layers show long martensite laths within a bainitic matrix which was evident in the optical micrographs and consistent with Ref. [336]. In the middle of case 3, fresh bainite with fine spacing is evident with small tempered martensite nodules similar to case 2. The bottom also contains tempered martensite within a tempered bainitic matrix consistent with [331].

The prescence of the cellular-like structure of allotriomorphic ferrite outlining the fine prior austenite grain boundaries is also observed. Considering the cooling rates were quite significant in these top few layers in both the 20s and 40s dwell case, the material was not held above the A3 temperature for along period of time and thus the austenite grains are much smaller than in the 0s dwell case. It is evident that as the dwell time increases from 0s to 40s, the presence of higher carbon phases is apparent through the etching effects. The simulation predicts a mostly martensitic and ferritic structure with trace amounts of bainite in the top half of the thinwall. Furthermore, the heat affected zone on the right side of the thinwall is also evident

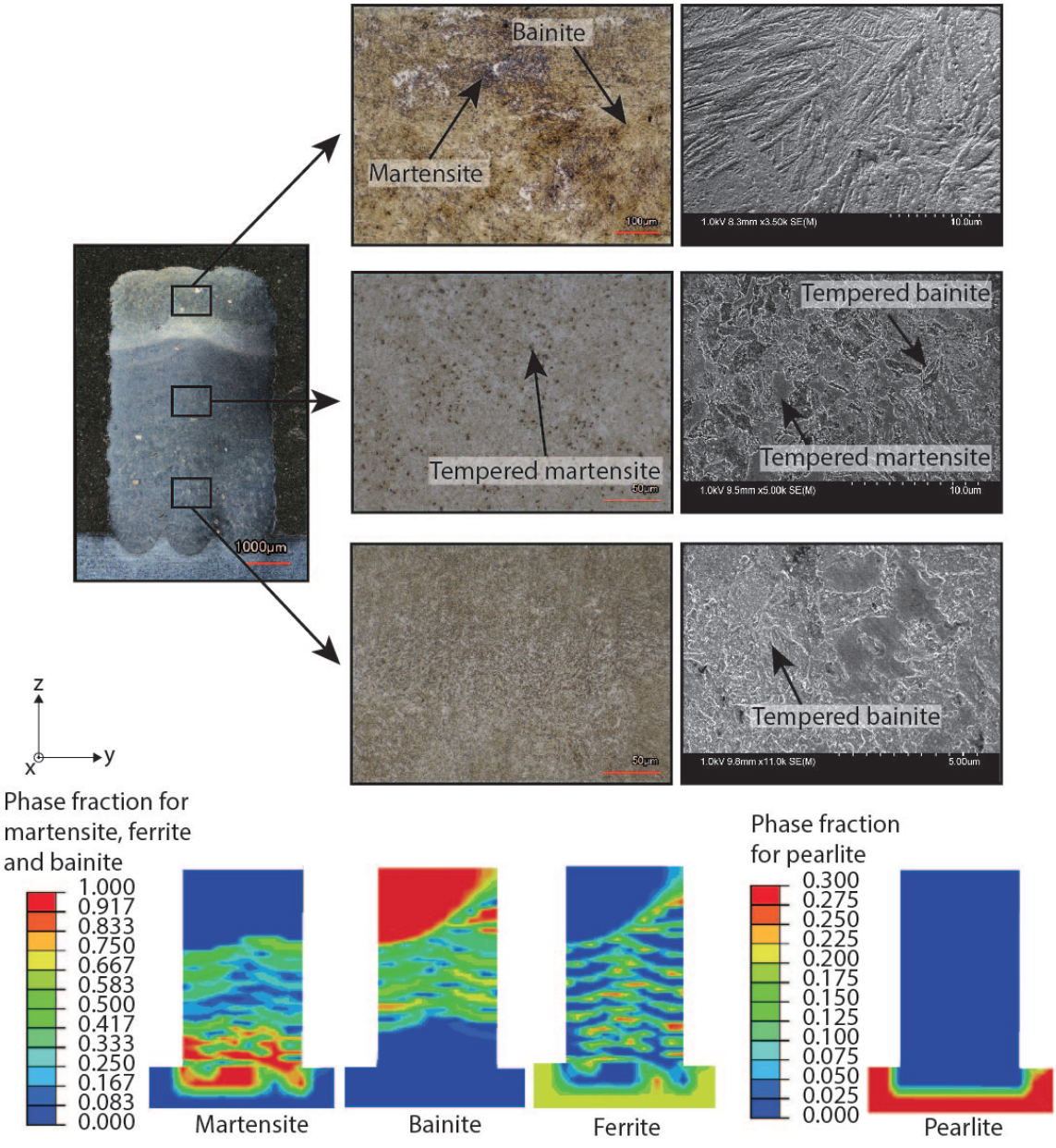

Figure 4.17: Experimental metallography analysis for case 2 on the top, middle and bottom sections. Simulated phase fractions along the middle cross-section is also compared with the observed microstructural constituents.

as revealed by the etchant in the optical micrograph due to the final laser pass of the build.

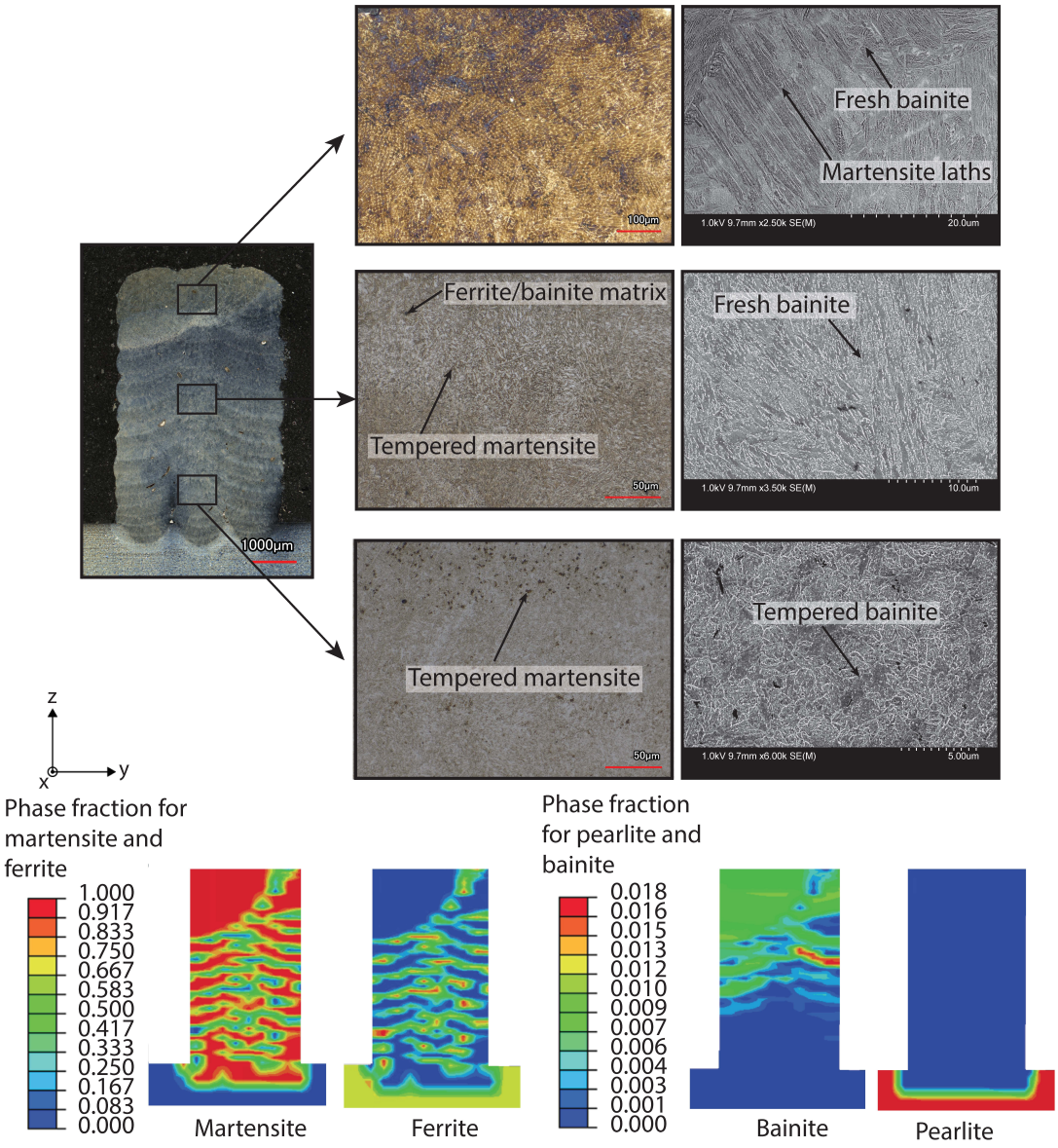

Figure 4.18: Experimental metallography analysis for case 3 on the top, middle and bottom sections. Simulated phase fractions along the middle cross-section is also compared with the observed microstructural constituents.

Case 4

Lastly, case 4 presents similar findings as case 1 with a mostly bainitic and ferritic structure and a small amount of pearlite. There is a clear columnar to equiaxed transition (CET) between the top and bottom half of the cube. This is likely due to the

fact that top portion of the cube is held above the A3 to allow significant grain growth while the bottom half resembles that of a heat affected zone with grain refinement. The top of the cube shows large grains of a bainite/ferrite matrix. Allotriomorphic ferrite is evident throughout the top and middle of the cube. There is also evidence of coalesced bainite at the top of the cube which is similar to the observations by Keehan et al. [331]. They state that this novel form of bainite devlops at compositions where the bainite start (Bs) temperature and martensite start (Ms) temperature are within a close range of eachother. In 4140 steel, where the Bs (545°C) and the Ms (345°C) are not within a close range of eachother, it is possible that the complex instrinsic heating and cooling cycles could be the cause of the coalesced bainite. For example, upon cooling form austenite, the cooling curve could be significantly fast to avoid the bainite nose but start to cool more slowly into the end of the bainite region near the martensite start temperature.

Furthermore, the distinct CET boundary between the top half and bottom half of the cube is captured in the model which shows a distinct separation of phases. The general presence and relative amount of ferrite, bainite and pearlite predicted in the model is in good agreement with the experiment. However, due to the simplicity of the metallurgical framework, the difference between grain size is obviously not captured. SEM imaging was able to reveal more complexities than could be seen in the optical micrographs. The middle section shows the fine equiaxed region with sub 10 μm grains. This region shows tempered bainite with pearlite clusters scattered throughout, while the bottom section shows mainly tempered bainite with little evidence of pearlite seen above.

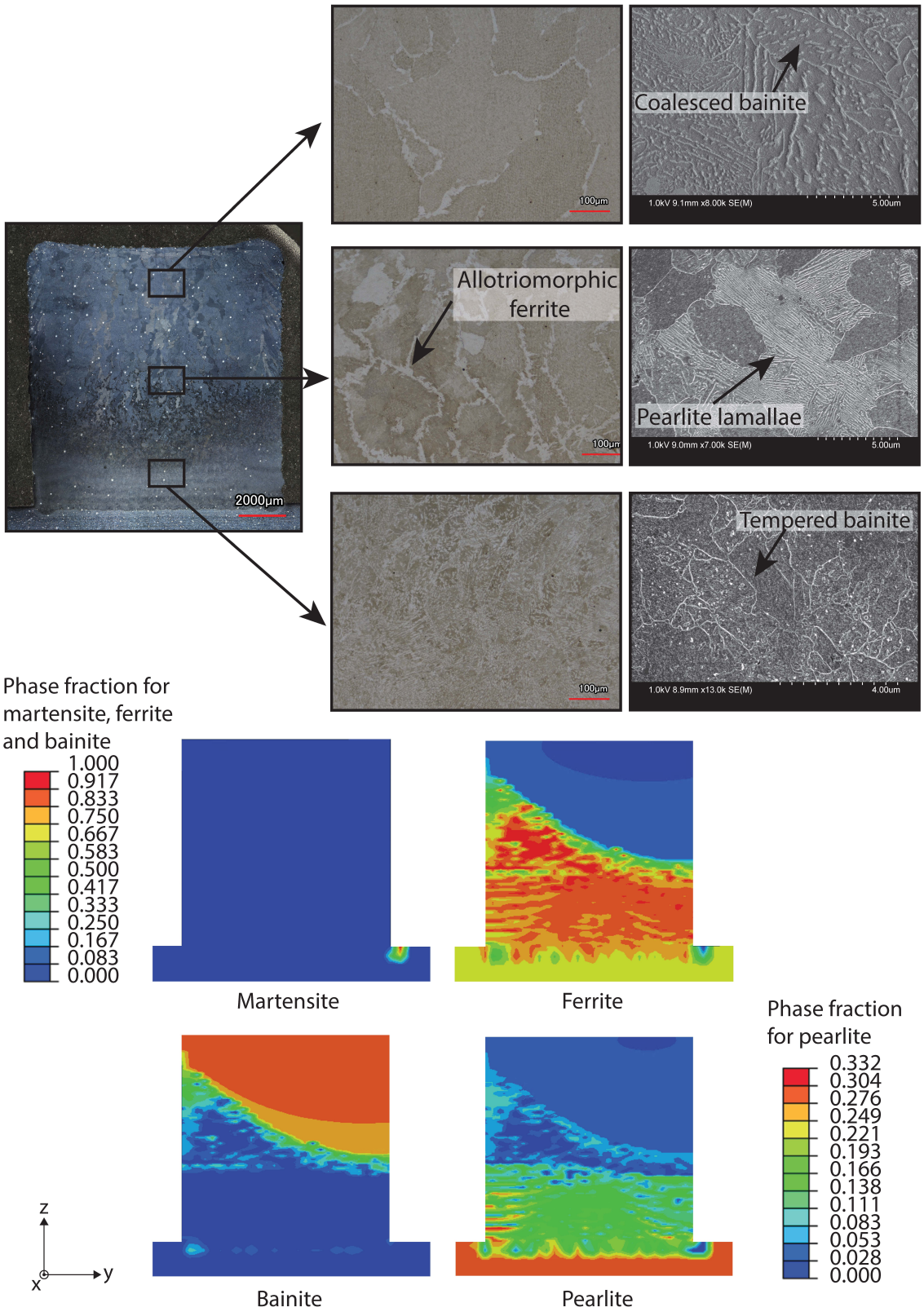

Figure 4.19: Experimental metallography analysis for case 4 on the top, middle and bottom sections. Simulated phase fractions along the middle cross-section is also compared with the observed microstructural constituents.

4.6.3 Mechanical analysis

Residual stress measurements were conducted through XRD analysis and the distortion measurements were recorded with a Keyence laser confocal microscope from the clamped end to the free end and compared with the model. Due to the large error in the thermal analysis for case 4, the mechanical results for case 4 were not conducted. Further development would be required in order to better approximate the temperature field before attempting to predict the residual stresses and substrate distortion. Figure 4.20 illustrates the simulated and experimental distortion profiles for cases 1-3.

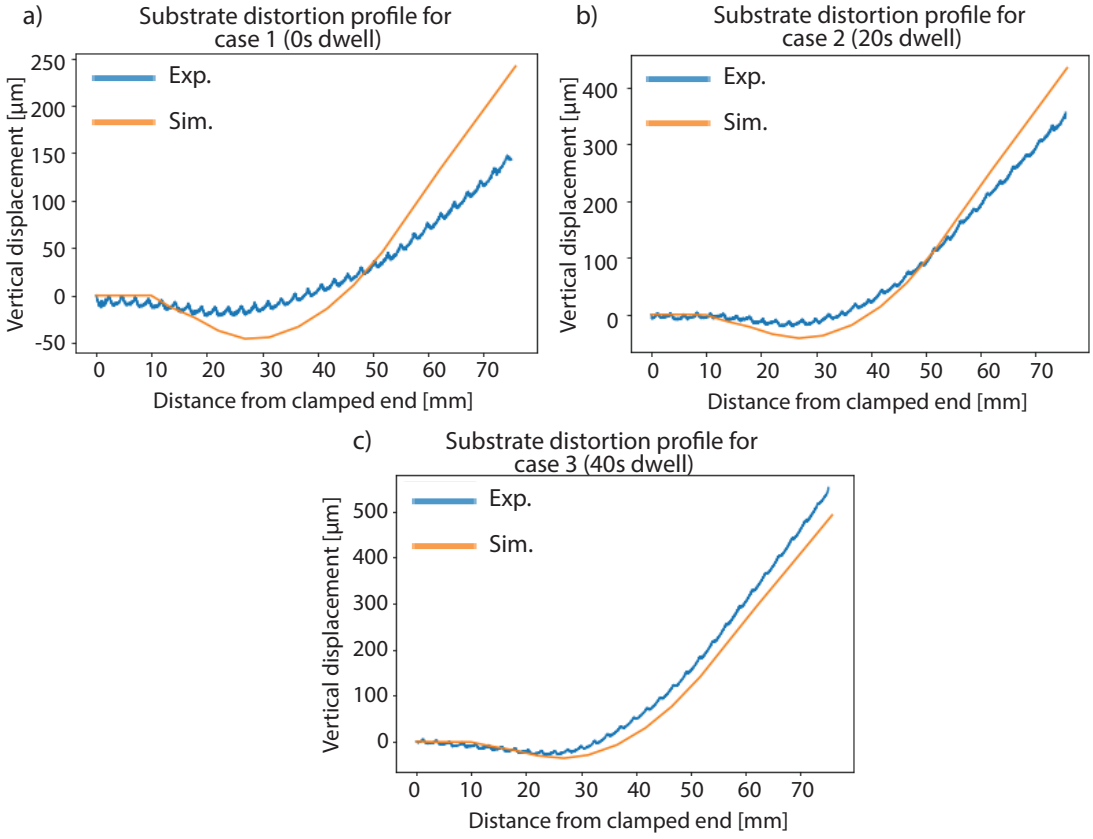

Figure 4.20: Post-build distortion profile from the clamped end to the free end of the AISI 4140 steel substrate used for a) case 1 b) case 2 and, c) case 3.

It can be seen that the distortion profile for case 1 shows a large deviation compared to the measured data. The simulated profile shows a larger negative displacement near the base and a larger positive displacement at the tip with a 60%

error. Furthermore, the simulated distortion curves for case 2 and 3 represent the experimental data very well with similar curvature and peak tip displacements presenting a 20% and 10.7% error from the experimental data, respectively. This trend clearly shows greater accuracy with a higher dwell time and consequently a lower maximum temperature encountered during printing.

Initially, this deviation was thought to arise from the steeper normalizing curve in the model compared to the experimental data. A constant ambient temperature of 27°C was set in the model whereas in reality it can increase quite significantly over the duration of the build and thus cause the part to cool slower after printing. However, a variable ambient temperature was tested to produce a similar normalizing curve to the experimental data for case 1. This was confirmed to have little effect on the resulting microstructure, residual stress and substrate distortion. Thus, the deviation in the substrate profile for the case 1 is likely caused by the material model not capturing the complex strain relief at temperatures below 815°C. As discussed earlier, as the integration point reaches 815°C, all prior work hardening is set to zero for that point. However, since the strain relief heat treatment for 4140 steel occurs at 540°C, it is likely that the substrate near the end of the build is experiencing some degree of strain relief as it reaches temperatures close to this point. Since the maximum temperature recorded by the thermocouple case 2 and 3 are much lower, little strain relief at this temperature is occurring and the material model is able to accurately predict the substrate distortion.

Furthermore, the residual stress measurements along the y-direction on the thinwalls were taken on the middle top surface and are plotted with the predicted stresses in Figure 4.21. A general trend of increasing stress is shown between the varying dwell times which is to be expected since the distortion displacement also increases with dwell time. The measured data shows the same residual stress for case 2 and 3, however the model shows higher stress in case 3 compared to case 2. It can be noted that in addition to the error associated with the measurements, a +/- 35 MPa uncertainty is also specified by the manufacturer. Thus, the simulated and measured values are in good agreement.

The stress contours from the simulation for case 1-3 are illustrated in Figure 4.22. Case 1 shows a relatively uniform stress-free profile within the thinwall with a slightly compressive center. Case 2 and 3 show a slightly tensile stress throughout

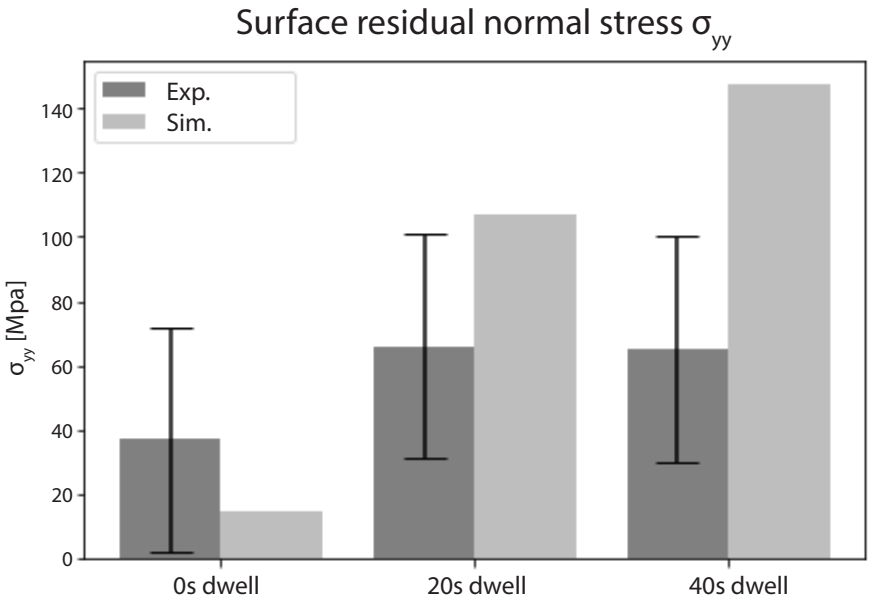

Figure 4.21: Measured and simulated normal residual stresses along the y-direction

the wall, however the meltpool boundaries outlined by ferrite in the metallurgical analysis show a compressive stress due to the softer phase being compressed by the expansion of martensite and bainite. The increasing tensile residual stress follows a similar pattern of increasing martensite prediction in the model. Since case 3 shows an over estimation of martensite throughout the build, a much larger tensile residual stress is also computed. However, for the experimental observations where a similar microstructure was observed in case 2 and 3, the same tensile residual stress was also measured between the two cases.

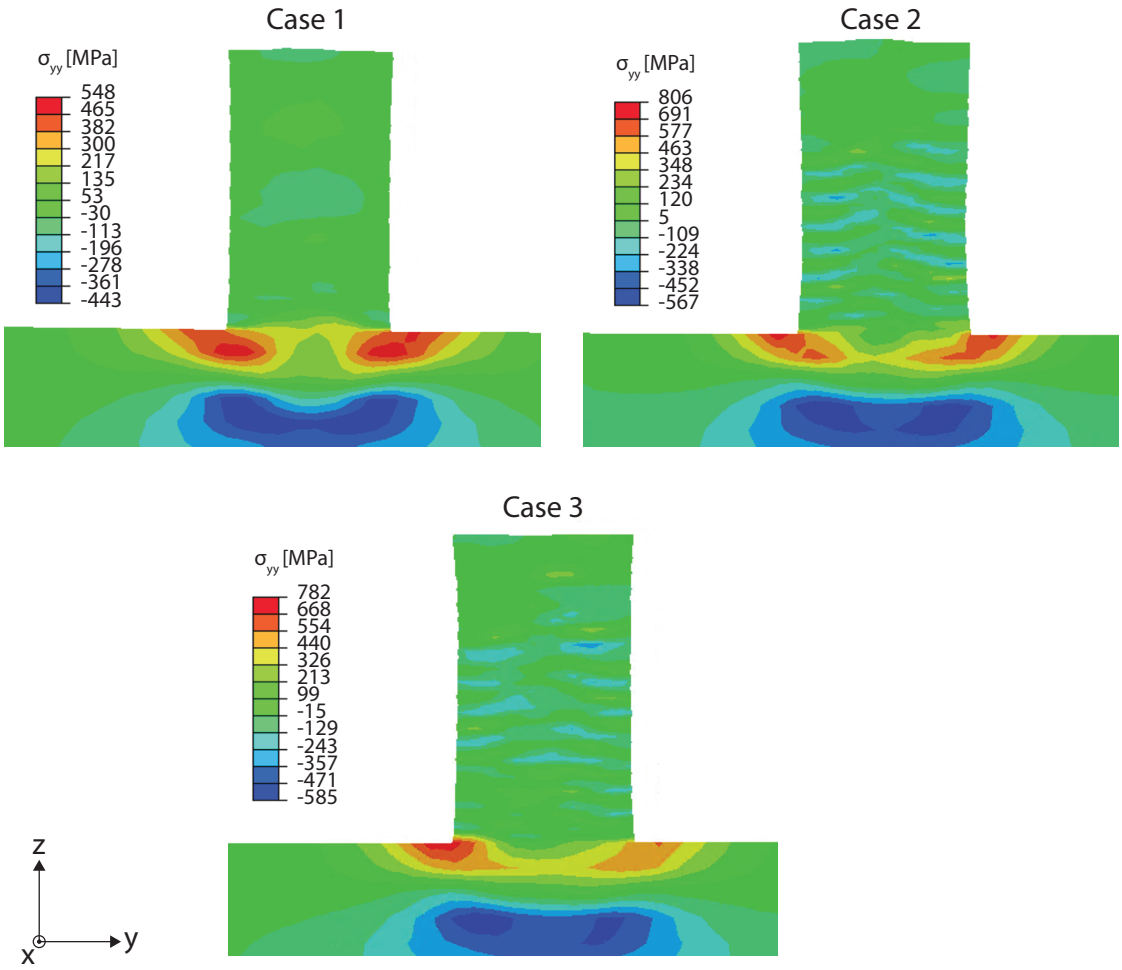

Figure 4.22: Simulated residual stress contours for thinwall cross-sections.

4.7 Conclusions

A TMM model of 42CrMo4 steel was developed for the DED process. Dwell times, laser power, geometry and scanning strategy was varied across four different cases to verify the fidelity of the model. The metallurgical phases were calculated in the heat transfer analysis and used to add their respective latent heats as well as dilational volume changes in the mechanical analysis. A common validation approach based on previous studies by Refs. [293] and [294] was implemented. The results from this study are summarized below.

- The largest error between the simulation and the thermocouple data for the thinwall cases was found the be 7.85% and 10.09% for the cube. The remainder of the thermocuple measurements for the thinwall cases presented errors between 3 and 4%.
- The observed microstructures generally agreed with the simulated phase fractions. A bainitic, ferritic and pearlitic microstructure was observed for the cases with no dwell while larger amounts of martensite and no evidence of pearlite were seen in cases with a longer dwell time.
- The substrate distortion for each thinwall case generally agreed with the measured values with the largest percent error being 60% in the case with no dwell while a 20% and 10% error for the tip deflection was determined for cases with increasing dwell time, respectively.
- The residual stresses were measured at the surface of the thinwall case. The case with no dwell had a measured value of 37 +/- 35 MPa and a simulated value of 15.2 MPa. The deviation in measured residual stress grew larger with increasing dwell time presenting measured and simulated values of 66 +/- 35 MPa and 107 MPa for the 20s dwell and 65 +/- 35 MPa and 147.5 MPa for the 40s dwell, respectively.

A more accurate forced and natural convection model needs to be developed to better encompass the conditions of this specific setup in order to model varying geometries and dwell times. It was evident than when using a convection model

measured for a thinwall on a cube, not enough heat was removed from the component during printing. Furthermore, the metallurgical framework does not capture the tempering of bainite, the decomposition of martensite below the eutectoid temperature or consider prior austenite grain size. Further development would be needed to consider carbon diffusion to better predict the microstructure and resulting effects of tempering. Lastly, contrast to the extremely fast cooling rates typically seen in DED processes, this study showed relatively slower cooling rates in cases with no dwell time due to the absence of martensite. Without any dwell time, the cantilevered substrate does not allow heat to be drawn away from the part as quickly as a larger substrate fixed to the trunnion. This causes the part to hold relatively high temperatures, prohibiting it from reaching the martensite start temperature before passing through the bainite nose on the TTT diagram. This perhaps is another process parameter that could be manipulated to alter the properties of the printed material and control the cooling rates. Further studies on this would be necessary.

4.8 Future work

A general relationship for the forced convection from the argon jets should be developed based on the general geometry of the printed component. Similar to the thinwall convection model modified from Ref. [294], the relationship would vary appropriately based on the bulk height, width and length. The same measurement method conducted by Ref. [294] could be ensued, however repeated on varying sizes of square prisms to develop this empirical model. Moreover, a CFD model could be developed to determine this relationship but would need to be validated with experimental data. Furthermore, the same method could be done with the varying ambient temperature. It is evident that the chamber temperature in case 1 was high enough to have a significant effect on the cooling curve after printing than compared to case 3. Several experiments could be conducted to determine a general trend in ambient temperature change as a function of build time and dwell time.

The pre-processing program developed for this model allows for the laser power and scanning speed to vary throughout the build depending on the pre-defined printing parameters. This allows the possibility to find optimal processing parameters in the model and apply them in reality. Further development of this model could

provide the capability to tune processing parameters before printing and optimize the residual stresses and microstructural. However, the acceleration and deceleration profiles of the trunnion and deposition head should be implemented in order accurately model the movements during printing. In this study, the traverse speed had to be adjusted to best match the speed profiles without any acceleration and deceleration. This error became quite apparent when the laser was moving across the build chamber between layers so the dwell time and traverse rate was tuned so the total build time was the same as the experiment. Thus, this would need to be implemented in order to make progress towards a model capable of predicting the residual stresses and microstructures of a printed component with minimal input.

Furthermore, the melt pool sensor has the capability to change the laser power based on the measured melt pool dimensions. Thus, at lower laser powers where spatter and incandescent vapour don't greatly affect the melt pool sensor measurements, the meltpool geometry could be manipulated through the processing parameters based on studies by [201,337]. Enhancing the metallurgical model to predict columnar or equiaxed grain growth could prove useful in determining the energy density require spatially throughout the build to achieve the desired properties [337,338].

Moreover, the laser power needs to be measured and compared with the nominal power since Heigel et al [294] demonstrated that the measured laser power was approximately 17% lower than the nominal power specified in the g-code. The laser melting efficiency also needs to be experimentally validated to further refine the model because in this study, it had to be calibrated to best match the experimental results. The metallurgical framework could be improved by using incubation times rather than constraining the nucleation of phases within cooling rates. This would allow for a smoother transition of phase growth and possibly provide a more accurate model. Additionally, it was observed that the prior austenite grain size was vastly different throughout the cases and even spatially throughout the component. This could be incorporated in the model the better predict the hardenability of steel depending on how long the steel was held above the A3 temperature.

Lastly, it would be useful to incorporate measured thermo-mechanical plasticity data from the printed alloy as it can differ from studies in the past which have determined this data from wrought 4140 steel components. Since AM components can exhibit anisotropic properties that may effect the reaction to the thermal load,

this significance on the mechanical analysis should also be determined. Tensile tests could be performed to determine the stress-strain curves for both the vertical and longitudinal axes and incorporated in the model for the specific processing parameters. For example, a study by Wang et al. [2] determined the mechanical properties of LPBF 4140 steel and found slight differences along the vertical and longitudinal axes. Although the yield strength and tensile strength along each axis were within 100 MPa from one another, the elongation was 13.8% and 12.3% along the longitudinal and vertical axes, respectively.

Chapter 5

Conclusion

This thesis provided a comprehensive literature review on metal additive manufacturing covering the various printing technologies such as DED, PBF and binder jetting. The melt pool physics and importance of processing parameters were also discussed while the most common defects in metal AM were presented. Following this, the current library of commercially available alloys were compared along side their wrought counterpart. Process optimization was then discussed and how the metal AM process can be manipulated in achieving specific properties while computer modelling using CFD, FEM and various microstructural modelling software was presented. Moreover, this paper discussed the main post-processing methods to reduce surface roughness, pores and improve the mechanical properties. Gaps in the literature were also identified and recommendations were made as to which areas need development in order to fully exploit the advantages of metal AM.

In chapter 3, 4140 steel manufactured by the Royal Canadian Navy was investigated through various microscopy methods in order to better understand the printed alloys' defects and characteristics. A mainly martensitic and bainitic microstructure was observed for the printed sample while a fine equiaxed pearlitic grain structure seen in the wrought counterpart. High resolution TEM imaging revealed nanoscale features such as grain boundaries and mechanical twins. Furthermore, lattice images were analyzed through a FFT to display its diffraction pattern where it was then indexed to determine its zone axis. Lastly, systematic row spacing was measured and compared with theoretical data to determine the miller indices and interplanar spacing. Lattice strain within the material was evident since the measured data was smaller than the calculated values.

In chapter 4, an FE model was developed for the DED process and was validated through a number of experiments conducted at Dalhousie University. Thermocouples were used to validate the thermal analysis and the largest error across all

cases was 10.09%. The simulated microstructures mostly agreed with the observations across all cases, however the metallurgical framework over predicted the amount of martensite as the dwell time increased. For the mechanical analysis, both substrate distortion and residual stresses were measured. The tip deflection on the case with no dwell presented a 60% error using a constant ambient temperature in the model whereas a 20% and 10% error for the tip deflection was determined for cases with increasing dwell time, respectively. The residual stresses were also measured at the surface of the thinwall case. The overestimation of martensite in the case with the longest dwell time consequently caused an over prediction of tensile residual stress on the surface while the cases with lower dwell times were accurately predicted within the measured uncertainties of +/- 35 Mpa.

The numerical and experimental study in this work provided insight into the physics underlying the DED process, however further development of the FE model could provide significant progress towards on-demand part validation and property manipulation. More in-depth analysis on 4140 steel dislocation networks, alloy segregation and compositional gradients compared to its wrought counterpart could help better understand the effects that the AM process has on the foundation of the printed alloy which dictate its mechanical properties.

Appendix A

Metallurgical data for AISI 4140 steel

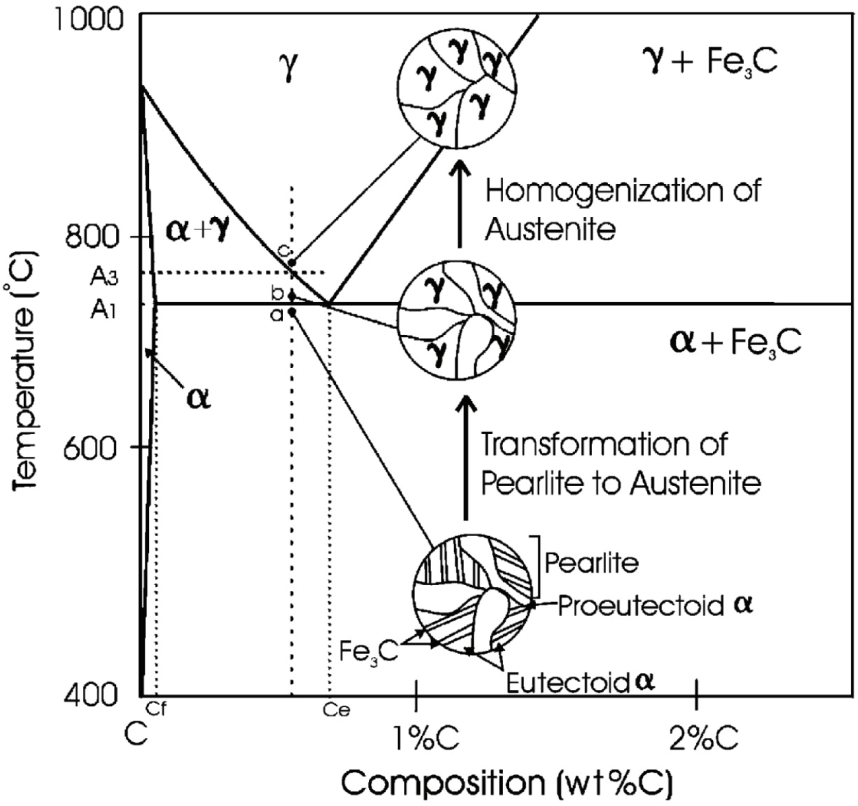

Figure A.1: Fe-C equilibrium phase diagram highlighting microstructural changes and the A1 and A3 points for a 0.4%C hypoeutectoid steel taken from [304, 339] with permission.

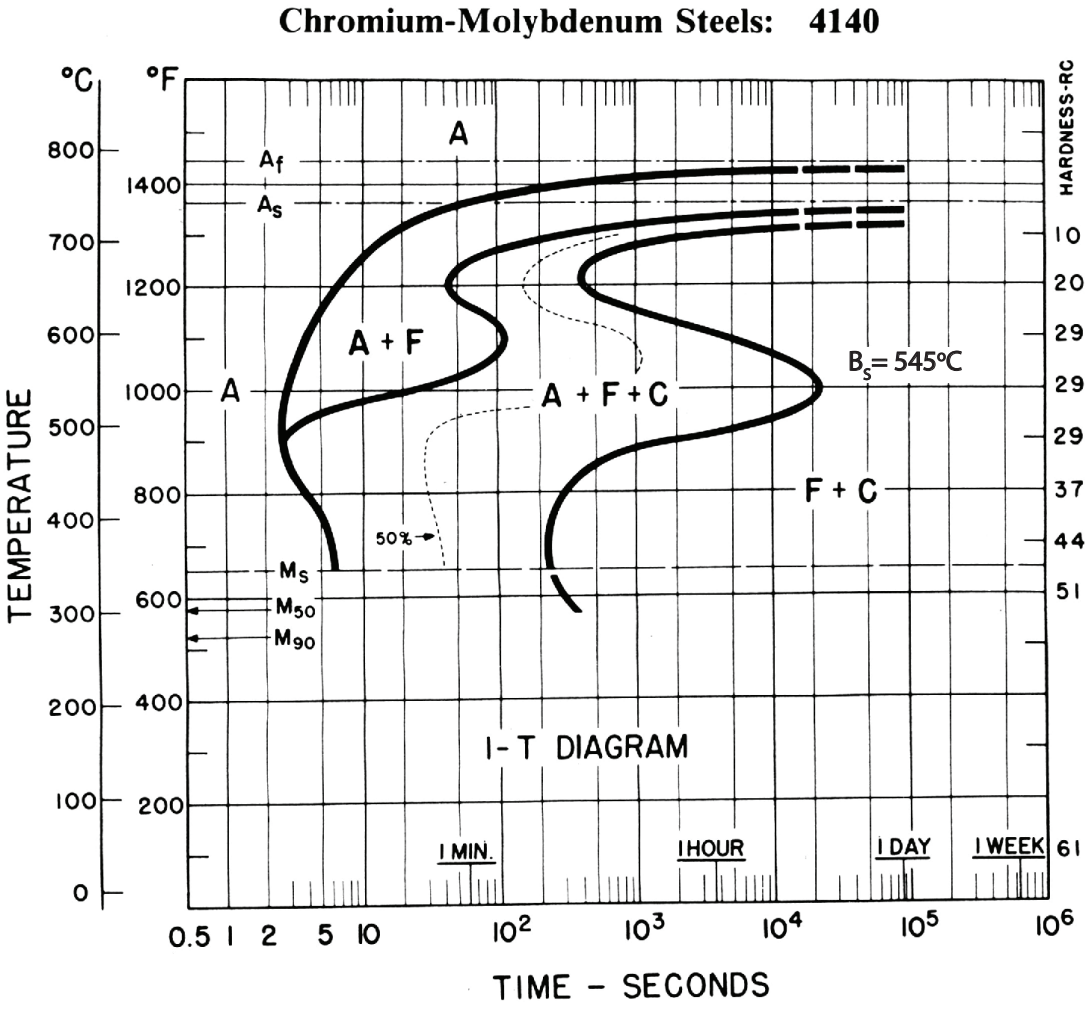

Figure A.2: Time-temperature-transformation diagram for 4140 steel taken from [304, 319] with permission.

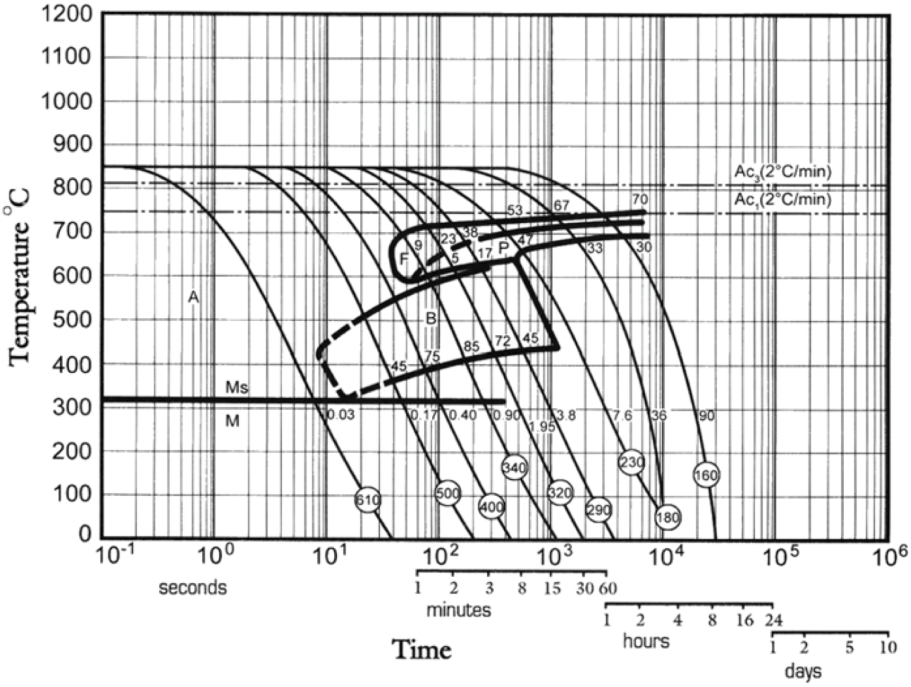

Figure A.3: Continuous-cooling-transformation diagram for 4140 steel indicating the percentages of each phase formed at a variety of cooling rates taken from [302, 323] with permission.

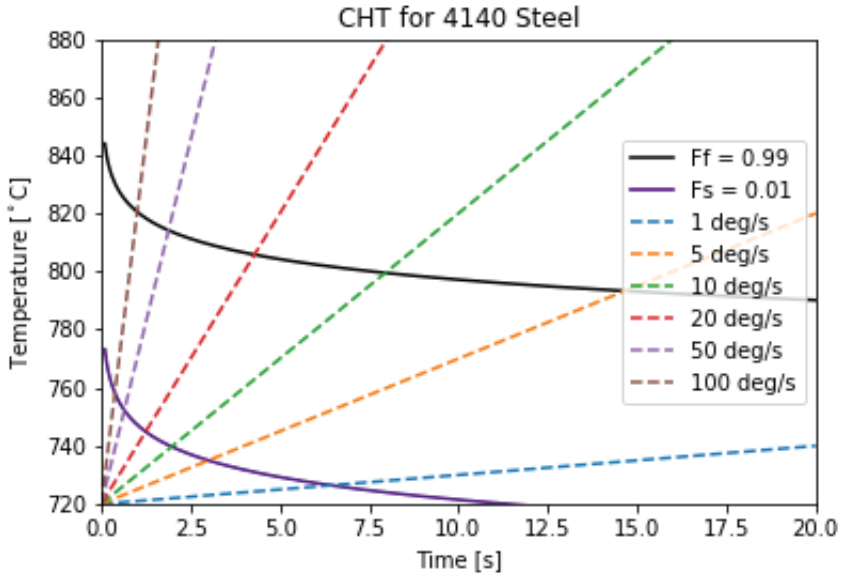

Figure A.4: Continuous heating transformation diagram for 4140 steel for various heating rates modified with permission from [340].

Appendix B

Johnson–Mehl–Avrami–Kolmogorov diffusional transformation model data

Figure B.1 shows the various isothermal Avrami curves for the determined JMAK coefficients, k and n.

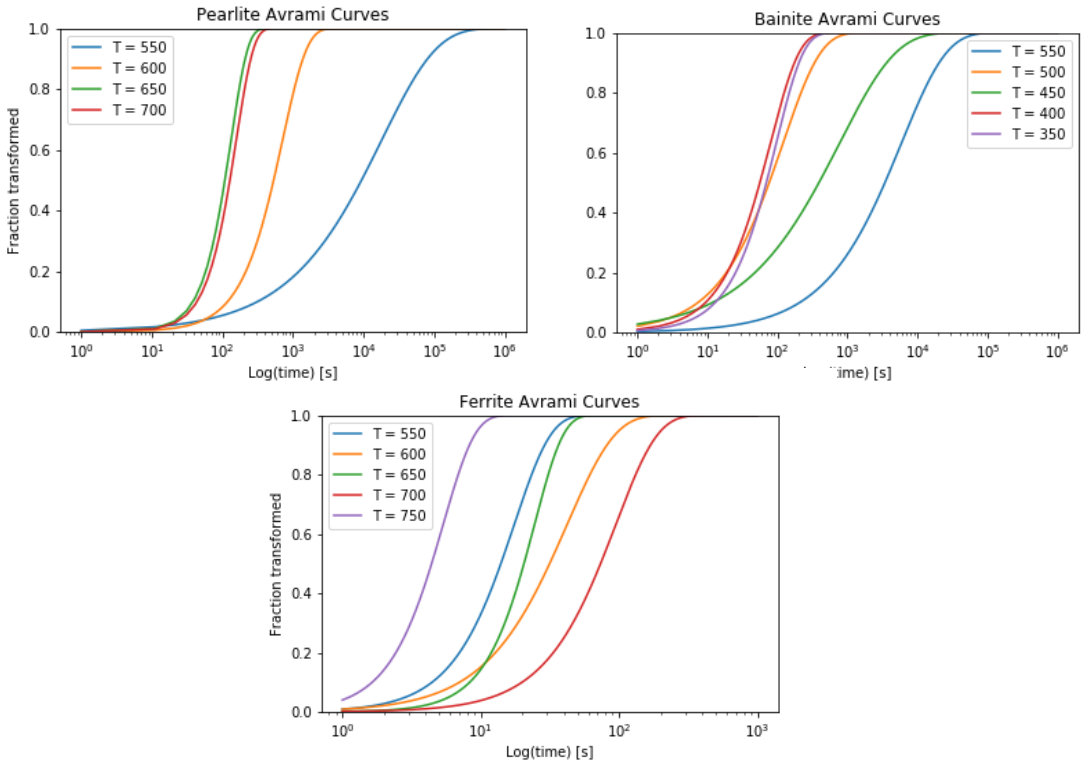

Figure B.1: Avrami curves calculated for each temperature based on determined k and n coefficients for 4140 steel

Since the JMAK equation is only valid under isothermal conditions, a modified implementation of the classic additivity rule was used to apply this equation to continuous cooling. The application of this rule deconstructs the continuous cooling

curve into a number of discrete isothermal steps. The amount of phase transformed at each time step is determined using the JMAK equation at each incremental temperature until the transformation finishes. The relationship at the next temperature T^{j+1} can be expressed as $X_i(t,T^j)$. However, a virtual time, θ_j in Equation B.1 is necessary to translate the relationship at the current temperature with the already transformed fraction at the previous time step to the newly transformed phases at the current time step such that $X_i^j = X_i(\theta_j,\ T^{j+1})$. Now the ith phase fraction of the next time step and temperature can be calculated as $X_i^{j+1} = X_i^j(\theta_j + \Delta t^j,\ T^{j+1})$ [302, 341–343]. Figure B.2 illustrates the additivity rule incorporated into the JMAK equations so it can be applied to continuous cooling.

$$\theta_j = \left[-\frac{\ln\left(1 - X_i^{j-1}\right)}{k} \right]^{1/n} \tag{B.1}$$

where θ_j is the virtual time for the current increment, j, X_i^{j-1} is the known calculated phase fraction stored from the previous increment, while k and n are the Avrami rate constants determined from the TTT diagram.

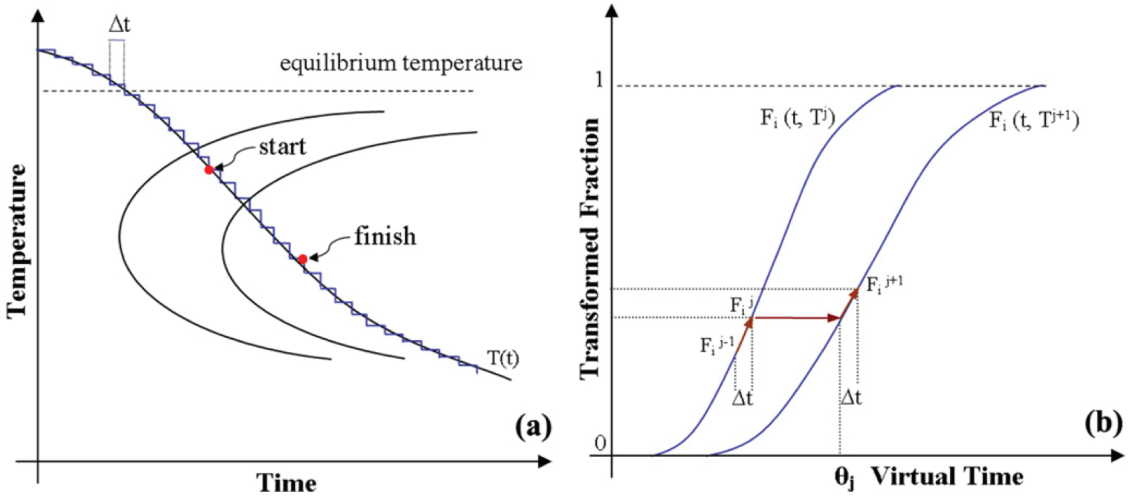

Figure B.2: Additivity rule used to transform the isothermal JMAK equations to an iso-kinetic formulation. Taken from [302] with permission.

Appendix C

Bead size determination

The influence of laser power and scanning speed on the bead size were characterized by conducting a number of tests at varying laser powers from 360 - 600W and scanning speeds from 4.2 - 10 mm/s. Correct knowledge of bead dimensions is important for the model to best capture the printing conditions. 20 separate single track tests were measured with a Keyence laser confocal microscope to generate a relationship between the laser power and scanning speed which yielded a corresponding bead width. The contour plot illustrating this relationship is shown in Figure C.1. For 600W and 8mm/s the corresponding bead size is determined to be 1.17mm while 500W at the same scanning speed yields a bead width of 1.07 mm. Thus for the simulations, a bead size of 1.2mm and 1.1 mm is used for 600W and 500W, respectively. Similarly, the influence of bead height was also investigated but it was found that scanning speed and powder feed rate were the main contributors to its variance. Thus for both 500W and 600W at 8mm/s, the bead height was measured to be approximately 0.3mm at a powder feed rate of 4.2 g/min. The relationship between laser power and scanning speed is shown below in Equation C.1.

$$b_W = -535 + 5.96P - 29.68F_s - 0.00454P^2 \tag{C.1}$$

where b_W is the bead width in µm, P is the laser power in Watts and F_s is the feed rate or scanning speed in mm/s.

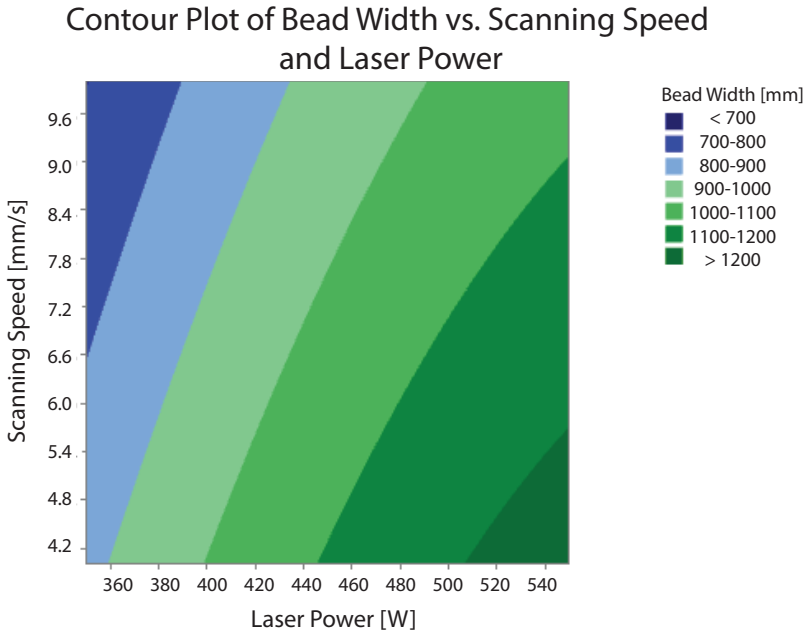

Figure C.1: Contour plot of bead width with respect to laser power and scanning speed. This relationship was determined empirically for the model so the element activation distance could be set within the model.

Bibliography

[1] Shaun Cooke, Keivan Ahmadi, Stephanie Willerth, and Rodney Herring. Metal additive manufacturing: Technology, metallurgy and modelling. *Journal of Manufacturing Processes*, 57:978–1003, 2020.

[2] Wesley Wang and Shawn Kelly. A metallurgical evaluation of the powder-bed laser additive manufactured 4140 steel material. *Jom*, 68(3):869–875, 2016.

[3] Christopher Bayley, Michael Kopac, et al. The implications of additive manufacturing on canadian armed forces operational functions. 2018.

[4] Lawrence E. Murr, Edwin Martinez, Krista N. Amato, Sara M. Gaytan, Jennifer Hernandez, Diana A. Ramirez, Patrick W. Shindo, Frank Medina, and Ryan B. Wicker. Fabrication of metal and alloy components by additive manufacturing: Examples of 3d materials science. *Journal of Materials Research and Technology*, 1(1):42–54, apr 2012.

[5] William E. Frazier. Metal additive manufacturing: A review. *Journal of Materials Engineering and Performance*, 23(6):1917–1928, apr 2014.

[6] Chunze Yan, Liang Hao, Ahmed Hussein, Simon Lawrence Bubb, Philippe Young, and David Raymont. Evaluation of light-weight alsi10mg periodic cellular lattice structures fabricated via direct metal laser sintering. *Journal of Materials Processing Technology*, 214(4):856–864, 2014.

[7] T. Mukherjee, J. S. Zuback, A. De, and T. DebRoy. Printability of alloys for additive manufacturing. *Scientific Reports*, 6(1), jan 2016.

[8] Tuan D. Ngo, Alireza Kashani, Gabriele Imbalzano, Kate T.Q. Nguyen, and David Hui. Additive manufacturing (3d printing): A review of materials, methods, applications and challenges. *Composites Part B: Engineering*, 143:172–196, jun 2018.

[9] Fuyao Yan, Wei Xiong, and Eric Faierson. Grain structure control of additively manufactured metallic materials. *Materials*, 10(11):1260, nov 2017.

[10] Bi Zhang, Yongtao Li, and Qian Bai. Defect formation mechanisms in selective laser melting: A review. *Chinese Journal of Mechanical Engineering*, 30(6):1476–1476, aug 2017.

[11] John H. Martin, Brennan D. Yahata, Jacob M. Hundley, Justin A. Mayer, Tobias A. Schaedler, and Tresa M. Pollock. 3d printing of high-strength aluminium alloys. *Nature*, 549(7672):365–369, sep 2017.

[12] R. Huff J. Kowen I. Campbell, O. Diegel and T. Wohlers. *Wohlers Report 2019*. Mary Ann Liebert Inc, 2019.

[13] W. J. Sames, F. A. List, S. Pannala, R. R. Dehoff, and S. S. Babu. The metallurgy and processing science of metal additive manufacturing. *International Materials Reviews*, 61(5):315–360, mar 2016.

[14] A. Townsend, N. Senin, L. Blunt, R.K. Leach, and J.S. Taylor. Surface texture metrology for metal additive manufacturing: a review. *Precision Engineering*, 46:34–47, oct 2016.

[15] Chong Teng, Deepankar Pal, Haijun Gong, Kai Zeng, Kevin Briggs, Nachiket Patil, and Brent Stucker. A review of defect modeling in laser material processing. *Additive Manufacturing*, 14:137–147, mar 2017.

[16] Gustavo Tapia and Alaa Elwany. A review on process monitoring and control in metal-based additive manufacturing. *Journal of Manufacturing Science and Engineering*, 136(6), oct 2014.

[17] Sarah K. Everton, Matthias Hirsch, Petros Stravroulakis, Richard K. Leach, and Adam T. Clare. Review of in-situ process monitoring and in-situ metrology for metal additive manufacturing. *Materials & Design*, 95:431–445, apr 2016.

[18] E Herderick. Additive manufacturing of metals: A review. *Materials science and technology*, 1413, 2011.

[19] David Bourell, Jean Pierre Kruth, Ming Leu, Gideon Levy, David Rosen, Allison M. Beese, and Adam Clare. Materials for additive manufacturing. *CIRP Annals*, 66(2):659–681, 2017.

[20] L.E. Murr. Metallurgy of additive manufacturing: Examples from electron beam melting. *Additive Manufacturing*, 5:40–53, jan 2015.

[21] Mohsen Seifi, Ayman Salem, Jack Beuth, Ola Harrysson, and John J. Lewandowski. Overview of materials qualification needs for metal additive manufacturing. *JOM*, 68(3):747–764, jan 2016.

[22] Bo Song, Xiao Zhao, Shuai Li, Changjun Han, Qingsong Wei, Shifeng Wen, Jie Liu, and Yusheng Shi. Differences in microstructure and properties between selective laser melting and traditional manufacturing for fabrication of metal parts: A review. *Frontiers of Mechanical Engineering*, 10(2):111–125, jun 2015.

[23] John J. Lewandowski and Mohsen Seifi. Metal additive manufacturing: A review of mechanical properties. *Annual Review of Materials Research*, 46(1):151–186, jul 2016.

[24] Y. Kok, X.P. Tan, P. Wang, M.L.S. Nai, N.H. Loh, E. Liu, and S.B. Tor. Anisotropy and heterogeneity of microstructure and mechanical properties in metal additive manufacturing: A critical review. *Materials & Design*, 139:565–586, feb 2018.

[25] Allison M. Beese and Beth E. Carroll. Review of mechanical properties of ti-6al-4v made by laser-based additive manufacturing using powder feedstock. *JOM*, 68(3):724–734, dec 2015.

[26] J. A. Slotwinski, E. J. Garboczi, P. E. Stutzman, C. F. Ferraris, S. S. Watson, and M. A. Peltz. Characterization of metal powders used for additive manufacturing. *Journal of Research of the National Institute of Standards and Technology*, 119:460, oct 2014.

[27] A. Strondl, O. Lyckfeldt, H. Brodin, and U. Ackelid. Characterization and control of powder properties for additive manufacturing. *JOM*, 67(3):549–554, jan 2015.

[28] Sunpreet Singh, Seeram Ramakrishna, and Rupinder Singh. Material issues in additive manufacturing: A review. *Journal of Manufacturing Processes*, 25:185–200, jan 2017.

[29] Zhu Jie, Luo Hao, Weng Ting, Li Zhi, Zong Wei, and Zeng Keli. Characterization of fine metal powders produced by hybrid by water–gas atomization for metal injection molding. In *Frontiers in Materials Processing, Applications, Research and Technology*, pages 391–397. Springer Singapore, nov 2017.

[30] Christopher T Schade, Thomas F Murphy, and Chris Walton. Development of atomized powders for additive manufacturing. In *Powder Metallurgy Word Congress, Accessed on 2nd July*, 2014.

[31] Baolong Zheng, Yaojun Lin, Yizhang Zhou, and Enrique J Lavernia. Gas atomization of amorphous aluminum powder: Part ii. experimental investigation. *Metallurgical and Materials Transactions B*, 40(6):995, 2009.

[32] Zhonghui Jiao, Donghui Li1 Ali Asgarian, Saikat Chatterjee, Bruno Girard, Vladimir Paserin, Francois Lavallee, and Kinnor Chattopadhyay. Influence of apex angle and nozzle design on energy and momentum transfer during the water atomization process. *POWDERMET, Las Vegas, USA*, 2016.

[33] Mohammad Ansari, Alireza Mohamadizadeh, Yuze Huang, Vladimir Paserin, and Ehsan Toyserkani. Laser directed energy deposition of water-atomized iron powder: Process optimization and microstructure of single-tracks. *Optics & Laser Technology*, 112:485–493, apr 2019.

[34] A.B. Spierings, N. Herres, and G. Levy. Influence of the particle size distribution on surface quality and mechanical properties in AM steel parts. *Rapid Prototyping Journal*, 17(3):195–202, apr 2011.

[35] Simon Hoeges, Christopher T Schade, and Robert Causton. Development of a maraging steel powder for additive manufacturing. In *Proceedings of the MPIF World Congress on Powder Metallurgy and Particulate Materials, San Diego, CA, USA*, pages 17–28, 2015.

[36] Haniyeh Fayazfar, Mehrnaz Salarian, Allan Rogalsky, Dyuti Sarker, Paola Russo, Vlad Paserin, and Ehsan Toyserkani. A critical review of powder-based additive manufacturing of ferrous alloys: Process parameters, microstructure and mechanical properties. *Materials & Design*, 144:98–128, apr 2018.

[37] Pavan Suri, Ryan P Koseski, and Randall M German. Microstructural evolution of injection molded gas-and water-atomized 316l stainless steel powder during sintering. *Materials Science and Engineering: A*, 402(1-2):341–348, 2005.

[38] Thomas Duda and L. Venkat Raghavan. 3d metal printing technology. *IFAC-PapersOnLine*, 49(29):103–110, 2016.

[39] Lawrence E. Murr, Sara M. Gaytan, Diana A. Ramirez, Edwin Martinez, Jennifer Hernandez, Krista N. Amato, Patrick W. Shindo, Francisco R. Medina, and Ryan B. Wicker. Metal fabrication by additive manufacturing using laser and electron beam melting technologies. *Journal of Materials Science & Technology*, 28(1):1–14, jan 2012.

[40] Loong-Ee Loh, Chee-Kai Chua, Wai-Yee Yeong, Jie Song, Mahta Mapar, Swee-Leong Sing, Zhong-Hong Liu, and Dan-Qing Zhang. Numerical investigation and an effective modelling on the selective laser melting (SLM) process with aluminium alloy 6061. *International Journal of Heat and Mass Transfer*, 80:288–300, jan 2015.

[41] Federico Mazzucato, Simona Tusacciu, Manuel Lai, Sara Biamino, Mariangela Lombardi, and Anna Valente. Monitoring approach to evaluate the performances of a new deposition nozzle solution for DED systems. *Technologies*, 5(2):29, may 2017.

[42] Paul A. Hooper. Melt pool temperature and cooling rates in laser powder bed fusion. *Additive Manufacturing*, 22:548–559, aug 2018.

[43] Manisha Bisht, Nachiketa Ray, Frederik Verbist, and Sam Coeck. Correlation of selective laser melting-melt pool events with the tensile properties of ti-6al-4v ELI processed by laser powder bed fusion. *Additive Manufacturing*, 22:302–306, aug 2018.

[44] Eyvind Engblom. Effect of oxygen concentration in build chamber during laser metal deposition of ti-64 wire, 2018.

[45] Bey Vrancken, Lore Thijs, Jean-Pierre Kruth, and Jan Van Humbeeck. Heat treatment of ti6al4v produced by selective laser melting: Microstructure and mechanical properties. *Journal of Alloys and Compounds*, 541:177–185, nov 2012.

[46] Prashanth Konda Gokuldoss, Sri Kolla, and Jürgen Eckert. Additive manufacturing processes: Selective laser melting, electron beam melting and binder jetting—selection guidelines. *Materials*, 10(6):672, jun 2017.

[47] Evan Wheat, Mihaela Vlasea, James Hinebaugh, and Craig Metcalfe. Sinter structure analysis of titanium structures fabricated via binder jetting additive manufacturing. *Materials & Design*, 156:167–183, 2018.

[48] Xin Xu, Simon Meteyer, Nicolas Perry, and Yaoyao Fiona Zhao. Energy consumption model of binder-jetting additive manufacturing processes. *International Journal of Production Research*, 53(23):7005–7015, jul 2014.

[49] Peeyush Nandwana, Amy M Elliott, Derek Siddel, Abbey Merriman, William H Peter, and Sudarsanam S Babu. Powder bed binder jet 3d printing of inconel 718: Densification, microstructural evolution and challenges. *Current Opinion in Solid State and Materials Science*, 21(4):207–218, 2017.

[50] Amir Mostafaei, Erica L. Stevens, Eamonn T. Hughes, Shannon D. Biery, Colleen Hilla, and Markus Chmielus. Powder bed binder jet printed alloy 625: Densification, microstructure and mechanical properties. *Materials & Design*, 108:126–135, oct 2016.

[51] Truong Do, Patrick Kwon, and Chang Seop Shin. Process development toward full-density stainless steel parts with binder jetting printing. *International Journal of Machine Tools and Manufacture*, 121:50–60, 2017.

[52] Yun Bai and Christopher B Williams. An exploration of binder jetting of copper. *Rapid Prototyping Journal*, 2015.

[53] Li Sun, Yong-Ha Kim, Dave Kim, and Patrick Kwon. Densification and properties of 420 stainless steel produced by three-dimensional printing with addition of si3n4 powder. *Journal of manufacturing science and engineering*, 131(6), 2009.

[54] Yun Bai, Grady Wagner, and Christopher B Williams. Effect of particle size distribution on powder packing and sintering in binder jetting additive manufacturing of metals. *Journal of Manufacturing Science and Engineering*, 139(8), 2017.

[55] Biagio Palumbo, Francesco Del Re, Massimo Martorelli, Antonio Lanzotti, and Pasquale Corrado. Tensile properties characterization of alsi10mg parts produced by direct metal laser sintering via nested effects modeling. *Materials*, 10(2):144, 2017.

[56] E.b.m. arcam, welcome to manufaturing unbound, education 40150, 2017.

[57] Wirefeed additive manufacturing vs. powder methods — sciaky, 2020.

[58] Ting Qi, Haihong Zhu, Hu Zhang, Jie Yin, Linda Ke, and Xiaoyan Zeng. Selective laser melting of al7050 powder: Melting mode transition and comparison of the characteristics between the keyhole and conduction mode. *Materials & Design*, 135:257–266, dec 2017.

[59] R Fabbro. Melt pool and keyhole behaviour analysis for deep penetration laser welding. *Journal of Physics D: Applied Physics*, 43(44):445501, oct 2010.

[60] Jie Yin, LiangLiang Yang, Xu Yang, Haihong Zhu, Dengzhi Wang, Linda Ke, Zemin Wang, Guoqing Wang, and Xiaoyan Zeng. High-power laser-matter interaction during laser powder bed fusion. *Additive Manufacturing*, 29:100778, oct 2019.

[61] Amir Reza Ansari Dezfoli, Weng-Sing Hwang, Wei-Chin Huang, and Tsung-Wen Tsai. Determination and controlling of grain structure of metals after laser incidence: Theoretical approach. *Scientific Reports*, 7(1), jan 2017.

[62] R. Fabbro and K. Chouf. Keyhole modeling during laser welding. *Journal of Applied Physics*, 87(9):4075–4083, may 2000.

[63] A Kaplan. A model of deep penetration laser welding based on calculation of the keyhole profile. *Journal of Physics D: Applied Physics*, 27(9):1805–1814, sep 1994.

[64] Ville-Pekka Matilainen, Heidi Piili, Antti Salminen, and Olli Nyrhilä. Preliminary investigation of keyhole phenomena during single layer fabrication in laser additive manufacturing of stainless steel. *Physics Procedia*, 78:377–387, 2015.

[65] Chunlei Qiu, Chinnapat Panwisawas, Mark Ward, Hector C. Basoalto, Jeffery W. Brooks, and Moataz M. Attallah. On the role of melt flow into the surface structure and porosity development during selective laser melting. *Acta Materialia*, 96:72–79, sep 2015.

[66] Saad A. Khairallah, Andrew T. Anderson, Alexander Rubenchik, and Wayne E. King. Laser powder-bed fusion additive manufacturing: Physics of complex melt

flow and formation mechanisms of pores, spatter, and denudation zones. *Acta Materialia*, 108:36–45, apr 2016.

[67] Manyalibo J. Matthews, Gabe Guss, Saad A. Khairallah, Alexander M. Rubenchik, Philip J. Depond, and Wayne E. King. Denudation of metal powder layers in laser powder bed fusion processes. *Acta Materialia*, 114:33–42, aug 2016.

[68] Behzad Fotovvati, Steven F. Wayne, Gladius Lewis, and Ebrahim Asadi. A review on melt-pool characteristics in laser welding of metals. *Advances in Materials Science and Engineering*, 2018:1–18, 2018.

[69] V. Gunenthiram, P. Peyre, M. Schneider, M. Dal, F. Coste, I. Koutiri, and R. Fabbro. Experimental analysis of spatter generation and melt-pool behavior during the powder bed laser beam melting process. *Journal of Materials Processing Technology*, 251:376–386, jan 2018.

[70] Shichun Li, Genyu Chen, Seiji Katayama, and Yi Zhang. Relationship between spatter formation and dynamic molten pool during high-power deep-penetration laser welding. *Applied Surface Science*, 303:481–488, jun 2014.

[71] Dongsheng Wu, Xueming Hua, Fang Li, and Lijin Huang. Understanding of spatter formation in fiber laser welding of 5083 aluminum alloy. *International Journal of Heat and Mass Transfer*, 113:730–740, oct 2017.

[72] Yang Liu, Yongqiang Yang, Shuzhen Mai, Di Wang, and Changhui Song. Investigation into spatter behavior during selective laser melting of AISI 316l stainless steel powder. *Materials & Design*, 87:797–806, dec 2015.

[73] Glenn E. Bean, David B. Witkin, Tait D. McLouth, Dhruv N. Patel, and Rafael J. Zaldivar. Effect of laser focus shift on surface quality and density of inconel 718 parts produced via selective laser melting. *Additive Manufacturing*, 22:207–215, aug 2018.

[74] M Saunders. X marks the spot-find ideal process parameters for your metal am parts. *White papers collection–Renishaw plc*, 2017.

[75] Ahmed H Maamoun, Yi F Xue, Mohamed A Elbestawi, and Stephen C Veldhuis. Effect of selective laser melting process parameters on the quality of al

alloy parts: Powder characterization, density, surface roughness, and dimensional accuracy. *Materials*, 11(12):2343, 2018.

[76] Beth E Carroll, Todd A Palmer, and Allison M Beese. Anisotropic tensile behavior of ti–6al–4v components fabricated with directed energy deposition additive manufacturing. *Acta Materialia*, 87:309–320, 2015.

[77] Shunyu Liu and Yung C Shin. Additive manufacturing of ti6al4v alloy: A review. *Materials & Design*, 164:107552, 2019.

[78] Haijun Gong, Khalid Rafi, Hengfeng Gu, Thomas Starr, and Brent Stucker. Analysis of defect generation in ti–6al–4v parts made using powder bed fusion additive manufacturing processes. *Additive Manufacturing*, 1-4:87–98, oct 2014.

[79] Chunlei Qiu, Nicholas J.E. Adkins, and Moataz M. Attallah. Microstructure and tensile properties of selectively laser-melted and of HIPed laser-melted ti–6al–4v. *Materials Science and Engineering: A*, 578:230–239, aug 2013.

[80] Karina Puebla, Lawrence E. Murr, Sara M. Gaytan, Edwin Martinez, Francisco Medina, and Ryan B. Wicker. Effect of melt scan rate on microstructure and macrostructure for electron beam melting of ti-6al-4v. *Materials Sciences and Applications*, 03(05):259–264, 2012.

[81] Jean-Pierre Kruth, Mohsen Badrossamay, Evren Yasa, Jan Deckers, Lore Thijs, and Jan Van Humbeeck. Part and material properties in selective laser melting of metals. In *Proceedings of the 16th international symposium on electromachining*, pages 1–12, 2010.

[82] J.P. Kruth, L. Froyen, J. Van Vaerenbergh, P. Mercelis, M. Rombouts, and B. Lauwers. Selective laser melting of iron-based powder. *Journal of Materials Processing Technology*, 149(1-3):616–622, jun 2004.

[83] S Tammas-Williams, H Zhao, Fabien Léonard, F Derguti, I Todd, and PB Prangnell. Xct analysis of the influence of melt strategies on defect population in ti–6al–4v components manufactured by selective electron beam melting. *Materials Characterization*, 102:47–61, 2015.

[84] Michael F Zäh and S Lutzmann. Modelling and simulation of electron beam melting. *Production Engineering*, 4(1):15–23, 2010.

[85] Amanda S Wu, Donald W Brown, Mukul Kumar, Gilbert F Gallegos, and Wayne E King. An experimental investigation into additive manufacturing-induced residual stresses in 316l stainless steel. *Metallurgical and Materials Transactions A*, 45(13):6260–6270, 2014.

[86] Amrita Basak and Suman Das. Epitaxy and microstructure evolution in metal additive manufacturing. *Annual Review of Materials Research*, 46(1):125–149, jul 2016.

[87] Saleem Hashmi. *Comprehensive materials finishing*. Elsevier, 2016.

[88] AM Bauristhene, Kalenda Mutombo, and Waldo E Stumpf. Alpha case formation mechanism in ti-6al-4v alloy investment castings using yfsz shell moulds. *Journal of the Southern African Institute of Mining and Metallurgy*, 113(4):357–361, 2013.

[89] I Weiss and SL Semiatin. Thermomechanical processing of alpha titanium alloys—an overview. *Materials Science and Engineering: A*, 263(2):243–256, 1999.

[90] E C Santos, K Osakada, M Shiomi, Y Kitamura, and F Abe. Microstructure and mechanical properties of pure titanium models fabricated by selective laser melting. *Proceedings of the Institution of Mechanical Engineers, Part C: Journal of Mechanical Engineering Science*, 218(7):711–719, jul 2004.

[91] Weichang Xue, B. Vamsi Krishna, Amit Bandyopadhyay, and Susmita Bose. Processing and biocompatibility evaluation of laser processed porous titanium. *Acta Biomaterialia*, 3(6):1007–1018, nov 2007.

[92] Mushtaq Khan and Phill Dickens. Selective laser melting (SLM) of pure gold. *Gold Bulletin*, 43(2):114–121, jun 2010.

[93] P.A. Lykov, E.V. Safonov, and A.M. Akhmedianov. Selective laser melting of copper. *Materials Science Forum*, 843:284–288, feb 2016.

[94] S.R. Pogson, P. Fox, C.J. Sutcliffe, and W. O'Neill. The production of copper parts using DMLR. *Rapid Prototyping Journal*, 9(5):334–343, dec 2003.

[95] D.A. Ramirez, L.E. Murr, E. Martinez, D.H. Hernandez, J.L. Martinez, B.I. Machado, F. Medina, P. Frigola, and R.B. Wicker. Novel precipitate–microstructural architecture developed in the fabrication of solid copper components by additive manufacturing using electron beam melting. *Acta Materialia*, 59(10):4088–4099, jun 2011.

[96] Toshi-Taka Ikeshoji, Kazuya Nakamura, Makiko Yonehara, Ken Imai, and Hideki Kyogoku. Selective laser melting of pure copper. *JOM*, 70(3):396–400, dec 2017.

[97] Robert Walker. The production, microstructure, and properties of wrought iron. *Journal of Chemical Education*, 79(4):443, apr 2002.

[98] Libo Zhou, Tiechui Yuan, Ruidi Li, Jianzhong Tang, Guohua Wang, and Kaixuan Guo. Selective laser melting of pure tantalum: Densification, microstructure and mechanical behaviors. *Materials Science and Engineering: A*, 707:443–451, nov 2017.

[99] Aljaž Iveković, Neda Omidvari, Bey Vrancken, Karel Lietaert, Lore Thijs, Kim Vanmeensel, Jef Vleugels, and Jean-Pierre Kruth. Selective laser melting of tungsten and tungsten alloys. *International Journal of Refractory Metals and Hard Materials*, 72:27–32, apr 2018.

[100] Ming Li, Wenchao Du, Alaa Elwany, Zhijian Pei, and Chao Ma. Binder jetting additive manufacturing of metals: A literature review. In *International Manufacturing Science and Engineering Conference*, volume 58745, page V001T01A033. American Society of Mechanical Engineers, 2019.

[101] Issa Rishmawi, Mehrnaz Salarian, and Mihaela Vlasea. Tailoring green and sintered density of pure iron parts using binder jetting additive manufacturing. *Additive Manufacturing*, 24:508–520, 2018.

[102] Dirk Herzog, Vanessa Seyda, Eric Wycisk, and Claus Emmelmann. Additive manufacturing of metals. *Acta Materialia*, 117:371–392, sep 2016.

[103] M. Badrossamay and T.H.C. Childs. Further studies in selective laser melting of stainless and tool steel powders. *International Journal of Machine Tools and Manufacture*, 47(5):779–784, apr 2007.

[104] Holly D. Carlton, Abdel Haboub, Gilbert F. Gallegos, Dilworth Y. Parkinson, and Alastair A. MacDowell. Damage evolution and failure mechanisms in additively manufactured stainless steel. *Materials Science and Engineering: A*, 651:406–414, jan 2016.

[105] P G E Jerrard, L Hao, and K E Evans. Experimental investigation into selective laser melting of austenitic and martensitic stainless steel powder mixtures. *Proceedings of the Institution of Mechanical Engineers, Part B: Journal of Engineering Manufacture*, 223(11):1409–1416, jun 2009.

[106] Amanda S. Wu, Donald W. Brown, Mukul Kumar, Gilbert F. Gallegos, and Wayne E. King. An experimental investigation into additive manufacturing-induced residual stresses in 316l stainless steel. *Metallurgical and Materials Transactions A*, 45(13):6260–6270, sep 2014.

[107] B Verlee, T Dormal, and J Lecomte-Beckers. Density and porosity control of sintered 316l stainless steel parts produced by additive manufacturing. *Powder Metallurgy*, 55(4):260–267, sep 2012.

[108] K. Saeidi, X. Gao, Y. Zhong, and Z.J. Shen. Hardened austenite steel with columnar sub-grain structure formed by laser melting. *Materials Science and Engineering: A*, 625:221–229, feb 2015.

[109] F Bartolomeu, M Buciumeanu, E Pinto, N Alves, O Carvalho, FS Silva, and G Miranda. 316l stainless steel mechanical and tribological behavior—a comparison between selective laser melting, hot pressing and conventional casting. *Additive Manufacturing*, 16:81–89, 2017.

[110] Hengfeng Gu, Haijun Gong, Deepankar Pal, Khalid Rafi, Thomas Starr, Brent Stucker, et al. Influences of energy density on porosity and microstructure of selective laser melted 17-4ph stainless steel. In *2013 Solid Freeform Fabrication Symposium*, volume 474, 2013.

[111] Zhiheng Hu, Haihong Zhu, Hu Zhang, and Xiaoyan Zeng. Experimental investigation on selective laser melting of 17-4ph stainless steel. *Optics & Laser Technology*, 87:17–25, jan 2017.

[112] Lawrence E Murr, Edwin Martinez, Jennifer Hernandez, Shane Collins, Krista N Amato, Sara M Gaytan, and Patrick W Shindo. Microstructures

and properties of 17-4 ph stainless steel fabricated by selective laser melting. *Journal of Materials Research and Technology*, 1(3):167–177, 2012.

[113] Yu Sun, Rainer J Hebert, and Mark Aindow. Effect of heat treatments on microstructural evolution of additively manufactured and wrought 17-4ph stainless steel. *Materials & Design*, 156:429–440, 2018.

[114] Christoph Turk, Horst Zunko, Christin Aumayr, Harald Leitner, and Marianne Kapp. Advances in maraging steels for additive manufacturing. *BHM Berg- und Hüttenmännische Monatshefte*, feb 2019.

[115] Eric A. Jägle, Zhendong Sheng, Liang Wu, Lin Lu, Jeroen Risse, Andreas Weisheit, and Dierk Raabe. Precipitation reactions in age-hardenable alloys during laser additive manufacturing. *JOM*, 68(3):943–949, jan 2016.

[116] D. Croccolo, M. De Agostinis, S. Fini, G. Olmi, A. Vranic, and S. Ciric-Kostic. Influence of the build orientation on the fatigue strength of EOS maraging steel produced by additive metal machine. *Fatigue & Fracture of Engineering Materials & Structures*, 39(5):637–647, feb 2016.

[117] Eric Jägle, Zhendong Sheng, Philipp Kürnsteiner, Sörn Ocylok, Andreas Weisheit, and Dierk Raabe. Comparison of maraging steel micro- and nanostructure produced conventionally and by laser additive manufacturing. *Materials*, 10(1):8, dec 2016.

[118] G. Casalino, S.L. Campanelli, N. Contuzzi, and A.D. Ludovico. Experimental investigation and statistical optimisation of the selective laser melting process of a maraging steel. *Optics & Laser Technology*, 65:151–158, jan 2015.

[119] R. Mertens, B. Vrancken, N. Holmstock, Y. Kinds, J.-P. Kruth, and J. Van Humbeeck. Influence of powder bed preheating on microstructure and mechanical properties of h13 tool steel SLM parts. *Physics Procedia*, 83:882–890, 2016.

[120] Andrew J. Pinkerton and Lin Li. Direct additive laser manufacturing using gas- and water-atomised h13 tool steel powders. *The International Journal of Advanced Manufacturing Technology*, 25(5-6):471–479, jun 2004.

[121] Zhenguo Nie, Gang Wang, James D. McGuffin-Cawley, Badri Narayanan, Shenjia Zhang, David Schwam, Michael Kottman, and Yiming (Kevin) Rong. Experimental study and modeling of h13 steel deposition using laser hot-wire additive

manufacturing. *Journal of Materials Processing Technology*, 235:171–186, sep 2016.

[122] Ryan Cottam, James Wang, and Vladimir Luzin. Characterization of microstructure and residual stress in a 3d h13 tool steel component produced by additive manufacturing. *Journal of Materials Research*, 29(17):1978–1986, aug 2014.

[123] Maciej Mazur, Martin Leary, Matthew McMillan, Joe Elambasseril, and Milan Brandt. SLM additive manufacture of h13 tool steel with conformal cooling and structural lattices. *Rapid Prototyping Journal*, 22(3):504–518, apr 2016.

[124] R. Dörfert, J. Zhang, B. Clausen, H. Freiße, J. Schumacher, and F. Vollertsen. Comparison of the fatigue strength between additively and conventionally fabricated tool steel 1.2344. *Additive Manufacturing*, 27:217–223, may 2019.

[125] ChangJun Chen, Kai Yan, Lanlan Qin, Min Zhang, Xiaonan Wang, Tao Zou, and Zengrong Hu. Effect of heat treatment on microstructure and mechanical properties of laser additively manufactured aisi h13 tool steel. *Journal of Materials Engineering and Performance*, 26(11):5577–5589, 2017.

[126] Chunlei Qiu, Nicholas J.E. Adkins, and Moataz M. Attallah. Selective laser melting of invar 36: Microstructure and properties. *Acta Materialia*, 103:382–395, jan 2016.

[127] Neil J. Harrison, Iain Todd, and Kamran Mumtaz. Thermal expansion coefficients in invar processed by selective laser melting. *Journal of Materials Science*, 52(17):10517–10525, may 2017.

[128] Hamed Asgari, Mehrnaz Salarian, Henry Ma, Adeola Olubamiji, and Mihaela Vlasea. On thermal expansion behavior of invar alloy fabricated by modulated laser powder bed fusion. *Materials & Design*, 160:895–905, dec 2018.

[129] Michael F McGuire. *Stainless steels for design engineers*. Asm International, 2008.

[130] Naoki Maruyama, Masaaki Sugiyama, Takuya Hara, and Hiroshi Tamehiro. Precipitation and phase transformation of copper particles in low alloy ferritic and martensitic steels. *Materials Transactions, JIM*, 40(4):268–277, 1999.

[131] J Gordine. Some problems in welding inconel 718. *WELD J*, 50(11):480, 1971.

[132] Tanja Trosch, Johannes Strößner, Rainer Völkl, and Uwe Glatzel. Microstructure and mechanical properties of selective laser melted inconel 718 compared to forging and casting. *Materials Letters*, 164:428–431, feb 2016.

[133] C. Li, R. anhite, X.Y. Fang, M. Weaver, and Y.B. Guo. Microstructure evolution characteristics of inconel 625 alloy from selective laser melting to heat treatment. *Materials Science and Engineering: A*, 705:20–31, sep 2017.

[134] Shuai Li, Qingsong Wei, Yusheng Shi, Zicheng Zhu, and Danqing Zhang. Microstructure characteristics of inconel 625 superalloy manufactured by selective laser melting. *Journal of Materials Science & Technology*, 31(9):946–952, sep 2015.

[135] N.H. Sateesh, G.C. Mohan Kumar, Krishna Prasad, Srinivasa C.K., and A.R. Vinod. Microstructure and mechanical characterization of laser sintered inconel-625 superalloy. *Procedia Materials Science*, 5:772–779, 2014.

[136] J.A. Gonzalez, J. Mireles, S.W. Stafford, M.A. Perez, C.A. Terrazas, and R.B. Wicker. Characterization of inconel 625 fabricated using powder-bed-based additive manufacturing technologies. *Journal of Materials Processing Technology*, 264:200–210, feb 2019.

[137] G.P. Dinda, A.K. Dasgupta, and J. Mazumder. Laser aided direct metal deposition of inconel 625 superalloy: Microstructural evolution and thermal stability. *Materials Science and Engineering: A*, 509(1-2):98–104, may 2009.

[138] Qingbo Jia and Dongdong Gu. Selective laser melting additive manufacturing of inconel 718 superalloy parts: Densification, microstructure and properties. *Journal of Alloys and Compounds*, 585:713–721, feb 2014.

[139] K. Moussaoui, W. Rubio, M. Mousseigne, T. Sultan, and F. Rezai. Effects of selective laser melting additive manufacturing parameters of inconel 718 on porosity, microstructure and mechanical properties. *Materials Science and Engineering: A*, 735:182–190, sep 2018.

[140] Dunyong Deng, Ru Lin Peng, Håkan Brodin, and Johan Moverare. Microstructure and mechanical properties of inconel 718 produced by selective laser melt-

ing: Sample orientation dependence and effects of post heat treatments. *Materials Science and Engineering: A*, 713:294–306, jan 2018.

[141] Xiaoqing Wang, Xibing Gong, and Kevin Chou. Review on powder-bed laser additive manufacturing of inconel 718 parts. *Proceedings of the Institution of Mechanical Engineers, Part B: Journal of Engineering Manufacture*, 231(11):1890–1903, 2017.

[142] Harald Ernst Helmer, Carolin Körner, and Robert Friedrich Singer. Additive manufacturing of nickel-based superalloy inconel 718 by selective electron beam melting: Processing window and microstructure. *Journal of Materials Research*, 29(17):1987–1996, aug 2014.

[143] V.A. Popovich, E.V. Borisov, A.A. Popovich, V.Sh. Sufiiarov, D.V. Masaylo, and L. Alzina. Functionally graded inconel 718 processed by additive manufacturing: Crystallographic texture, anisotropy of microstructure and mechanical properties. *Materials & Design*, 114:441–449, jan 2017.

[144] K.N. Amato, S.M. Gaytan, L.E. Murr, E. Martinez, P.W. Shindo, J. Hernandez, S. Collins, and F. Medina. Microstructures and mechanical behavior of inconel 718 fabricated by selective laser melting. *Acta Materialia*, 60(5):2229–2239, mar 2012.

[145] C.-M. Kuo, Y.-T. Yang, H.-Y. Bor, C.-N. Wei, and C.-C. Tai. Aging effects on the microstructure and creep behavior of inconel 718 superalloy. *Materials Science and Engineering: A*, 510-511:289–294, jun 2009.

[146] Vani Shankar, K Bhanu Sankara Rao, and S.L Mannan. Microstructure and mechanical properties of inconel 625 superalloy. *Journal of Nuclear Materials*, 288(2-3):222–232, feb 2001.

[147] Lawrence E. Murr, Edwin Martinez, Jennifer Hernandez, Shane Collins, Krista N. Amato, Sara M. Gaytan, and Patrick W. Shindo. Microstructures and properties of 17-4 PH stainless steel fabricated by selective laser melting. *Journal of Materials Research and Technology*, 1(3):167–177, oct 2012.

[148] Theodoros Koutsoukis, Spiros Zinelis, George Eliades, Khalid Al-Wazzan, Mohammed Al Rifaiy, and Youssef S. Al Jabbari. Selective laser melting technique of co-cr dental alloys: A review of structure and properties and comparative

analysis with other available techniques. *Journal of Prosthodontics*, 24(4):303–312, jun 2015.

[149] Kedar Mallik Mantrala, Mitun Das, Vamsi Krishna Balla, Ch. Srinivasa Rao, and V. V. S. Kesava Rao. Additive manufacturing of co-cr-mo alloy: Influence of heat treatment on microstructure, tribological, and electrochemical properties. *Frontiers in Mechanical Engineering*, 1, mar 2015.

[150] Atsushi Takaichi, Suyalatu, Takayuki Nakamoto, Natsuka Joko, Naoyuki Nomura, Yusuke Tsutsumi, Satoshi Migita, Hisashi Doi, Shingo Kurosu, Akihiko Chiba, Noriyuki Wakabayashi, Yoshimasa Igarashi, and Takao Hanawa. Microstructures and mechanical properties of co–29cr–6mo alloy fabricated by selective laser melting process for dental applications. *Journal of the Mechanical Behavior of Biomedical Materials*, 21:67–76, may 2013.

[151] J.V. Giacchi, C.N. Morando, O. Fornaro, and H.A. Palacio. Microstructural characterization of as-cast biocompatible co–cr–mo alloys. *Materials Characterization*, 62(1):53–61, jan 2011.

[152] B.S. Murty, J.W. Yeh, and S. Ranganathan. High-entropy alloy solid solutions. In *High Entropy Alloys*, pages 91–118. Elsevier, 2014.

[153] X.P. Tan, P. Wang, Y. Kok, W.Q. Toh, Z. Sun, S.M.L. Nai, M. Descoins, D. Mangelinck, E. Liu, and S.B. Tor. Carbide precipitation characteristics in additive manufacturing of co-cr-mo alloy via selective electron beam melting. *Scripta Materialia*, 143:117–121, jan 2018.

[154] A Bordin, A Ghiotti, S Bruschi, L Facchini, and F Bucciotti. Machinability characteristics of wrought and ebm cocrmo alloys. *Procedia CIRP*, 14:89–94, 2014.

[155] Tanja Matković, Prosper Matković, and Jadranka Malina. Effects of ni and mo on the microstructure and some other properties of co–cr dental alloys. *Journal of Alloys and Compounds*, 366(1-2):293–297, mar 2004.

[156] Nesma T. Aboulkhair, Nicola M. Everitt, Ian Ashcroft, and Chris Tuck. Reducing porosity in AlSi10mg parts processed by selective laser melting. *Additive Manufacturing*, 1-4:77–86, oct 2014.

[157] K. Kempen, L. Thijs, J. Van Humbeeck, and J.-P. Kruth. Mechanical properties of AlSi10mg produced by selective laser melting. *Physics Procedia*, 39:439–446, 2012.

[158] M. Javidani, J. Arreguin-Zavala, J. Danovitch, Y. Tian, and M. Brochu. Additive manufacturing of AlSi10mg alloy using direct energy deposition: Microstructure and hardness characterization. *Journal of Thermal Spray Technology*, 26(4):587–597, dec 2016.

[159] Noriko Read, Wei Wang, Khamis Essa, and Moataz M. Attallah. Selective laser melting of AlSi10mg alloy: Process optimisation and mechanical properties development. *Materials & Design (1980-2015)*, 65:417–424, jan 2015.

[160] L.P. Lam, D.Q. Zhang, Z.H. Liu, and C.K. Chua. Phase analysis and microstructure characterisation of AlSi10mg parts produced by selective laser melting. *Virtual and Physical Prototyping*, 10(4):207–215, oct 2015.

[161] Erhard Brandl, Ulrike Heckenberger, Vitus Holzinger, and Damien Buchbinder. Additive manufactured AlSi10mg samples using selective laser melting (SLM): Microstructure, high cycle fatigue, and fracture behavior. *Materials & Design*, 34:159–169, feb 2012.

[162] Idan Rosenthal, Adin Stern, and Nachum Frage. Microstructure and mechanical properties of AlSi10mg parts produced by the laser beam additive manufacturing (AM) technology. *Metallography, Microstructure, and Analysis*, 3(6):448–453, oct 2014.

[163] Y. Ding, J.A. Muñiz-Lerma, M. Trask, S. Chou, A. Walker, and M. Brochu. Microstructure and mechanical property considerations in additive manufacturing of aluminum alloys. *MRS Bulletin*, 41(10):745–751, oct 2016.

[164] Syed Z. Uddin, Lawrence E. Murr, Cesar A. Terrazas, Philip Morton, David A. Roberson, and Ryan B. Wicker. Processing and characterization of crack-free aluminum 6061 using high-temperature heating in laser powder bed fusion additive manufacturing. *Additive Manufacturing*, 22:405–415, aug 2018.

[165] Christopher E. Roberts, David Bourell, Trevor Watt, and Julien Cohen. A novel processing approach for additive manufacturing of commercial aluminum alloys. *Physics Procedia*, 83:909–917, 2016.

[166] D. Carluccio, M.J. Bermingham, Y. Zhang, D.H. StJohn, K. Yang, P.A. Rometsch, X. Wu, and M.S. Dargusch. Grain refinement of laser remelted al-7si and 6061 aluminium alloys with tibor® and scandium additions. *Journal of Manufacturing Processes*, 35:715–720, oct 2018.

[167] T. Wang, Y.Y. Zhu, S.Q. Zhang, H.B. Tang, and H.M. Wang. Grain morphology evolution behavior of titanium alloy components during laser melting deposition additive manufacturing. *Journal of Alloys and Compounds*, 632:505–513, may 2015.

[168] Yan-Yan Zhu, Hai-Bo Tang, Zhuo Li, Cheng Xu, and Bei He. Solidification behavior and grain morphology of laser additive manufacturing titanium alloys. *Journal of Alloys and Compounds*, 777:712–716, mar 2019.

[169] L.E. Murr, S.A. Quinones, S.M. Gaytan, M.I. Lopez, A. Rodela, E.Y. Martinez, D.H. Hernandez, E. Martinez, F. Medina, and R.B. Wicker. Microstructure and mechanical behavior of ti–6al–4v produced by rapid-layer manufacturing, for biomedical applications. *Journal of the Mechanical Behavior of Biomedical Materials*, 2(1):20–32, jan 2009.

[170] W. Xu, M. Brandt, S. Sun, J. Elambasseril, Q. Liu, K. Latham, K. Xia, and M. Qian. Additive manufacturing of strong and ductile ti–6al–4v by selective laser melting via in situ martensite decomposition. *Acta Materialia*, 85:74–84, feb 2015.

[171] Sarah Wolff, Taekyung Lee, Eric Faierson, Kornel Ehmann, and Jian Cao. Anisotropic properties of directed energy deposition (DED)-processed ti–6al–4v. *Journal of Manufacturing Processes*, 24:397–405, oct 2016.

[172] W. Xu, E.W. Lui, A. Pateras, M. Qian, and M. Brandt. In situ tailoring microstructure in additively manufactured ti-6al-4v for superior mechanical performance. *Acta Materialia*, 125:390–400, feb 2017.

[173] Manikandakumar Shunmugavel, Ashwin Polishetty, and Guy Littlefair. Microstructure and mechanical properties of wrought and additive manufactured ti-6al-4 v cylindrical bars. *Procedia Technology*, 20:231–236, 2015.

[174] L Jyothish Kumar and CG Krishnadas Nair. Current trends of additive manufacturing in the aerospace industry. In *Advances in 3D printing & additive manufacturing technologies*, pages 39–54. Springer, 2017.

[175] Edward Chlebus, Bogumiła Kuźnicka, Tomasz Kurzynowski, and Bogdan Dybała. Microstructure and mechanical behaviour of ti__6al__7nb alloy produced by selective laser melting. *Materials Characterization*, 62(5):488–495, may 2011.

[176] Zongge Jiao, Jun Fu, Zhuo Li, Xu Cheng, Haibo Tang, and Huaming Wang. The spatial distribution of phase in laser melting deposition additive manufactured ti-10v-2fe-3al alloy. *Materials & Design*, 154:108–116, sep 2018.

[177] Hamid Azizi, Hatem Zurob, Bipasha Bose, S. Reza Ghiaasiaan, Xiang Wang, Simon Coulson, Vlad Duz, and A.B. Phillion. Additive manufacturing of a novel ti-al-v-fe alloy using selective laser melting. *Additive Manufacturing*, 21:529–535, may 2018.

[178] Xinhua Wu, Jing Liang, Junfa Mei, C. Mitchell, P.S. Goodwin, and W. Voice. Microstructures of laser-deposited ti–6al–4v. *Materials & Design*, 25(2):137–144, apr 2004.

[179] Lore Thijs, Frederik Verhaeghe, Tom Craeghs, Jan Van Humbeeck, and Jean-Pierre Kruth. A study of the microstructural evolution during selective laser melting of ti–6al–4v. *Acta Materialia*, 58(9):3303–3312, may 2010.

[180] S. S. Al-Bermani, M. L. Blackmore, W. Zhang, and I. Todd. The origin of microstructural diversity, texture, and mechanical properties in electron beam melted ti-6al-4v. *Metallurgical and Materials Transactions A*, 41(13):3422–3434, aug 2010.

[181] Beth E. Carroll, Todd A. Palmer, and Allison M. Beese. Anisotropic tensile behavior of ti–6al–4v components fabricated with directed energy deposition additive manufacturing. *Acta Materialia*, 87:309–320, apr 2015.

[182] Avi Leon, Amnon Shirizly, and Eli Aghion. Corrosion behavior of alsi10mg alloy produced by additive manufacturing (am) vs. its counterpart gravity cast alloy. *Metals*, 6(7):148, 2016.

[183] G Pitchayyapillai, P Seenikannan, P Balasundar, and P Narayanasamy. Effect of nano-silver on microstructure, mechanical and tribological properties of cast 6061 aluminum alloy. *Transactions of Nonferrous Metals Society of China*, 27(10):2137–2145, 2017.

[184] W. Kurz, C. Bezençon, and M. Gäumann. Columnar to equiaxed transition in solidification processing. *Science and Technology of Advanced Materials*, 2(1):185–191, jan 2001.

[185] Sindo Kou. Welding metallurgy. *New Jersey, USA*, pages 431–446, 2003.

[186] Edouard Chauvet, Catherine Tassin, Jean-Jacques Blandin, Rémy Dendievel, and Guilhem Martin. Producing ni-base superalloys single crystal by selective electron beam melting. *Scripta Materialia*, 152:15–19, jul 2018.

[187] X.P. Li, M.P. Roberts, S. O'Keeffe, and T.B. Sercombe. Selective laser melting of zr-based bulk metallic glasses: Processing, microstructure and mechanical properties. *Materials & Design*, 112:217–226, dec 2016.

[188] Ning Li, Jianji Zhang, Wei Xing, Di Ouyang, and Lin Liu. 3d printing of fe-based bulk metallic glass composites with combined high strength and fracture toughness. *Materials & Design*, 143:285–296, apr 2018.

[189] Di Ouyang, Ning Li, Wei Xing, Jianji Zhang, and Lin Liu. 3d printing of crack-free high strength zr-based bulk metallic glass composite by selective laser melting. *Intermetallics*, 90:128–134, nov 2017.

[190] J.D. Hunt. Steady state columnar and equiaxed growth of dendrites and eutectic. *Materials Science and Engineering*, 65(1):75–83, jul 1984.

[191] J. A. Spittle. Columnar to equiaxed grain transition in as solidified alloys. *International Materials Reviews*, 51(4):247–269, aug 2006.

[192] Thomas Lienert, Thomas Siewert, Sudarsanam Babu, Viola Acoff, and Standard Welding Procedure Specifications. *ASM Handbook, Volume 6A: Welding Fundamentals and Processes*. ASM International Materials Park, OH, 2011.

[193] Johannes A. Koepf, Martin R. Gotterbarm, Matthias Markl, and Carolin Körner. 3d multi-layer grain structure simulation of powder bed fusion additive manufacturing. *Acta Materialia*, 152:119–126, jun 2018.

[194] Zhuqing Wang, Todd A. Palmer, and Allison M. Beese. Effect of processing parameters on microstructure and tensile properties of austenitic stainless steel 304l made by directed energy deposition additive manufacturing. *Acta Materialia*, 110:226–235, may 2016.

[195] Guo-Chao Li, Jia Li, Xiang-Jun Tian, Xu Cheng, Bei He, and Hua-Ming Wang. Microstructure and properties of a novel titanium alloy ti-6al-2v-1.5 mo-0.5 zr-0.3 si manufactured by laser additive manufacturing. *Materials Science and Engineering: A*, 684:233–238, 2017.

[196] Guillaume Marion, Georges Cailletaud, Christophe Colin, and Matthieu Mazière. A finite element model for the simulation of direct metal deposition. In *International Congress on Applications of Lasers & Electro-Optics*. Laser Institute of America, 2014.

[197] J Ronda and GJ Oliver. Consistent thermo-mechano-metallurgical model of welded steel with unified approach to derivation of phase evolution laws and transformation-induced plasticity. *Computer Methods in Applied Mechanics and Engineering*, 189(2):361–418, 2000.

[198] Qi Zhang, Jiawen Xie, Zhenyuan Gao, Tyler London, David Griffiths, and Victor Oancea. A metallurgical phase transformation framework applied to slm additive manufacturing processes. *Materials & Design*, 166:107618, 2019.

[199] Joy Gockel, Jack Beuth, and Karen Taminger. Integrated control of solidification microstructure and melt pool dimensions in electron beam wire feed additive manufacturing of ti-6al-4v. *Additive Manufacturing*, 1-4:119–126, oct 2014.

[200] Sneha P. Narra, Ross Cunningham, Jack Beuth, and Anthony D. Rollett. Location specific solidification microstructure control in electron beam melting of ti-6al-4v. *Additive Manufacturing*, 19:160–166, jan 2018.

[201] Joy Gockel and Jack Beuth. Understanding ti-6al-4v microstructure control in additive manufacturing via process maps. *Solid Freeform Fabrication Proceedings, Austin, TX, Aug*, pages 12–14, 2013.

[202] Trevor Keller, Greta Lindwall, Supriyo Ghosh, Li Ma, Brandon M. Lane, Fan Zhang, Ursula R. Kattner, Eric A. Lass, Jarred C. Heigel, Yaakov Idell, Mau-

reen E. Williams, Andrew J. Allen, Jonathan E. Guyer, and Lyle E. Levine. Application of finite element, phase-field, and CALPHAD-based methods to additive manufacturing of ni-based superalloys. *Acta Materialia*, 139:244–253, oct 2017.

[203] Liang-Xing Lu, N. Sridhar, and Yong-Wei Zhang. Phase field simulation of powder bed-based additive manufacturing. *Acta Materialia*, 144:801–809, feb 2018.

[204] Theron M. Rodgers, Jonathan D. Madison, and Veena Tikare. Simulation of metal additive manufacturing microstructures using kinetic monte carlo. *Computational Materials Science*, 135:78–89, jul 2017.

[205] Ranadip Acharya, John A. Sharon, and Alexander Staroselsky. Prediction of microstructure in laser powder bed fusion process. *Acta Materialia*, 124:360–371, feb 2017.

[206] Lawrence E. Murr. Frontiers of 3d printing/additive manufacturing: from human organs to aircraft fabrication†. *Journal of Materials Science & Technology*, 32(10):987–995, oct 2016.

[207] TS Srivatsan and TS Sudarshan. *Additive manufacturing: innovations, advances, and applications*. CRC Press, 2015.

[208] Shuo Yin, Chaoyue Chen, and Rocco Lupoi. Nanostructured metal coatings via cold spray. In *Advanced Nanomaterials and Coatings by Thermal Spray*, pages 27–60. Elsevier, 2019.

[209] ZF Zhang, J Eckert, and L Schultz. Difference in compressive and tensile fracture mechanisms of zr59cu20al10ni8ti3 bulk metallic glass. *Acta Materialia*, 51(4):1167–1179, 2003.

[210] Douglas C Hofmann, Jin-Yoo Suh, Aaron Wiest, Gang Duan, Mary-Laura Lind, Marios D Demetriou, and William L Johnson. Designing metallic glass matrix composites with high toughness and tensile ductility. *Nature*, 451(7182):1085, 2008.

[211] Yong Zhang, Ting Ting Zuo, Zhi Tang, Michael C. Gao, Karin A. Dahmen, Peter K. Liaw, and Zhao Ping Lu. Microstructures and properties of high-entropy alloys. *Progress in Materials Science*, 61:1–93, apr 2014.

[212] Simon Pauly, Lukas Löber, Romy Petters, Mihai Stoica, Sergio Scudino, Uta Kühn, and Jürgen Eckert. Processing metallic glasses by selective laser melting. *Materials Today*, 16(1-2):37–41, 2013.

[213] Andrew Dickins, S Lawes, P Stravroulakis, and R Leach. Design of a multi-sensor in-situ inspection system for additive manufacturing. *Proc. ASPE/euspen Advancing Precision in Additive Manufacturing*, pages 248–242, 2018.

[214] Ralph B. Dinwiddie, Ryan R. Dehoff, Peter D. Lloyd, Larry E. Lowe, and Joe B. Ulrich. Thermographic in-situ process monitoring of the electron-beam melting technology used in additive manufacturing. In Gregory R. Stockton and Fred P. Colbert, editors, *Thermosense: Thermal Infrared Applications XXXV*. SPIE, may 2013.

[215] S. Clijsters, T. Craeghs, S. Buls, K. Kempen, and J.-P. Kruth. In situ quality control of the selective laser melting process using a high-speed, real-time melt pool monitoring system. *The International Journal of Advanced Manufacturing Technology*, 75(5-8):1089–1101, aug 2014.

[216] Mohammad H. Farshidianfar, Amir Khajepour, and Adrian Gerlich. Real-time control of microstructure in laser additive manufacturing. *The International Journal of Advanced Manufacturing Technology*, 82(5-8):1173–1186, jul 2015.

[217] S.A. Shevchik, C. Kenel, C. Leinenbach, and K. Wasmer. Acoustic emission for in situ quality monitoring in additive manufacturing using spectral convolutional neural networks. *Additive Manufacturing*, 21:598–604, may 2018.

[218] A Thompson, I Maskery, and R K Leach. X-ray computed tomography for additive manufacturing: a review. *Measurement Science and Technology*, 27(7):072001, jun 2016.

[219] Chu Lun Alex Leung, Sebastian Marussi, Robert C. Atwood, Michael Towrie, Philip J. Withers, and Peter D. Lee. In situ x-ray imaging of defect and molten pool dynamics in laser additive manufacturing. *Nature Communications*, 9(1), apr 2018.

[220] Cang Zhao, Kamel Fezzaa, Ross W. Cunningham, Haidan Wen, Francesco De Carlo, Lianyi Chen, Anthony D. Rollett, and Tao Sun. Real-time monitoring of

laser powder bed fusion process using high-speed x-ray imaging and diffraction. *Scientific Reports*, 7(1), jun 2017.

[221] Farshid Hajializadeh and Ayhan Ince. Finite element–based numerical modeling framework for additive manufacturing process. *Material Design & Processing Communications*, 1(1):e28, feb 2019.

[222] Panagiotis Michaleris. Modeling metal deposition in heat transfer analyses of additive manufacturing processes. *Finite Elements in Analysis and Design*, 86:51–60, sep 2014.

[223] P Peyre, P Aubry, R Fabbro, R Neveu, and A Longuet. Analytical and numerical modelling of the direct metal deposition laser process. *Journal of Physics D: Applied Physics*, 41(2):025403, jan 2008.

[224] I.A. Roberts, C.J. Wang, R. Esterlein, M. Stanford, and D.J. Mynors. A three-dimensional finite element analysis of the temperature field during laser melting of metal powders in additive layer manufacturing. *International Journal of Machine Tools and Manufacture*, 49(12-13):916–923, oct 2009.

[225] Panagis Foteinopoulos, Alexios Papacharalampopoulos, and Panagiotis Stavropoulos. On thermal modeling of additive manufacturing processes. *CIRP Journal of Manufacturing Science and Technology*, 20:66–83, jan 2018.

[226] M.M. Francois, A. Sun, W.E. King, N.J. Henson, D. Tourret, C.A. Bronkhorst, N.N. Carlson, C.K. Newman, T. Haut, J. Bakosi, J.W. Gibbs, V. Livescu, S.A. Vander Wiel, A.J. Clarke, M.W. Schraad, T. Blacker, H. Lim, T. Rodgers, S. Owen, F. Abdeljawad, J. Madison, A.T. Anderson, J-L. Fattebert, R.M. Ferencz, N.E. Hodge, S.A. Khairallah, and O. Walton. Modeling of additive manufacturing processes for metals: Challenges and opportunities. *Current Opinion in Solid State and Materials Science*, 21(4):198–206, aug 2017.

[227] V. Manvatkar, A. De, and T. DebRoy. Spatial variation of melt pool geometry, peak temperature and solidification parameters during laser assisted additive manufacturing process. *Materials Science and Technology*, 31(8):924–930, nov 2014.

[228] Mahdi Jamshidinia, Fanrong Kong, and Radovan Kovacevic. The coupled cfd-fem model of electron beam melting®(ebm). 2013.

[229] S Marimuthu, RM Eghlio, AJ Pinkerton, and L Li. Coupled computational fluid dynamic and finite element multiphase modeling of laser weld bead geometry formation and joint strengths. *Journal of Manufacturing Science and Engineering*, 135(1):011004, 2013.

[230] F-J Gürtler, M Karg, K-H Leitz, and M Schmidt. Simulation of laser beam melting of steel powders using the three-dimensional volume of fluid method. *Physics Procedia*, 41:881–886, 2013.

[231] Saad A Khairallah and Andy Anderson. Mesoscopic simulation model of selective laser melting of stainless steel powder. *Journal of Materials Processing Technology*, 214(11):2627–2636, 2014.

[232] M.J. Baker, S. Daniels, P.G. Young, and G.R. Tabor. Investigation of flow through a computationally generated packed column using CFD and additive layer manufacturing. *Computers & Chemical Engineering*, 67:159–165, aug 2014.

[233] Bastian E. Rapp. Engineering mathematics. In *Microfluidics: Modelling, Mechanics and Mathematics*, pages 21–50. Elsevier, 2017.

[234] Shengyong Pang, Xin Chen, Jianxin Zhou, Xinyu Shao, and Chunming Wang. 3d transient multiphase model for keyhole, vapor plume, and weld pool dynamics in laser welding including the ambient pressure effect. *Optics and Lasers in Engineering*, 74:47–58, nov 2015.

[235] L Parry, IA Ashcroft, and Ricky D Wildman. Understanding the effect of laser scan strategy on residual stress in selective laser melting through thermo-mechanical simulation. *Additive Manufacturing*, 12:1–15, 2016.

[236] Andreas Lundbäck and Lars-Erik Lindgren. Modelling of metal deposition. *Finite Elements in Analysis and Design*, 47(10):1169–1177, oct 2011.

[237] Matthew J Dantin, William M Furr, and Matthew W Priddy. Towards an open-source, preprocessing framework for simulating material deposition for a directed energy deposition process. 2018.

[238] John Goldak, Aditya Chakravarti, and Malcolm Bibby. A new finite element model for welding heat sources. *Metallurgical Transactions B*, 15(2):299–305, jun 1984.

[239] M Hashemzadeh and B Chen. Comparison between different heat sources types in thin-plate welding simulation. In *Developments in Maritime Transportation and Exploitation of Sea Resources*, pages 329–335. CRC Press, oct 2013.

[240] T. Mukherjee, W. Zhang, and T. DebRoy. An improved prediction of residual stresses and distortion in additive manufacturing. *Computational Materials Science*, 126:360–372, jan 2017.

[241] Dean Deng, Hidekazu Murakawa, and Wei Liang. Numerical and experimental investigations on welding residual stress in multi-pass butt-welded austenitic stainless steel pipe. *Computational Materials Science*, 42(2):234–244, 2008.

[242] A Longuet, Y Robert, E Aeby-Gautier, B Appolaire, JF Mariage, C Colin, and G Cailletaud. A multiphase mechanical model for ti–6al–4v: Application to the modeling of laser assisted processing. *Computational Materials Science*, 46(3):761–766, 2009.

[243] Fei Huyan, Peter Hedström, and Annika Borgenstam. Modelling of the fraction of martensite in low-alloy steels. *Materials Today: Proceedings*, 2:S561–S564, 2015.

[244] Z Zhang, ZJ Tan, XX Yao, CP Hu, P Ge, ZY Wan, JY Li, and Q Wu. Numerical methods for microstructural evolutions in laser additive manufacturing. *Computers & Mathematics with Applications*, 78(7):2296–2307, 2019.

[245] Ying Liu, Matthias Militzer, and Michel Perez. Phase field modelling of abnormal grain growth. *Materials*, 12(24):4048, 2019.

[246] Marco Berghoff, Michael Selzer, and Britta Nestler. Phase-field simulations at the atomic scale in comparison to molecular dynamics. *The Scientific World Journal*, 2013:1–8, 2013.

[247] Sen Luo, Miaoyong Zhu, and Seppo Louhenkilpi. Numerical simulation of solidification structure of high carbon steel in continuous casting using cellular automaton method. *ISIJ International*, 52(5):823–830, 2012.

[248] Shijia Chen, Gildas Guillemot, and Charles-André Gandin. 3d coupled cellular automaton (CA)–finite element (FE) modeling for solidification grain structures in gas tungsten arc welding (GTAW). *ISIJ International*, 54(2):401–407, 2014.

[249] Hsiun Chang Peng and Long Sun Chao. Simulation of dendritic growth in solidification of al-cu alloy by applying the modified cellular automaton model with the growth calculation of nucleus within a cell. *Materials Science Forum*, 594:22–28, aug 2008.

[250] W. Tillmann, C. Schaak, J. Nellesen, M. Schaper, M.E. Aydinöz, and K.-P. Hoyer. Hot isostatic pressing of IN718 components manufactured by selective laser melting. *Additive Manufacturing*, 13:93–102, jan 2017.

[251] Bandar AlMangour, Dariusz Grzesiak, and Jenn-Ming Yang. Selective laser melting of TiB2/316l stainless steel composites: The roles of powder preparation and hot isostatic pressing post-treatment. *Powder Technology*, 309:37–48, mar 2017.

[252] Samuel Tammas-Williams, Philip J. Withers, Iain Todd, and Philip B. Prangnell. The effectiveness of hot isostatic pressing for closing porosity in titanium parts manufactured by selective electron beam melting. *Metallurgical and Materials Transactions A*, 47(5):1939–1946, mar 2016.

[253] S. Tammas-Williams, P.J. Withers, I. Todd, and P.B. Prangnell. Porosity regrowth during heat treatment of hot isostatically pressed additively manufactured titanium components. *Scripta Materialia*, 122:72–76, sep 2016.

[254] Luca Girelli, Marialaura Tocci, Marcello Gelfi, and Annalisa Pola. Study of heat treatment parameters for additively manufactured AlSi10mg in comparison with corresponding cast alloy. *Materials Science and Engineering: A*, 739:317–328, jan 2019.

[255] Naoki Takata, Hirohisa Kodaira, Keito Sekizawa, Asuka Suzuki, and Makoto Kobashi. Change in microstructure of selectively laser melted AlSi10mg alloy with heat treatments. *Materials Science and Engineering: A*, 704:218–228, sep 2017.

[256] Sasan Dadbakhsh, Liang Hao, and Choon Yen Kong. Surface finish improvement of LMD samples using laser polishing. *Virtual and Physical Prototyping*, 5(4):215–221, nov 2010.

[257] A. Lamikiz, J.A. Sánchez, L.N. López de Lacalle, and J.L. Arana. Laser polishing of parts built up by selective laser sintering. *International Journal of Machine Tools and Manufacture*, 47(12-13):2040–2050, oct 2007.

[258] Olusola Oyelola, Peter Crawforth, Rachid M'Saoubi, and Adam T. Clare. Machining of additively manufactured parts: Implications for surface integrity. *Procedia CIRP*, 45:119–122, 2016.

[259] Brandon M Lane, Shawn P Moylan, and Eric P Whitenton. Post-process machining of additive manufactured stainless steel. In *Proceedings of the 2015 ASPE Spring Topical Meeting: Achieving Precision Tolerances in Additive Manufacturing*, pages 27–29, 2015.

[260] Stephen T Newman, Zicheng Zhu, Vimal Dhokia, and Alborz Shokrani. Process planning for additive and subtractive manufacturing technologies. *CIRP Annals*, 64(1):467–470, 2015.

[261] Lin Li, Azadeh Haghighi, and Yiran Yang. A novel 6-axis hybrid additive-subtractive manufacturing process: Design and case studies. *Journal of Manufacturing Processes*, 33:150–160, 2018.

[262] Ashwath Yegyan Kumar, Yun Bai, Anders Eklund, and Christopher B. Williams. The effects of hot isostatic pressing on parts fabricated by binder jetting additive manufacturing. *Additive Manufacturing*, 24:115–124, dec 2018.

[263] Nesma T. Aboulkhair, Ian Maskery, Chris Tuck, Ian Ashcroft, and Nicola M. Everitt. The microstructure and mechanical properties of selectively laser melted AlSi10mg: The effect of a conventional t6-like heat treatment. *Materials Science and Engineering: A*, 667:139–146, jun 2016.

[264] Will Philpott, Mark AE Jepson, and Rachel C Thomson. Comparison of the effects of a conventional heat treatment between cast and selective laser melted in939 alloy. 2016.

[265] Jonathan Pegues, Michael Roach, R. Scott Williamson, and Nima Shamsaei. Surface roughness effects on the fatigue strength of additively manufactured ti-6al-4v. *International Journal of Fatigue*, 116:543–552, nov 2018.

[266] P. Edwards and M. Ramulu. Fatigue performance evaluation of selective laser melted ti–6al–4v. *Materials Science and Engineering: A*, 598:327–337, mar 2014.

[267] A.B. Spierings, T.L. Starr, and K. Wegener. Fatigue performance of additive manufactured metallic parts. *Rapid Prototyping Journal*, 19(2):88–94, mar 2013.

[268] Li Yang, Hengfeng Gu, and Austin Lassell. Surface treatment of ti6al4v parts made by powder bed fusion additive manufacturing processes using electropolishing. In *Proceedings of the Solid Freeform Fabrication (SFF) Symposium, Austin, TX, USA*, pages 4–6, 2014.

[269] V. Urlea and V. Brailovski. Electropolishing and electropolishing-related allowances for powder bed selectively laser-melted ti-6al-4v alloy components. *Journal of Materials Processing Technology*, 242:1–11, apr 2017.

[270] Jae-Hyun Jung, Hyung-Ki Park, Byoung Soo Lee, Jaeho Choi, Bosung Seo, Hyo Kyu Kim, Gun Hee Kim, and Hyung Giun Kim. Study on surface shape control of pure ti fabricated by electron beam melting using electrolytic polishing. *Surface and Coatings Technology*, 324:106–110, sep 2017.

[271] Debajyoti Bhaduri, Pavel Penchev, Afif Batal, Stefan Dimov, Sein Leung Soo, Stella Sten, Urban Harrysson, Zhenxue Zhang, and Hanshan Dong. Laser polishing of 3d printed mesoscale components. *Applied Surface Science*, 405:29–46, may 2017.

[272] Wojciech S. Gora, Yingtao Tian, Aldara Pan Cabo, Marcus Ardron, Robert R.J. Maier, Philip Prangnell, Nicholas J. Weston, and Duncan P. Hand. Enhancing surface finish of additively manufactured titanium and cobalt chrome elements using laser based finishing. *Physics Procedia*, 83:258–263, 2016.

[273] Bandar AlMangour and Jenn-Ming Yang. Improving the surface quality and mechanical properties by shot-peening of 17-4 stainless steel fabricated by additive manufacturing. *Materials & Design*, 110:914–924, nov 2016.

[274] Naor Elad Uzan, Shlomo Ramati, Roni Shneck, Nachum Frage, and Ori Yeheskel. On the effect of shot-peening on fatigue resistance of AlSi10mg

specimens fabricated by additive manufacturing using selective laser melting (AM-SLM). *Additive Manufacturing*, 21:458–464, may 2018.

[275] Shengping Wang, Yongjun Li, Mei Yao, and Renzhi Wang. Compressive residual stress introduced by shot peening. *Journal of Materials Processing Technology*, 73(1-3):64–73, jan 1998.

[276] Robert E. ReedHill Reza Abbaschlan, Lara Abbaschlan. *Physical Metallurgy Principles*. Cengage Learning, 4 edition, 2009.

[277] Andrew Bobel, Louis G Hector Jr, Isaac Chelladurai, Anil K Sachdev, Tyson Brown, Whitney A Poling, Robert Kubic, Benjamin Gould, Cang Zhao, Niranjan Parab, et al. In situ synchrotron x-ray imaging of 4140 steel laser powder bed fusion. *Materialia*, 6:100306, 2019.

[278] G Castro, J Rodríguez, MA Montealegre, JL Arias, A Yañez, S Panedas, and L Rey. Laser additive manufacturing of high added value pieces. *Procedia Engineering*, 132:102–9, 2015.

[279] Donald R Askeland and Wendelin J Wright. *The Science and Engineering of Materials: Seventh Edition*. Van Nostrand Reinhold (International), 2014.

[280] Leifeng Liu, Qingqing Ding, Yuan Zhong, Ji Zou, Jing Wu, Yu-Lung Chiu, Jixue Li, Ze Zhang, Qian Yu, and Zhijian Shen. Dislocation network in additive manufactured steel breaks strength–ductility trade-off. *Materials Today*, 21(4):354–361, 2018.

[281] Zaloa Arechabaleta, Peter van Liempt, and Jilt Sietsma. Unravelling dislocation networks in metals. *Materials Science and Engineering: A*, 710:329–333, 2018.

[282] MA Meyers, O Vöhringer, and VA Lubarda. The onset of twinning in metals: a constitutive description. *Acta materialia*, 49(19):4025–4039, 2001.

[283] MS Pham, B Dovgyy, and PA Hooper. Twinning induced plasticity in austenitic stainless steel 316l made by additive manufacturing. *Materials Science and Engineering: A*, 704:102–111, 2017.

[284] 4140 annealed (lpa) cold drawn steel bar — eaton steel bar company. `https://www.eatonsteel.com/4140-lpa-cold-drawn-steel-bar.html`. Accessed: 2021-05-10.

[285] Jeffrey William Edington. Electron diffraction in the electron microscope. In *Electron Diffraction in the Electron Microscope*, pages 1–77. Springer, 1975.

[286] David B Williams and C Barry Carter. Diffraction in tem. In *Transmission Electron Microscopy*, pages 197–209. Springer, 2009.

[287] Edgar Collins Bain and Harold W Paxton. Alloying elements in steel. *1966, 291 P. AMERICAN SOCIETY FOR METALS, METALS PARK, OHIO*, 1966.

[288] N Stanford, U Carlson, and MR Barnett. Deformation twinning and the hall–petch relation in commercial purity ti. *Metallurgical and Materials Transactions A*, 39(4):934–944, 2008.

[289] William J Sames, FA List, Sreekanth Pannala, Ryan R Dehoff, and Sudarsanam Suresh Babu. The metallurgy and processing science of metal additive manufacturing. *International materials reviews*, 61(5):315–360, 2016.

[290] Lawrence E Murr, Edwin Martinez, Krista N Amato, Sara M Gaytan, Jennifer Hernandez, Diana A Ramirez, Patrick W Shindo, Frank Medina, and Ryan B Wicker. Fabrication of metal and alloy components by additive manufacturing: examples of 3d materials science. *Journal of Materials Research and technology*, 1(1):42–54, 2012.

[291] Lawrence E Murr, Sara M Gaytan, Diana A Ramirez, Edwin Martinez, Jennifer Hernandez, Krista N Amato, Patrick W Shindo, Francisco R Medina, and Ryan B Wicker. Metal fabrication by additive manufacturing using laser and electron beam melting technologies. *Journal of Materials Science & Technology*, 28(1):1–14, 2012.

[292] Manuela Galati, Luca Iuliano, Alessandro Salmi, and Eleonora Atzeni. Modelling energy source and powder properties for the development of a thermal fe model of the ebm additive manufacturing process. *Additive Manufacturing*, 14:49–59, 2017.

[293] Erik R Denlinger and Pan Michaleris. Effect of stress relaxation on distortion in additive manufacturing process modeling. *Additive Manufacturing*, 12:51–59, 2016.

[294] JC Heigel, P Michaleris, and Edward William Reutzel. Thermo-mechanical model development and validation of directed energy deposition additive manufacturing of ti–6al–4v. *Additive manufacturing*, 5:9–19, 2015.

[295] Cengiz Baykasoglu, Oncu Akyildiz, Duygu Candemir, Qingcheng Yang, and Albert C To. Predicting microstructure evolution during directed energy deposition additive manufacturing of ti-6al-4v. *Journal of Manufacturing Science and Engineering*, 140(5), 2018.

[296] Guillaume Marion, Georges Cailletaud, Christophe Colin, and Matthieu Maziere. A finite element model for the simulation of direct metal deposition. In *International Congress on Applications of Lasers & Electro-Optics*, volume 2014, pages 834–841. Laser Institute of America, 2014.

[297] Guglielmo Vastola, Gang Zhang, QX Pei, and Y-W Zhang. Controlling of residual stress in additive manufacturing of ti6al4v by finite element modeling. *Additive Manufacturing*, 12:231–239, 2016.

[298] Benoit de La Batut, Omar Fergani, Vegard Brotan, Markus Bambach, and Mohamed El Mansouri. Analytical and numerical temperature prediction in direct metal deposition of ti6al4v. *Journal of Manufacturing and Materials Processing*, 1(1):3, 2017.

[299] Qingcheng Yang, Pu Zhang, Lin Cheng, Zheng Min, Minking Chyu, and Albert C To. Finite element modeling and validation of thermomechanical behavior of ti-6al-4v in directed energy deposition additive manufacturing. *Additive Manufacturing*, 12:169–177, 2016.

[300] Xufei Lu, Xin Lin, Michele Chiumenti, Miguel Cervera, Yunlong Hu, Xianglin Ji, Liang Ma, Haiou Yang, and Weidong Huang. Residual stress and distortion of rectangular and s-shaped ti-6al-4v parts by directed energy deposition: Modelling and experimental calibration. *Additive Manufacturing*, 26:166–179, 2019.

[301] A Suárez, MJ Tobar, A Yáñez, I Pérez, Jesús Sampedro, V Amigó, and JJ Candel. Modeling of phase transformations of ti6al4 v during laser metal deposition. *Physics Procedia*, 12:666–673, 2011.

[302] M Eshraghi Kakhki, A Kermanpur, and MA Golozar. Numerical simulation of continuous cooling of a low alloy steel to predict microstructure and hardness. *Modelling and simulation in Materials science and Engineering*, 17(4):045007, 2009.

[303] K Babu and TS Prasanna Kumar. Comparison of austenite decomposition models during finite element simulation of water quenching and air cooling of aisi 4140 steel. *Metallurgical and Materials Transactions B*, 45(4):1530–1544, 2014.

[304] Neil S Bailey, Wenda Tan, and Yung C Shin. Predictive modeling and experimental results for residual stresses in laser hardening of aisi 4140 steel by a high power diode laser. *Surface and Coatings Technology*, 203(14):2003–2012, 2009.

[305] Mahmoud Yaakoubi, Mounir Kchaou, and Fakhreddine Dammak. Simulation of the thermomechanical and metallurgical behavior of steels by using abaqus software. *Computational materials science*, 68:297–306, 2013.

[306] Chaowen Li, Yong Wang, Huanxiao Zhan, Tao Han, Bin Han, and Weimin Zhao. Three-dimensional finite element analysis of temperatures and stresses in wide-band laser surface melting processing. *Materials & Design*, 31(7):3366–3373, 2010.

[307] Ritesh S Lakhkar, Yung C Shin, and Matthew John M Krane. Predictive modeling of multi-track laser hardening of aisi 4140 steel. *Materials science and engineering: a*, 480(1-2):209–217, 2008.

[308] W Piekarska. Modelling and analysis of phase transformations and stresses in laser welding process. *Archives of Metallurgy and Materials*, 60, 2015.

[309] Wei Chen, Lianyong Xu, Yongdian Han, Lei Zhao, and Hongyang Jing. Control of residual stress in metal additive manufacturing by low-temperature solid-state phase transformation: An experimental and numerical study. *Additive Manufacturing*, page 102016, 2021.

[310] Matthew J Dantin, William M Furr, and Matthew W Priddy. Towards an open-source, preprocessing framework for simulating material deposition for a directed energy deposition process. *Solid Freeform Fabrication*, pages 1903–1912, 2018.

[311] Lawrence S Darken, Robert W Gurry, and Michael B Bever. Physical chemistry of metals. page 415, 1953.

[312] T Ericsson, S Sjostrom, M Knuuttila, and B Hildenwall. Predicting residual stresses in cases. *Case-Hardened Steels: Microstructural and Residual Stress Effects*, pages 113–139, 1983.

[313] C Sainte-Catherine, Michel Jeandin, D Kechemair, J-P Ricaud, and L Sabatier. Study of dynamic absorptivity at 10.6 μm (co2) and 1.06 μm (nd-yag) wavelengths as a function of temperature. *Le Journal de Physique IV*, 1(C7):C7–151, 1991.

[314] R Indhu, V Vivek, L Sarathkumar, A Bharatish, and S Soundarapandian. Overview of laser absorptivity measurement techniques for material processing. *Lasers in Manufacturing and Materials Processing*, 5(4):458–481, 2018.

[315] Lars-Erik Lindgren. *Computational welding mechanics*. Elsevier, 2014.

[316] Gaoyang Mi, Yanhong Wei, Xiaohong Zhan, Cheng Gu, and Fengyi Yu. A coupled thermal and metallurgical model for welding simulation of ti–6al–4v alloy. *Journal of Materials Processing Technology*, 214(11):2434–2443, 2014.

[317] SH Kang and Yong-Taek Im. Thermo-elasto-plastic finite element analysis of quenching process of carbon steel. *Journal of Materials Processing Technology*, 192:381–390, 2007.

[318] Jayprakash Chipalkatti. *Modeling of austenite decomposition in an AISI 4140 steel*. PhD thesis, University of British Columbia, 1999.

[319] HE Boyer and AG Gray. Allas of isothermal transformation and cooling transformation diagrams, american society for metals. *Metals Park, Ohio, USA*, 1977.

[320] Jiawen Xie, Victor Oancea, and Juan Hurtado. Phase transformations in metals during additive manufacturing processes. In *NAFEMS World Congress*, 2017.

[321] N Kobasko, M Aronov, J Powell, and J Vanas. Intensive quenching of steel parts: Equipment and method. In *Proceedings of the 7th IASME/WSEAS International Conference on Health Transfer, Thermal Engineering and Environment, Moscow, Russia*, pages 20–22, 2009.

[322] HP Hougardy. Werkstoffkunde stahl band 1: grundlagen. *Verlag Stahleisen GmbH, Düsseldorf*, 10:978–3, 1984.

[323] Technical report 2007 the guide for heat treatment of iasc7225 steel (isfahan, iran: Isfahan alloy steel co.). 2007.

[324] Michael Smith. *ABAQUS/Standard User's Manual, Version 6.9*. Dassault Systèmes Simulia Corp, United States, 2009.

[325] George E Totten. *Handbook of residual stress and deformation of steel*. ASM international, 2002.

[326] Valery Rudnev and George E Totten. Asm handbook volume 4c: Induction heating and heat treatment. *ASM International, Ohio*, 2014.

[327] High-Strength Low-Alloy Steels. Asm handbook, volume 1, properties and selection: irons, steels, and high performance alloys section: carbon and low-alloy steel plate. 2005.

[328] Abdil Kus, Yahya Isik, M Cemal Cakir, Salih Coşkun, and Kadir Özdemir. Thermocouple and infrared sensor-based measurement of temperature distribution in metal cutting. *Sensors*, 15(1):1274–1291, 2015.

[329] Tsung-Pin Hung, Hao-En Shi, and Jao-Hwa Kuang. Temperature modeling of aisi 1045 steel during surface hardening processes. *Materials*, 11(10):1815, 2018.

[330] Farid Abed, Catrine ElSayegh, and Akrum Abdul-Latif. Thermo-mechanical description of aisi4140 steel at elevated temperatures. In *Proceedings of the TMS Middle East—Mediterranean Materials Congress on Energy and Infrastructure Systems (MEMA 2015)*, pages 491–499. Springer, 2015.

[331] Enda Keehan, Leif Karlsson, Mattias Thuvander, and E Bergquist. Microstructural characterisation of as-deposited and reheated weld metal—high strength steel weld metals. *Welding in the World*, 51(3):44–49, 2007.

[332] Pingguang Xu, Bingzhe Bai, Fuxing Yin, Hongsheng Fang, and Kotobu Nagai. Microstructure control and wear resistance of grain boundary allotriomorphic ferrite/granular bainite duplex steel. *Materials Science and Engineering: A*, 385(1-2):65–73, 2004.

[333] TA Palmer and JW Elmer. Direct observations of the formation and growth of austenite from pearlite and allotriomorphic ferrite in a c–mn steel arc weld. *Scripta materialia*, 53(5):535–540, 2005.

[334] Haitham El Kadiri, Liang Wang, Mark F Horstemeyer, Reza S Yassar, John T Berry, Sergio Felicelli, and Paul T Wang. Phase transformations in low-alloy steel laser deposits. *Materials Science and Engineering: A*, 494(1-2):10–20, 2008.

[335] R S Amano and PK Rohatgi. Laser engineered net shaping process for sae 4140 low alloy steel. *Materials Science and Engineering: A*, 528(22-23):6680–6693, 2011.

[336] Vahid Javaheri, Satish Kolli, Bjørnar Grande, and David Porter. Insight into the induction hardening behavior of a new 0.40% c microalloyed steel: Effects of initial microstructure and thermal cycles. *Materials Characterization*, 149:165–183, 2019.

[337] Joy Gockel, Jack Beuth, and Karen Taminger. Integrated control of solidification microstructure and melt pool dimensions in electron beam wire feed additive manufacturing of ti-6al-4v. *Additive Manufacturing*, 1:119–126, 2014.

[338] Sneha P Narra, Ross Cunningham, Jack Beuth, and Anthony D Rollett. Location specific solidification microstructure control in electron beam melting of ti-6al-4v. *Additive Manufacturing*, 19:160–166, 2018.

[339] Rahul Patwa and Yung C Shin. Predictive modeling of laser hardening of aisi5150h steels. *International Journal of Machine Tools and Manufacture*, 47(2):307–320, 2007.

[340] Joseph R. Davis. *Metals Handbook Desk Edition, 2nd Ed.* ASM International, 12 1998.

[341] Mark Lusk and Herng-Jeng Jou. On the rule of additivity in phase transformation kinetics. *Metallurgical and Materials Transactions A*, 28(2):287–291, 1997.

[342] Siamak Serajzadeh. Modelling of temperature history and phase transformations during cooling of steel. *Journal of Materials Processing Technology*, 146(3):311–317, 2004.

[343] F Liu, C Yang, G Yang, and Y Zhou. Additivity rule, isothermal and non-isothermal transformations on the basis of an analytical transformation model. *Acta Materialia*, 55(15):5255–5267, 2007.